Precision Determination of the Electroweak Mixing Angle and Test of Neutral Current Universality from the Tau Polarization Measurements at OPAL

by

Kevin Graham
B.Sc., University of Western Ontario, 1993
M.Sc., University of Victoria, 1996

A Dissertation Submitted in Partial Fulfillment of the
Requirements for the Degree of

DOCTOR OF PHILOSOPHY

in the Department of Physics and Astronomy

We accept this thesis as conforming
to the required standard

Dr. J.M. Roney, Supervisor (Department of Physics and Astronomy)

Dr. R.K. Keeler, Departmental Member (Department of Physics and Astronomy)

Dr. A. Astbury, Departmental Member (Department of Physics and Astronomy)

Dr. C. Bohne, Outside Member (Department of Chemistry)

Dr. P. Renton, External Examiner (University of Oxford)

Supervisor: Dr. J.M. Roney

ABSTRACT

Measurements of the τ lepton polarization and forward-backward polarization asymmetry near the Z^0 resonance using the OPAL detector are described. The measurements are based on analyses of $\tau \rightarrow e\bar{\nu}_e\nu_\tau$, $\tau \rightarrow \mu\bar{\nu}_\mu\nu_\tau$, $\tau \rightarrow \pi\,\nu_\tau$, $\tau \rightarrow \rho\nu_\tau$ and $\tau \rightarrow a_1\,\nu_\tau$ decays from a sample of $144,810$ $e^+e^- \rightarrow \tau^+\tau^-$ candidates corresponding to an integrated luminosity of 151 pb^{-1}. Assuming that the τ lepton decays according to V$-$A theory, the average τ polarization near $\sqrt{s} = m_Z$ is measured to be $\langle P_\tau \rangle = (-14.10 \pm 0.73 \pm 0.55)\%$ and the τ polarization forward-backward asymmetry to be $A^{FB}_{pol} = (-10.55 \pm 0.76 \pm 0.25)\%$, where the first error is statistical and the second systematic. Taking into account the small effects of the photon propagator, photon-Z^0 interference and photonic radiative corrections, these results can be expressed in terms of the lepton neutral current asymmetry parameters:

$$\begin{aligned} A_\tau &= 0.1456 \pm 0.0076 \pm 0.0057, \\ A_e &= 0.1454 \pm 0.0108 \pm 0.0036. \end{aligned}$$

These measurements are consistent with the hypothesis of lepton universality and combine to give $\mathcal{A}_\ell = 0.1455 \pm 0.0073$. Within the context of the standard model this combined result corresponds to $\sin^2\theta^{\mathrm{lept}}_{\mathrm{eff}} = 0.23172 \pm 0.00092$. Combining these results with those from the other OPAL neutral current measurements yields a value of $\sin^2\theta^{\mathrm{lept}}_{\mathrm{eff}} = 0.23211 \pm 0.00068$.

Examiners:

Dr. J.M. Roney, Supervisor (Department of Physics and Astronomy)

Dr. R.K. Keeler, Departmental Member (Department of Physics and Astronomy)

Dr. A. Astbury, Departmental Member (Department of Physics and Astronomy)

Dr. C. Bohne, Outside Member (Department of Chemistry)

Dr. P. Renton, External Examiner (University of Oxford)

Contents

List of Tables

List of Figures

Acknowledgements

A great number of people have contributed, both directly and indirectly, to the efforts that have culminated in this analysis. I would like to thank all of those involved whose perserverance, intellectual creativity, and emotional support have guided these efforts and allowed this work to be realized.

“as if science were a factory and every minute’s delay would bring punishment after it”

“What will become of science if it does not have time for culture”

- Nietzsche

Chapter 1

Introduction

"For there are many things that hinder sure knowledge, the obscurity of the subject and the shortness of human life" - Protagoras

---

The earliest recorded histories indicate that civilizations have ubiquitously deemed it important to increase their knowledge of the physical universe. Motivations vary, but the common threads are simple curiosity and desire for control over the environment.

The increased ability to predict and control the behaviour of physical objects acts as a feedback mechanism, leading to an increasingly precise understanding of the physical world through the use of new manipulative techniques. Knowledge begets knowledge.

At present, more is understood about nature and the fundamental forces at work, and by more people, than at any previous time. It is no surprise. More people with more resources are currently engaged in the undertaking, and the work is always built on what has come before. Although a proper historical account of the development of this understanding would commence with a much earlier historical period, a convenient point of departure here is the time of the Enlightenment. The description that follows is rather painfully concise, but will provide a rudimentary introduction to how the fundamental forces have become known.

During the seventeenth and eighteenth centuries, Galileo, Newton, and others succeeded in creating a practical theory of motion. The theory was based on empirical evidence at hand and is constructed in terms of forces; in particular the *gravitational force* between objects. Newton's theory was revolutionary in that it successfully described both celestial motions and the local motions of objects in the earth's gravitational field. It is since Newton's time that the formalized concept of forces has been applied to the description of physical interactions in nature.

Although such interactions were known to exist long before in various manifestations, it was not until the end of the nineteenth century that a consistent theory of electricity and magnetism was constructed. It was shown, principally by Maxwell, that these phenomena were actually different aspects of a single *electromagnetic* interaction. This unification of seemingly disparate forces is rightly viewed as one of the greatest achievements of the nineteenth century.

In the last century, fundamental changes to our understanding of the universe occured. Planck and others showed that matter and energy are not continuously distributed, but are quantized; packaged in discrete bundles. This led to the development of quantum mechanics which, in contrast to previous physical theories, describes interactions in terms of a probabilistic framework. During the same period, Einstein led the development of the *Special Theory of Relativity* which postulates that the speed of light in vacuum is a universal constant and suggests that matter and energy are equivalent. This was followed by the construction of the *General Theory of Relativity* with which Einstein wanted to combine the ideas of Special Relativity with the equivalence principle. Simply put, the equivalence principle postulates that physical phenomena perceived by an observer in a uniformly accelerating reference frame must be equivalent to phenomena perceived by an observer in an analogous gravitational field.

At the beginning of the twentieth century, the gravitational and electromagnetic forces were thought to be well understood and the theories describing these interactions were highly successful. Through a variety of experiments examining increasingly small length scales, it became apparent that, in addition to the gravitational and electromagnetic forces,

Interaction	Typical Range (m)	Typical Lifetime (sec)	Typical Cross-section (mb)	Coupling
Strong	10^{-15}	10^{-23}	10	1
EM	∞	$10^{-16} - 10^{-20}$	$10^{-2} - 10^{-3}$	10^{-2}
Weak	10^{-18}	$10^{-12} - 10^{-18}$	$10^{-11} - 10^{-13}$	10^{-6}

Table 1.1: Comparison of the fundamental forces [1][2][3].

two previously unobserved forces are also at work in nature.

The first of these, the strong nuclear force, is responsible for binding together the nucleons within atoms while the second, the weak force, is responsible for nuclear beta decay. Interactions involving all four of the known forces have now been studied widely, but much is still not understood.

So, four forces. An uncomfortable number for scientists who follow an Occam's Razor principle. Why (at least) four? If the simplest theory is best, then perhaps a cue can be taken from electromagnetic theory. As noted above, it was not realized until long after electric and magnetic interactions were observed that such phenomena were aspects of a single electromagnetic force. Perhaps a similar result is true for all of the forces?

Establishing the connections between and ultimately unifying these four forces is one of the principle goals of current scientific endeavour.

As will be described in great detail below, the research presented here explores certain aspects of weak interactions central to the unification of the weak and electromagnetic interactions. In particular, a precise determination the *weak mixing angle* is presented; a parameter which, as described below, relates the coupling strength of weak interactions to that of electromagnetic interactions.

1.1 Standard Model

Three of the forces of nature, the electromagnetic, the weak, and the strong, are well described by a collection of theories generically termed the standard model. To provide

Particles			Charge	Spin	Interactions
Leptons					
e 0.511 MeV	μ 106. MeV	τ 1777. MeV	-1	1/2	EM, Weak
ν_e <15 eV	ν_μ <0.17 MeV	ν_τ <18.2 MeV	0	1/2	Weak
Quarks					
u 1.5-5 MeV	c 1.1-1.4 GeV	t 174. GeV	+2/3	1/2	EM, Weak, Strong
d 3.-9. MeV	s 60-170 MeV	b 4.1-4.4 GeV	-1/3	1/2	EM, Weak, Strong
Gauge Bosons					
γ (Massless)			0	1	EM
W 80.4 GeV			±1	1	EM, Weak
Z 91.2 GeV			0	1	Weak
g (Massless)			0	1	Strong

Table 1.2: Particle content in the standard model with particle masses given in eV.

an indication of the differences between these forces, some of their properties are given in Table 1.1. A cursory examination of these properties, some of which exhibit many orders of magnitude difference, suggests that a unification of forces, or rather constructing a unified theory describing these forces, may not be trivial.

In order to give an adequate summary of the current standard model framework, it is necessary to provide a description of what is interacting via these forces; namely the *fundamental particles*. A summary of our current knowledge of what are believed to be fundamental particles is given in Table 1.2[1]. Here, *fundamental* roughly means that such particles are indivisible; without substructure and not composed of yet more 'fundamental' objects. As may be seen, all particles do not interact via all forces. The charged leptons only interact weakly or electromagnetically, the neutrinos only interact weakly, while the quarks are subject to all three forces. Half-integer spin particles are referred to as fermions while particles with integer spin are called bosons.

As it turns out, the theories that describe the interactions of these particles via the three

---

[1] As is conventional in high energy physics, units are defined in this document such that $c = \hbar = 1$. Thus energies, momenta, and masses are all given in terms of eV.

forces can, at small length scales, be described by analogous mathematical structures. In all cases, the models describe the interaction of particles via the exchange of mediating particles. The electromagnetic interactions are mediated by the exchange of photons, strong interactions by gluon exchange, and weak interactions by the exchange of W or Z bosons.

The fact that these theories are built upon the same principles already goes a long way to achieving unification. But to really unify the forces, a single consistent theory is required which relates the interaction couplings without introducing additional unwanted parameters. Current research appears promising, but as of yet no one has successfully unified all of these forces. As is described next, however, unification has been achieved, to a certain extent, for the electromagnetic and weak interactions.

1.2 Fundamental Parameters

The standard model contains five free parameters, apart from the fermion masses and mixings, which must be determined experimentally. Different parameterizations are possible, but a convenient set for the purposes of this discussion includes the strong interaction coupling constant α_s , the electromagnetic interaction coupling constant α_{QED} , the electroweak mixing angle in the form $\sin^2\theta_{\mathrm{W}}$, the mass of the Z^0 boson, and the mass of the Higgs particle $\mathrm{m_H}$ [7]. Table 1.3 indicates the current most precise measured values of these parameters and the experimental method used to obtain them, including the contribution from this work.

In order to study and verify the standard model structure, examine potential inconsistencies, and search for new physics, precision determinations of the standard model parameters, preferably extracted from a variety of independent and complementary measurements, are necessary. Measurements of a given quantity using similar data and analysis techniques provide cross-checks on potential systematic effects and, where statistical errors dominate, allow an improvement in precision by combining results. In cases where measurements of a given parameter are extracted from widely varying processes, important checks on the consistency of standard model predictions across different sectors of

Parameter	Measured Value	Experimental Method
α_s	0.1185 ± 0.0020	Tau Decays Deep Inelastic Scattering Z^0 Width Various Hadronic Measurements
α_{QED}	$0.7297352533 \times 10^{-2} \pm 0.27 \times 10^{-10}$	Quantum Hall Effect
$\sin^2\theta_W$	0.23152 ± 0.00017	Z^0 Asymmetries including Tau Polarization
m_Z	91.1882 ± 0.0026 GeV	Z^0 Lineshape
m_H	60^{+52}_{-29} GeV > 114 GeV (95% CL)	Standard Model Indirect Fit LEP Direct Search

Table 1.3: Free parameters of the standard model determined by experiment [4][5][6].

the model are made possible.

In addition, the precision determination of these parameters facilitates, both in the context of the consistency of the measured parameters themselves and in terms of their derivative effects on the calculation of other predicted phenomena, the search for new physics. [2]

1.3 This Work

The analysis presented here describes a precision measurement of the weak mixing angle, θ_W, expressed as $\sin^2\theta_W$. This document gives, in great detail, a description of the methods and results of the analysis to be published in [8].

---

[2] The term 'new physics' is a potentially misleading. In this document, the expression is specifically used to refer to phenomena, whether conjectured to exist or not, that have not been experimentally observed.

The measurement is performed through an examination of $\tau^+\tau^-$ pair events produced via e^+e^-annihilation at interaction energies near the Z^0 mass. These interactions are mediated via the exchange of a Z^0 boson and both the coupling of the electrons to the Z^0 and the coupling of the Z^0 to the tau pairs provide sensitivity to $\sin^2\theta_W$.

Within the context of the standard model, all leptons are assumed to have equal couplings to the Z^0 boson. This is an assumption, known as lepton universality, that must be tested experimentally and, as will be seen, is done so by this analysis for electron and tau leptons.

In addition, the measurement of $\sin^2\theta_W$ presented here is indirectly sensitive to both the mass of the top quark and the mass of the Higgs boson. Since the mass of the top quark is known [9][10], an indirect measurement of the Higgs mass, within the context of the standard model, can be made.

The specific theoretical details regarding the interactions of interest to this analysis and the measurement of $\sin^2\theta_W$ provide the focus of the following chapter.

Chapter 2

Theory

"The explanations offered are all a bit dubious, conditioned by hypothesis, wavering among various alternatives; and this is only natural, since these are rumours that pass from mouth to mouth, while even science, which should confirm or deny them, is apparently uncertain" - Italo Calvino

---

2.1 Electroweak Theory

In the 1960's, Glashow, Weinberg, and Salam constructed a model termed the *Electroweak* model [11] that appears to successfully describe both the electromagnetic and weak interactions. The model is based on $\mathrm{SU(2)_L}$ weak isospin invariance and $\mathrm{U(1)_Y}$ weak hypercharge invariance.

For example, the electron neutrino is the +1/2 weak isospin partner of the electron and the down quark is the -1/2 weak isospin partner of the up quark. Hypercharge is defined as $\mathrm{Y} = 2(\mathrm{Q}+\mathrm{T_3})$ where Q is the particle charge and $\mathrm{T_3}$ is the third component of isospin.

In the construction of the model, the fields representing the interactions are initially massless. They consist of a weak isospin triplet of fields, $\mathrm{W}^1_\mu, \mathrm{W}^2_\mu, \mathrm{W}^3_\mu$, and a singlet field B_μ. After symmetry breaking is applied, the physical fields representing each of the mediating particles emerge and are related to the massless fields in the form

$$\begin{aligned} W^\pm_\mu &= (W^1_\mu \mp iW^2_\mu)/\sqrt{2}, \\ A_\mu &= B_\mu \cos\theta_W + W^3_\mu \sin\theta_W, \\ Z_\mu &= -B_\mu \sin\theta_W + W^3_\mu \cos\theta_W, \end{aligned} \tag{2.1}$$

where $W^\pm_\mu$ are the W boson fields, A_μ is the photon field, and Z_μ is the field representing the Z boson. In the process, the charged and weak neutral interaction mediating particles become massive. As may be seen, the weak mixing angle is so termed because it regulates the mixing of the W^3_μ and B_μ fields in the construction of the photon and Z^0 fields.

The Lagrangian density for the electroweak interaction of fermions, once symmetry breaking is applied, is given by [4]

$$\begin{aligned} \mathcal{L} &= \sum_i \overline{\psi}_i(i\partial\!\!\!/ - m_i - \frac{e}{\sin\theta_W}\frac{m_i H}{2m_W})\psi_i \\ &- \frac{e}{2\sqrt{2}\sin\theta_W}\sum_i \overline{\psi}_i\gamma^\mu(1-\gamma^5)(T^+W^+_\mu + T^-W^-_\mu)\psi_i \\ &- e\sum_i q_i\overline{\psi}_i\gamma^\mu\psi_i A_\mu \\ &- \frac{e}{2\cos\theta_W\sin\theta_W}\sum_i \overline{\psi}_i\gamma^\mu(g^i_V - g^i_A\gamma^5)\psi_i Z_\mu \end{aligned} \tag{2.2}$$

where ψ_i are the fermion fields with masses m_i and charges q_i; m_W is the W boson mass; H is the Higgs field; $W^\pm_\mu$ are the W boson fields which mediate the charged weak interaction; A_μ is the photon field mediating the electromagnetic interaction; Z_μ is the Z boson field which mediates the neutral weak interaction with vector and axial-vector couplings given by $g^i_V = T_{3(i)} - 2q_i\sin^2\theta_W$ and $g^i_A = T_{3(i)}$ for fermion type i; and $T^\pm$ are the weak isospin raising and lowering operators [4]. In analogy to classical mechanics, the electroweak Lagrangian density can be used to make calculate various observables, such as cross-sections; asymmetries; and decay rates, of electroweak interaction phenomena.

Apart from boson and fermion particle masses and fermion mixings, there are only two parameters in the electroweak theory that must be determined by experiment. In Equation 2.2, these parameters appear as the electric charge, e, and θ_W; but in practice the usefulness of the parameterization depends on the experiment in question. For example, an alternate parameterization might include the Fermi constant, $G_F = \sqrt{2}e^2/(\sin^2\theta_W\, 8m_W^2)$, which can be precisely measured by examining muon decay.

The point here is that the weak mixing angle is as fundamental a parameter as the electric charge. This can easily be seen in Equation 2.2 where the strengths of the charged and neutral weak interactions are proportional to the electric charge modulo factors of the weak mixing angle.

In terms of this analysis, however, it is not the strength of the interaction that is measured, but as will be seen, it is the effects of parity violation associated with the g_V^i and g_A^i coupling constants of the neutral weak interaction.

Line 3 of Equation 2.2 describes the electromagnetic interaction where it may be seen that the Dirac matrix γ^μ appears.

A large number of subtleties have been omitted in this discussion, but in principle Equation 2.2 describes all electroweak interactions. That a two parameter theory can accurately describe such a myriad of interaction configurations is truly astonishing. From an experimental point of view, the task is to analyze as many of these interactions as possible in order to measure the electroweak parameters and to verify that the theory accurately and consistently describes nature.

The experimental analysis described here is an important contribution to this undertaking. The primary focus has been to produce an accurate measurement of the parameter $\sin^2\theta_W$ through an examination of the tau polarization asymmetries from tau pairs produced via the neutral weak interaction $e^+e^- \to Z^0 \to \tau^+\tau^-$.

One of the 'subtleties' neglected to this point in the description is the Higgs mechanism. When the electroweak theory was initially being constructed, it was unclear how to produce a Lagrangian that is gauge invariant when particle masses are included. Clearly particles have mass and in order to overcome this obstacle, Peter Higgs developed an electroweak symmetry hiding mechanism that can successfully give masses to the particles in a gauge invariant fashion [7].

Without describing the details of the Higgs mechanism, the basic postulate requires

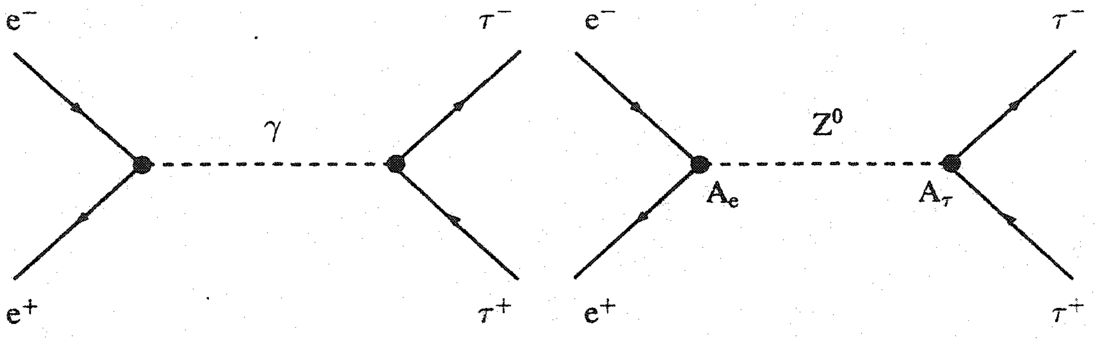

Figure 2.1: Lowest order Feynman diagrams representing tau pair production via photon exchange (left) and Z^0 exchange (right). Each Z^0 vertex is labelled by the neutral coupling asymmetry parameter, A_e or A_τ .

the existence of at least one massive scalar boson, usually referred to as the Higgs particle. Such a particle has not yet been discovered, but if it does exist, it must have an effect on the measurements of various electroweak quantities. The perturbative expansion representing the interactions examined in this analysis is logarithmically sensitive to the mass of the Higgs particle in the higher order radiative correction terms. Thus this measurement, when combined with complementary electroweak measurements and knowledge of the top quark mass, can provide an indirect measurement of the Higgs particle.

2.2 Tau Pair Production and Polarization

Oppositely charged tau pair particles are produced from e^+e^-annihilations when the total centre-of-mass (CM) energy is above approximately 3.55 GeV. At low energies, just above this threshold, production is dominated by the exchange of a virtual photon as depicted in the Feynman diagram in Figure 2.1. At CM energies near the 91.2 GeV mass of the Z^0 , tau pair production is dominated by the neutral weak interaction, also shown in Figure 2.1, via the exchange of a Z^0 particle.

The initial $e^+e^-$and final τ^+ τ^- fermions in these processes are all spin-1/2 particles, while the mediating γ and Z^0 bosons are spin-1 particles. Since no orbital angular momentum exists in these interactions, spin must be conserved.

Although helicity, the projection of spin along a particles momentum vector, is not conserved in general, it is conserved to a good approximation for the case of highly relativistic particles. It is the observable effects of the tau spin, formulated in terms of helicity, that is of primary interest in this analysis. Throughout this paper, a spin-1/2 particle with spin aligned parallel to its flight trajection will be referred to as a 'right-handed' particle and as a 'left-handed' particle when the spin is aligned anti-parallel.

Choosing the electron flight direction as the spin quantization axis, electron-positron pairs annihilate when their spins are aligned as shown in the two configurations given in Figure 2.2. Allowing for both forward and backward going τ^- cases, Figure 2.2 describes the four final state spin configurations of the taus; two for each e^+e^-case. Note in particular that the final state taus are produced with anti-correlated helicities; events in which the τ^- is right-handed will contain a left-handed τ^+ and vice versa. In fact, this is not quite always true for the neutral weak interaction, but the probability for producing a $\tau^+\tau^-$ pair with correlated helicities is suppressed by a factor of $m_\tau{}^2/m_Z{}^2$ [12].

As has been well tested [13], the electromagnetic interaction is a purely vector interaction that conserves parity (spatial inversion: $\vec{r} \rightarrow -\vec{r}$). The matrix element for $e^+e^- \rightarrow \gamma \rightarrow \tau^+\tau^-$ interactions, including an explicit axial-vector term, can be written to lowest order as [1][2]

$$\mathcal{M}_\gamma = \frac{i4\pi\alpha_{QED}}{s}\overline{v}_e\gamma^\mu(g_v^{e,\gamma} - g_a^{e,\gamma}\gamma^5)u_e\overline{u}_\tau\gamma_\mu(g_v^{\tau,\gamma} - g_a^{\tau,\gamma}\gamma^5)v_\tau, \tag{2.3}$$

where s is the CM energy, $\overline{v}_e$ is the positron wavefunction, u_e is the electron wavefunction, $\overline{u}_\tau$ is the τ^- wavefunction, v_τ is the τ^+ wavefunction, and γ_μ and γ^5 are Dirac matrices. The square of the matrix element $|\mathcal{M}_\gamma|^2$ is proportional to the cross-section for the process $e^+e^- \rightarrow \gamma \rightarrow \tau^+\tau^-$.

This matrix element is essentially constructed from line 3 of Equation 2.2, with a generalization of the Lorentz structure to include an explicit axial-vector term. The Dirac matrix γ_μ transforms under parity as a Lorentz vector while the product $\gamma_\mu\gamma^5$ transforms as an axial-vector. Interactions that are purely vector or purely axial-vector conserve parity, but interactions that are a combination of vector and axial-vector do not.

The constants $g_v^{f,\gamma}$ and $g_a^{f,\gamma}$ are the photon vector and axial-vector couplings which take the values $g_v^{f,\gamma} = |Q_f|$ and $g_a^{f,\gamma} = 0$ for fermion f with charge Q_f and the interaction is

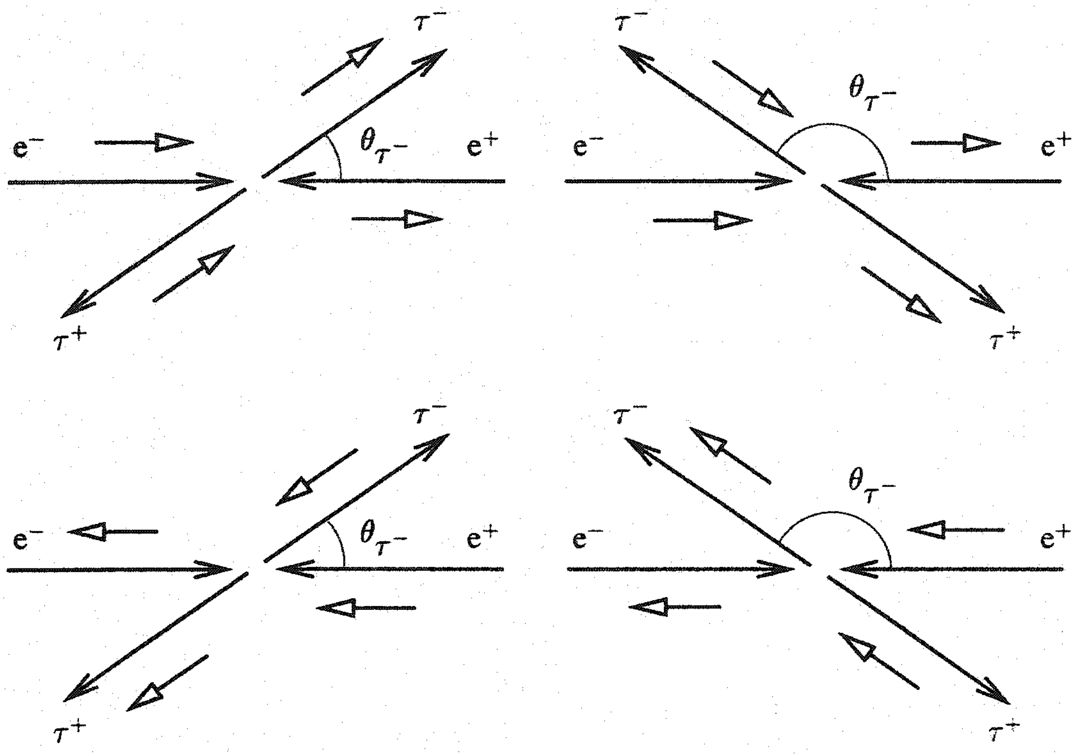

Figure 2.2: The four tau pair production helicity configurations are shown; two for each initial electron-positron case. As may be seen from an examination of the short arrows which represent the projection of particle spin along flight direction, the electron-positron pairs annihilate with anti-correlated helicities and produce tau pairs whose helicities are also anti-correlated.

manifestly parity conserving.

A consequence of this symmetry is that the probability for producing a right-handed τ^- and left-handed τ^+ pair, through photon exchange and assuming unpolarized e^+e^- beams, is equal to the probability for producing a left-handed τ^- and right-handed τ^+ pair.

Defining tau polarization, $\langle P_\tau \rangle$, as

$$P_\tau \equiv (\sigma_R - \sigma_L)/(\sigma_R + \sigma_L), \tag{2.4}$$

where $\sigma_R(\sigma_L)$ represents the cross-section for producing a right(left)-handed τ^- , it is evident that $\langle P_\tau \rangle = 0$ when parity is conserved.

In contrast, it is well known that parity is not conserved in weak interactions [14]. For charged weak interactions, parity appears to be violated maximally. To illustrate, this means that the decay of a tau to a spin-0 pion and spin-1/2 neutrino will, assuming the neutrino is massless, *always* produce a left-handed neutrino and *never* a right-handed one. The matrix element for this decay, neglecting terms suppressed by factors of m^2/m_W^2 where $m \le m_\tau$, can be written as [1][2]

$$\mathcal{M}_W = \frac{G_F \cos\theta_C}{\sqrt{2}} f_\pi \overline{u}_{\nu_\tau} \gamma^\mu (g_v^{f,W} + g_a^{f,W} \gamma^5) u_\tau j_\pi^\mu. \tag{2.5}$$

Here, $\cos\theta_C$ is the Cabibbo angle, f_π is the pion decay constant, j_π^μ is the current representing the pion, and $g_v^{f,W}$ and $g_a^{f,W}$ are the charged current vector and axial-vector couplings respectively. Note that $g_v^{f,W}$ and $g_a^{f,W}$ are assumed to be universal in that their values are the same for all fermions, f. Maximal parity violation in this decay specifically means that the vector and axial-vector contributions are equal and opposite, $g_v^{f,W} = -g_a^{f,W} = 1$, and hence the designation 'V-A' to charged weak interactions. This decay will be discussed further in the following section.

Neutral weak interactions, however, do not violate parity maximally and, as described in Chapter 1, the analogous neutral current vector and axial-vector couplings depend on $\sin^2\theta_W$ and on the charge and third component of weak isospin of the interacting particles.

For example, the matrix element for neutral weak tau pair production, $e^+e^- \to Z^0 \to \tau^+\tau^-$, can be written as [1][2]

$$\mathcal{M}_{Z^0} = \frac{i\sqrt{2}G_F m_Z^2}{s - m_Z^2} \overline{v}_e \gamma^\mu (g_v^{e,Z} - g_a^{e,Z} \gamma^5) u_e \overline{u}_\tau \gamma_\mu (g_v^{\tau,Z} - g_a^{\tau,Z} \gamma^5) v_\tau, \tag{2.6}$$

where it is recalled that the neutral couplings $g_v^{f,Z}$ and $g_a^{f,Z}$ for fermions f are given by

$$\begin{aligned} g_v^{f,Z} &= T_{3(f)} - 2\, Q_f \sin^2\theta_W \, , \\ g_a^{f,Z} &= T_{3(f)} . \end{aligned} \tag{2.7}$$

The dependence on particle type is clear, but it is also apparent that particles with the same charge and isospin, such as the charged leptons, have identical couplings to the Z^0 particle. This universality of the couplings is a theoretical assumption in the standard model that must be tested experimentally, as is done in this work.

For negatively charged leptons, the coupling parameters are $g_v^{f,Z} = -1/2 + 2\sin^2\theta_W$ and $g_a^{f,Z} = -1/2$. Thus for $\sin^2\theta_W \neq 1/4$, parity is violated in the neutral weak interactions of charged leptons.

The form of the couplings given in 2.7 have no radiative corrections included. The actual value of $\sin^2\theta_W$ that is quoted depends on the details of the calculational scheme applied in terms of the level and type of the radiative corrections included. The approach adopted by the LEP experiments has been to use the 'effective' neutral coupling parameter and $\sin^2\theta_W$ forms in which to present results.

The effective forms are defined as

$$\begin{aligned} g_V^f &= \sqrt{\rho_f}\,(T_3^f - 2\, Q_f\, \kappa_f \sin^2\theta_W\,), \\ g_A^f &= \sqrt{\rho_f}\, T_3^f, \\ \sin^2\theta_{\mathrm{eff}}^{\mathrm{lept}} &= \kappa_f \sin^2\theta_W \, , \end{aligned} \tag{2.8}$$

where $\sin^2\theta_W$ is the 'on-shell' value defined as $\sin^2\theta_W = 1 - m_W^2/m_Z^2$ and ρ_f and κ_f contain the electroweak radiative correction factors [4].

In terms of the interactions of interest to this analysis, a consequence of this parity violation is that the probability for producing a right-handed τ^- through Z^0 exchange is *not* equal to the probability for producing a left-handed τ^- and hence the average tau polarization, as will be seen, is non-zero.

Assuming unpolarized e^+e^-beams, the Born level differential cross-sections for producing $\tau^+\tau^-$ pairs with a right-handed (R) or left-handed (L) τ^- particle, $\frac{d\sigma_{R(L)}}{d\cos\theta_{\tau^-}}$, can be written as

$$\begin{aligned} \frac{1}{\sigma_{tot}}\frac{d\sigma_R}{d\cos\theta_{\tau^-}} &= \tfrac{3}{16}[(1+\langle P_\tau\rangle)(1+\cos^2\theta_{\tau^-}) + \tfrac{8}{3}(A_{FB} + A_{pol}^{FB})\cos\theta_{\tau^-}], \\ \frac{1}{\sigma_{tot}}\frac{d\sigma_L}{d\cos\theta_{\tau^-}} &= \tfrac{3}{16}[(1-\langle P_\tau\rangle)(1+\cos^2\theta_{\tau^-}) + \tfrac{8}{3}(A_{FB} - A_{pol}^{FB})\cos\theta_{\tau^-}], \quad (2.9) \end{aligned}$$

where θ_{τ^-} is the polar angle between the e^-beam and the τ^- flight direction. The three parameters in 2.9 are defined by

$$\langle P_\tau\rangle = \frac{\sigma_{R-1<\cos\theta_{\tau^-}<1} - \sigma_{L-1<\cos\theta_{\tau^-}<1}}{\sigma_{tot}}, \tag{2.10}$$

$$A_{pol}^{FB} = \frac{(\sigma_R - \sigma_L)_{\cos\theta_{\tau^-}>0} - (\sigma_R - \sigma_L)_{\cos\theta_{\tau^-}<0}}{\sigma_{tot}}, \tag{2.11}$$

and

$$A_{FB} = \frac{(\sigma)_{\cos\theta_{\tau^-}>0} - (\sigma)_{\cos\theta_{\tau^-}<0}}{\sigma_{tot}}, \tag{2.12}$$

where $\sigma_{tot} = \sigma_R + \sigma_L$ for σ_R and σ_L integrated over $\cos\theta_{\tau^-}$ from -1 to +1. The connection to the vector and axial-vector couplings is made via the neutral current asymmetry parameters A_e and A_τ where, for pure Z^0 exchange,

$$\begin{aligned} \langle P_\tau\rangle &= -A_\tau\,, && (2.13) \\ A_{pol}^{FB} &= -\frac{3}{4}A_e\,, && (2.14) \\ A_{FB} &= \frac{3}{4}A_e\,A_\tau\,, && (2.15) \\ & && (2.16) \end{aligned}$$

with the asymmetry parameters defined by

$$A_\ell \equiv \frac{2g_V^\ell/g_A^\ell}{1+(g_V^\ell/g_A^\ell)^2}, \tag{2.17}$$

for lepton ℓ. Again, if universality is assumed, all of the lepton neutral coupling asymmetry parameters are equal. Since it is the ratio of the effective vector and axial-vector couplings that appears in the cross-section formulae, it useful to present the relationship between this ratio and $\sin^2\theta_{\mathrm{W}}$ given by

$$\frac{g_V^\ell}{g_A^\ell} = 1 - 4\sin^2\theta_{\mathrm{eff}}^{\mathrm{lept}}\,, \tag{2.18}$$

where $\sin^2\theta_{\mathrm{eff}}^{\mathrm{lept}}$ is the effective weak mixing angle for leptons defined by equation 2.18. It is evident from Equations 2.10-2.12 that measurements of $\langle P_\tau \rangle$, $A_{\mathrm{pol}}^{\mathrm{FB}}$, and A_{FB} will allow the universality of the couplings of electrons and taus to be tested and provide a determination of $\sin^2\theta_{\mathrm{eff}}^{\mathrm{lept}}$.

The measurement of A_{FB} is made as part of the OPAL lineshape analysis [15] and is used as input to this analysis. Measurements of the average tau polarization $\langle P_\tau \rangle$ and the polarization forward-backward asymmetry $A_{\mathrm{pol}}^{\mathrm{FB}}$ are the purpose of this analysis.

The equations given in 2.9 imply a variation of the tau polarization as a function of the tau production angle in the form

$$P_\tau\,(\cos\theta_{\tau^-}) = \frac{\langle P_\tau \rangle\,(1+\cos^2\theta_{\tau^-}) + \frac{8}{3}A_{\mathrm{pol}}^{\mathrm{FB}}\,\cos\theta_{\tau^-}}{(1+\cos^2\theta_{\tau^-}) + \frac{8}{3}A_{\mathrm{FB}}\,\cos\theta_{\tau^-}}. \tag{2.19}$$

In order to determine A_e and A_τ in this analysis, thereby testing universality and producing a precision measurement of $\sin^2\theta_{\mathrm{eff}}^{\mathrm{lept}}$, it is necessary to determine the tau polarization as a function $\cos\theta_{\tau^-}$.

It is not possible to measure the tau polarization by measuring the tau helicities on an event by event basis with OPAL, and as will be seen in the next section, the properties of tau decays must be utilized for this purpose.

2.3 Tau Decays and Polarization

As suggested above, the tau is a spin-1/2 charged lepton with mass approximately $m_\tau =$ 1.77 GeV. The heavy nature of the tau allows it to decay through numerous decay channels and its relatively short lifetime of 290 fs causes it to do so close to the e^+e^-collision point in OPAL detector. Thus it is actually the ‘visible’, or measured, decay products of the tau that are analyzed and not the tau directly.

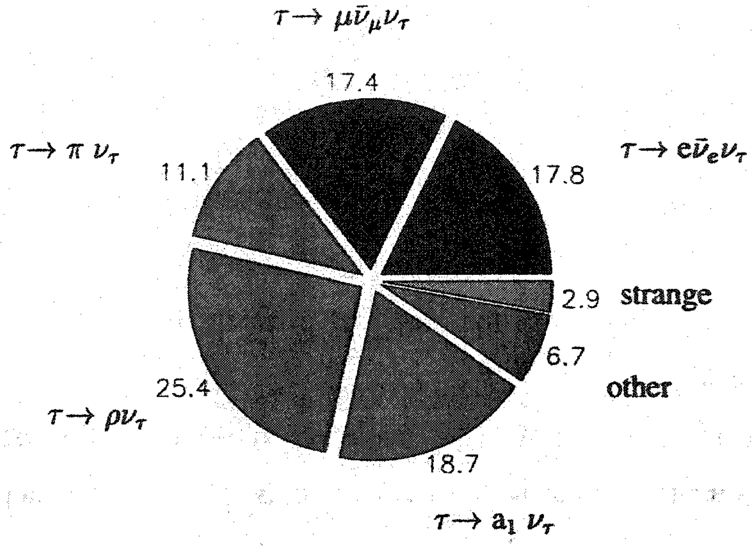

Figure 2.3: Tau decay branching ratios.

Since it is properties of the taus that are of interest here, this indirect measurement might appear to be disadvantageous. But in fact, in contrast to $e^+e^-\to Z^0\to\mu^+\mu^-$ and $e^+e^-\to Z^0\to e^+e^-$ events in which the polarization can not be measured, it is the comparatively rapid decay of the tau via the maximally parity violating charged weak interaction that makes the tau polarization measurement possible.

The breakdown of the tau decay branching ratios is given in Figure 2.3. As is shown, more than 80% of taus decay through the five channels $\tau\to\rho\nu_\tau$, $\tau\to\pi\ \nu_\tau$, $\tau\to e\bar{\nu}_e\nu_\tau$, $\tau\to\mu\bar{\nu}_\mu\nu_\tau$, and $\tau\to a_1\ \nu_\tau$ [1]. The three hadronic tau decays are most sensitive to the polarization (see Table 2.1), with the $\tau\to\rho\nu_\tau$ and $\tau\to a_1\ \nu_\tau$ channels losing some sensitivity owing to the additional complexity introduced by the non-zero angular momentum of the mesons [16].

---

[1] In this analysis, no distinction is made between the decays $\tau^-\to\pi^-\ \nu_\tau$ and $\tau^-\to K^-\nu_\tau$ or between $\tau^-\to\rho^-\nu_\tau$ (noting that $\rho^-\to\pi^-\ \pi^0$) and $\tau^-\to K^-\pi^0\ \nu_\tau$. Reference to $\tau^-\to\pi^-\ \nu_\tau$ always means $\tau^-\to\pi^-\ \nu_\tau$ and/or $\tau^-\to K^-\nu_\tau$ while reference to $\tau^-\to\rho^-\nu_\tau$ will always mean $\tau^-\to\pi^-\ \pi^0\ \nu_\tau$ and/or $\tau^-\to K^-\pi^0\ \nu_\tau$.

	$\tau\rightarrow e\bar{\nu}_e\nu_\tau$	$\tau\rightarrow \mu\bar{\nu}_\mu\nu_\tau$	$\tau\rightarrow \pi\ \nu_\tau$	$\tau\rightarrow \rho\nu_\tau$ $\rho^\pm\rightarrow \pi^\pm\pi^0$	$\tau\rightarrow a_1\ \nu_\tau$ $a_1^\pm\rightarrow \pi^\pm\pi^+\ \pi^-$
Branching ratio	0.18	0.17	0.12	0.25	0.09
Maximum sensitivity	0.22	0.22	0.58	0.49	0.45
Normalized ideal weight	0.06	0.06	0.30	0.44	0.13

Table 2.1: The branching ratios, maximum sensitivity and normalized ideal weight for the five decay modes used in the analysis. The ideal weight is calculated as the product of the branching ratio and the square of the maximum sensitivity. Presented in the last line of the table is the ideal weight for each channel divided by the sum of the ideal weights of the five channels.

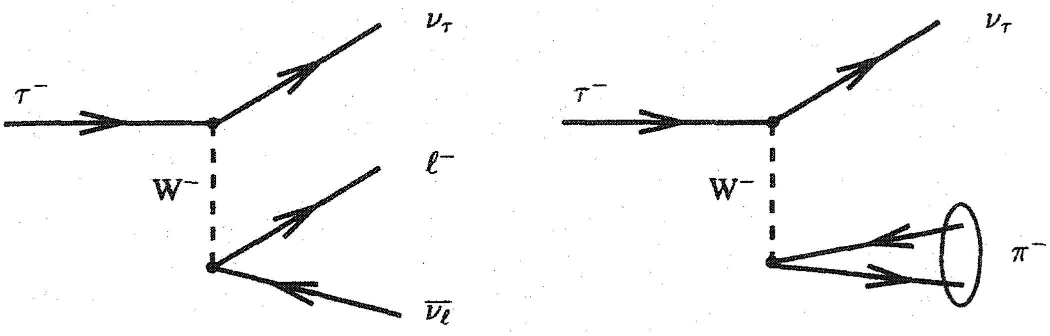

Figure 2.4: Lowest order Feynman diagrams representing purely leptonic tau decay (left) and semi-leptonic (or hadronic) tau decay (right).

2.3.1 The Case $\tau\rightarrow \pi\ \nu_\tau$

The decay $\tau\rightarrow \pi\ \nu_\tau$, briefly described in the previous section, is the simplest case in which to elucidate the connection between tau polarization and tau decay products. Like all tau decays, this is a charged weak interaction mediated by the exchange of a virtual W particle as depicted in the Feynman diagram in Figure 2.4.

Since this is a V-A interaction, the tau neutrino produced, which is assumed to be massless, must be left-handed. The pion is a spin-0 particle produced in a state with no orbital angular momentum, and thus, in order to conserve total angular momentum, the neutrino momentum will be preferentially produced against the direction of tau spin. In particular, with a tau at rest and spin quantization axis to the right as depicted in Figure 2.5, and recognizing that the pion will emerge in the opposite direction to the neutrino in the

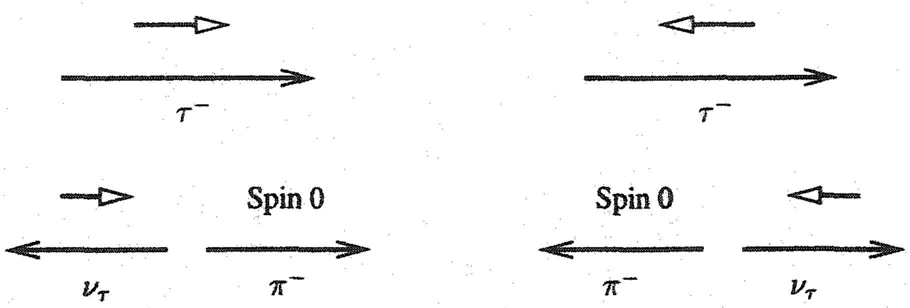

Figure 2.5: Decay configurations for each tau polarization for the case $\tau \to \pi\ \nu_\tau$.

tau rest frame to conserve momentum, the decay of right-handed taus will preferentially produce pions emerging to the right and the decay of left-handed taus will produce pions with momentum to the left.

Using the matrix element given in 2.5, the partial decay width for $\tau \to \pi\ \nu_\tau$ in the tau rest frame can be written as

$$\frac{1}{\Gamma}\frac{d\Gamma}{d\cos\theta^*} = 1 + \mathrm{P}_\tau \cos\theta^* \ , \tag{2.20}$$

where $\cos\theta^*$ is the cosine of the angle between the tau spin direction and the pion momentum.

Transforming to the lab frame by boosting to the right in Figure 2.5, the partial decay width becomes

$$\frac{1}{\Gamma}\frac{d\Gamma}{dx} = 1 + \mathrm{P}_\tau\ (2x_\pi - 1), \tag{2.21}$$

where $x_\pi = \frac{\mathrm{E}_\pi}{\mathrm{E}_\tau}$ is the pion energy scaled by the maximum energy and terms of order $(\frac{\mathrm{m}_\pi}{\mathrm{m}_\tau})^2$ are ignored. Thus the decay of completely right-handed taus, for which $\mathrm{P}_\tau = 1$, will produce more energetic pions, on average, than the decay of left-handed taus, for which $\mathrm{P}_\tau = -1$. This is shown explicitly in Figure 2.6 where the pion energy spectrum is given for both right-handed and left-handed $\tau \to \pi\ \nu_\tau$ decays.

As can be seen, the slope of the of the energy spectrum of pions from $\tau \to \pi\ \nu_\tau$ decays allows a determination of the average polarization. From a more practical point of view, the polarization can be extracted by fitting a linear combination of the left-handed and right-handed distributions to a sample with arbitrary polarization.

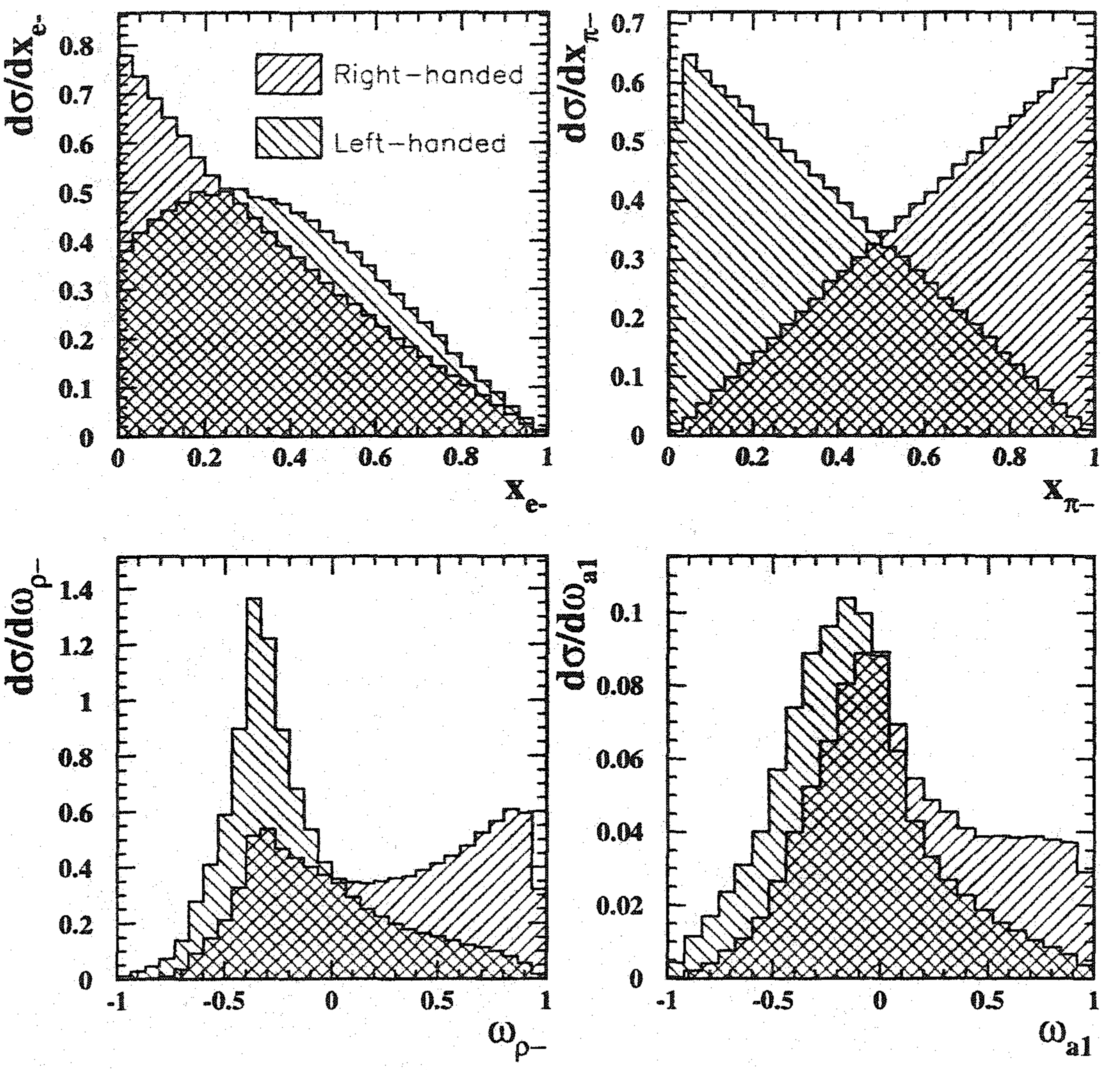

Figure 2.6: Monte Carlo simulated distributions of $\tau \rightarrow e\bar{\nu}_e\nu_\tau$, $\tau \rightarrow \pi\ \nu_\tau$, $\tau \rightarrow \rho\nu_\tau$, and $\tau \rightarrow a_1\ \nu_\tau$ tau decays for completely left-handed and completely-right handed taus are shown.

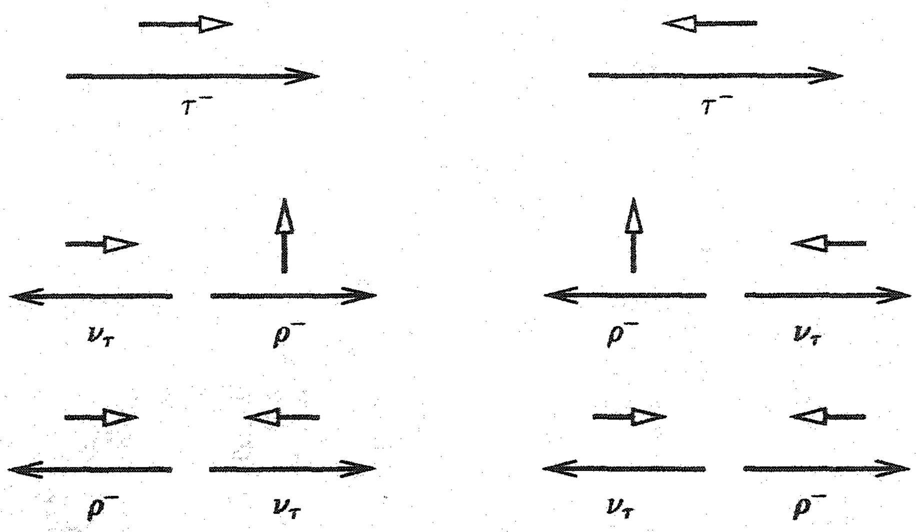

Figure 2.7: Helicity configurations for the case $\tau \rightarrow \rho\nu_\tau$. In contrast to $\tau \rightarrow \pi\nu_\tau$ decays, it may be seen here that, since the ρ is a spin-1 particle, two ρ polarization states are possible for each tau polarization.

2.3.2 The Case $\tau \rightarrow \rho\nu_\tau$

Unlike the pion, the charged ρ is a spin-1 particle with mass approximately 770 GeV which decays quickly via $\rho^\pm \rightarrow \pi^\pm\pi^0$. The additional spin of the ρ reduces the kinematical constraints, allowing two possible spin configurations for each tau helicity state as depicted in Figure 2.7. The cases in which the ρ is longitudinally polarized are equivalent to the $\tau \rightarrow \pi\ \nu_\tau$ configurations, but the transversely polarized cases produce the opposite angular distribution.

The partial width for $\tau \rightarrow \rho\nu_\tau$ is given in the tau rest frame by

$$\frac{1}{\Gamma}\frac{d\Gamma^{\mathrm{L}}}{d\cos\theta^*} = \frac{\mathrm{m}_\rho^2/2}{\mathrm{m}_\tau^2 + 2\mathrm{m}_\rho^2} 1 + \mathrm{P}_\tau \cos\theta^* \,, \tag{2.22}$$

for the longitudinal case and

$$\frac{1}{\Gamma}\frac{d\Gamma^{\mathrm{T}}}{d\cos\theta^*} = \frac{\mathrm{m}_\rho^2}{\mathrm{m}_\tau^2 + 2\mathrm{m}_\rho^2} 1 - \mathrm{P}_\tau \cos\theta^* \,, \tag{2.23}$$

for the transverse case, where $\cos\theta^*$ is the angle between the ρ and the tau flight direction in the rest frame of the tau [17]. The transverse case effectively diminishes the sensitivity to P_τ when only the $\rho \cos\theta^*$ angle is observed, or in the lab frame, when only the ρ energy is measured.

Much of this sensitivity, however, may be recovered by using information from the ρ decay products, in effect, to spin analyze the ρ. The variable chosen to do this, $\cos\psi$, is the angle between the charged pion relative to the flight direction of the ρ in the ρ rest frame. The variables $\cos\theta^*$ and $\cos\psi$ are related to measured lab variables through

$$\begin{aligned}\cos\theta^* &= \frac{2\mathrm{m}_\tau^2 x_\rho - \mathrm{m}_\tau^2 - \mathrm{m}_\rho^2}{\mathrm{m}_\tau^2 - \mathrm{m}_\rho^2}, \\ \cos\psi &= \frac{\mathrm{m}_\rho}{\sqrt{\mathrm{m}_\rho^2 - 4\mathrm{m}_\pi^2}}(2x_\rho - 1), \end{aligned} \tag{2.24}$$

where $x_\rho = E_\rho / E_\tau$ [16].

The inclusion of an additional variable for the $\tau \to \rho\nu_\tau$ case analysis means that a fit to extract the polarization in this channel requires the linear combination of two 2-dimensional distributions. This increase in dimensionality may prove undesirable from a practical point of view, owing to statistical effects. However, as described by Davier et. al [18], the two variables can be combined to form a single variable without loss of polarization sensitivity. This optimal variable, ω_ρ, is given by

$$\omega_\rho = \frac{\mathrm{W_R}(\cos\theta^*, \cos\psi) - \mathrm{W_L}(\cos\theta^*, \cos\psi)}{\mathrm{W_R}(\cos\theta^*, \cos\psi) + \mathrm{W_L}(\cos\theta^*, \cos\psi)}, \tag{2.25}$$

where $\mathrm{W_{R(L)}}$, given in the Appendix A, is proportional to the partial decay width for completely right(left)-handed $\tau \to \rho\nu_\tau$ decays, as a function of $\cos\theta^*$ and $\cos\psi$. The distributions of ω_ρ, for both left-handed and right-handed tau decays, are presented in Figure 2.6.

2.3.3 Generalized $\langle \mathrm{P}_\tau \rangle$ Dependence and the Decays $\tau \to \mathrm{e}\bar{\nu}_e\nu_\tau$, $\tau \to \mu\bar{\nu}_\mu\nu_\tau$, and $\tau \to \mathrm{a}_1\,\nu_\tau$

The previous sections presented the details regarding the polarization sensitive observables for the decays $\tau \to \pi\,\nu_\tau$ and $\tau \to \rho\nu_\tau$. In this section, a generalized description is presented followed by the details concerning the specific decay channels $\tau \to \mathrm{e}\bar{\nu}_e\nu_\tau$, $\tau \to \mu\bar{\nu}_\mu\nu_\tau$, and $\tau \to \mathrm{a}_1\,\nu_\tau$.

Tau decay distributions, in general, are linearly dependent on polarization and can be written in the form

$$\frac{1}{\Gamma}\frac{d^n\Gamma}{d^n\vec{\xi}} = f(\vec{\xi}) + \mathrm{P}_\tau\, g(\vec{\xi}), \tag{2.26}$$

where $\vec{\xi}$ is an n-dimensional set of decay mode dependent kinematic variables, and $f(\vec{\xi})$ and $g(\vec{\xi})$ are mode dependent functions of these variables. For the $\tau \rightarrow \pi\ \nu_\tau$ channel, $\vec{\xi}$ is simply the scaled pion energy x_π, $f = 1$, and $g = 2x_\pi - 1$. For the $\tau \rightarrow \rho\nu_\tau$ channel, $\vec{\xi}$ includes $\cos\theta^*$ and $\cos\psi$ with ω_ρ related to the f and g functions by $\omega_\rho = \frac{f}{g}$.

The purely leptonic tau decays, $\tau \rightarrow e\bar{\nu}_e\nu_\tau$ and $\tau \rightarrow \mu\bar{\nu}_\mu\nu_\tau$, are three body decays in which an additional neutrino is produced (see Figure 2.4). The neutrinos are not measured, and the additional loss of information results in a decreased sensitivity to the polarization as shown in Table 2.1. For these decays, $\vec{\xi}$ is again the scaled energy of the charged decay product, $x_e = \frac{\mathrm{E}_e}{\mathrm{E}_\tau}$ and $x_\mu = \frac{\mathrm{E}_\mu}{\mathrm{E}_\tau}$, with the f and g functions now given by

$$\begin{aligned} f &= 5 - 9x^2 + 4x^3, \\ g &= 1 + 9x^2 - 8x^3. \end{aligned} \tag{2.27}$$

The decay distributions, which are already 1-dimensional and thus not transformed to the ω variable, are given in Figure 2.6 for both right-handed and left-handed tau decays. The decrease in sensitivity is apparent. It should also be noted that, in contrast to the $\tau \rightarrow \pi\ \nu_\tau$ channel, the right-handed case now produces a charged lepton with *lower* energy, on average, than the left-handed case.

The final channel to be discussed is the decay $\tau \rightarrow \mathrm{a}_1\ \nu_\tau$. The a_1 is a spin-1 particle with mass and width on the order of 1230 MeV and 500 MeV, respectively, which quickly decays to $\pi^-\ \pi^-\ \pi^+$ or $\pi^-\ \pi^0\ \pi^0$ with approximately equal probability. Owing to the difficulty in identifying the latter configuration with the OPAL detector, it is the 3 charged pion or '3-prong' case with which this analysis is concerned.

In analogous fashion to the $\tau \rightarrow \rho\nu_\tau$ case, the a_1 channel exhibits significantly reduced polarization sensitivity when only the a_1 energy is measured in the lab frame. There are again two possible spin configurations and much of the sensitivity can regained through a spin analysis of the a_1 via utilization of the momentum information of the three pions. In this case six variables are used which include the angle θ^* between the a_1 and τ momenta in the τ rest frame, the angle (ψ) between the perpendicular to the a_1 decay plane and the a_1 flight direction in the rest frame of the a_1, the angle (γ) in the a_1 rest frame between the unlike-sign pion momentum in the a_1 rest frame and the a_1 flight direction projected into the a_1 decay plane, the 3π-invariant mass, and the two $\pi^+\pi^-$ mass combinations present in the $a_1^\pm \rightarrow \pi^\pm\pi^+\pi^-$ decay.

The multi-dimensional decay distribution resulting from use of these variables is impractical and the variables are combined into the optimal 1-dimensional variable ω_{a_1}. The form of ω_{a_1} for this decay channel are given in the Appendix B.

2.4 Electroweak and $\sqrt{s}$ Corrections

In order to extract measurements of $\langle P_\tau \rangle$ and A^{FB}_{pol} from data, a linear combination of Monte Carlo reference distributions of completely right-handed and left-handed tau decays is fit to the data. The Monte Carlo simulation provides the kinematical distributions for tau pairs produced via pure Z^0 exchange, but the data include additional effects which must be accounted for to enable an interpretation of the results. Such effects include several types of higher order corrections to the Monte Carlo calculation, γ exchange and γ-Z^0 interference effects, and the effects of the centre-of-mass energy at which the data were collected.

2.4.1 Pure QED Radiative Corrections

The Z^0 exchange Feynman diagram given in figure 2.1 represents the 'tree level' or lowest order contribution to the perturbative expansion describing the production of tau pairs via Z^0 exchange. In practice, lowest order calculations can provide relatively accurate theoretical approximations to the description of particle interactions in nature. However, many precision measurements, including the work described here, are sensitive to higher order correction terms.

Pure QED corrections are those in which the tree level diagram has additional real and/or virtual photons added to it. The first order corrections of this type include all

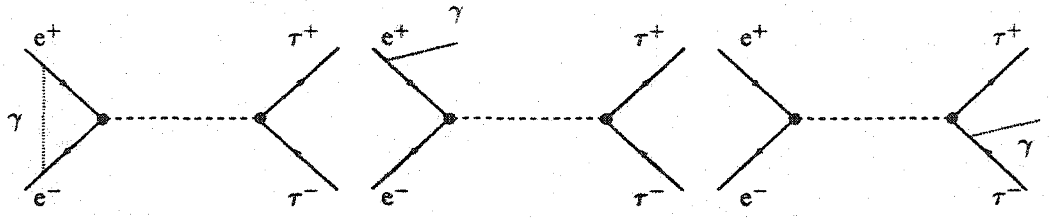

Figure 2.8: Three examples of first order pure QED radiative corrections are shown.

diagrams containing a single extra photon; either as real bremsstrahlung or as a virtual loop as indicated by the examples in Figure 2.8. Corrections are included in the simulation to order α^2 for initial state radiation (ISR) and final state radiation (FSR) in which the initial $e^+e^-$and/or final $\tau^+ \tau^-$ particles emit photons. All other QED corrections in the Z^0 production of $\tau^+ \tau^-$ pairs are included to order α.

In addition, QED radiation must be accounted for in the decay of the taus. Complete order α decay radiation is included in the simulation for the purely leptonic tau decays, while for the semi-leptonic decays the leading logarithmic approximation is applied. Potential systematic effects associated with the modelling of decay radiation are described in Chapter 7.

These radiative corrections affect the polarization sensitive kinematical distributions and inclusion of these higher order effects allows the simulation to more accurately model the data.

2.4.2 Weak Corrections

In addition to the pure QED corrections, a second set of higher order corrections, termed Weak corrections, must be taken into account. To first order, these include all other one-loop diagrams. As described in Figure 2.9, these include propagator corrections, vertex corrections, and box diagram terms. Such corrections are not included in the simulated Monte Carlo events but are absorbed into the definition of the effective neutral coupling asymmetry parameters, A_τ and A_e , and into the definition of the effective weak mixing angle, $\sin^2 \theta_W$, given in Equation 2.8.

The Weak corrections are of particular importance because they imply an explicit

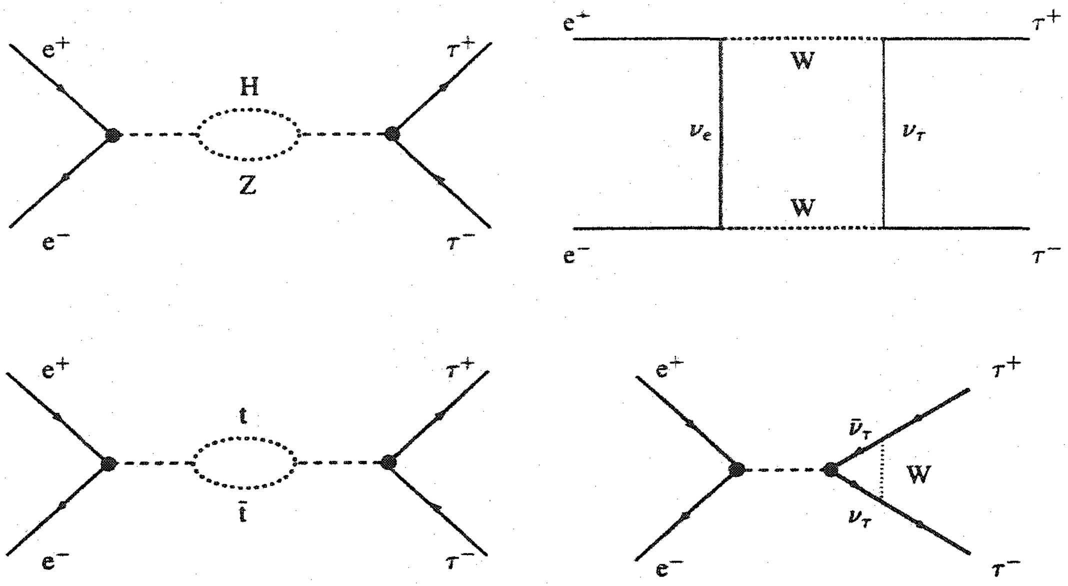

Figure 2.9: Examples of three types of weak correction diagrams, including propagator corrections (left); vertex correction (bottom right); and box correction (top right), are presented.

dependence of the modelled interaction on the mass of the top quark and the mass of the Higgs particle. This is a beautiful example of a quantum mechanical effect; measurements with a suitable degree of precision can provide indirect information via higher order loop corrections regarding particles that are otherwise inaccessible at present day interaction energies. Precisely because of this type of effect, the measurement of standard model parameters such as $\sin^2\theta_W$ are important, not only as fundamental parameters themselves, but as tools with which to search for new physics such as the existence of the conjectured Higgs particle. Figure 2.10 illustrates the dependence of tau polarization on the mass of the top quark and on the mass of the Higgs particle.

2.4.3 Photon Exchange, ISR, and Interaction Energy Dependence

While tau pair data collected during the initial phase of LEP operation is dominated by Z^0 exchange, the effects of γ exchange production, represented by the first Feynman diagram in Figure 2.1, and of γ-Z^0 interference must be taken in account. The relative γ exchange contribution increases for data collected at energies away from the Z^0 mass and

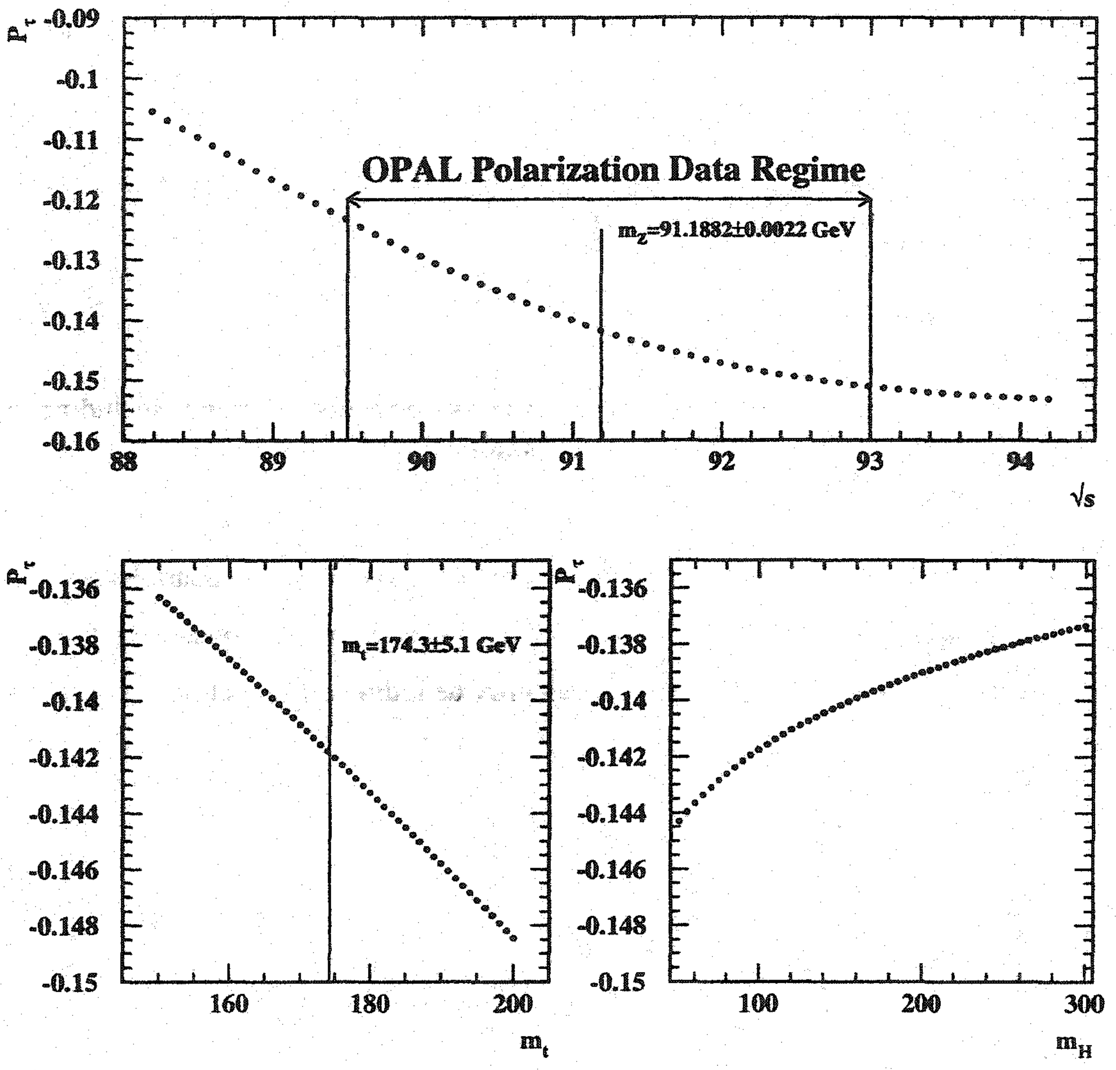

Figure 2.10: Shown is the variation of the tau polarization as a function of centre-of-mass energy, $\sqrt{s}$ (top); as a function of the mass of the top quark, m_t (bottom left); and as a function of the mass of the Higgs particle, m_H (bottom right).

thus these effects are energy dependent. These effects are not included in the Monte Carlo simulation but are accounted for by transforming the $\langle P_\tau \rangle$ and A_{pol}^{FB} fit values to the neutral current asymmetry parameters, A_τ and A_e , by using the ZFITTER program as described below [20].

The measured values of the polarization asymmetry parameters depend roughly linearly on the the centre-of-mass energy at which events are generated; Figure 2.10 indicates the level of this dependence. As described below, the precisely measured interaction energies at which the data for this analysis were collected varied as much as 2 GeV around the Z^0 peak energy. In addition, initial state radiation alters the effective centre-of-mass energy.

In order to produce a measurement of $\sin^2 \theta_{eff}^{lept}$ at an energy corresponding to the mass of the Z^0 , it is necessary to correct the fit results for this variation in interaction energies. As with the γ exchange corrections, the centre-of-mass corrections are also determined using the ZFITTER software package and are applied in the transformation of P_τ and A_{pol}^{FB} to A_τ and A_e .

It should be clearly stated that these are not correction factors in the sense that the radiative corrections are, since it is entirely valid to measure the tau polarization asymmetries at energies away from the Z^0 peak. Such measurements, in fact, validate the conjectured standard model dependence of the polarization on interaction energy. But assuming this dependence is established, an effective way in which to interpret, compare, and combine the statistical power of the collected data is to translate the measurements from these various energies to equivalent values at the Z^0 peak in terms of the effective couplings. This is the strategy adopted by all LEP experiments, thus allowing a straight-forward comparison of results to be made and facilitating the combining of the LEP results.

2.4.4 ZFITTER Correction

ZFITTER (version 6.22 used here) [20] is a semi-analytical software package used to calculate e^+e^-annihilation process observables including differential cross-sections and asymmetries. The program includes complete order α QED radiative corrections, complete order α weak corrections, γ exchange, Z^0 exchange and γ-Z^0 interference terms. For this analysis, ZFITTER is used to transform from the fit parameters to the neutral coupling asymmetry parameters, A_τ and A_e , defined at the mass of the Z^0 .

In order to interpret the $\langle P_\tau \rangle$ and A_{pol}^{FB} measurements in terms of the neutral current asymmetry parameters, A_τ and A_e , corrections on the order of 0.5% are applied to the measured parameters to account for the small contributions to $\langle P_\tau \rangle$ and A_{pol}^{FB} arising from the γ and Z-γ propagator terms and for the effects of photonic radiative corrections. The differences between A_τ and $\langle P_\tau \rangle$ and between $4/3 A_{pol}^{FB}$ and A_e arising from these known effects are calculated using the ZFITTER program. These ZFITTER-computed differences enable values of A_τ and A_e to be quoted which correspond to the measurements of $\langle P_\tau \rangle$ and A_{pol}^{FB} . These small corrections are calculated in the following manner.

For a set of standard model parameters (Z mass, top mass, Higgs mass, α_{QED} and α_s) ZFITTER provides A_τ and A_e as well as values for $\langle P_\tau \rangle$ and A_{pol}^{FB} . Because of the non-Z contributions, different centre-of-mass energies yield different values for $\langle P_\tau \rangle$ and A_{pol}^{FB} . In addition, the $\cos\theta$ dependence is not precisely the same as for pure Z-exchange with no radiation. Therefore, for each of the three centre-of-mass energy bins in this analysis, ZFITTER is used to compute $\langle P_\tau \rangle$ as a function of $\cos\theta$ which is then fitted with the same form assumed in this analysis to extract $\langle P_\tau \rangle$ and A_{pol}^{FB} . The difference between $\langle P_\tau \rangle$ and A_τ and $4/3 A_{pol}^{FB}$ and A_e are taken as the correction for a particular set of standard model parameters. If the difference in $\cos\theta$ dependencies were to be ignored, a 0.04% bias to the quoted asymmetry values would be introduced.

The size of the correction has a slight dependence on the value of the input standard model parameters and in particular to the assumed top mass; this is cast as a dependence on $\langle P_\tau \rangle$ and A_{pol}^{FB} . Therefore, a series of corrections are calculated for different values of the top mass and the correction which corresponds to our measured values of $\langle P_\tau \rangle$ and A_{pol}^{FB} is employed. Although the dependence is very small with respect to the systematic errors in the analysis, this approach minimizes the reliance on other measurements.

The systematic uncertainty on the quoted values for A_τ and A_e arising from these corrections is 0.02% and is dominated by sensitivity of the correction to the assumed

Higgs mass for a fixed top mass.

Chapter 3

The OPAL Experiment at LEP

"Every union of parts must make a whole and exhaust all the notes necessary to the most complex expression of the contents, so that no deficiency should anywhere be sensible by which another part might be rendered possible" - Johann Forkel

---

The OPAL (Omni-Purpose Apparatus at LEP) experiment [21] is one of four similar and complementary particle physics detectors located on the LEP (Large Electron Positron) storage ring near Geneva, Switzerland. Designed to make a broad range of measurements of particle interactions arising from electron-positron collisions at centre-of-mass energies near and above the Z^0 pole, the OPAL detector is a multipurpose detector composed of several sub-detector components. A description of the OPAL sub-detectors of primary importance to this analysis, along with a brief outline of the LEP accelerator and storage system, is found below.

3.1 LEP

The LEP storage ring is one of several particle accelerators operated by the European Organization for Nuclear Research (CERN). It is an approximately circular electron synchrotron with a circumference of 26.66 km; the largest such device in the world (Figure

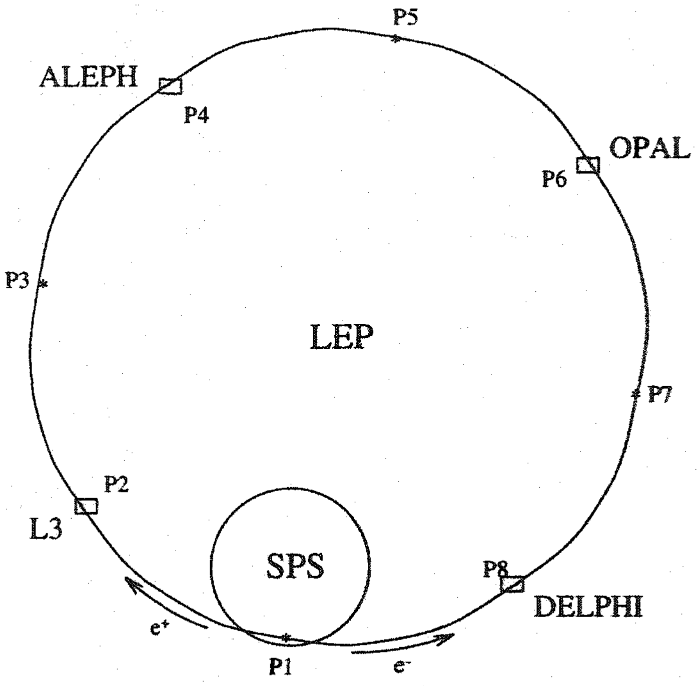

Figure 3.1: Layout of the LEP storage ring including location of the four experiments (not to scale).

3.1). The purpose of LEP is to deliver intense beams of electrons and positrons for collision inside the detectors located at four interaction points on the ring. Counter-rotating electron and positron beams circulate within the LEP vacuum tube and are merged at each of these points.

Operation of the main LEP synchrotron storage ring requires the concerted operation of a number of smaller accelerators (Figure 3.2) [22][23]. To initiate a fill, a supply of positrons must be produced in an $e^- \rightarrow e^+$ converter in which a high intensity beam of 200 MeV electrons is focused at a tungsten target to create the positrons. Electrons for the fill are generated near the converter from a low intensity electron gun. The positrons and electrons are then introduced into a 600 MeV linear accelerator and subsequently transferred to the 600 MeV Electron Positron Accumulation (EPA) ring. During each stage, the beams are accelerated to increasingly higher energies. Each particle type is

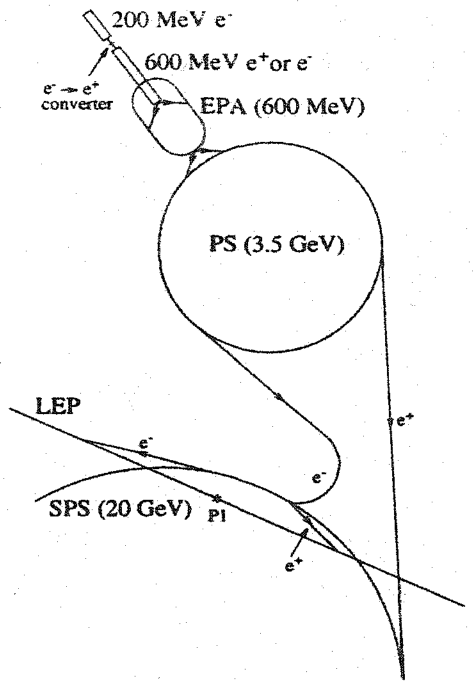

Figure 3.2: The injection system used at LEP to fill the main electron-positron storage ring (not to scale).

collected separately into 8 bunches and injected into the Proton Synchrotron (PS) where they are accelerated to 3.5 GeV. From the PS the beams are transferred to the Super Proton Synchrotron (SPS) and accelerated to 20 GeV. Finally, the beams are injected into the main LEP ring where, during running at the Z^0 peak, they are ultimately accelerated to a total beam energy of approximately 45.6 GeV. The beams are then brought into collision at the interaction points in the four detectors and physics events are recorded at a centre-of-mass energy near 91 GeV.

3.2 OPAL Detector

The effective selection of tau pair events and their subsequent decays requires the collation of information collected from all of the OPAL sub-detectors. The OPAL apparatus (Figure 3.3) is an approximately cylindrical, multi-purpose magnetic spectrometer and calorimeter with a hermeticity of almost 98 percent. For reference, the z coordinate is

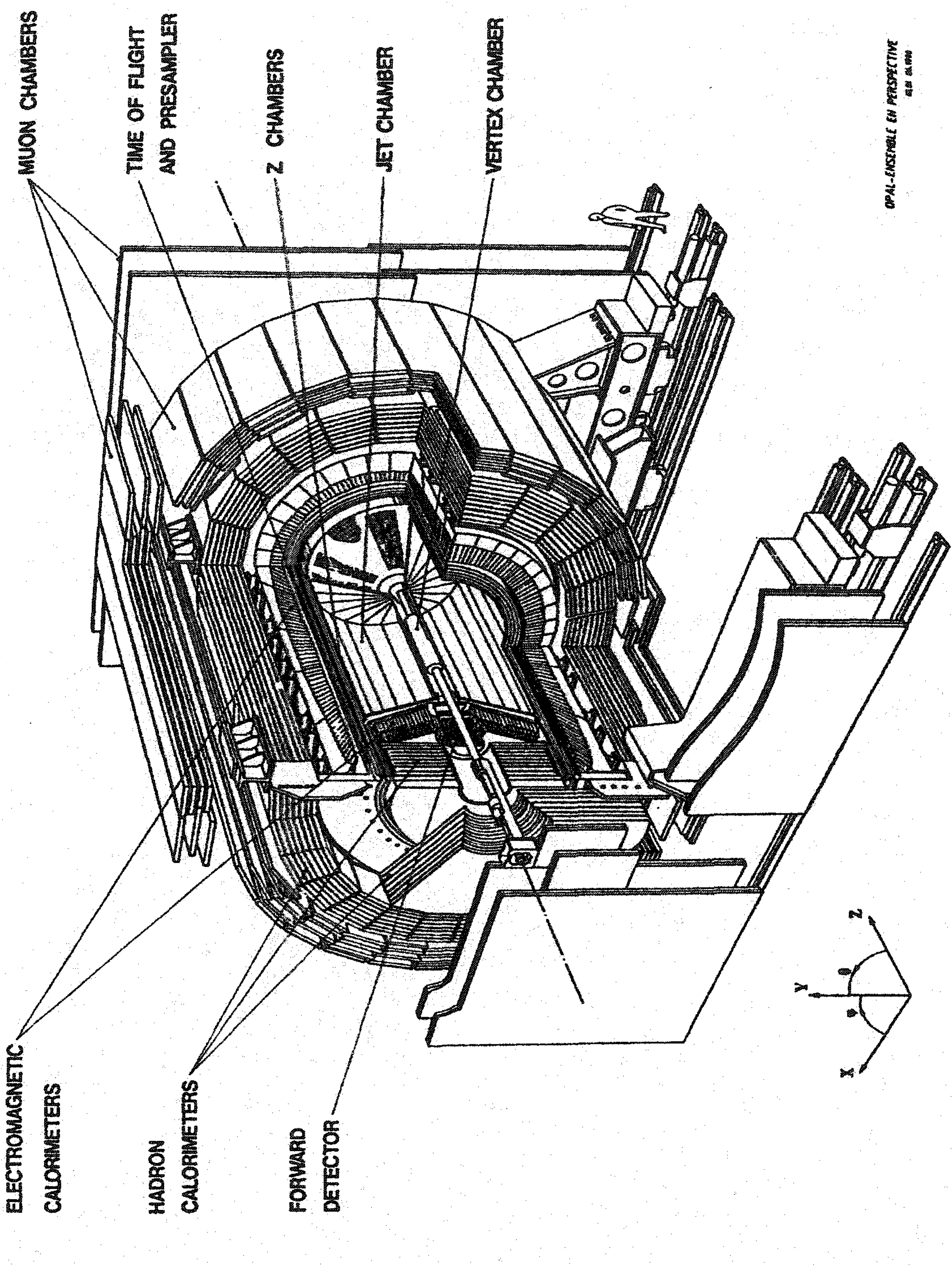

Figure 3.3: The OPAL detector at LEP. An indication of the scale is given by the figure standing at the bottom left.

defined as parallel to the direction of the electron beam. It is then convenient to define a conventional right handed coordinate system with the inward radial direction defined as x. In cylindrical coordinates, θ gives the polar angle with respect to the z-axis and ϕ the azimuthal angle from the x-axis.

The detector is composed of a central 'barrel' region which extends in polar angle to approximately $|\cos\theta| < 0.72$ and two conical endcap sections which increase the geometric acceptance to $|\cos\theta| < 0.98$. Cross-sectional views of each part of the detector are given in Figure 3.4. Conceptually, OPAL may be divided into three sections located at increasing radii from the interaction point. The inner portion of the detector consists of a system of tracking chambers enclosed in a pressure vessel and surrounded by a solenoid. A time-of-flight (TOF) system and electromagnetic calorimeter (ECAL) with presampler comprise the middle section while the outer section includes the iron return yoke of the magnet instrumented as a hadronic calorimeter (HCAL) and muon detectors.

For the purposes of this analysis, it is convenient to define three detector $|\cos\theta|$ regions: a barrel region defined by $|\cos\theta| < 0.72$, an 'overlap' region defined by $0.72 < |\cos\theta| < 0.81$, and an 'endcap' region defined by $0.81 < |\cos\theta| < 0.90$. As may be seen in Figure 3.5, the barrel region corresponds to the uniform central cylinder of the detector, the endcap region to relatively uniform regions of the two detector endcaps, and the overlap region to the complicated transition area of the detector where the barrel and endcap sub-detectors overlap.

3.2.1 Tracking Detectors

The innermost part of the OPAL detector consists of a series of vertex and drift chambers designed to track charged particles and provide measurements of momenta, energy loss, and primary and secondary vertex positions. This assembly of sub-detectors includes a silicon micro-vertex detector (μVTX) [24] introduced in 1992 and upgraded in 1994, a high resolution vertex detector (CV) [25], a large volume 'central jet' drift chamber (CJ) [26], and a series of 'z-chamber' drift chambers (CZ) [27]. To allow precision momentum measurement and charge determination, these detectors operate in the presence of a 0.435

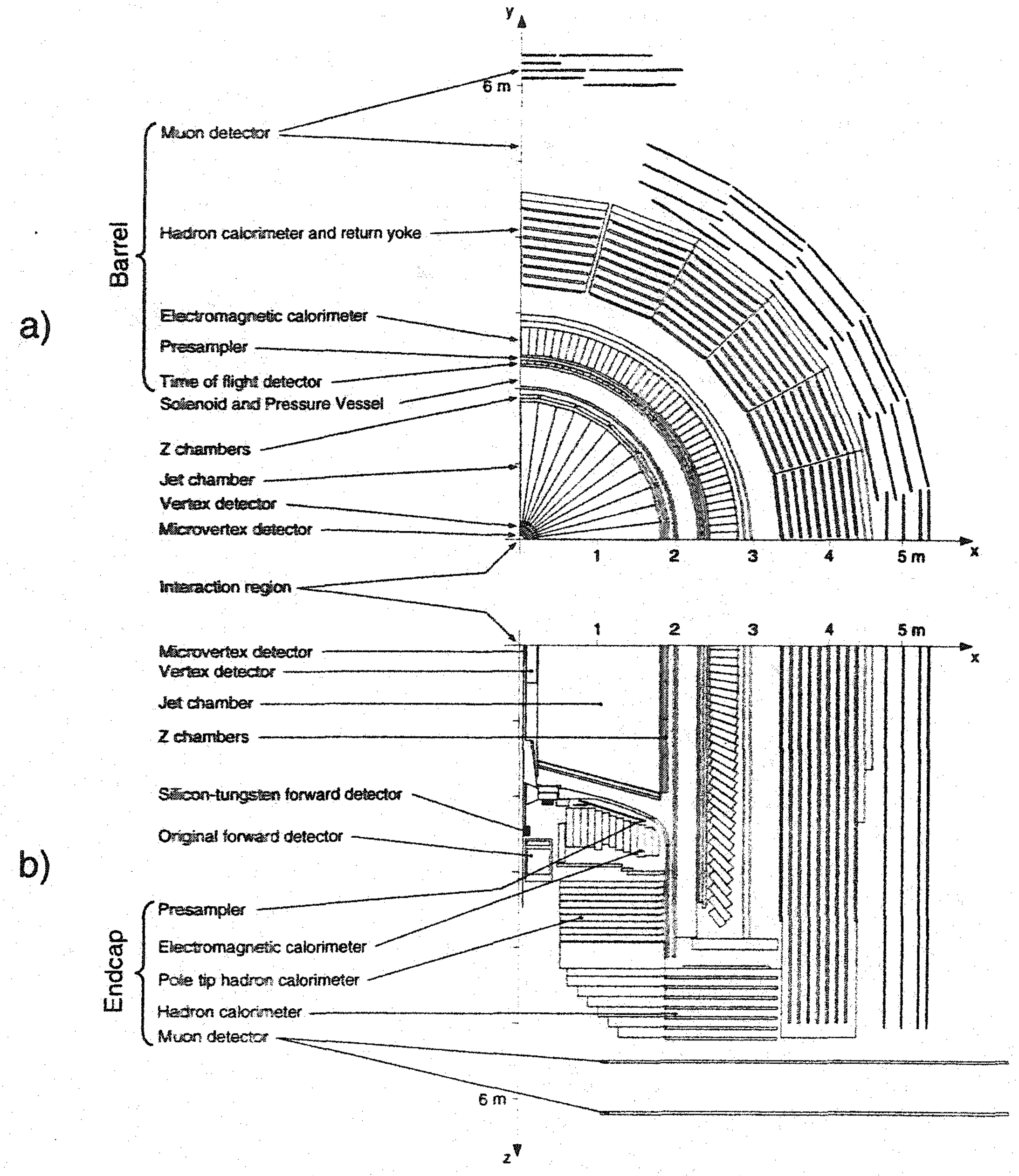

Figure 3.4: Cross-sectional view (a) in x-y of the barrel portion and (b) in x-z of the endcap region of the OPAL detector.

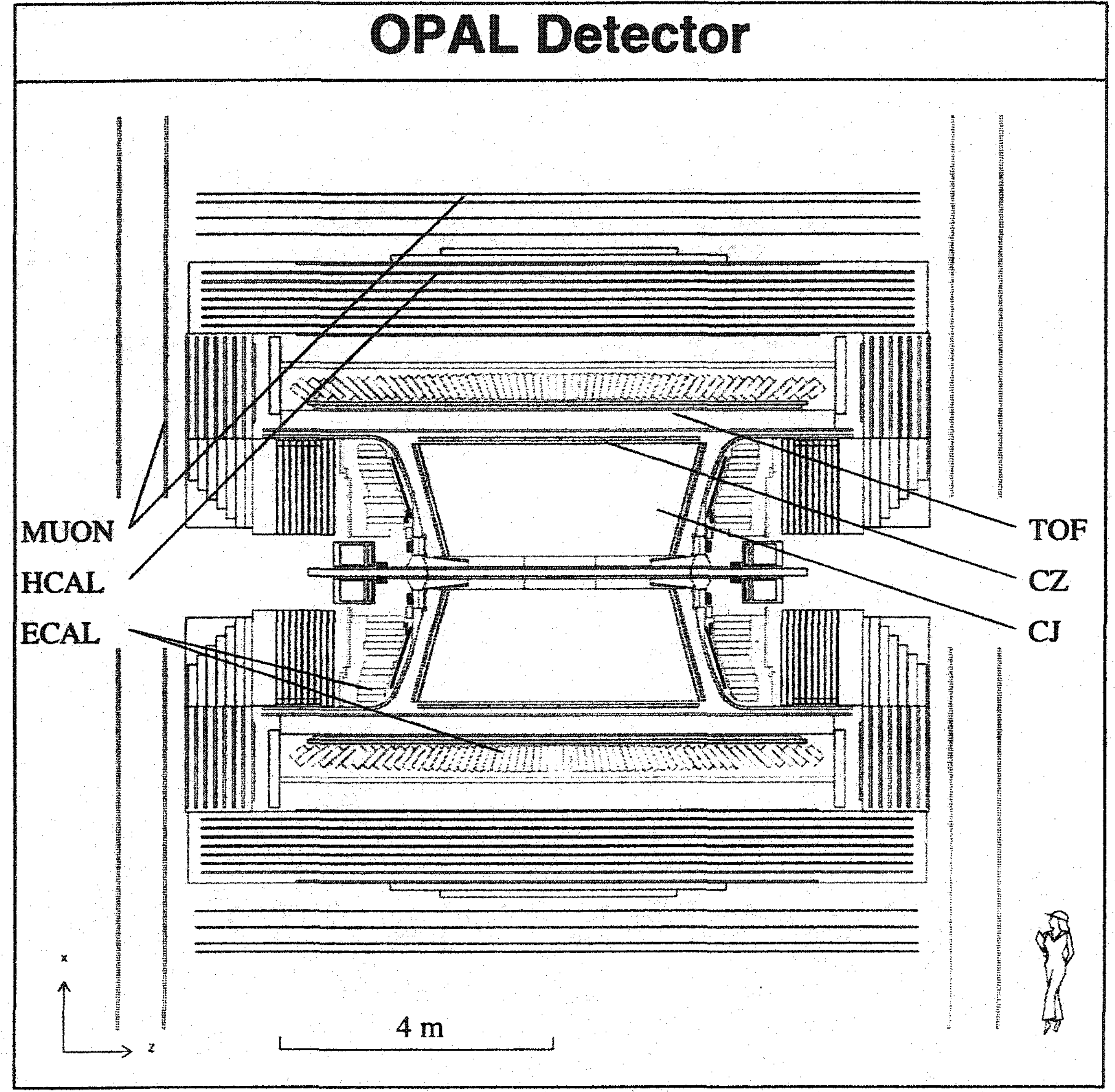

Figure 3.5: Top view (in r-z) of the OPAL detector.

Tesla axial magnetic field aligned along the electron beam direction and generated by a solenoidal coil with iron return yoke. A pressure vessel inside the solenoid encloses the central tracking system and contains a gaseous mixture of argon, methane and isobutane (88.2%, 9.8%, and 2.0% respectively) held at 4 bar pressure.

Situated closest to the beam pipe is the silicon micro-vertex detector. The μVTX is constructed from 11 inner (61 mm radius) and 14 outer (75 mm radius) ladders of silicon detector wafers. Primarily important for b quark identification and particle lifetime studies, the μVTX detector provides precision position measurements of charged particles close to the beam pipe and assists in improving momentum measurement resolution. Each μVTX layer provides a position measurement with a resolution of approximately 10 μm.

Surrounding the μVTX is a 1 m long, 470 mm diameter cylindrical drift chamber. This precision vertex detector (CV) provides position information close to the interaction region which aids in the determination of event topologies and reconstruction of the primary and secondary decay vertices. The CV is constructed from 2 layers, each divided into 36 azimuthal cells corresponding to the geometry of the central jet chamber. The inner layer contains axial wires for measurements in the $r - \phi$ plane while the outer layer contains stereo wires for accurate z coordinate measurements. The average spatial resolutions for this detector are estimated to be 50 μm in the $r - \phi$ plane and 700 μm in z.

The μVTX and CV detectors are embedded in a large volume drift chamber, the central jet chamber (CJ), which provides the primary charged particle information. Approximately 4 m in length, this detector has a cylindrical geometry with an inner radius of 0.5 m and an outer diameter of 3.7 m. It consists of 24 identical azimuthal sectors. each containing 159 axial wires arranged in a radial plane. Cathode and anode planes are separated by 7.5° in ϕ with the first cathode plan occurring at 0°. The CJ provides spatial measurements of charged particle trajectories (i.e. 'tracks') and energy loss measurements used for particle identification. The pressure at which gas in the chamber is kept has been chosen to optimize dE/dx sensitivity without loss of momentum resolution. Figure 3.6 indicates the usefulness of the dE/dx information for particle identification with the typical track momenta measured by OPAL.

Position measurements have been shown to provide an average resolution of 135 μm in the $r - \phi$ plane and 6 cm in z. In addition, momentum measurements, obtained by measuring the curvature of the track in the magnetic field, have a resolution σ_p/p^2 estimated to be $2.2 \times 10^{-3}\mathrm{GeV}^{-1}$. The energy loss resolution $\sigma_{\frac{dE}{dx}}/\frac{dE}{dx}$ is approximately 3.8%.

Outside of, and arranged cylindrically around the CJ, is a series of 24 drift chambers denoted as the z-chambers (CZ). The CZ provides measurements of the z coordinate of charged particles exiting the central system of tracking detectors. The average resolution in z for this detector is approximately 300 μm and the average $r - \phi$ resolution is approximately 1.5 cm.

3.2.2 Time-of-flight and Electromagnetic calorimeter

Immediately exterior to the central tracking chambers and the magnet solenoid are 160 scintillation counters assembled in a cylindrical geometry [21]. These counters measure the time-of-flight (TOF) of particles passing through the OPAL detector. The counters are 6.84 m long and range from 89 to 91 cm in width with gaps of no more than 2.6 mm between each counter. The TOF sub-detector, with a timing resolution of 460 ps and a z resolution of 7.5 cm, is primarily used for event triggering and rejection of cosmic ray background events reaching the 100 m underground depth of OPAL.

Crucial to many OPAL analyses are the energy and position measurements provided by the electromagnetic calorimeter system [21]. This system, located between the solenoid coil and the iron return yoke, includes the primary calorimeter itself and, since most electromagnetic showers are initiated before the calorimeter, additional presampling devices. Material located in front of the calorimeter, largely associated with the pressure vessel housing the vertex and tracking chambers, and with the magnet coil, is primarily responsible for pre-ECAL showering. Both the presampler and calorimeter components are composed of overlapping barrel and endcap sections.

The barrel presampler (PB) [21] consists of a set of 16 gas chamber detectors operated in limited streamer mode. Constructed in a cylindrical fashion, the PB is positioned in

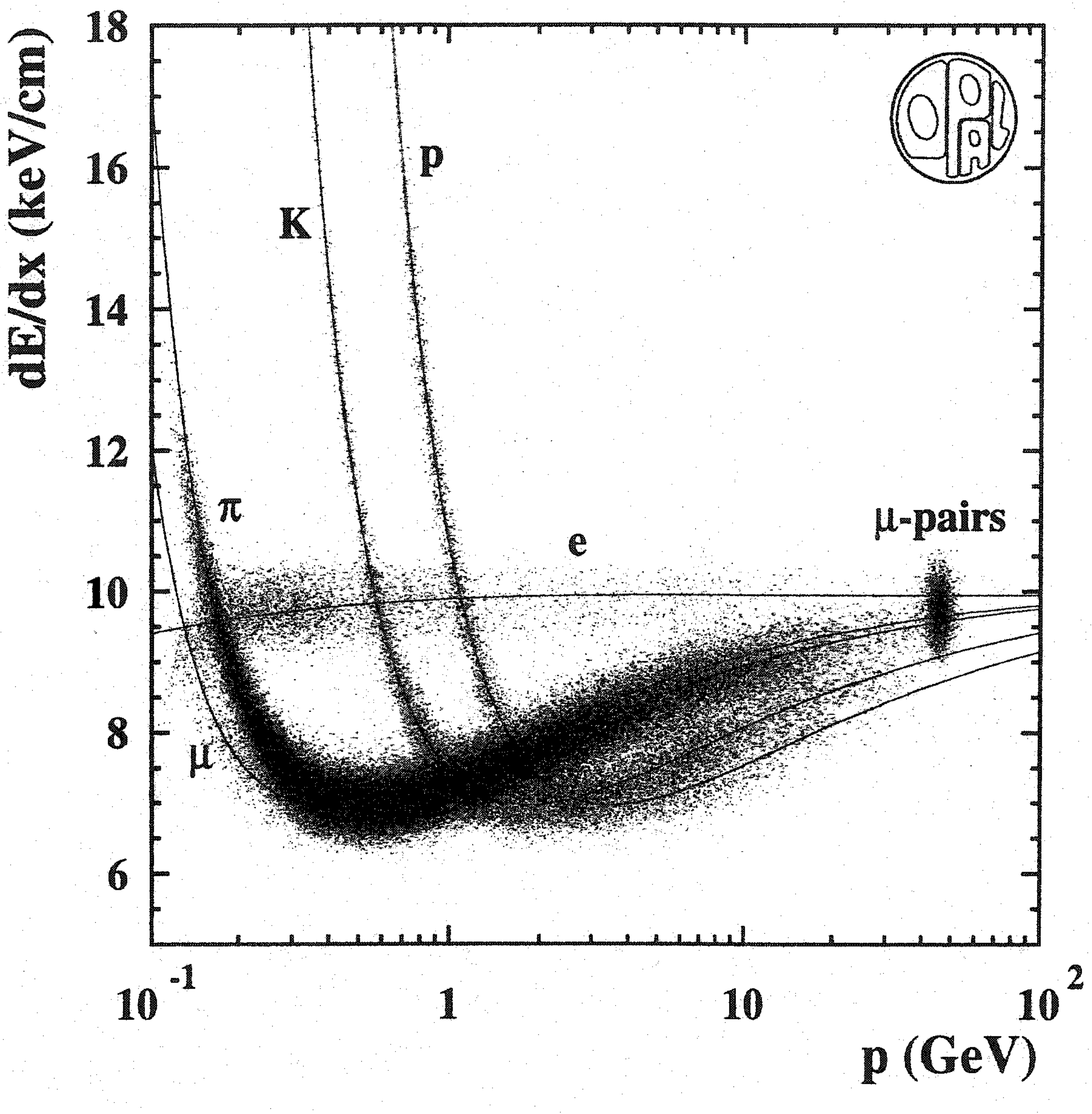

Figure 3.6: The specific energy loss (dE/dx) as a function of momenta for various particle types in the OPAL detector is shown. It is evident that particle identification can be effected with this information, particularly between muons/hadrons and electrons between 0.5 and 10 GeV.

front of the calorimeter at a radius of 2.39 m from the interaction point and extends a total length of 6.62 m. The angular resolution of electromagnetic showers measured with PB is on the order of 2 mrad.

Covering a geometric acceptance $0.83 < |\cos\theta| < 0.95$, each half of the endcap presampler (PE) consists of 32 multiwire chambers arranged in an umbrella shape. The PE provides information analogous to the PB in the endcap region of the detector.

The electromagnetic calorimeter (ECAL) itself consists of a barrel region (EB) containing 9440 lead glass blocks and two endcap regions (EE) each containing 1132 blocks. The lead glass blocks used in both regions have a 10×10 cm^2 cross-sectional area corresponding to an angular coverage of 40×40 mrad^2. The angular resolution of the ECAL is important for separating showers arising from different particles entering the detector in close proximity. For example, the selection of $\tau \rightarrow \rho\nu_\tau$ events requires the separation and and identification of both the single charged pion and the neutral pion produced in such tau decays. Relativistic charged particles entering the lead glass blocks produce Cerenkov light which is then detected by photomultiplier tubes fitted to the back of each block.

The EB covers the full azimuthal angle, a polar acceptance of $|\cos\theta| < 0.82$, and has an inner radius of 2.46 m. The central design principle requires the ECAL detector to completely absorb electrons and photons while allowing muons and some hadrons to reach the hadronic calorimeter. The 37 cm depth of each block represents 24.6 radiation lengths ($\mathrm{X_0}$) and 2 interaction lengths (λ_{int}) of material and, with the additional $2\mathrm{X_0}$ of material in front of the ECAL, is suitable for this purpose. The calorimeter is divided into 59 blocks in the z direction and 160 blocks in the ϕ direction. To maximize the probability that a particle shower will largely be confined to a small number of blocks, each block points towards the interaction region. However, to prevent particles from escaping through gaps between the blocks, the EB is constructed with a small offset from a true pointing geometry. Analysis of e^+e^-collision data has demonstrated that the EB provides an energy resolution of $\sigma_{\mathrm{E}}/\mathrm{E} = 1.5\pm0.3\%\oplus16\pm0.3\%/\sqrt{\mathrm{E}}$ for electromagnetic showers [28] where the first term represents instrumental uncertainties and the second corresponds to intrinsic statistical fluctuations associated with shower development.

Each of the two domed-shaped EE components covers the full azimuthal angle and a polar angle of $0.81 < |\cos\theta| < 0.98$. Owing to geometric constraints, lead glass blocks in these regions are aligned parallel to the beam axis and were manufactured with depths ranging from 38 to 52 cm. From this arrangement, a minimum depth of 20.5 X_0 is achieved for particles emerging from the interaction region. The energy resolution in this part of the ECAL is estimated to be $\sigma_E/E = 1.8 \pm 1.3\% \oplus 21.8 \pm 2.5\%/\sqrt{E}$ [28]. Again, the first term represents instrumental uncertainties while the second corresponds to intrinsic statistical fluctuations inherent in electromagnetic shower development.

3.2.3 Hadronic Calorimeter and Muon Chambers

Surrounding the ECAL lies the iron return yoke of the magnet. The return yoke has been instrumented as a hadronic calorimeter (HCAL) to allow for hadronic shower energy measurement and tracking between the ECAL and the muon chambers [29].

The barrel portion of the HCAL consists of 9 layers of gas chambers, each 25 mm thick, interleaved with 8 slabs of 100 mm thick iron and fills the region from radii 3.39 m to 4.39 m. Each endcap portion of the HCAL contains 8 active layers with 35 mm gaps separated by 7 slabs of 100 mm thick iron.

The material in front of the HCAL amounts to 2.2 interaction lengths while the HCAL itself constitutes nearly 4 interaction lengths. Therefore, most hadronic showers will be initiated in or before the ECAL but will not reach beyond the HCAL. Studies of e^+e^-collision data estimate the energy resolution of the HCAL to be $\sigma_E/E = (0.165 \pm 0.024) + (0.847 \pm 0.100)/\sqrt{E}$ [30]. It is expected that nearly all muons above 2 GeV will pass through the HCAL and reach the muon chambers.

Comprising the outermost part of the OPAL detector, the muon chambers enclose all of the previously described sub-detectors and are designed for muon identification [31].

The barrel muon chambers (MB) consist of four detector layers covering an angular region of $|\cos\theta| < 0.68$ with a fifth layer covering an angle of $|\cos\theta| < 0.72$. The layers are composed of a total of 110 drift chambers; each chamber has a width of 1.2 m and a depth of 90 mm. The layers are arranged in a staggered geometry to cause most muons to register in at least four layers. Muons are identified by matching tracks from the central tracking chambers with signals generated in the muon chambers. The muon detector is able to measure particle positions in the ϕ direction with an accuracy of 1.5 mm and in the z direction with an accuracy of 2 mm.

Overlapping with the barrel muon chambers, the two muon endcap detectors (ME) cover the polar angle $|0.67 < \cos\theta| < 0.985$. Each ME is constructed from four layers of limited streamer tubes mounted perpendicular to the beam axis. These detectors are used in an analogous fashion to the MB and provide position measurements of comparable precision.

3.2.4 Triggering and Detector Status

As already indicated, the effective collection of high quality data using the OPAL detector requires the simultaneous operation of many complex sub-detector components. In order to ensure that detector components crucial to a given analysis are operating satisfactorily during data collection, detector status bits are encoded with the stored event data for each event.

Each detector component can have one of four possible states. They are

$$\begin{aligned} 0 &= \text{Status Unknown} \\ 1 &= \text{Not On} \\ 2 &= \text{Partially On (low voltage or readout problems)} \\ 3 &= \text{Operating Nominally.} \end{aligned} \tag{3.1}$$

For the tau polarization analysis, the detector status requirements are given in Table 3.1. As is shown, the CV, CJ, ECAL, barrel HCAL, and barrel muon chambers are all required to be in good working order. Any events not passing these requirements are removed from the analysis.

The fact that almost all sub-detector types are represented in Table 3.1 emphasizes that information from all components of the OPAL detector is needed in order to successfully

	CV	CJ	TB	PB	EB	EE	HS	MB
Detector:	3	3	3	2	3	3	3	3

Table 3.1: The detector and trigger status requirements are shown. The acronyms represent CV=vertex chamber, CJ=central jet chamber, TB=time-of-flight, PB=barrel presampler, EB=barrel calorimeter, EE=endcap calorimeter, HS=barrel hadronic calorimeter, MB=barrel muon chambers.

separate the signal and background events for this measurement.

In order to record physics events, the OPAL detector triggers [32] on information received from the various sub-detectors. For the tau polarization analysis, it is important to ensure that the collection of tau pair events is unbiased in terms of the trigger efficiency. As determined in [33], the OPAL trigger is nearly 100% efficient for triggering on $\tau^+ \tau^-$ events, and thus no such bias exists.

Chapter 4

Data and Monte Carlo Summary

"The only difference between water and space is a matter of density" - The Man From Planet X

4.1 Data

The data used for this analysis were collected during the LEP Z^0 operating period from 1990-1995. This constitutes the complete OPAL Z^0 data set and includes the final reprocessing with optimal calibration. Approximately 6.5 million Z^0 events were produced in OPAL during this period, with approximately 3.36% of these decaying to a $\tau^+ \tau^-$ final state pair.

Although tau pair events are the focus of this analysis, the Z^0 can decay to any fermion anti-fermion pair, apart from top quarks. Such events include quark anti-quark ($e^+e^- \rightarrow q\bar{q}$)) pairs, referred to as 'multihadron' events which produce back-to-back 'jets' of particles in the detector; electron-positron pairs ($e^+e^- \rightarrow e^+e^-$) including both s-channel and t-channel processes; and muon anti-muon pairs ($e^+e^- \rightarrow \mu^+\mu^-$). In addition, non-Z^0 exchange two-photon events ($\gamma\gamma f\bar{f}$) can be produced in which the electron and positron interact via emitted photons that combine to create fermion anti-fermion pairs ($f\bar{f}$). In such events, the initial electron and positron typically pass down the beam pipe without being detected in OPAL.

As will be seen, these non-tau pair events constitute backgrounds to the tau pair sample selected by this analysis. Figure 4.1 provides sample Feynman diagrams representing the most important of these background processes.

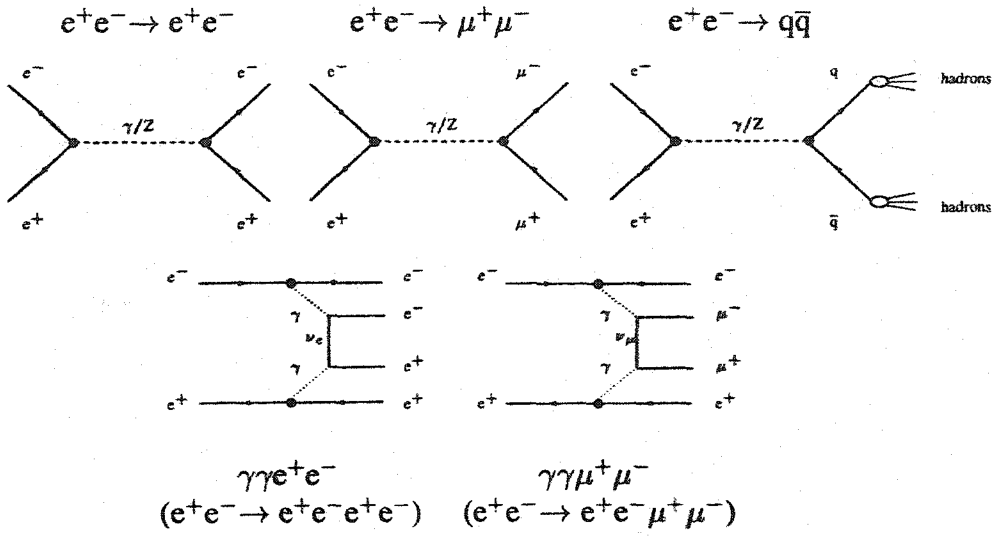

Figure 4.1: Feyman diagrams representing the five most significant non-tau backgrounds are shown. Note that only the s-channel diagram for e^-e^+production is given as an example but the t-channel process is significant as well.

Data were collected within approximately 2 GeV of the Z^0 peak and, for the purposes of this analysis, separated into the three energy ranges defined as defined in Table 4.1. Note that the determination of the beam energy for a given collection period is extremely

	Beam Energy Range	Average Centre-of-mass Energy
Peak-2	$E_{beam} < 45.3$ GeV	89.5 ± 0.2 GeV
Peak	45.3 GeV $< E_{beam} < 45.8$ GeV	91.25 ± 0.05 GeV
Peak+2	45.8 GeV $< E_{beam}$	93.0 ± 0.2 GeV

Table 4.1: The three defined energy regimes. The values in the right-hand column represent the average centre-of-mass energy of data collected within the given range including the rms spread of energies.

precise with the beam energy known to better than 0.02% [34].

Year	Peak-2		Peak		Peak+2	
	Int. Lumi.	Events	Int. Lumi.	Events	Int. Lumi.	Events
1990-91	3.8 pb^{-1}	1900	10.7 pb^{-1}	15900	4.1 pb^{-1}	2900
1992	–	–	23.3 pb^{-1}	34400	–	–
1993	8.3 pb^{-1}	4100	14.4 pb^{-1}	21300	7.7 pb^{-1}	5400
1994	–	–	50.6 pb^{-1}	74900	–	–
1995	6.7 pb^{-1}	3300	13.6 pb^{-1}	20200	7.4 pb^{-1}	5200

Table 4.2: Data collected during each year of Z^0 running for the three energy regimes. The numbers of $e^+e^- \to \tau^+ \tau^-$ events given in each case are the estimated numbers of events produced in OPAL based on the integrated luminosities quoted.

The largest sample of peak events was collected in 1994 with a smaller sample collected in 1992. Both on and off-peak events were produced during the remaining years with the 1993 and 1995 years contributing the largest samples. Table 4.2 indicates the approximate integrated luminosity[1] and number of $\tau^+ \tau^-$ events generated for each year at each energy.

4.2 Monte Carlo Simulation

The tau polarization analysis requires the use of a large sample of simulated Monte Carlo events. The event selection relies on the Monte Carlo method to accurately simulate both signal and background events in order to optimize the data selection criteria and for the generation of likelihood selection distributions. In addition, the subsequent polarizaton parameter fits are carried out with distributions extracted from the Monte Carlo simulation.

Not only must the modelling of the data be adequate, a subject discussed at length in Chapter 7, but a sufficient quantity of simulated events must be available in order to minimize the statistical effects of the finite Monte Carlo sample. Approximately 10 times

---

[1] Luminosity is a measure of the intensity of the colliding beams and is proportional to the number of particles in the beams, the frequency of rotation of the beams, and the beam profiles. Integrated luminosity, given here in units of barns (b) where 1 b = 10^{-24} cm^{-2}, is simply the luminosity integrated over time.

the data statistics in Monte Carlo events has been generated and used by this analysis.

Simulated events are first generated at the physics or ‘four vector’ level using the various Monte Carlo generators described below. The OPAL detector simulation [35], based on the GEANT software package [36], is subsequently added to include the effects of interactions with the OPAL detector materials and to fully model the complete readout of the detector. The Monto Carlo events are passed through the same event reconstruction software as the data, and thus can be treated in exactly the same fashion as the data.

Monte Carlo tau pair and muon pair events were generated with the KORALZ generator [37] while the electron pair events were generated by the BHWIDE progam [38]. The decay of each tau in a Monte Carlo tau pair event is simulated using the TAUOLA package [39]. The VERMASEREN software [40] was used to produce the primary two-photon samples with two leptons in the final state, and JETSET [41], tuned to OPAL reference distributions [42], was used for the simulation of $e^+e^- \to q\bar{q}$ events. Two-photon events with hadronic final states were generated using the PHOJET [43], F2GEN [43], and HERWIG [44] packages while four-fermion events were generated with FERMISV [45] and GRC4f [46]. Note that the hadronic two-photon and four-fermion events have been studied and contribute a negligible effect to this analysis.

All of the Monte Carlo event samples used in this analysis are listed in Table 4.3 including such details as the number of events generated and the estimated integrated luminosity represented.

Event Type	MC Run	Generator	Events	Luminosity	Energy
$\tau^+\tau^-$	1520	KORALZ	600k	405 pb^{-1}	Peak
	1535	KORALZ	70k	142 pb^{-1}	Peak-2
	1536	KORALZ	375k	253 pb^{-1}	Peak
	1537	KORALZ	100k	142 pb^{-1}	Peak+2
	1560	KORALZ	800k	541 pb^{-1}	Peak
	1565	KORALZ	500k	338 pb^{-1}	Peak
$\mu^+\mu^-$	1620	KORALZ	600k	404 pb^{-1}	Peak
	1635	KORALZ	70k	142 pb^{-1}	Peak-2
	1636	KORALZ	375k	253 pb^{-1}	Peak
	1637	KORALZ	100k	143 pb^{-1}	Peak+2
	1618	KORALZ	800k	540 pb^{-1}	Peak
	1619	KORALZ	500k	337 pb^{-1}	Peak
e^+e^-	1336	BHWIDE	150k	41 pb^{-1}	Peak-2
	1335	BHWIDE	300k	74 pb^{-1}	Peak
	1337	BHWIDE	150k	55 pb^{-1}	Peak+2
	1360	BHWIDE	800k	195 pb^{-1}	Peak
	1365	BHWIDE	500k	123 pb^{-1}	Peak
	1370	BHWIDE	400k	97 pb^{-1}	Peak
$\gamma\gamma\mu^+\mu^-$	1745	VERMASEREN	400k	456 pb^{-1}	Peak
	1053	VERMASEREN	500k	576 pb^{-1}	Peak
	1054	VERMASEREN	300k	345 pb^{-1}	Peak
$\gamma\gamma e^+e^-$	1746	VERMASEREN	400k	392 pb^{-1}	Peak
	1063	VERMASEREN	500k	493 pb^{-1}	Peak
	1064	VERMASEREN	300k	296 pb^{-1}	Peak
$q\bar{q}$	2291	JETSET	1000k	32 pb^{-1}	Peak
	2917	JETSET	900k	29 pb^{-1}	Peak
	2926	JETSET	750k	24 pb^{-1}	Peak
	5020	JETSET	900k	29 pb^{-1}	Peak
$\gamma\gamma\ q\bar{q}$	1014	PHOJET/JETSET	1000k	209 pb^{-1}	Peak
$\gamma\gamma\ q\bar{q}$	1039	F2GEN	100k	152 pb^{-1}	Peak
$\gamma\gamma\ q\bar{q}$	1065	HERWIG	200k	329 pb^{-1}	Peak
$e^+e^-q\bar{q}$	6503	FERMISV	4290	1000 pb^{-1}	Peak
$\mu^+\mu^-q\bar{q}$	6504	FERMISV	3860	1000 pb^{-1}	Peak
$\tau^+\tau^-\ q\bar{q}$	6505	FERMISV	1020	1000 pb^{-1}	Peak
$e^+e^-e^+e^-$	6506	FERMISV	5550	1000 pb^{-1}	Peak
$e^+e^-\mu^+\mu^-$	6507	FERMISV	5600	1000 pb^{-1}	Peak
$e^+e^-\tau^+\tau^-$	6508	FERMISV	4170	1000 pb^{-1}	Peak
$\mu^+\mu^-\mu^+\mu^-$	6509	FERMISV	570	1000 pb^{-1}	Peak
$\mu^+\mu^-\tau^+\tau^-$	6510	FERMISV	510	1000 pb^{-1}	Peak
$Z^0\ e^+e^-$	6513	GRC4f	51415	500 pb^{-1}	Peak

Table 4.3: Monte Carlo event samples used for the OPAL tau polarization analysis. See text for descriptions and references. The numbers of events listed for each case are the actual number of generated events. The corresponding integrated luminosities are calculated based on these numbers of events and the estimated cross-section for the given process. The definition of the centre-of-mass energy regions are defined in Table 4.1

Chapter 5

Event Selection

"Don't be silly. The important drinking hasn't started yet!" - Ingrid Bergman, Notorious

---

5.1 Introduction

The selection of tau decays used for the polarization fit occurs in two stages. First, tau pair candidates are selected from the general OPAL Z^0 data set by placing requirements on the total number of charged particles and by examining such quantities as the total event energy measured in the ECAL and the total track momentum. These requirements, or 'cuts', provide a sample of tau pair candidates with high efficiency and low background.

'Likelihood' selections for each of the five tau decay channels used in the analysis ($\tau \rightarrow e\bar{\nu}_e\nu_\tau$, $\tau \rightarrow \mu\bar{\nu}_\mu\nu_\tau$, $\tau \rightarrow \pi\,\nu_\tau$, $\tau \rightarrow \rho\nu_\tau$, and $\tau \rightarrow a_1\,\nu_\tau$) are then applied.

In the following sections, the definitions of the selection variables are provided and the details of each of the two steps in the selection process are described.

5.2 Tau Pair Selection

5.2.1 Introduction

The selection of tau pair candidates relies on the use of cuts on event variable distributions designed to distinguish such events from the general OPAL Z^0 data set. The 'standard' OPAL tau pair selection [47] is used for this analysis with additional selection cuts applied, particularly in the overlap and endcap regions, in order to reduce various non-tau backgrounds. These additional cuts are described in the Appendix D.

The principle non-tau pair backgrounds in the selection include multihadron $e^+e^- \rightarrow q\bar{q}$ events, $e^+e^- \rightarrow \mu^+\mu^-$ events, $e^+e^- \rightarrow e^+e^-$ events, and two-photon events. The general selection strategy is to apply cuts on measured event quantities to successively eliminate the majority of each of these backgrounds.

Since all $\tau^+ \tau^-$ events contain at least two unobserved neutrinos, less than the total centre-of-mass energy is measured in the detector and the total transverse momentum is imbalanced for these events.

As will be seen, multihadron $e^+e^- \rightarrow q\bar{q}$ events are removed by requiring that only a small number of tracks are produced in an event; $e^+e^- \rightarrow e^+e^-$ and $e^+e^- \rightarrow \mu^+\mu^-$ lepton pair backgrounds are removed by rejecting events with total measured energy close to the centre-of-mass energy when there are exactly two back-to-back tracks; and two-photon events are removed by requiring a minimum amount of energy to be measured in an event and by rejecting events in which the total measured momentum in the transverse plane of the detector is balanced.

5.2.2 Variable Definitions

In order to specify the details of the tau pair selection, the definition of various quantities, such as a 'track' in the central tracking chamber and a 'cluster' in the ECAL, must be provided.

A track in the CJ is recognized as a 'good track' if it has

$$N_{hit}(CJ) \geq 20, \tag{5.1}$$

$$p_t \geq 0.1\,\mathrm{GeV}, \tag{5.2}$$

$$|d_0| \leq 2\,\mathrm{cm}, \tag{5.3}$$

$$|z_0| \leq 75\,\mathrm{cm}, \tag{5.4}$$

$$R_{min} \leq 75\,\mathrm{cm}, \tag{5.5}$$

where $N_{hit}(CJ)$ is the number of hits in the jet chamber; p_t, the transverse momentum, is the component of track momentum perpendicular to the beam axis; $|d_0|$ is the distance of closest approach of the track to the beam axis in the plane transverse to the beam axis; $|z_0|$ is the distance of the track from the interaction point along the beam axis; and R_{min} is the radial separation between the beam axis and the first hit in the jet chamber. Such a track will have associated with it an absolute momentum determined from the track curvature, a charge, and θ and ϕ direction values. In general, these requirements ensure the reliability of the measured track properties and that the track has been produced in association with an electron-positron annihilation at the interaction point.

In the electromagnetic calorimeter, 'clusters' are formed from contiguous groups of lead glass blocks containing deposited energy. Ideally, such clusters will each arise from the showering of a single particle entering the ECAL and the measured energy will be associated with that particle. In practice, particle showers can overlap and a given cluster may correspond to more than one particle.

A 'good' cluster is defined in the barrel region with

$$N_{blk} \geq 1, \tag{5.6}$$

$$E_{cls(raw)} \geq 0.1\,\mathrm{GeV}, \tag{5.7}$$

and in the endcap with

$$N_{blk} \geq 2, \tag{5.8}$$

$$E_{cls(raw)} \geq 0.2\,\mathrm{GeV}, \tag{5.9}$$

where N_{blk} is the number of lead glass blocks associated to the cluster and $E_{cls(raw)}$ is the raw measured cluster energy before being corrected for energy loss occurring prior to a particle's entry into the ECAL (the energy loss is caused by interactions in the material in front of the ECAL). Each defined cluster has a corrected measured energy associated to it, based on the assumption that the particle is an electron, as well as θ and ϕ position measurements.

Tau pairs produced in OPAL have a large boost and hence the decay products of each tau are normally confined within a relatively narrow cone. In order to aid selection and to specify tau decay topologies, it is useful to define a tau jet for each tau candidate in an event. A jet is defined by

$$\Theta_{\text{half-cone}} = 35^\circ\text{, and} \tag{5.10}$$

$$P_{\text{cone}} \geq 0.01E_{\text{beam}}\,, \tag{5.11}$$

where E_{beam} is the beam energy, $\Theta_{\text{half-cone}}$ is the half-angle of the cone around the direction constructed from the vector sum of track and ECAL cluster momenta associated to the cone, and P_{cone} is the total track and ECAL cluster energy in the cone. Events are selected if the number of cones with at least one charged track and passing the P_{cone} requirement is equal to two.

Finally, a quantity that is used throughout this analysis is the $\cos\theta$ of the τ^- jet where θ is the polar angle between the τ^- flight direction and the e^- beam direction. To determine θ, the τ^- angle and the negative of the τ^+ angle, each constructed from track and ECAL information, are averaged and the cosine of the resulting value designated $\cos\theta_{\tau^-}$.

5.2.3 Multihadron Event Rejection

The primary observable difference between multihadron events and lepton events produced through electron-positron annihilation at the Z^0 peak is the number of particles created. In multihadron production for example, the average event charged particle multiplicity, is greater than 6 over 99% of the time [48], while for tau pair production, the number of charged particles produced in OPAL is less than 7 over 98% of the time (estimated from Monte Carlo). Hence, the multihadron background is largely eliminated by requiring

$$\begin{aligned} 1 &\leq N^{Tot}_{chrg} \leq 6, \text{and} && (5.12) \\ N^{Tot}_{clust} &\leq 10, && (5.13) \end{aligned}$$

where N^{Tot}_{chrg} is the total number of good charged particles measured in the event and N^{Tot}_{clust} is the number of good clusters. Figure 5.1 shows the distributions of N^{Tot}_{chrg} for Monte Carlo tau pair and $e^+e^- \rightarrow q\bar{q}$ events before selection; the effectiveness of the N^{Tot}_{chrg} cut may be seen.

5.2.4 Cosmic Ray Rejection

Cosmic ray rejection cuts are applied based on the assumption that these background events will not appear to have originated at the interaction point and/or will exhibit timing measurements inconsistent with a true physics event. Such events are rejected by requiring that all physics events satisfy

$$\begin{aligned} |d_0|_{min} &\leq 0.5\,\text{cm}, && (5.14) \\ |z_0|_{min} &\leq 20\,\text{cm, and} && (5.15) \\ |z_0|_{ave} &\leq 20\,\text{cm}, && (5.16) \end{aligned}$$

where, for all tracks in an event, $|d_0|_{min}$ is the minimum $|d_0|$; $|z_0|_{min}$ is the minimum $|z_0|$; and $|z_0|_{ave}$ is the average $|z_0|$. In addition, events within the geometrical acceptance of the time-of-flight detector ($|\cos\theta| < 0.8$) are rejected unless at least one of the time-of-flight counters returns

$$|t_{mes} - t_{exp}| \leq 10\,\text{ns}, \tag{5.17}$$

where t_{mes} is the measured time-of-flight and t_{exp} is the time-of-flight expected for an event generated at the nominal interaction point. An event is further rejected if all counter pairs satisfying

$$\delta\phi(i,j) \geq 165^\circ, \tag{5.18}$$

measure

$$|t_i - t_j| \geq 10\,\text{ns}, \tag{5.19}$$

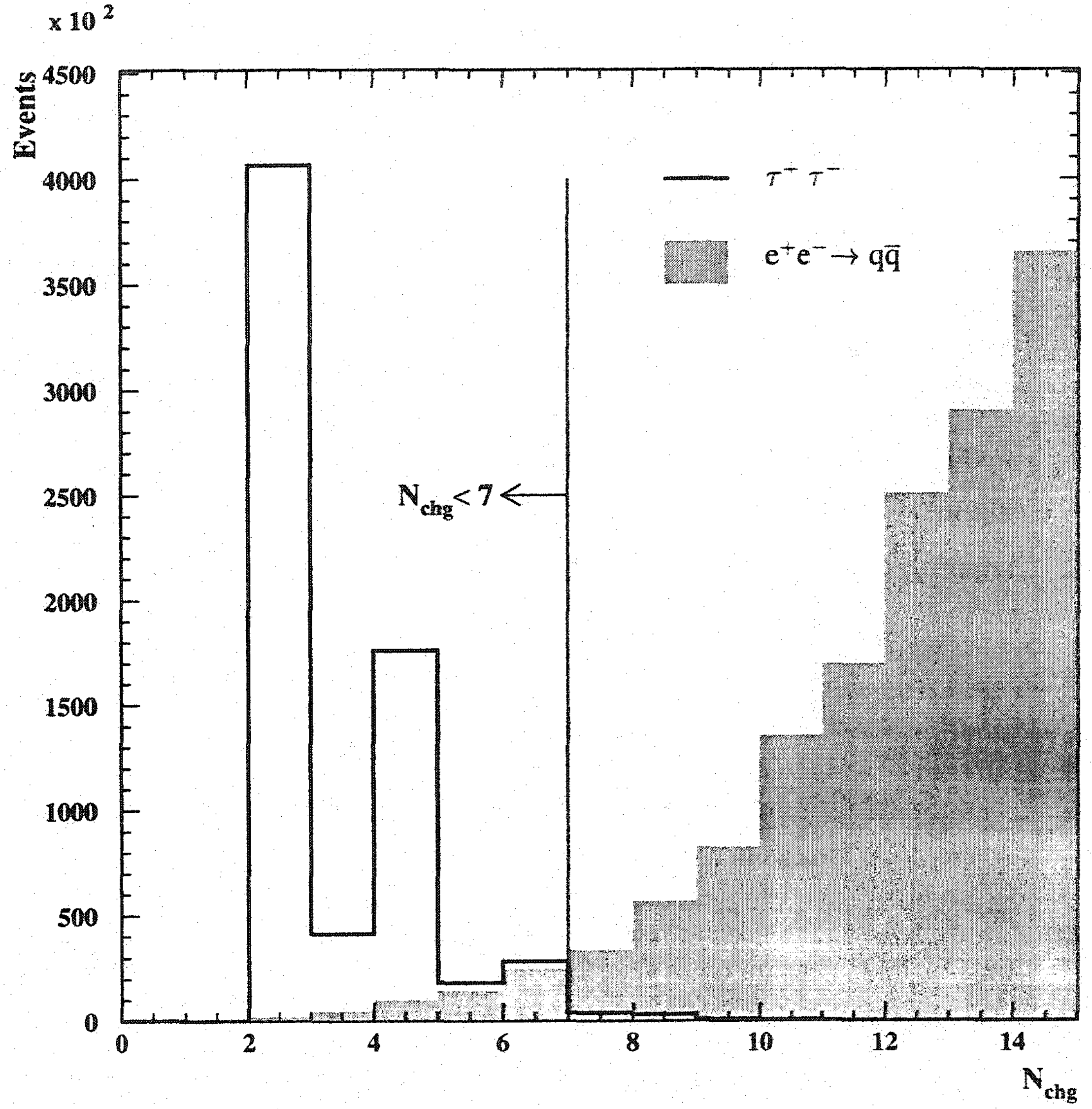

Figure 5.1: The distributions of the total number of charged tracks is shown for tau pairs (open) and $e^+e^- \to q\bar{q}$ events (solid) from Monte Carlo simulation. The vertical line on the upper figure indicates the track multiplicity cut applied to remove $e^+e^- \to q\bar{q}$ background.

where $\delta\phi(\mathrm{i,j})$ is the angular separation between counters i and j and $|t_i - t_j|$ is the measured time-of-flight difference. These requirements effectively remove all cosmic ray events from the sample [49].

5.2.5 Two-photon Event Rejection

A potentially significant background arises from two-photon events; particularly those events in which a muon pair or an electron-positron occur in the final state. Such events will primarily contaminate the selected tau pair sample in which both taus are subsequently classified as decaying through the muon channel, both taus are classified as decaying through the electron channel, or those events in which the decay of one tau is not classified and the other is classified as decaying through the muon or electron channel.

Two-photon events typically exhibit low total energy measured in the detector, balanced total transverse momentum, and imbalanced longitudinal momentum. Hence, the two-photon background is greatly reduced by only accepting events with

$$\theta_{\mathrm{acol}} \leq 15°\text{, and} \tag{5.20}$$

$$\mathrm{E_{vis}} = \sum_{\mathrm{cone}} \mathrm{Max}(\mathrm{E_{cls}}, \mathrm{E_{trk}}) \geq 0.03\mathrm{E_{cm}}, \tag{5.21}$$

where $\mathrm{E_{cm}}$ is the total centre-of-mass energy, $\mathrm{E_{vis}}$ is the total measured, or 'visible', event energy and θ_{acol}, the acolinearity, is the angle between the direction of the highest energy charged cone and the negative direction of the second highest energy charged cone. Figure 5.2 shows distributions of θ_{acol} vs $\mathrm{E_{vis}/E_{cm}}$ for simulated tau pairs and the two-photon backgrounds. It is clear that the two-photon events are largely eliminated by these cuts.

For $\mathrm{E_t(cls)}$ and $\mathrm{P_t(trk)}$ denoting the vector sums of the transverse cluster energy and track momentum respectively, events with $\mathrm{E_{vis}} \leq 0.2\mathrm{E_{beam}}$ are removed if

$$\mathrm{E_t(cls)} \leq 2\,\mathrm{GeV}\text{, and} \tag{5.22}$$

$$\mathrm{P_t(trk)} \leq 2\,\mathrm{GeV}. \tag{5.23}$$

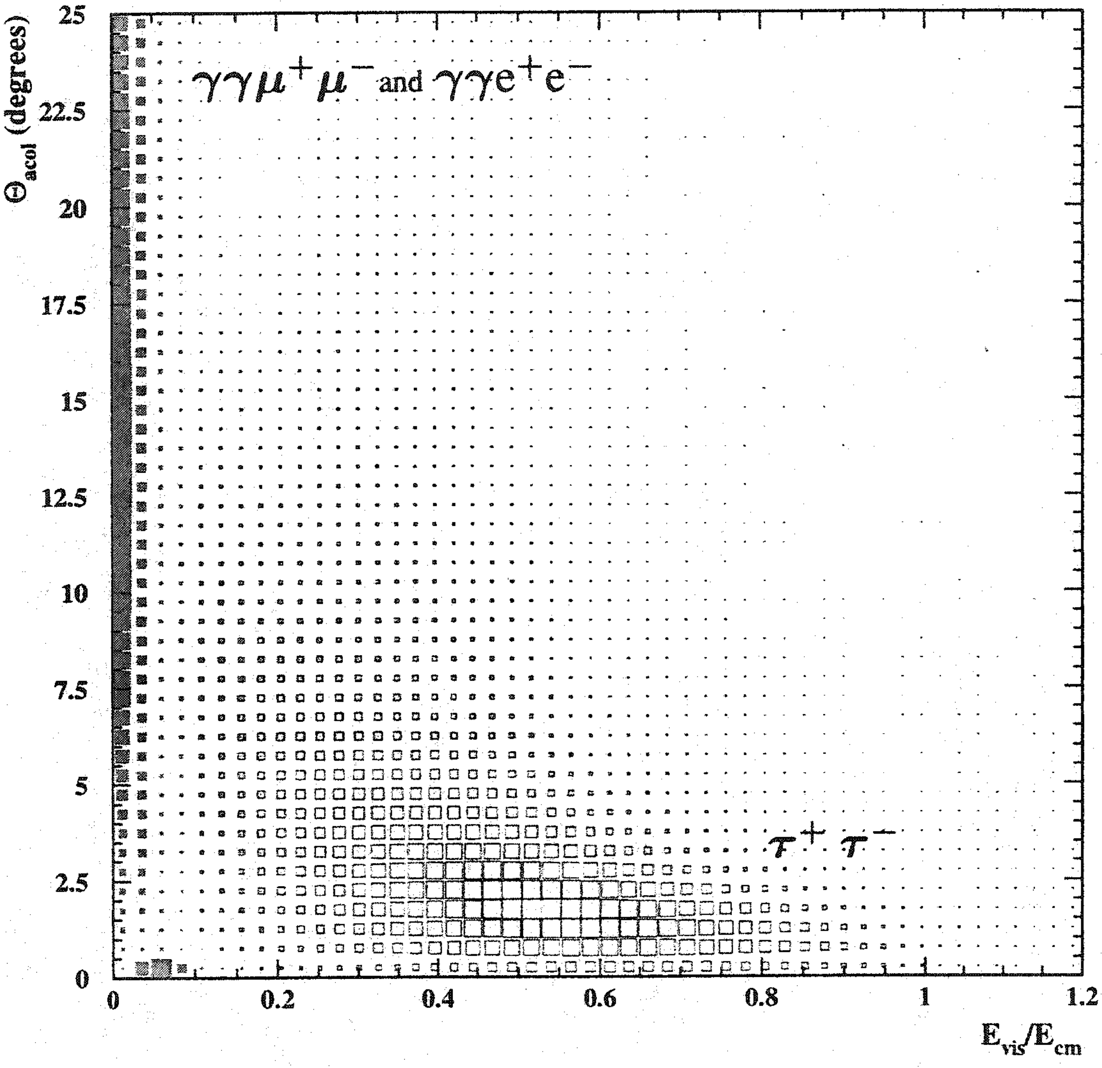

Figure 5.2: Monte Carlo distributions of event acolinearity vs. total visible energy divided by centre-of-mass energy for signal (open) and two-photon background (shaded) are shown.

5.2.6 $e^+e^- \to e^+e^-$ and $e^+e^- \to \mu^+\mu^-$ Event Pair Rejection

The majority of events passing the preceding cuts are lepton pair events (i.e. $e^+e^- \to e^+e^-$, $e^+e^- \to \mu^+\mu^-$, or $e^+e^- \to \tau^+\tau^-$). The $e^+e^- \to e^+e^-$ events in this sample are typically characterized by a pair of back-to-back tracks with a total ECAL energy deposit near the centre-of-mass energy. Thus, these events may be largely removed by requiring

$$\sum_i E_i(\mathrm{cls}) \leq 0.8 E_{CM}, \tag{5.24}$$

or

$$\sum_i E_i(\mathrm{cls}) + 0.3 \sum_j E_j(\mathrm{trk}) \leq E_{CM}, \tag{5.25}$$

where the sum is over all cluster energies $E_i(\mathrm{cls})$ and all track energies $E_j(\mathrm{trk})$ (assuming a pion mass for each track) in the event. As an illustration of the discrimination power of the event total cluster energy and total momentum (scalar sum) variables, the separation between tau pairs and $e^+e^- \to e^+e^-$ events may be clearly seen in Figure 5.3 which shows the distributions of $\sum_j P_j(\mathrm{trk})/E$ vs $\sum_i E_i(\mathrm{cls})/E$ for Monte Carlo tau pairs and $e^+e^- \to e^+e^-$ pairs before selection.

Finally, muon pair events must be removed from the remaining sample. To proceed, events must first be recognized as containing two muons. A particle is loosely identified as a muon if it passes one of the following criteria:

$$N^{MU}_{\mathrm{layers}} \geq 2, \tag{5.26}$$

or

$$N^{HC}_{\mathrm{layers}} \geq 4, \quad N^{HC}_{\mathrm{last3}} \geq 1 \quad \text{and} \quad N^{HC}_{\mathrm{hits/layer}} > 2, \tag{5.27}$$

or

$$E_{\mathrm{cls}} < 2\,\mathrm{GeV}. \tag{5.28}$$

Here, N^{MU}_{layers} is the number of layers registering a signal in the muon chambers, N^{HC}_{layers} is the number of HCAL layers associated with a track and registering a signal, N^{HC}_{last3} is the number of HCAL layers with hits in the last three HCAL layers, $N^{HC}_{\mathrm{hits/layer}}$ is the total number of HCAL hits divided by the total HCAL layers registering signal for the cone

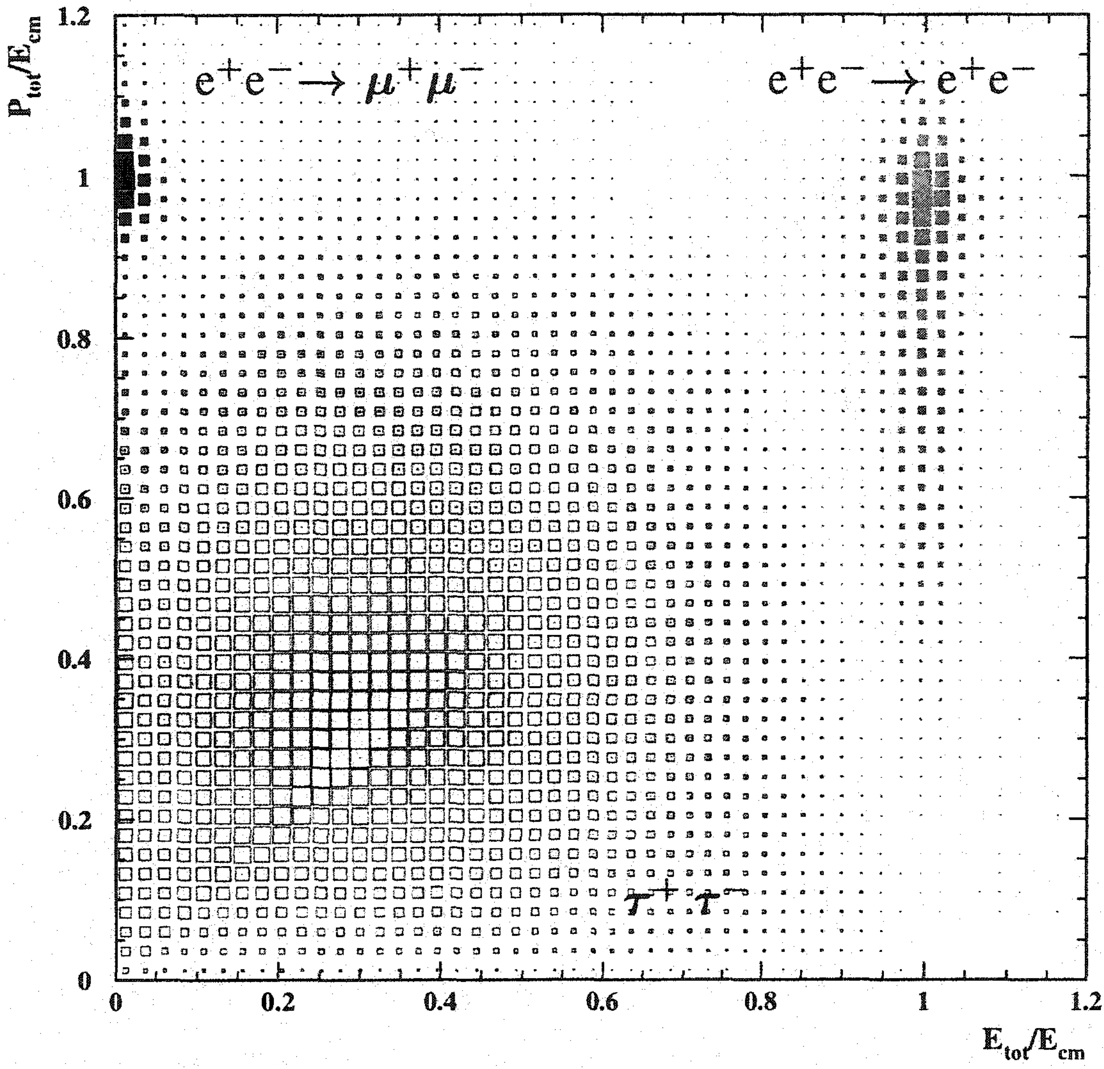

Figure 5.3: Depicted are Monte Carlo simulated distributions of total track momentum divided by centre-of-mass energy vs total event ECAL energy divided by centre-of-mass energy for tau pair signal (open), electron pair background (light shaded), and muon pair background (dark shaded).

containing the track, and E_{cls} is the raw cluster energy of the most energetic ECAL cluster in the cone. The first and second criteria reflect the fact that muons are expected to pass completely out of the detector, while the third criterion reflects the minimum ionizing property of muons as they pass through the ECAL.

Once events have been tagged as containing two muons, the muon pair events, which are characterized by a pair of back-to-back charged tracks identified as muons with total momentum near the collision energy, are removed by requiring

$$\sum_{\mathrm{cone}=1}^{2} [E^{\mathrm{clust}}_{\mathrm{cone}} + E^{\mathrm{track}}_{\mathrm{cone}}] \leq 0.6E_{\mathrm{CM}}, \tag{5.29}$$

where $E^{\mathrm{clust}}_{\mathrm{cone}}$ is the total cluster energy in each charged cone and $E^{\mathrm{track}}_{\mathrm{cone}}$ is the scalar sum of track energies, assuming pion masses, for tracks associated to the cone. Figure 5.3 illustrates the separation power between tau pairs and muon pairs when examining these types of variables.

5.2.7 Tau pair Selection Summary

The events remaining in the sample after these cuts have been made are largely tau pair events. Table 5.1 indicates the selection efficiency and estimated non-tau background in each of the three detector regions. As may be seen, the non-tau background is less than 2% after selection while an efficiency of nearly 89% within the fiducial acceptance is maintained.

Region	$\cos\theta$	Efficiency	Purity
Barrel	$\cos\theta < 0.72$	93 %	98 %
Overlap	$0.72 < \cos\theta < 0.81$	75 %	98 %
Endcap	$0.81 < \cos\theta < 0.90$	79 %	97 %

Table 5.1: Tau pair selection efficiencies and purities for the different fiducial regions of the detector.

5.3 Tau Decay Selection

5.3.1 Introduction

Each tau in an event which passes the tau-pair selection is processed through the tau decay selection and uniquely classified as $\tau \rightarrow e\bar{\nu}_e\nu_\tau$, $\tau \rightarrow \mu\bar{\nu}_\mu\nu_\tau$, $\tau \rightarrow \pi\ \nu_\tau$, $\tau \rightarrow \rho\nu_\tau$, $\tau \rightarrow \mathrm{a}_1\ \nu_\tau$, or not-identified (nid). Figure 5.4 indicates the decay configurations for each of these channels and the general strategy for identifying the relevant particle types. Note that in the $\tau \rightarrow \rho\nu_\tau$ case it is the decay products of the ρ, a $\pi^-$and π^0, that are identified [1], and for the $\tau \rightarrow \mathrm{a}_1\ \nu_\tau$ case it is the three charged pion decay products of the a_1.

Separate selections are generated for each of the five decay channels and consist of an initial set of loose, mode-dependent cuts, followed by a likelihood selection.

The procedure for creating the likelihood selections utilized the software package described in [50]. The likelihood selections are generated separately for each of the three detector regions (barrel, overlap, and endcap) and, except for the $\tau \rightarrow \mathrm{a}_1\ \nu_\tau$ channel, are further divided into cases based on various measured quantities as described below. This last division provides an improvement in discrimination by allowing the likelihood cuts to be optimized based on the predominant background in the sample.

The likelihood variables used for each channel are chosen to maximize the selection discrimination while, as discussed in Chapter 7, minimizing sensitivity to polarization bias and modelling uncertainty. Monte Carlo simulated events are used to generate the likelihood distributions and the likelihood cuts are optimized to maximize the product of the efficiency and purity for each channel. If a given tau passes more than one decay selection, it is uniquely identified as decaying through the channel having the largest relative likelihood.

Since the $\tau \rightarrow \pi\ \nu_\tau$ and $\tau \rightarrow \rho\nu_\tau$ channels contribute approximately 80 % of the sensitivity, the success of this analysis particularly relies on the efficient selection of pure samples of these events. As noted above, the large boost of the tau jets at LEP causes the tau decay products to emerge in a highly collimated cone. While this effect assists

---

[1] The π^0 immediately decays to two photons ($\pi^0 \rightarrow \gamma\gamma$)and it is the photons that are actually measured by OPAL.

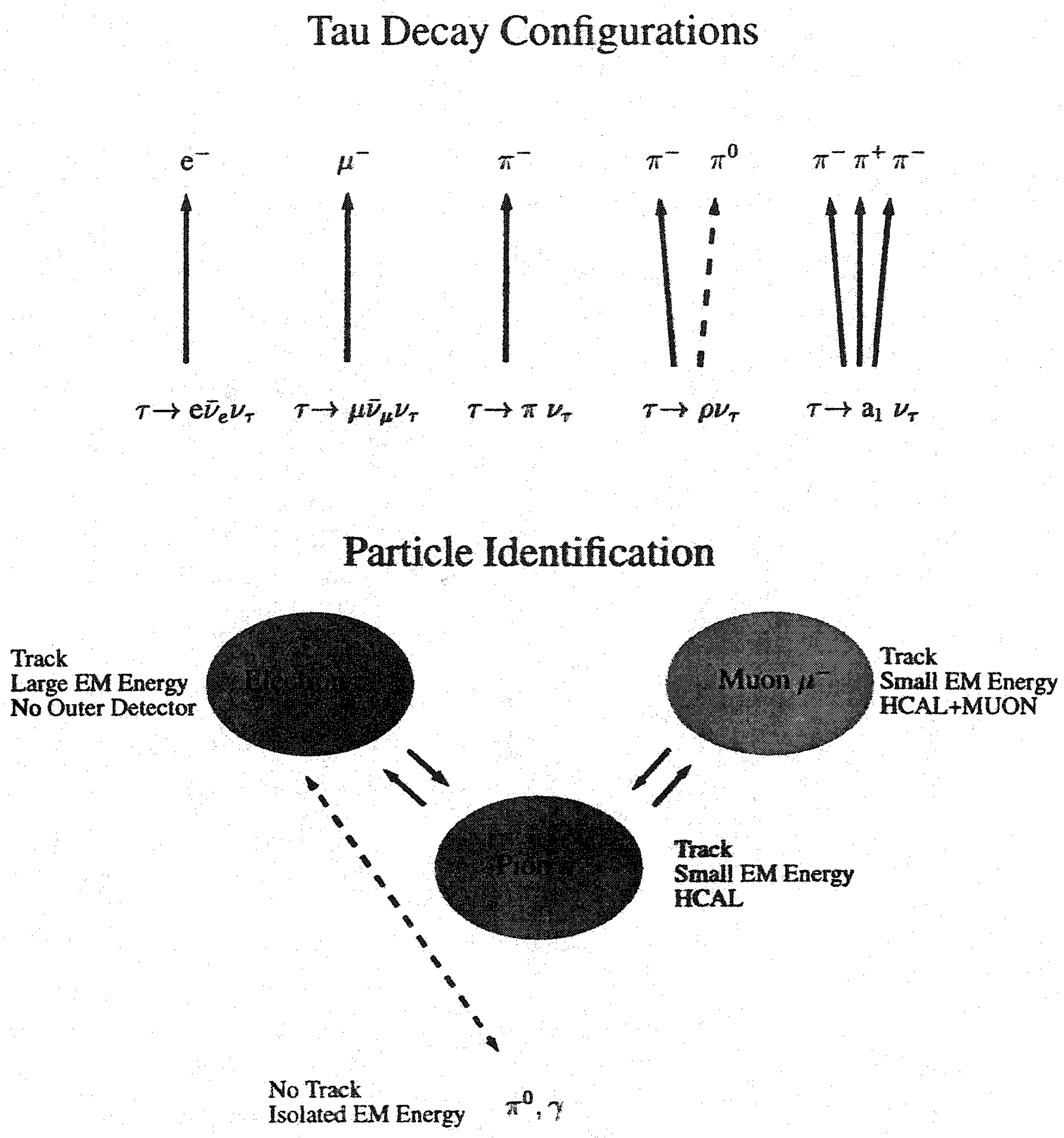

Figure 5.4: Depicted at the top are the decay configurations for the particles measured in the OPAL detector for each of the five selected tau decay channels. As can be seen, four types of particles must be identified: electrons; muons; charged pions; and neutral pions. A simple representation of the particle identification criteria is given at the bottom. The dual arrows connecting particle types indicate that the signatures for such particles in OPAL can be similar and lead to mis-identification. The dashed line connecting electrons and neutral pions indicates that the neutral pion signature is similar to the electron, but with no associated track.

in the selection of tau pairs, it increases the difficulty of separating jets which contain either no π^0's, exactly one π^0, or more than one π^0, and hence in distinguishing among $\tau \rightarrow \pi\ \nu_\tau$ decays, $\tau \rightarrow \rho\nu_\tau$ decays, and tau decays containing more than one π^0. Many of the variables described in the next section have been specifically chosen in order to maximize the efficient separation of these events in the OPAL data.

5.3.2 The Likelihood Selection Method

The Monte Carlo simulation provides normalized distributions for a set of observables, O_i, for each of the decay modes. These are subsequently used to calculate for each decay channel j, the likelihood, $\ell_i^j(O_i)$, that the measured O_i would be observed [50]. The likelihood that decay mode j produces the measured observables in a given tau jet is obtained from the product of the likelihoods: $\mathcal{L}(j) = \prod_i \ell_i^j(O_i)$. In order to select decays from mode k, a cut is applied to its relative likelihood, $L(k) = \mathcal{L}(k)/\sum_j \mathcal{L}(j)$; events with a likelihood value higher than the cut are selected and those with a value below the cut are rejected. From this definition, $L(k)$ lies between 0 and 1 and the value of the cut is chosen to maximize the product of purity and efficiency. The requirement that decays have large values of $L(k)$ produces a sample with low background normally at the cost of some efficiency for selecting mode k decays. In this work, each of the five decay mode selections employ different observables and therefore exploit a different set of likelihoods, $\mathcal{L}(j)$. If a tau jet is classified in more than one channel after applying the likelihood cut, then it is reclassified into the channel having the largest relative likelihood. In this case, the likelihood $L(k) = w_k\mathcal{L}(k)/\sum_j w_j\mathcal{L}(j)$ is used where w_j are weighting factors representing the relative tau decay branching ratios.

The likelihood variables used to discriminate between each of the selected tau decay channels and the backgrounds are constructed from information measured in the central tracking chamber, the ECAL, and the outer detectors. While the definition of a track is given above, the ECAL clusters used for the decay selections are constructed using a maximum entropy (ME) clustering algorithm as described in [51]. In particular, this algorithm attempts to utilize the available ECAL information in order to enable the selections to distinguish events with no π^0's, exactly one π^0, and two or more π^0's. The existence of 'neutral clusters' in a tau jet, as defined below, usually indicates the presence of one or more π^0's.

Each track in a tau jet is processed through a track-ECAL cluster matching algorithm. A χ^2 value is calculated by taking the difference between the measured track and cluster positions using the position of the track when it exited the central tracking system. A track is associated to the ECAL cluster for which the χ^2 probability is greatest and when the probability is greater than 2 %. ECAL clusters not associated to tracks are designated 'neutral clusters' if they pass the energy threshold cuts described below.

Including variables from all of the five decay channels selected, the twenty likelihood variables calculated for each tau jet are:

- N^{cls}_{neut} - number of neutral maximum entropy (ME) clusters associated to the tau jet; clusters are designated as neutral if they are not associated to a track and if they pass a region-dependent energy cut; the energy cut is 0.650 GeV in the barrel, 1.25 GeV in the overlap and 1 GeV in the endcap,

- E_{ass} - energy of the ME cluster associated to the most energetic track,

- E_{resid} - sum of the residual energy from ME clusters for clusters not associated to tracks and not passing the neutral cluster cutoff,

- E_{ass}/p - energy of the ME cluster associated to the most energetic track divided by that track's momentum,

- E_{tot}/p - total ME cluster energy divided by the momentum of the most energetic track,

- E_{max}/p - energy of the ME cluster with maximum energy divide by the momentum of the most energetic track,

- E_{neut}/p - sum of the energy from ME clusters not associated to tracks and passing the neutral cluster cutoff divided by the momentum of the most energetic track,

- dE/dx(e) - pull of the specific energy loss measured in the CJ, $[(\mathrm{dE/dx})_{\mathrm{meas}} - (\mathrm{dE/dx})_{\text{e-hypothesis}}]/\sigma_{\text{e-hypothesis}}$ (where $(\mathrm{dE/dx})_{\text{e-hypothesis}}$ is the expected dE/dx assuming the particle is an electron with resolution $\sigma_{\text{e-hypothesis}}$), of the most energetic track under electron hypothesis,

- dE/dx(π) -pull of the specific energy loss measured in the CJ, $[(\mathrm{dE/dx})_{\mathrm{meas}} - (\mathrm{dE/dx})_{\pi\text{-hypothesis}}]/\sigma_{\pi\text{-hypothesis}}$ (where $(\mathrm{dE/dx})_{\pi\text{-hypothesis}}$ is the expected dE/dx assuming the particle is a pion with resolution $\sigma_{\pi\text{-hypothesis}}$), of the most energetic track under pion hypothesis,

- E_{π^0} - energy of the two most energetic neutral clusters added in quadrature with the π^0 mass; if only one neutral cluster exists it is the energy of this cluster and a π^0 mass; if no neutral clusters exist then the cluster associated to the most energetic track is used,

- ϕ_{pres}- maximum angle in ϕ between the most energetic track and presampler clusters assigned to the tau jet,

- m_{π^0} - invariant mass of the two highest energy neutral ME clusters,

- m_ρ - invariant mass of the two highest energy neutral ME clusters and the most energetic track assuming the ME clusters arise from a π^0 decay and the track to be a charged pion; if only one neutral cluster exists, then it is assumed to be the π^0; if no neutral clusters exist then the associated cluster is used,

- m_{jet} - invariant mass constructed from the most energetic track and all neutral clusters associated to the tau jet,

- $m_{\text{1-prong}}$- invariant mass calculated from the most energetic track and the most energetic neutral clusters, to a maximum of four clusters, when at least two neutral clusters exist (and is set to 0 when less than two exist),

- m_{a_1} - invariant mass constructed from charged tracks assuming the tracks to be charged pions when at least three tracks are associated to the tau jet,

- $\mathrm{HCAL_{tot}}$ - total number of HCAL layers with hits associated to most energetic track,
- $\mathrm{MUON_{tot}}$ - total number of MUON layers with hits associated to most energetic track,
- $\mathrm{HM_{last7}}$ - sum of $\mathrm{MUON_{tot}}$ and the number of HCAL layers registering hits in the last three HCAL layers,
- $\mathrm{MU\text{-}CT_{wght}}$ - weight for matching most energetic track to hits in the muon chambers,

Table 5.2 indicates which variables are used in the construction of the likelihood for each of the five channels.

Variable	$\tau \rightarrow e\bar{\nu}_e\nu_\tau$	$\tau \rightarrow \mu\bar{\nu}_\mu\nu_\tau$	$\tau \rightarrow \pi\ \nu_\tau$	$\tau \rightarrow \rho\nu_\tau$	$\tau \rightarrow \mathrm{a}_1\ \nu_\tau$
$\mathrm{N_{neut}^{cls}}$			X	X	
$\mathrm{E_{ass}}$		X			
$\mathrm{E_{resid}}$				X	
$\mathrm{E_{ass}/p}$	X	X	X		X
$\mathrm{E_{tot}/p}$	X		X	X	X
$\mathrm{E_{max}/p}$					X
$\mathrm{E_{neut}/p}$			X		
dE/dx(e)	X	X	X	X	X
dE/dx(π)	X	X	X	X	X
$\mathrm{E_{\pi^0}}$				X	X
ϕ_{pres}		X	X		
$\mathrm{m_{\pi^0}}$			X	X	
$\mathrm{m_\rho}$	X	X	X	X	
$\mathrm{m_{jet}}$			X	X	
$\mathrm{m_{1\text{-}prong}}$				X	X
$\mathrm{m_{a_1}}$					X
$\mathrm{HCAL_{tot}}$		X	X		
$\mathrm{MUON_{tot}}$		X	X	X	X
$\mathrm{HM_{last7}}$		X		X	X
$\mathrm{MU\text{-}CT_{wght}}$	X	X	X	X	X

Table 5.2: Likelihood selection variables used for each τ-decay selection channel.

In the following sections, the specific details and results of each selection will be provided.

5.3.3 $\tau \rightarrow e\bar{\nu}_e\nu_\tau$ Decays

As noted in Chapter 3, OPAL has been constructed such that electromagnetic showers arising from electrons entering the ECAL will be completely contained to a high degree of probability. In order to select $\tau \rightarrow e\bar{\nu}_e\nu_\tau$ events then, the basic criteria consists of identifying tau jets with a single charged track whose momentum is approximately equal to the associated ECAL cluster energy, with little neutral cluster energy, and with little or no activity in the outer detectors. In addition, the pull of the specific energy loss, dE/dx(e), can be used to distinguish between electrons and other charged particles; particularly in the momentum range between 0.3 and 20 GeV.

To improve the likelihood discrimination, the $\tau \rightarrow e\bar{\nu}_e\nu_\tau$ pre-selection cuts are designed to remove obvious background before the likelihood stage and include

$$\begin{aligned}
1 \leq \mathrm{N_{trk}} &\leq 2, \\
\mathrm{m}_{\pi^0} &\leq 0.4\mathrm{GeV}, \\
\mathrm{N^{cls}_{neut}} &\leq 3, \\
\mathrm{HCAL_{tot}} &\leq 3, \\
\mathrm{MUON_{tot}} &\leq 3, \\
\mathrm{HC_{last3}} &\leq 1, \text{and} \\
\mathrm{HM_{last7}} &\leq 4,
\end{aligned}$$

where $\mathrm{N_{trk}} = 2$, the number of charged particles associated to the jet, allows for the possibility of a second track arising from radiation and the second track is ignored, the $\mathrm{N^{cls}_{neut}}$ cut removes jets with neutral cluster components, and the final four cuts remove jets containing muons and some hadrons. The remaining events are passed through the likelihood selection which uses the variables specified in Table 5.2.

As well as dividing the likelihood selection into separate cases for each detector region, the $\tau \rightarrow e\bar{\nu}_e\nu_\tau$ selection is further divided into the case where no neutral clusters are identified in the jet and the case where one or more neutral clusters are identified. In the first case the tau background arises predominately from $\tau\rightarrow\ \pi\ \nu_\tau$ decays, while in the second case it is dominated by $\tau\rightarrow\ \rho\nu_\tau$ events.

To provide an indication of their discrimination power, Figure 5.5 shows four of the variables used in this selection. Note that in each case, the Monte Carlo distributions are normalized to the number of events in the data. The variables are plotted after tau pair selection but before the decay selection is applied so that an indication of the good agreement between the data and Monte Carlo may be noted.

Figures 5.6 and 5.7 show four plots of selection variables after the $\tau\rightarrow\ e\bar{\nu}_e\nu_\tau$ selection has been made. The plots are divided into the three detector regions and, as may be seen, the agreement between Monte Carlo and data is satisfactory in all cases. The apparent small differences between the Monte Carlo and data distributions, such as dE/dx(e) , are adequately accounted for by the systematic error analysis described in Chapter 7. Figure 5.8 provides plots of all variables used in this selection with the detector regions combined. The combined likelihood distribution is shown in Figure 5.9, where the good agreement between data and the Monte Carlo simulation is evident. Recall that no single cut is placed on this combined distribution; cuts are optimized separately for each detector region and each likelihood subset within each region. As described above, there are six separate likelihood distributions for this decay mode on which these cuts are made: two neutral cluster configurations for each of the three defined detector regions.

The final $\tau\rightarrow\ e\bar{\nu}_e\nu_\tau$ selection provides a sample of 44083 candidates with, as indicated in Table 5.3, an efficiency of 92%, where the efficiency is estimated after tau pair selection and with the fiducial acceptance of the analysis, and total background of 4.6%. Non-tau background comprises approximately one third of the total background and primarily arises from $\gamma\gamma e^+e^-$and $e^+e^-\rightarrow\ e^+e^-$ events.

5.3.4 $\tau\rightarrow\ \mu\bar{\nu}_\mu\nu_\tau$ Decays

As is well known, muons are highly penetrating leptons owing to their mass and relatively long lifetime. The selection of $\tau\rightarrow\ \mu\bar{\nu}_\mu\nu_\tau$ decays in OPAL exploits this property by identifying events with a single track in the CJ, a small energy deposit in the ECAL, and with

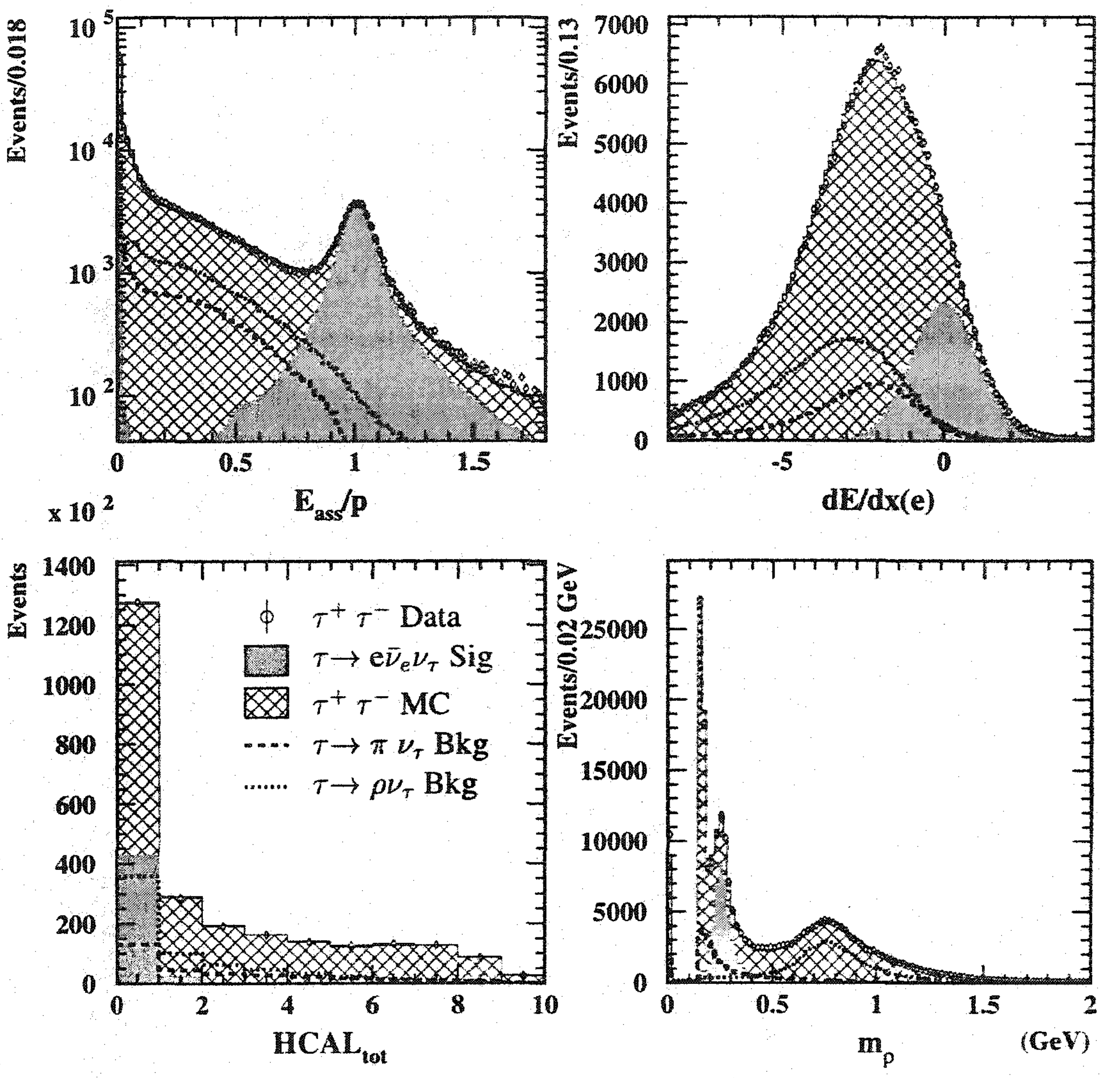

Figure 5.5: Distributions of E_{ass}/p , dE/dx(e) , $HCAL_{tot}$, and m_ρ are given for tau pair selected events over all detector regions. The circles with error bars represents the data, the hatched histogram the Monte Carlo for all tau decays, and the shaded area the Monte Carlo $\tau \rightarrow e\bar{\nu}_e\nu_\tau$ signal. To provide an indication of the separation between the signal and the predominant tau decay backgrounds, the distributions for the $\tau \rightarrow \pi\,\nu_\tau$ and $\tau \rightarrow \rho\nu_\tau$ channels are overlayed as dashed and dotted distributions respectively.

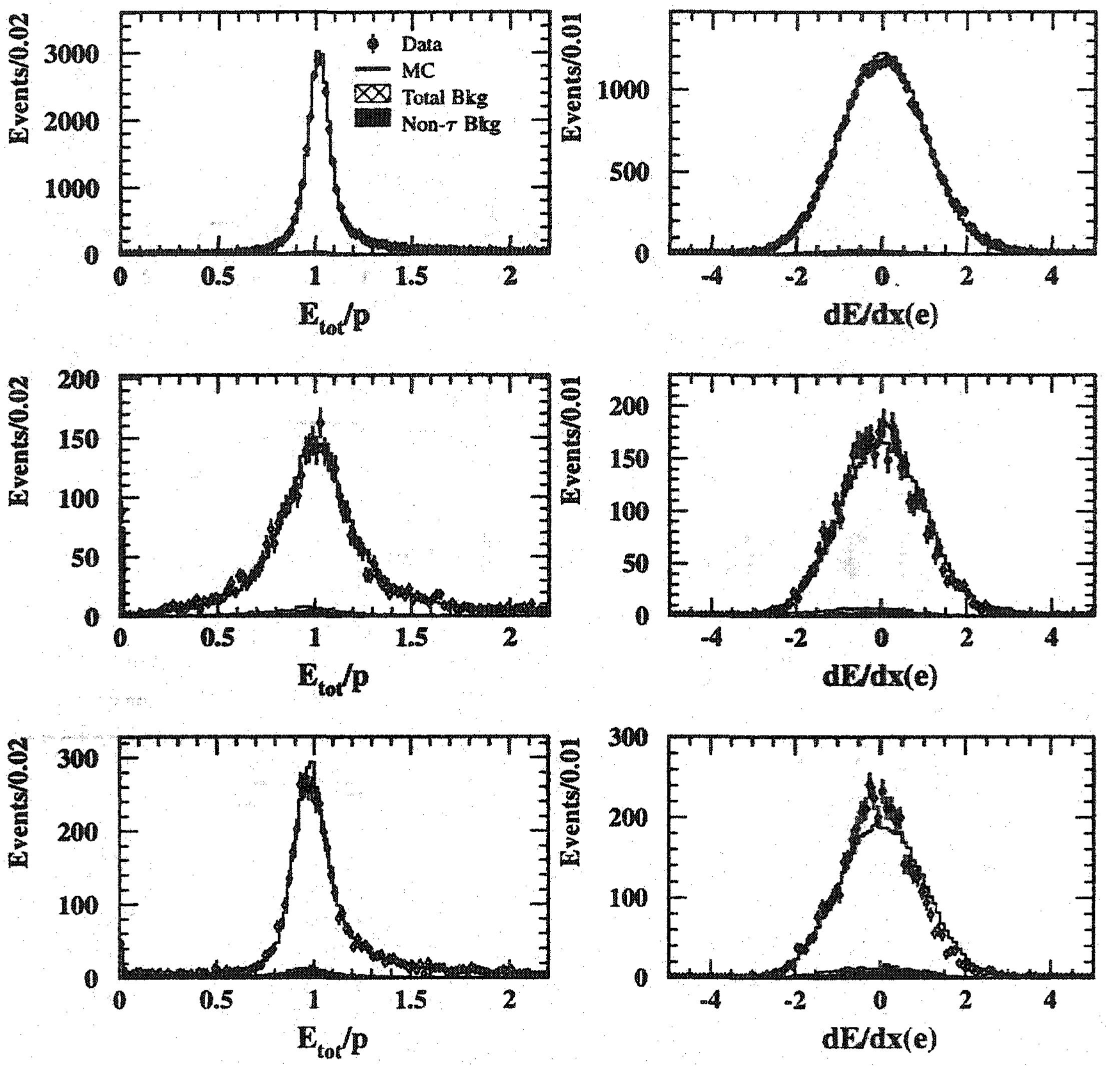

Figure 5.6: Depicted are distributions of E_{tot}/p (left) and dE/dx(e) (right), for $\tau \to e\bar{\nu}_e\nu_\tau$ selected events in the barrel (top), overlap (middle), and endcap (bottom) regions of the detector. The data are represented by the open circles with error bars, while the Monte Carlo signal is given by the open histogram, the tau background contributions shown hatched, and the non-tau contributions shaded.

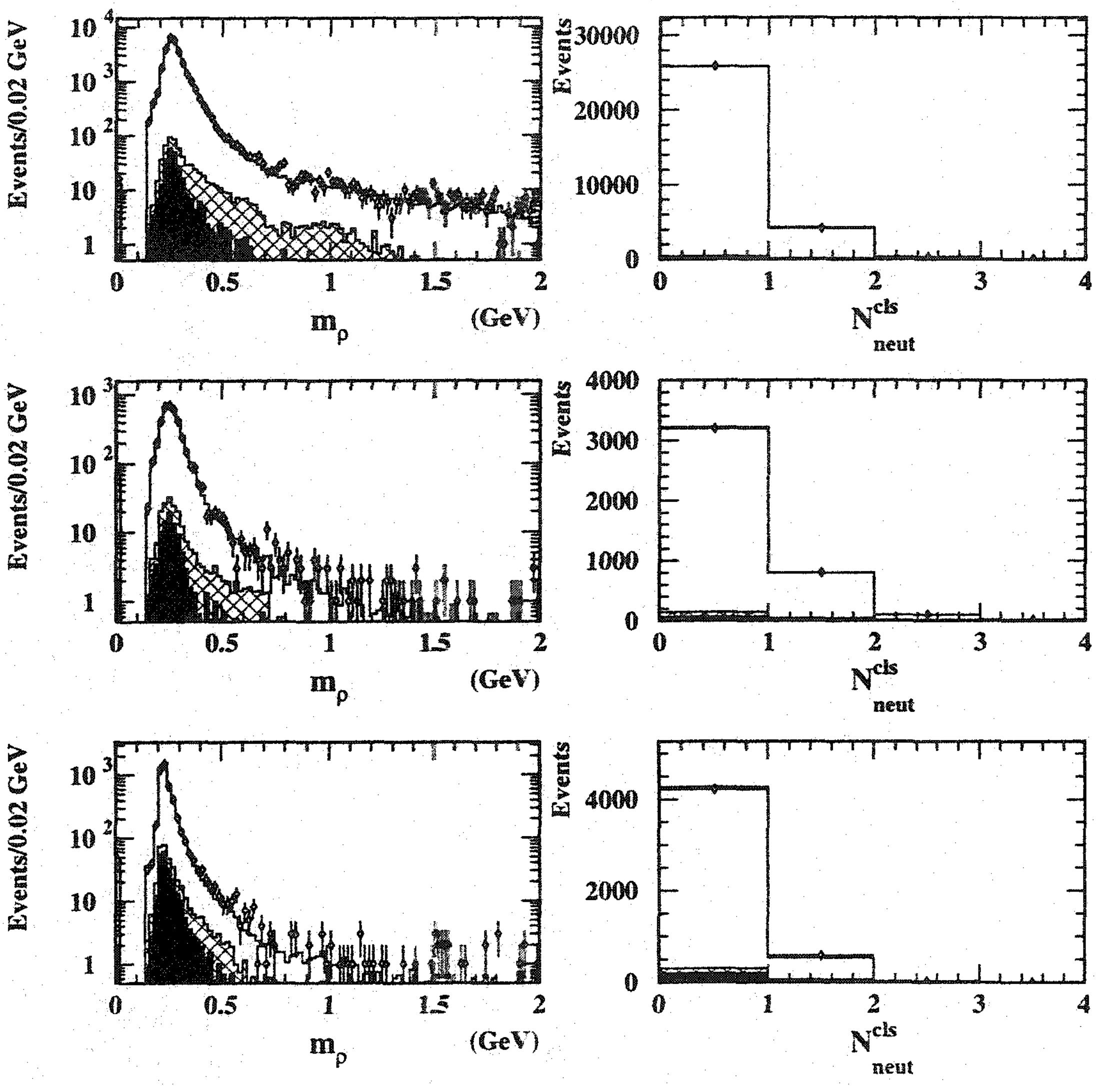

Figure 5.7: Depicted are distributions of m_ρ (left) and N^{cls}_{neut} (right), for $\tau \to e\bar{\nu}_e\nu_\tau$ selected events in the barrel (top), overlap (middle), and endcap (bottom) regions of the detector. The data are represented by the open circles with error bars, while the Monte Carlo signal is given by the open histogram, the tau background contributions shown hatched, and the non-tau contributions shaded.

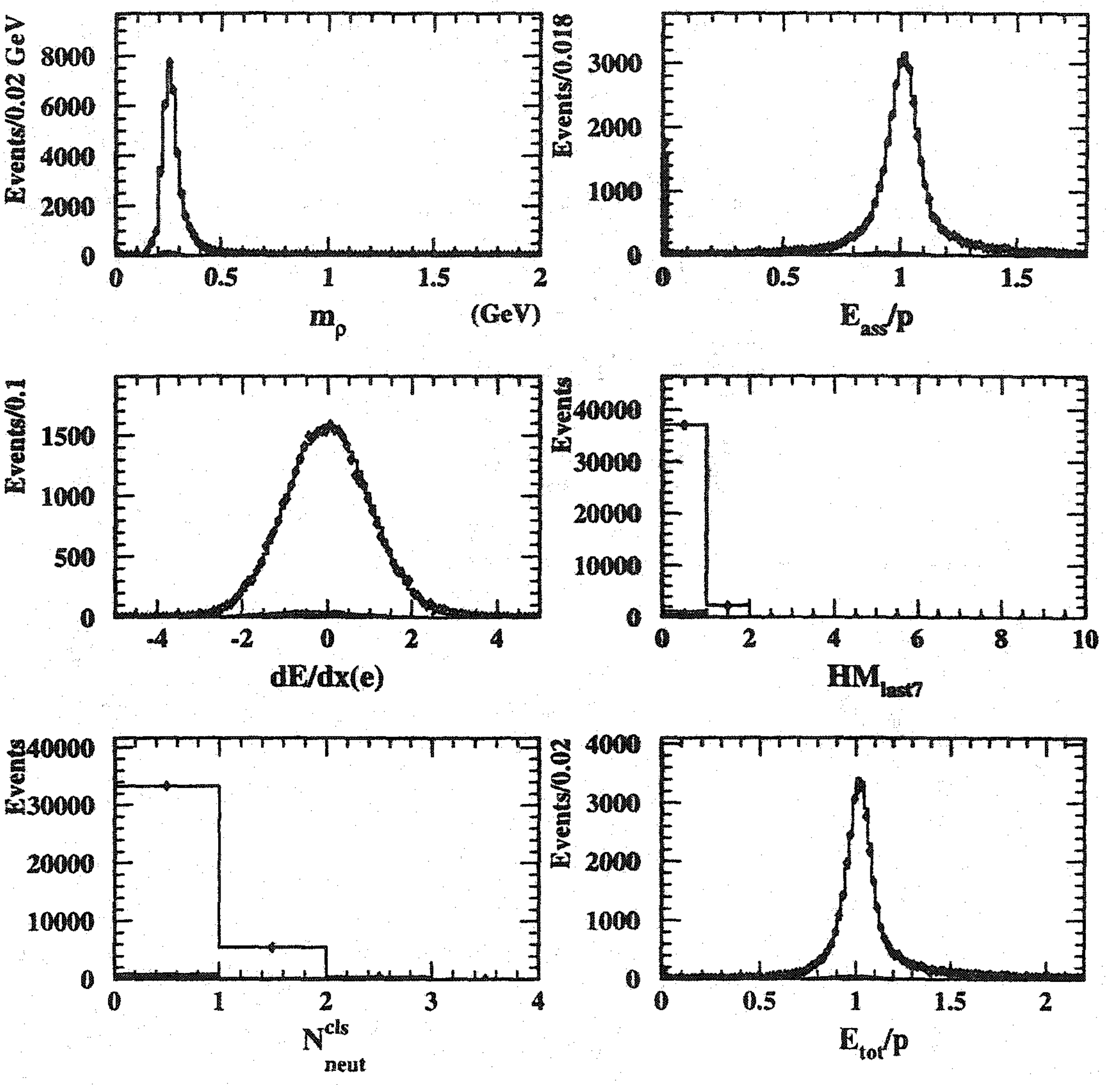

Figure 5.8: The distributions of all $\tau \rightarrow e\bar{\nu}_e\nu_\tau$ likelihood variables are given for selected $\tau \rightarrow e\bar{\nu}_e\nu_\tau$ events. The data are represented by the open circles with error bars, while the Monte Carlo signal is given by the open histogram, the tau background contributions shown hatched, and the non-tau contributions shaded.

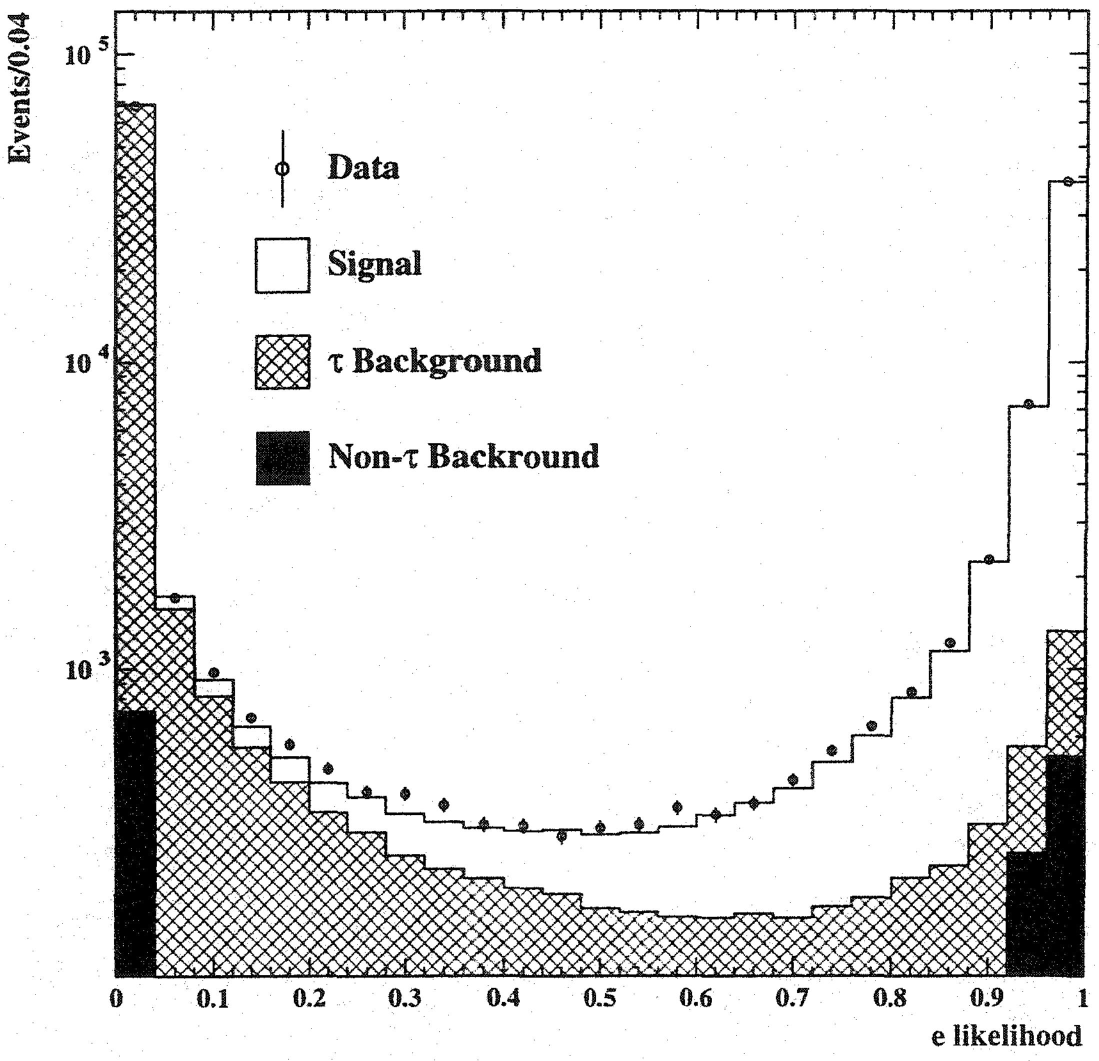

Figure 5.9: Presented is the combined likelihood distribution for the $\tau\rightarrow e\bar{\nu}_e\nu_\tau$ selection. The data are represented by the open circles with error bars, while the Monte Carlo signal is given by the open histogram, the tau background contributions shown hatched, and the non-tau contributions shaded.

	Barrel	Overlap	Endcap	All
Efficiency (%)	93.7	85.8	88.9	92.3
Composition (%)				
e^-	**96.5**	**93.4**	**90.7**	**95.4**
π^- (K^-)	0.7	1.6	1.2	0.9
$\pi^-\pi^0(\rho)$	1.1	1.7	1.9	1.3
$\pi^-\pi^+\pi^-(a1)$	0.2	0.2	0.2	0.2
$\pi^-\pi^0\pi^0(a1)$	0.3	0.5	0.7	0.4
$\pi^-\pi^+\pi^-\pi^0$	0.1	0.1	0.1	0.1
$\pi^-\pi^0\pi^0\pi^0$	0.1	0.1	0.1	0.1
$e^+e^-\rightarrow e^+e^-$	0.3	1.1	2.6	0.7
$\gamma\gamma ee$	0.5	1.2	2.2	0.8

Table 5.3: $\tau\rightarrow e\bar{\nu}_e\nu_\tau$ selection efficiencies and composition of selected events in each detector region and combined. Background channels contributing less than 0.1% are not listed.

hits registered in the outer detectors.

The $\tau\rightarrow \mu\bar{\nu}_\mu\nu_\tau$ pre-selection cuts consist of the requirements

$$\begin{aligned} N_{\mathrm{trk}} &= 1, \\ P_{\mathrm{trk}}/E_{\mathrm{beam}} &> 0.04, \\ N^{\mathrm{cls}}_{\mathrm{neut}} &\leq 2, \text{and} \\ m_{\pi^0} &\leq 0.2\mathrm{GeV}, \end{aligned}$$

where the ratio of track momentum to centre-of-mass energy cut, $P_{\mathrm{trk}}/E_{\mathrm{beam}}$, removes the low momentum region where it is difficult to distinguish between muons and pions, and the final two cuts remove events registering neutral cluster energy.

Events passing these cuts are subsequently processed by the likelihood selection using the variables denoted in Table 5.2. For this selection, the likelihoods are additionally separated into the cases where the muon weighting variable, $\mathrm{MU\text{-}CT}_{\mathrm{wght}}$, is zero and not zero. The first case includes the sample in which the background arises predominantly from $\tau\rightarrow \pi\ \nu_\tau$ decays, while the second case includes the majority of the non-tau background contributions arising from $\gamma\gamma\mu^+\mu^-$and $e^+e^-\rightarrow \mu^+\mu^-$ events.

Figure 5.10 provides distributions of four of the variables used for this selection after tau pair selection but prior to effecting the decay selections. As may be seen, the data agree well with the Monte Carlo and the discrimination power for selecting muons is evident.

Additional plots of muon channel selection variables are given in Figures 5.11 and 5.12 after the $\tau \rightarrow \mu\bar{\nu}_\mu\nu_\tau$ selection has been made. Good agreement between the data and Monte Carlo simulation in each of the three detector regions for the variables presented is apparent. The small disagreement between data and Monte Carlo simulation for the MU-CT$_{\mathrm{wght}}$ variable has negligible effect on the analysis and is discussed in Chapter 7. Figure 5.13 provides the distributions for all variables used in this selection with the three detector regions combined. The combined likelihood distribution, shown in Figure 5.14, characterizes the quality of agreement between data and Monte Carlo for this set of likelihood variables.

The $\tau \rightarrow \mu\bar{\nu}_\mu\nu_\tau$ selection provides 41291 candidates with an estimated efficiency of 87% and total background of 3.3%. Table 5.4 provides the detailed breakdown of efficiencies and backgrounds for this selection in each of the detector regions.

	Barrel	Overlap	Endcap	All
Efficiency (%)	86.7	86.3	85.9	86.5
Composition (%)				
e^-	0.0	0.2	0.1	0.0
μ^-	**97.6**	**92.9**	**94.9**	**96.7**
π^- (K^-)	1.4	5.3	2.2	2.0
$\pi^-\pi^0$ or $K^-(\rho)$	0.2	0.5	0.6	0.3
$e^+e^- \rightarrow \mu^+\mu^-$	0.4	0.4	0.4	0.4
$\gamma\gamma\mu\mu$	0.3	0.7	1.6	0.5

Table 5.4: $\tau \rightarrow \mu\bar{\nu}_\mu\nu_\tau$ selection efficiencies and composition of selected events in each detector region and combined.

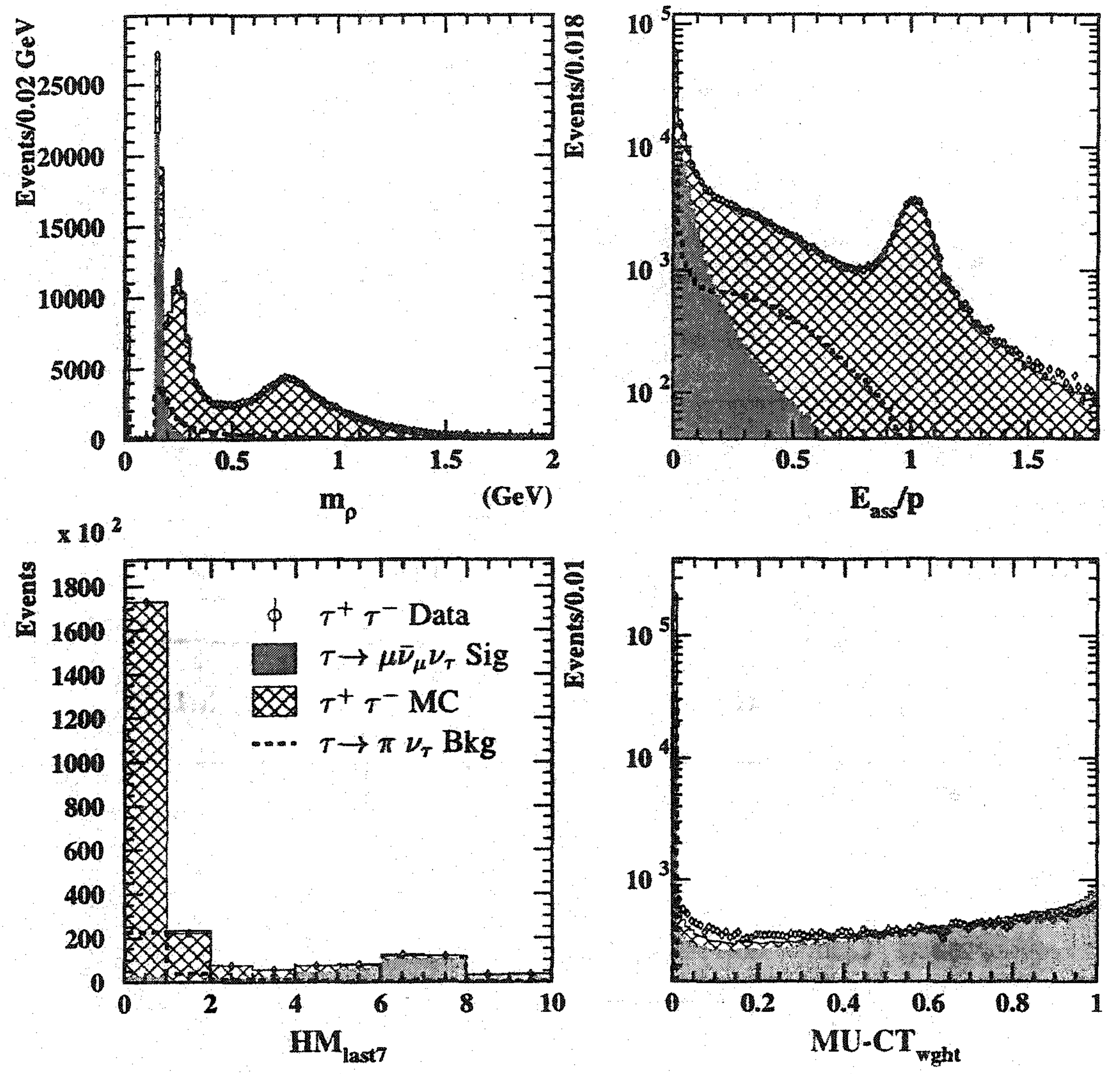

Figure 5.10: Distributions of m_ρ , E_{ass}/p , HM_{last7} , and $MU\text{-}CT_{wght}$ are given for tau pair selected events over all detector regions. The circles with error bars represents the data, the hatched histogram the Monte Carlo for all tau decays, and the shaded area the Monte Carlo $\tau \rightarrow \mu \bar{\nu}_\mu \nu_\tau$ signal. To provide an indication of the separation between the signal and the predominant tau decay background, the distributions for the $\tau \rightarrow \pi \, \nu_\tau$ channel are overlayed as dashed distributions.

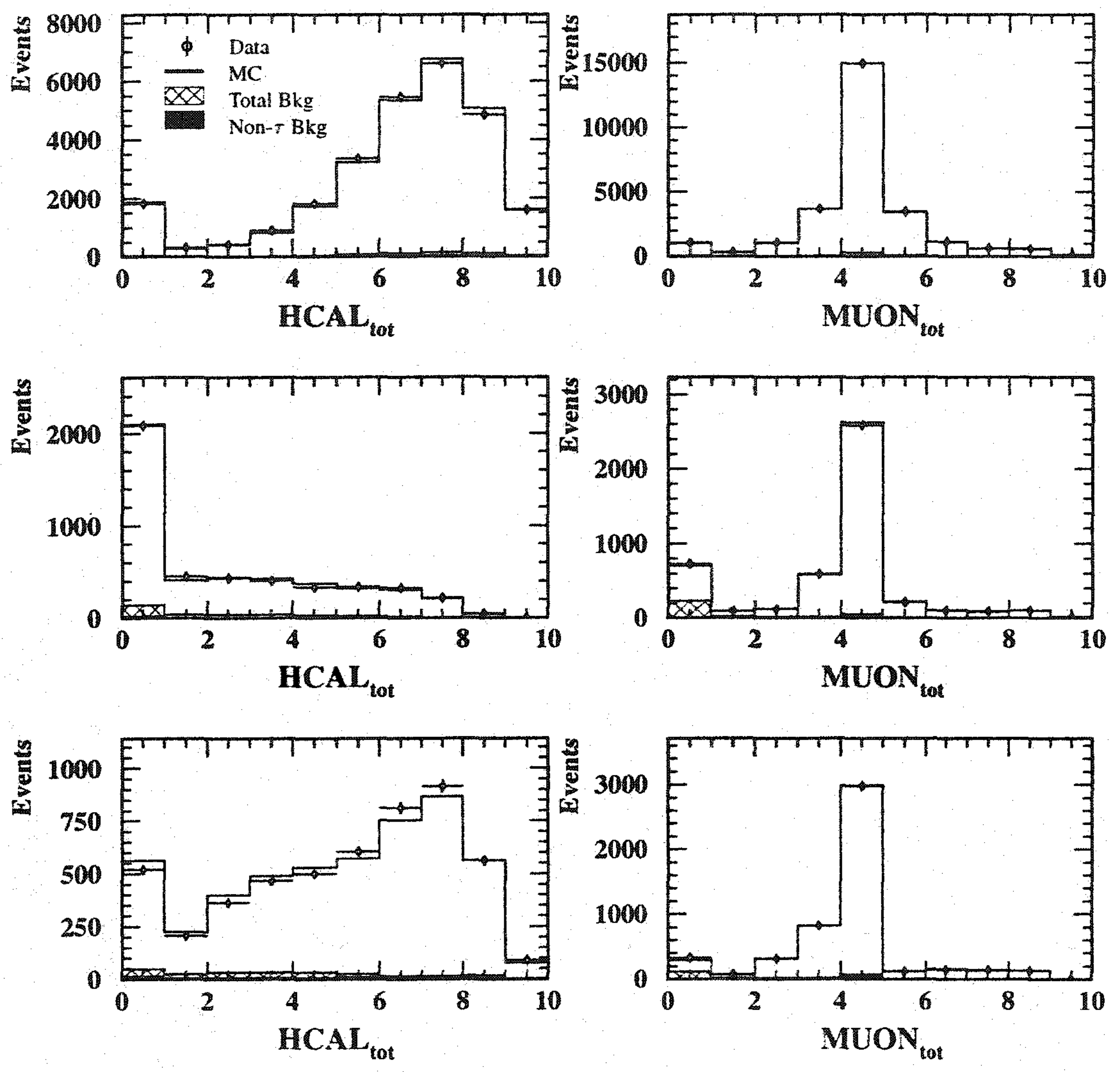

Figure 5.11: Depicted are distributions of HCAL$_{\text{tot}}$ (left) and MUON$_{\text{tot}}$ (right), for $\tau \to \mu\bar{\nu}_\mu\nu_\tau$ selected events in the barrel (top), overlap (middle), and endcap (bottom) regions of the detector. The data are represented by the open circles with error bars, while the Monte Carlo signal is given by the open histogram, the tau background contributions shown hatched, and the non-tau contributions shaded.

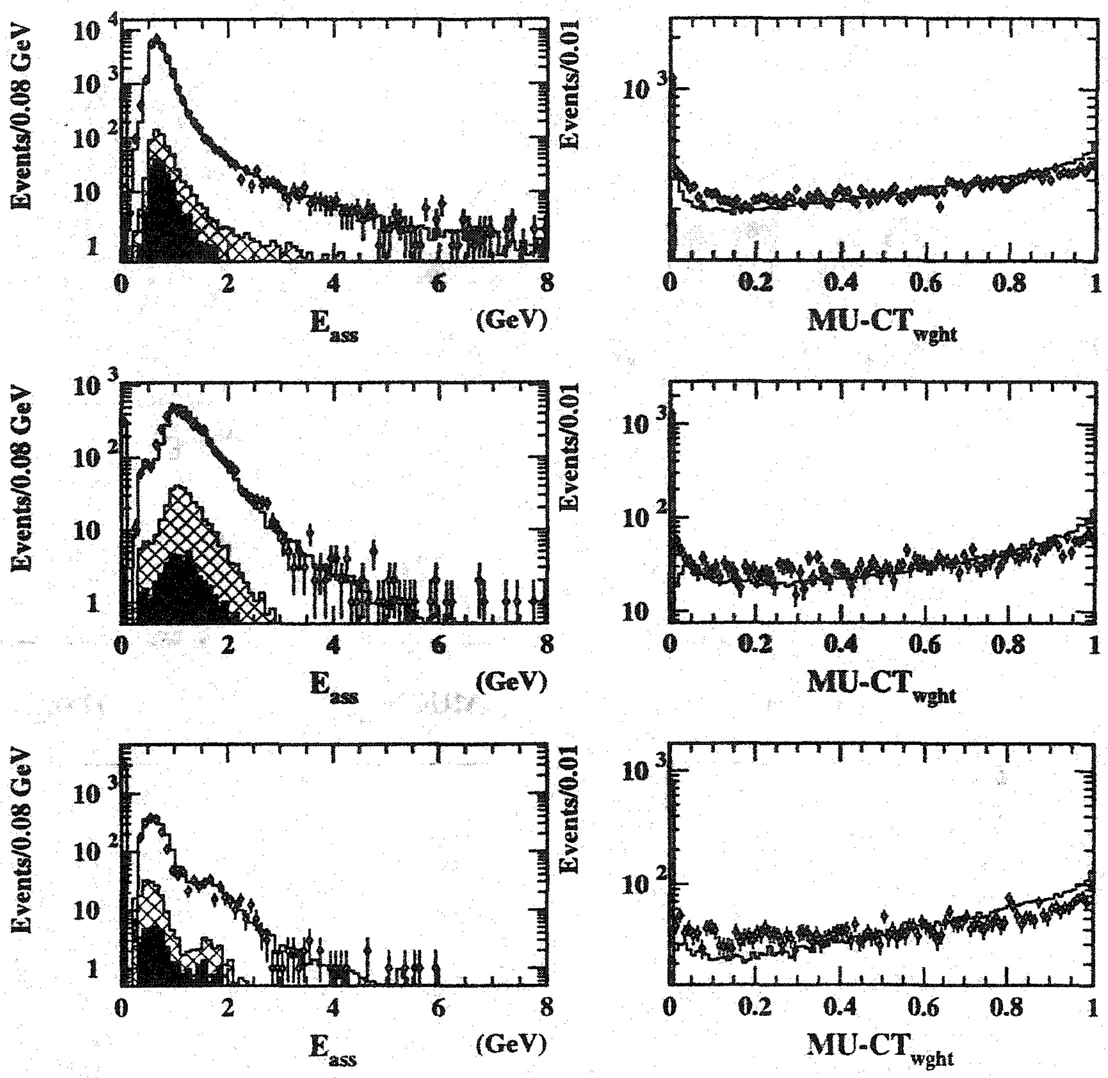

Figure 5.12: Depicted are distributions of E_{ass} (left) and MU-CT_{wght} (right), for $\tau \rightarrow \mu\bar{\nu}_\mu\nu_\tau$ selected events in the barrel (top), overlap (middle), and endcap (bottom) regions of the detector. The data are represented by the open circles with error bars, while the Monte Carlo signal is given by the open histogram, the tau background contributions shown hatched, and the non-tau contributions shaded.

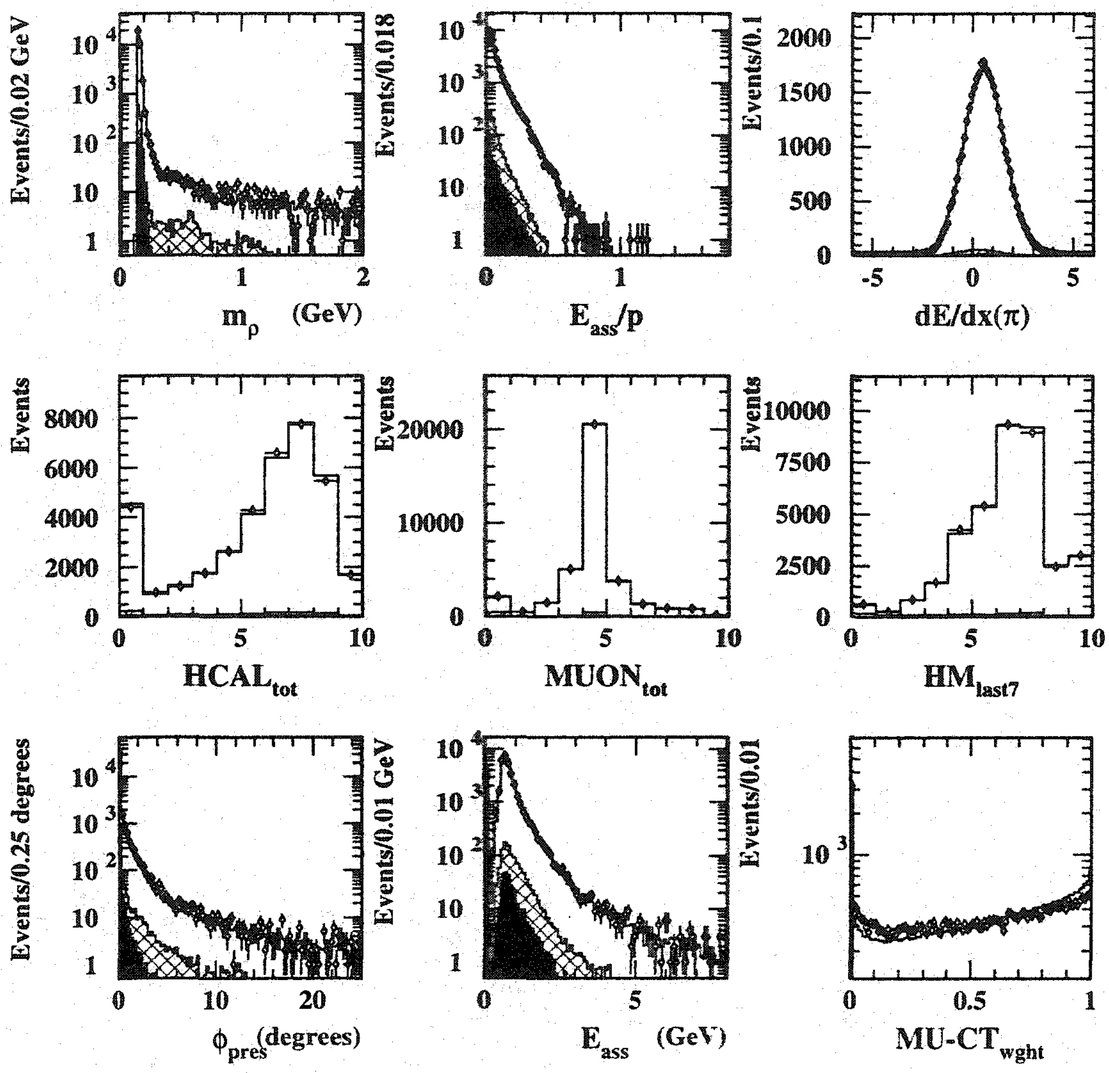

Figure 5.13: The distributions of all $\tau \to \mu\bar{\nu}_\mu\nu_\tau$ likelihood variables are given for selected $\tau \to \mu\bar{\nu}_\mu\nu_\tau$ events. The data are represented by the open circles with error bars, while the Monte Carlo signal is given by the open histogram, the tau background contributions shown hatched, and the non-tau contributions shaded.

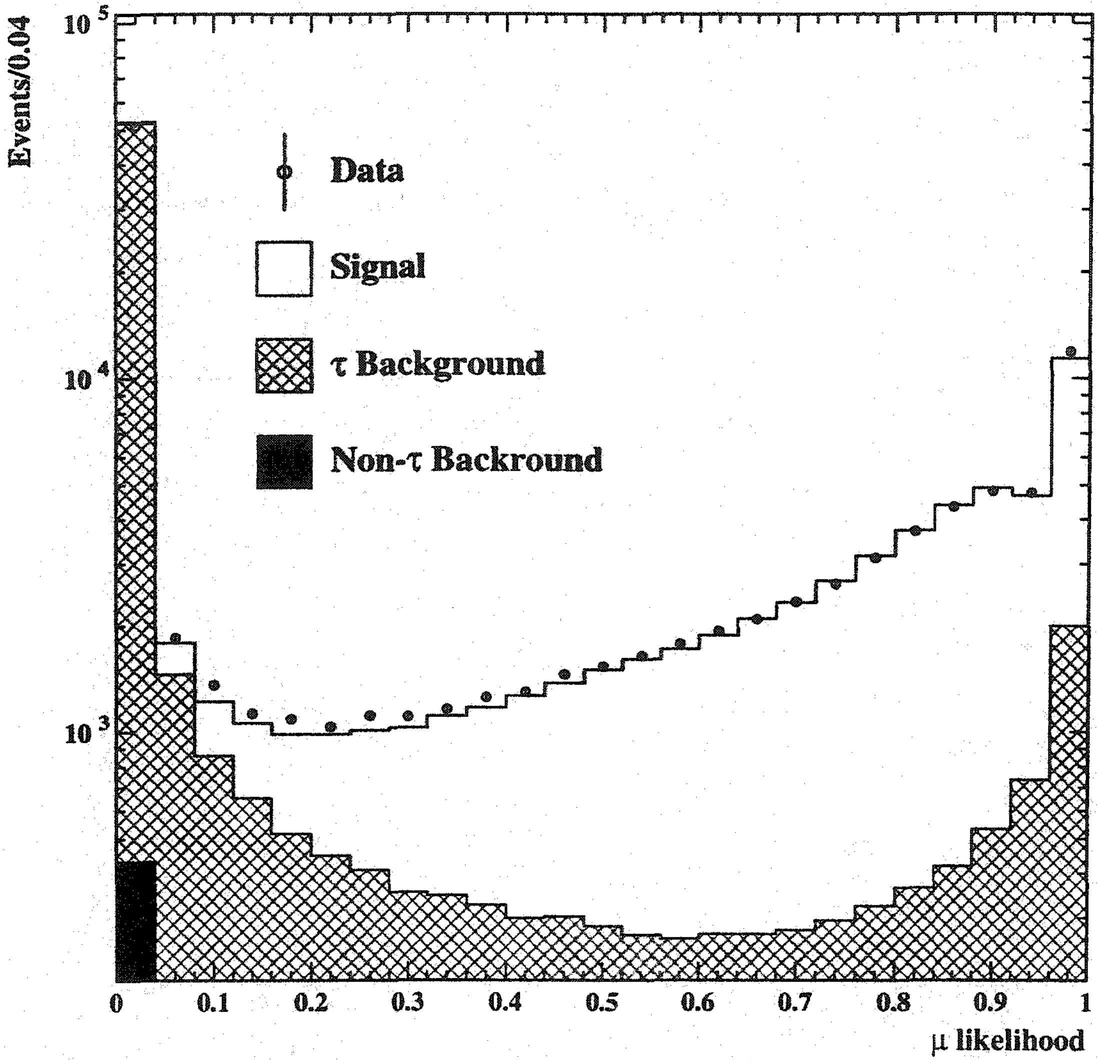

Figure 5.14: Presented is the combined likelihood distribution for the $\tau \to \mu\bar{\nu}_\mu\nu_\tau$ selection. The data are represented by the open circles with error bars, while the Monte Carlo signal is given by the open histogram, the tau background contributions shown hatched, and the non-tau contributions shaded.

5.3.5 $\tau \rightarrow \pi\ \nu_\tau$ Decays

Recall that, as indicated in Chapter 2, the $\tau \rightarrow \pi\ \nu_\tau$ selection channel does not distinguish charged pions from charged kaons and thus $\tau \rightarrow \pi\ \nu_\tau$ refers to either $\tau \rightarrow \pi\ \nu_\tau$ decays or $\tau \rightarrow \mathrm{K}\ \nu_\tau$ decays. Discussion of charged pions in this selection should be interpreted as referring to either a charged pion *or* a charged kaon.

In terms of their interactions in the OPAL detector, charged pions produced from tau decays fall somewhere between electrons and muons. They can leave significant energy deposits in the ECAL, but unlike electrons, the $\mathrm{E_{ass}/p}$ value is usually less than 1. Conversely, they are unlikely to exit the detector completely and hence register less activity in the outer detectors, on average, than muons. The selection of $\tau \rightarrow \pi\ \nu_\tau$ events focuses on identifying tau jets with a single charged particle inconsistent with being an electron or muon and with minimal evidence for neutral cluster energy. The principal background in this channel are $\tau \rightarrow \rho\nu_\tau$ decays since it is often difficult to resolve the ECAL clusters associated with the charged and neutral pions in such events.

The pre-selection cuts for the $\tau \rightarrow \pi\ \nu_\tau$ selection consist of

$$\mathrm{N_{trk}} = 1,$$
$$\mathrm{P_{trk}/E_{beam}} > 0.02,$$

where the $\mathrm{P_{trk}/E_{beam}}$ cut is again designed to remove the momentum regime in which the separation of pions and muons is problematic.

Events passing these cuts are separated for the likelihood selection into sets corresponding to the three detector regions, and subsequently into subsets in which the jets contain no neutral clusters, one neutral cluster, and two or more neutral clusters. In addition, each of these cases is further divided into a set exhibiting no HCAL activity and a set in which HCAL hits are recorded. The background for the case with no neutral clusters and registering HCAL hits arises predominantly from $\tau \rightarrow \mu\bar{\nu}_\mu\nu_\tau$ events, while the case with no HCAL hits and two or more neutral clusters is largely contaminated by $\tau \rightarrow \rho\nu_\tau$ background. The variables used in this selection are described in Table 5.2.

Four variables used in this selection, plotted after tau pair selection but before $\tau \rightarrow \pi\ \nu_\tau$

selection, are given in Figure 5.15. As may be seen, the good agreement between data and Monte Carlo and the discrimination power between signal and background are evident.

Figures 5.16 and 5.17 show four plots of selection variables after the $\tau \rightarrow \pi\ \nu_\tau$ selection has been made. The plots are divided into the three detector regions and, as may be seen, the agreement between Monte Carlo and data is satisfactory in all cases. The small discrepancies between data and Monte Carlo, such as in the E_{tot}/p distributions, have a negligible effect on the analysis and are treated by the systematic studies described in Chapter 7. Plots for all of the variables used in this selection, when all detector regions are combined, are given in Figure 5.18. In order to illustrate the good agreement between data and Monte Carlo for the combination of these likelihood variables, the likelihood distribution for the $\tau \rightarrow \pi\ \nu_\tau$ selection is given in Figure 5.19.

The results of the selection are summarized in Table 5.5. A total of 30440 events are selected with an efficiency of 75%, within the fiducial acceptance and after tau pair selection, and a background of 26%. As expected, the largest background arises from $\tau \rightarrow \rho\nu_\tau$ events with a small but significant contribution from $\tau \rightarrow \mu\bar{\nu}_\mu\nu_\tau$ events.

5.3.6 $\tau \rightarrow \rho\nu_\tau$ Decays

The ρ particle contains the same basic quark content as pions, but instead of combining to create a spin-0 particle, the two spin-1/2 quarks combine to produce a spin-1 particle. This additional angular momentum causes the ρ to be more massive than the pion, allowing the charged ρ to decay to a π^- and π^0 . Recall that the π^0 immediately decays to two photons ($\pi^0 \rightarrow \gamma\gamma$). No distinction is made in this analysis between $\tau \rightarrow \pi^-\ \pi^0\ \nu_\tau$ tau decay events and $\tau \rightarrow K\pi^0\ \nu_\tau$ tau decays.

The highly collimated tau decays at OPAL cause π^0 identification in these events to be challenging because the ECAL showers arising from the two photons and the π^- can overlap. The great difficulty in selecting $\tau \rightarrow \rho\nu_\tau$ decays at OPAL is in distinguishing these events, which contain a single π^0 , from jets with no π^0 's, such as those arising from $\tau \rightarrow \pi\ \nu_\tau$ decays, and from multi-π^0 jets such as the one-prong a_1 tau decays. In addition to the likelihood variables which provide neutral cluster information, the invari-

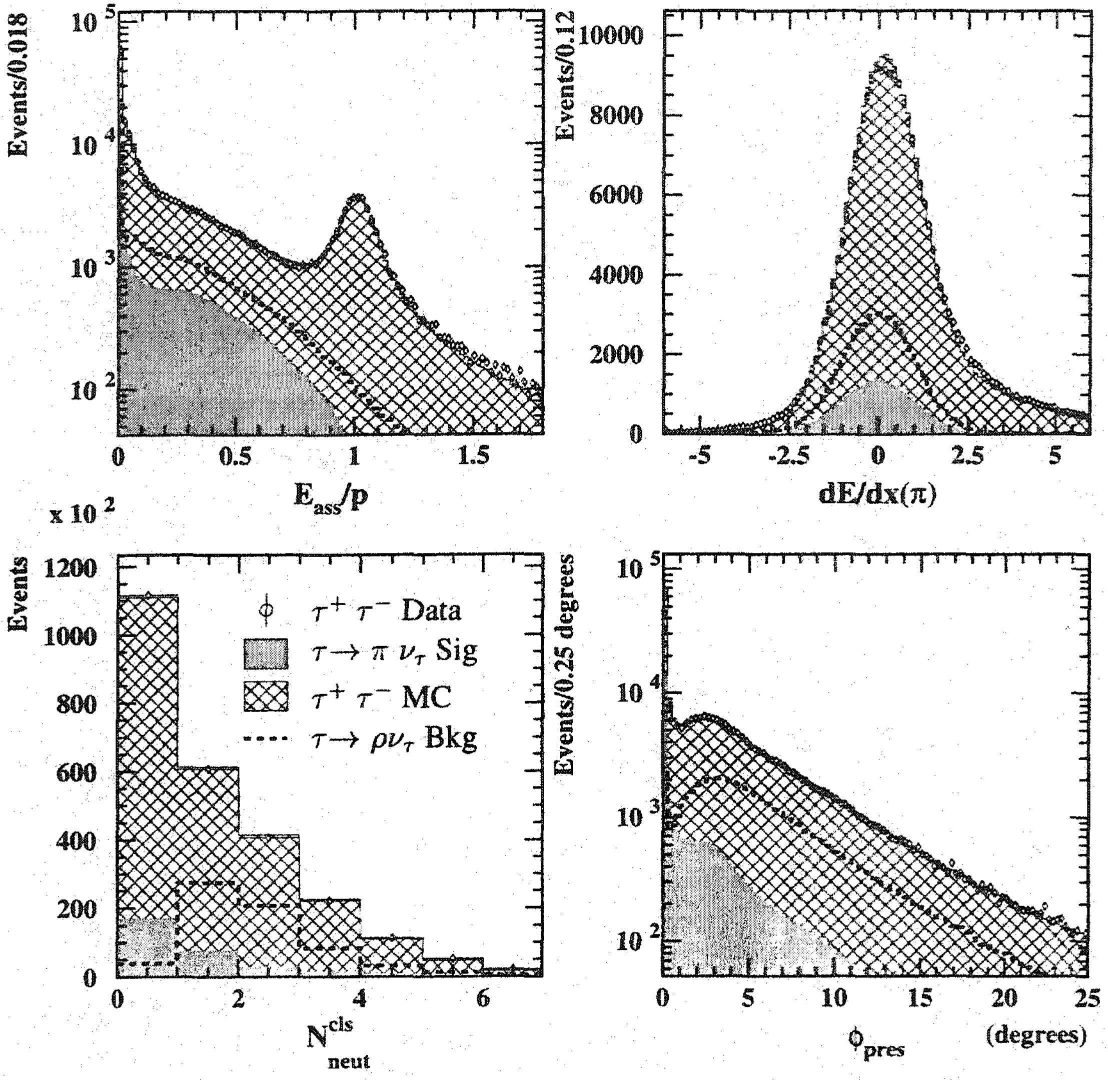

Figure 5.15: Distributions of $\mathrm{E_{ass}/p}$, $\mathrm{dE/dx}(\pi)$, $\mathrm{N^{cls}_{neut}}$, and $o_{\rm pres}$are given for tau pair selected events over all detector regions. The circles with error bars represents the data, the hatched histogram the Monte Carlo for all tau decays, and the shaded area the Monte Carlo $\tau \rightarrow \pi\ \nu_\tau$ signal. To provide an indication of the separation between the signal and the predominant tau decay background, the distributions for the $\tau \rightarrow \rho\nu_\tau$ channel are overlayed as dashed distributions.

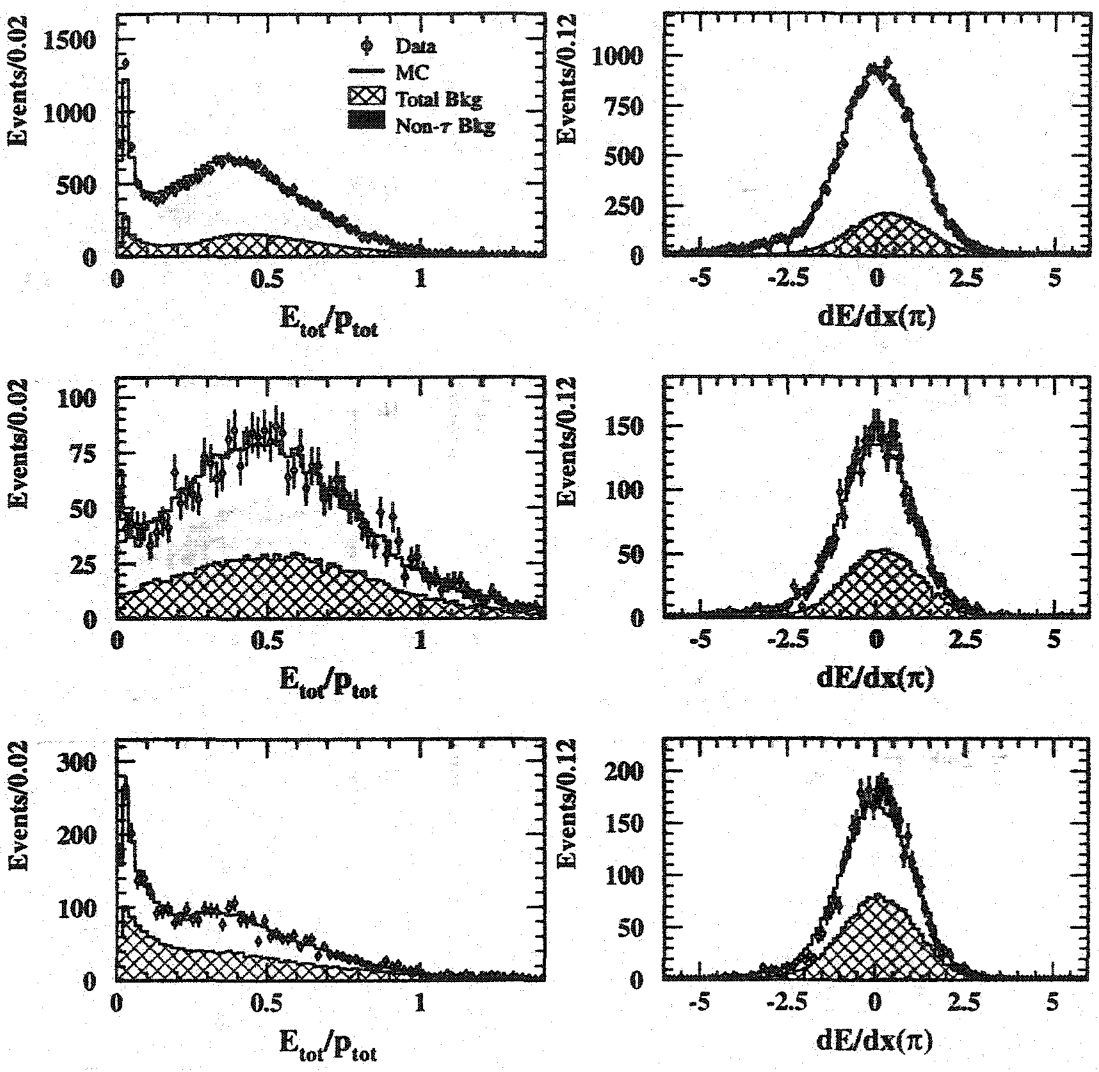

Figure 5.16: Depicted are distributions of E_{tot}/p (left) and dE/dx(π) (right), for $\tau \to \pi\nu_\tau$ selected events in the barrel (top), overlap (middle), and endcap (bottom) regions of the detector. The data are represented by the open circles with error bars, while the Monte Carlo signal is given by the open histogram, the tau background contributions shown hatched, and the non-tau contributions shaded.

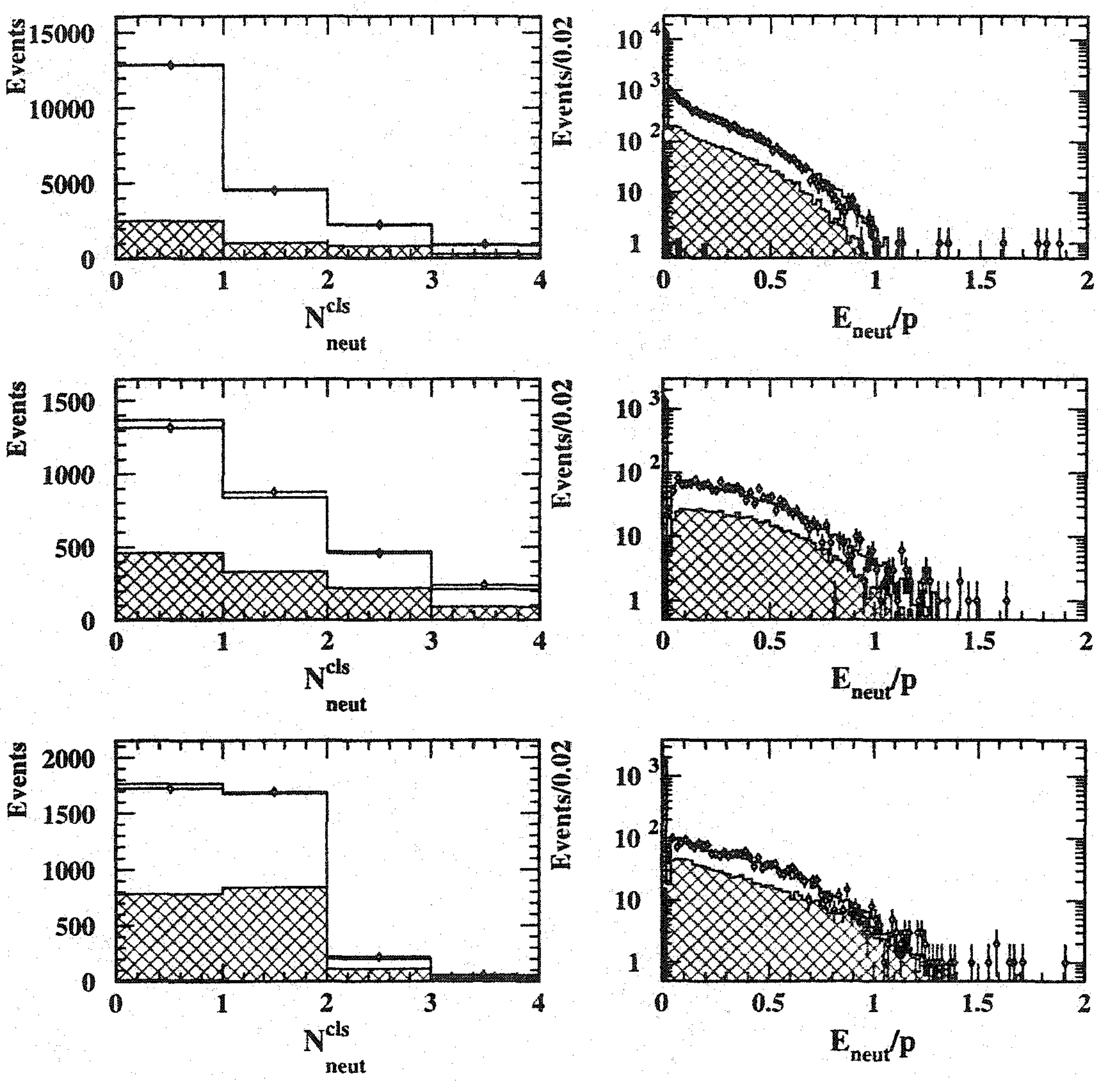

Figure 5.17: Depicted are distributions of N^{cls}_{neut} (left) and E_{neut}/p (right), for $\tau \to \pi\nu_\tau$ selected events in the barrel (top), overlap (middle), and endcap (bottom) regions of the detector. The data are represented by the open circles with error bars, while the Monte Carlo signal is given by the open histogram, the tau background contributions shown hatched, and the non-tau contributions shaded.

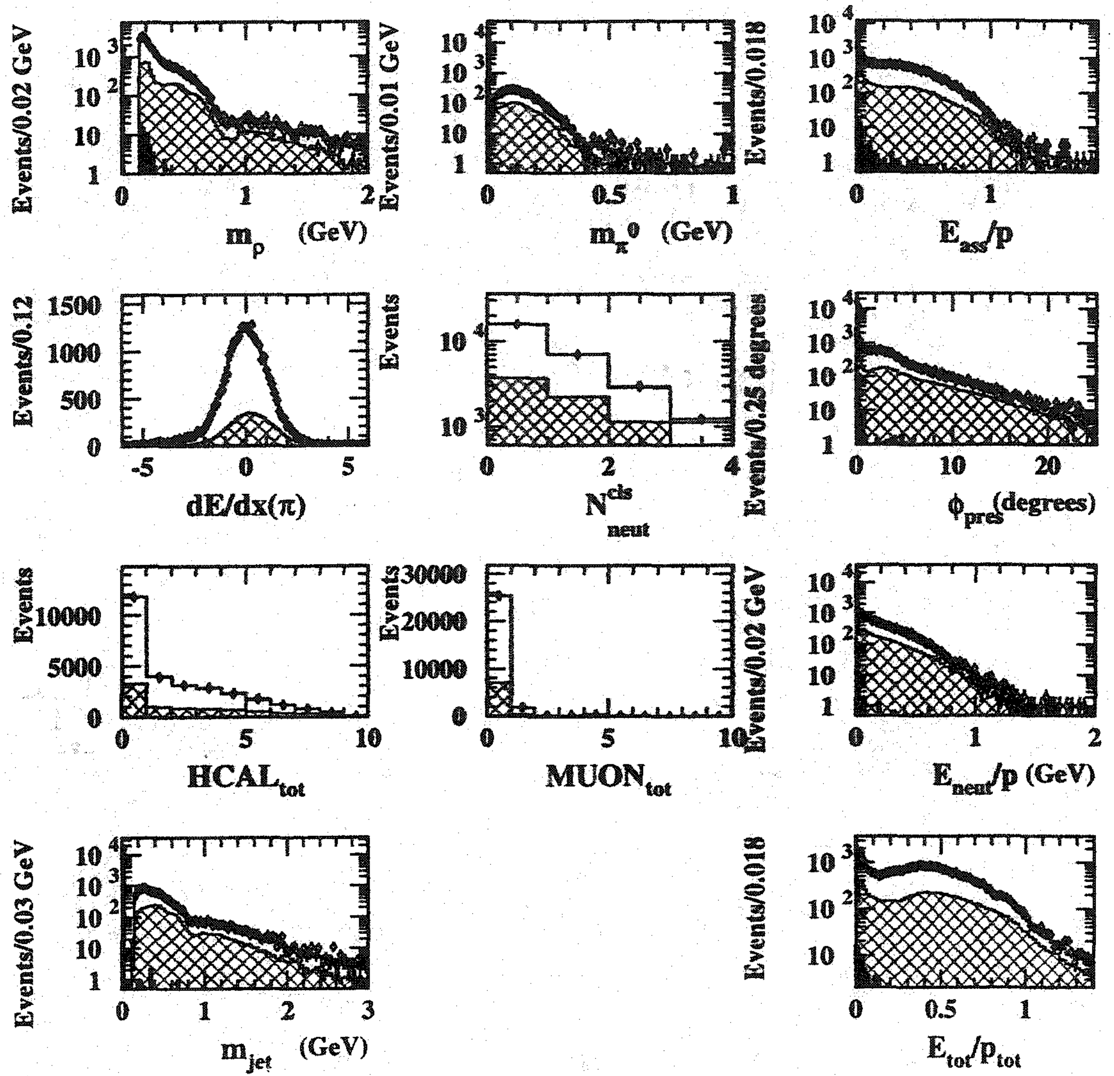

Figure 5.18: The distributions of all $\tau \rightarrow \pi\ \nu_\tau$ likelihood variables are given for selected $\tau \rightarrow \pi\ \nu_\tau$ events. The data are represented by the open circles with error bars, while the Monte Carlo signal is given by the open histogram, the tau background contributions shown hatched, and the non-tau contributions shaded.

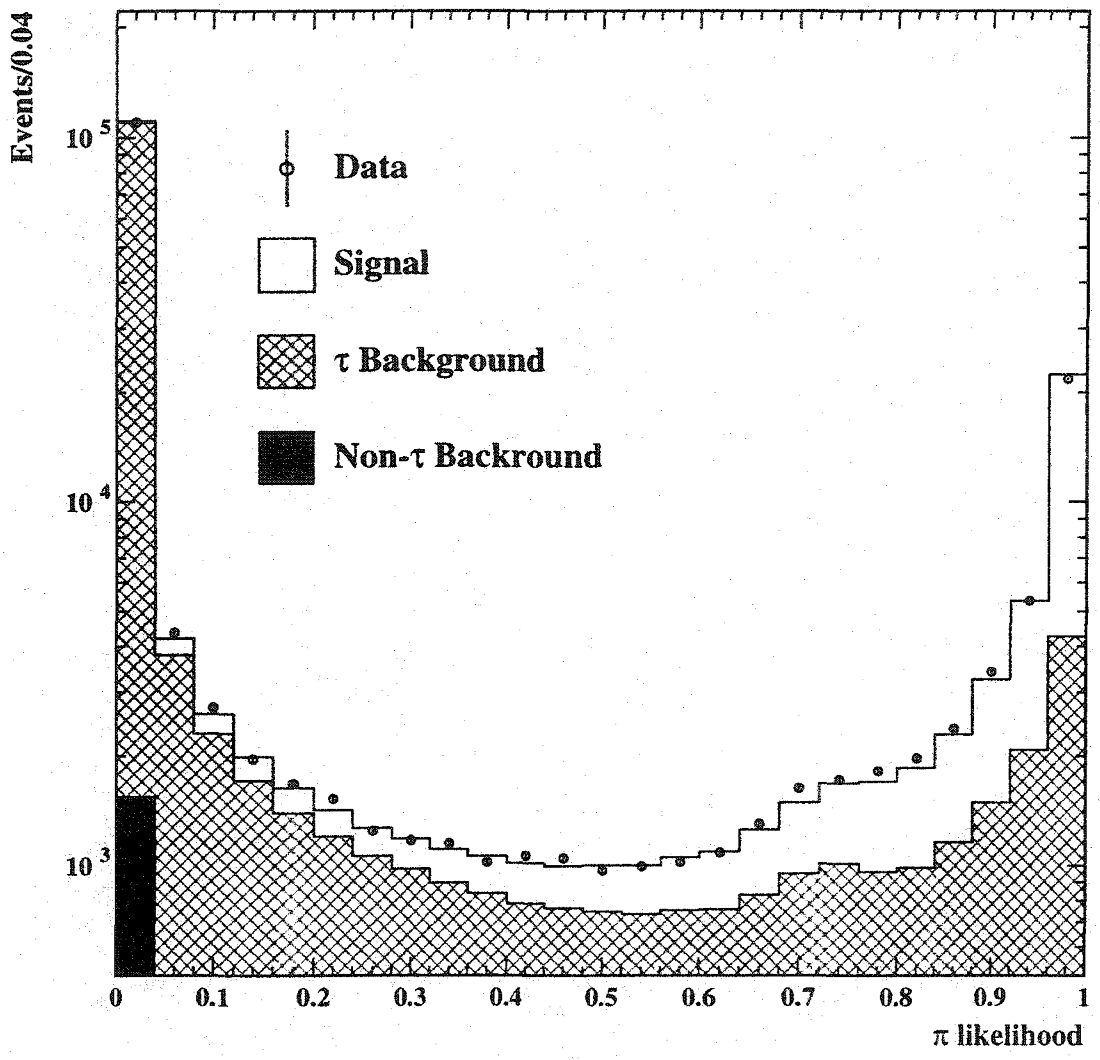

Figure 5.19: Presented is the combined likelihood distribution for the $\tau \rightarrow \pi\nu_\tau$ selection. The data are represented by the open circles with error bars, while the Monte Carlo signal is given by the open histogram, the tau background contributions shown hatched, and the non-tau contributions shaded.

	Barrel	Overlap	Endcap	All
Efficiency (%)	78.1	65.5	61.2	74.7
Composition (%)				
e^-	0.3	2.8	2.0	0.8
μ^-	4.8	4.1	3.9	4.6
π^- (K$^-$)	**79.6**	**63.2**	**53.8**	**74.3**
$\pi^-\pi^0$ or K$^-(\rho)$	12.1	24.7	29.3	15.8
$\pi^-\pi^+\pi^-(a1)$	0.0	0.0	0.3	0.1
$\pi^-\pi^0\pi^0(a1)$	0.7	3.2	6.6	1.8
$\pi^-K^0(K^*)$	1.6	1.1	1.6	1.6
$\pi^-\pi^0\pi^0\pi^0$	0.0	0.2	0.8	0.2
$K^-\pi^0K^0$	0.1	0.1	0.2	0.1
$\pi^-\overline{K}^0\pi^0$	0.0	0.1	0.3	0.1
K^0K^-	0.4	0.3	0.4	0.4
e$^+$e$^-\rightarrow\mu^+\mu^-$	0.2	0.1	0.2	0.2
e$^+$e$^-\rightarrow$ e$^+$e$^-$	0.0	0.1	0.1	0.0
$\gamma\gamma\mu\mu$	0.0	0.1	0.1	0.0

Table 5.5: $\tau\rightarrow\pi\,\nu_\tau$ selection efficiencies and composition of selected events in each detector region and combined.

ant mass m$_\rho$, constructed from charged track and neutral cluster energy, is an important discriminator for selecting $\tau\rightarrow\rho\nu_\tau$ events.

The only pre-selection cut applied in this selection is to require that the jets have exactly one track associated to them (N$_{\rm trk}$ $= 1$). All such jets are passed through the likelihood selection using the variables listed in Table 5.2. As with the $\tau\rightarrow\pi\,\nu_\tau$ selection, this likelihood selection is separated into cases in which the jets contain no neutral clusters, exactly one neutral cluster, and more than one neutral cluster. It is similarly further divided into the set of jets containing no HCAL activity and those with HCAL hits. Typically, $\tau\rightarrow\pi\,\nu_\tau$ events dominate the background in the case with no neutral clusters and with HCAL hits while $\tau\rightarrow\pi 2\pi^0\;\;\nu_\tau$ background primarily populates the case with two or more neutral clusters and no HCAL hits.

To provide an indication of their discrimination power, Figure 5.20 shows four of the variables used by this selection. The variables are plotted after tau pair selection but before the decay selection is applied. The high level of consistency between data and the

Monte Carlo simulation for these variables is apparent.

Figures 5.21 and 5.22 show plots of four selection variables after the $\tau\rightarrow\ \rho\nu_\tau$ selection has been made. The plots are divided into the three detector regions and, as may be seen, the agreement between Monte Carlo and data is satisfactory in all cases. Figure 5.23 provides plots of all variables used in this selection with the three detector regions combined. In Figure 5.24 the combined $\tau\rightarrow\ \rho\nu_\tau$ selection likelihood distribution is shown. The good agreement between data and Monte Carlo reflects the high quality of the simulation for all of the likelihood variables employed in this selection.

The $\tau\rightarrow\ \rho\nu_\tau$ selection provides 67682 candidates for the polarization analysis with an efficiency of 73% and total background of 29%. As shown in Table 5.6, the majority of background arises from single prong a_1 tau decays.

5.3.7 $\tau\rightarrow\ a_1\ \nu_\tau$ Decays

The $\tau\rightarrow\ a_1\ \nu_\tau$ decays selected for this analysis are those in which the a_1 subsequently decays to three charged pions. Thus, in contrast to the previous selections, the $\tau\rightarrow\ a_1\ \nu_\tau$ pre-selection requires exactly three tracks in a jet ($N_{trk} = 3$), none of which is consistent with being a conversion track[2].

The decay products in this channel, as with all tau decays, are highly collimated and the predominant backgrounds arise from tau decays with three charged hadrons and one or more neutral pions. The general selection method relies on the search for jets with exactly three tracks and minimal neutral cluster energy. For this selection, the three-prong invariant mass variable is a particularly important discriminator.

Events passing the pre-selection cut are separated into samples corresponding to the three detector regions and passed through the likelihood selection using the variables indicated in Table 5.2.

Four examples of the distributions of variables used in this selection are given in Fig-

---

[2] A 'conversion' track is an electron or positron produced via pair production from a photon interacting in the material of the detector. Thus conversion tracks are not associated directly with tau decay and, in order to properly determine the number of tracks arising from the tau decay itself, must be removed in the counting of tracks in a tau jet.

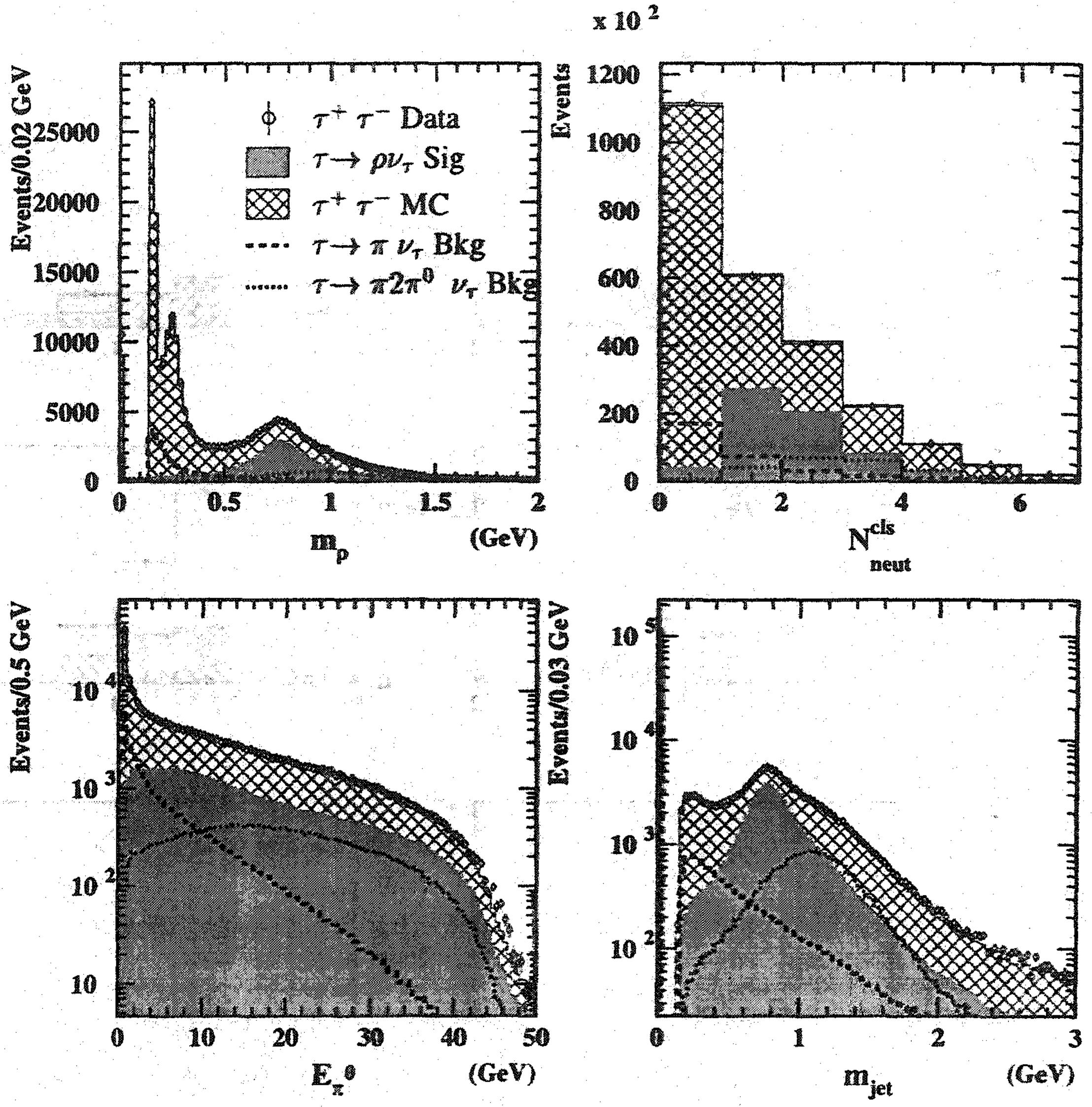

Figure 5.20: Distributions of m_ρ , N^{cls}_{neut} , E_{π^0} , and m_{jet} are given for tau pair selected events over all detector regions. The circles with error bars represents the data, the hatched histogram the Monte Carlo for all tau decays, and the shaded area the Monte Carlo $\tau \to \rho\nu_\tau$ signal. To provide an indication of the separation between the signal and the predominant tau decay backgrounds, the distributions for the $\tau \to \pi\ \nu_\tau$ and $\tau \to \pi 2\pi^0\ \nu_\tau$ channels are overlayed as the dashed and dotted distributions respectively.

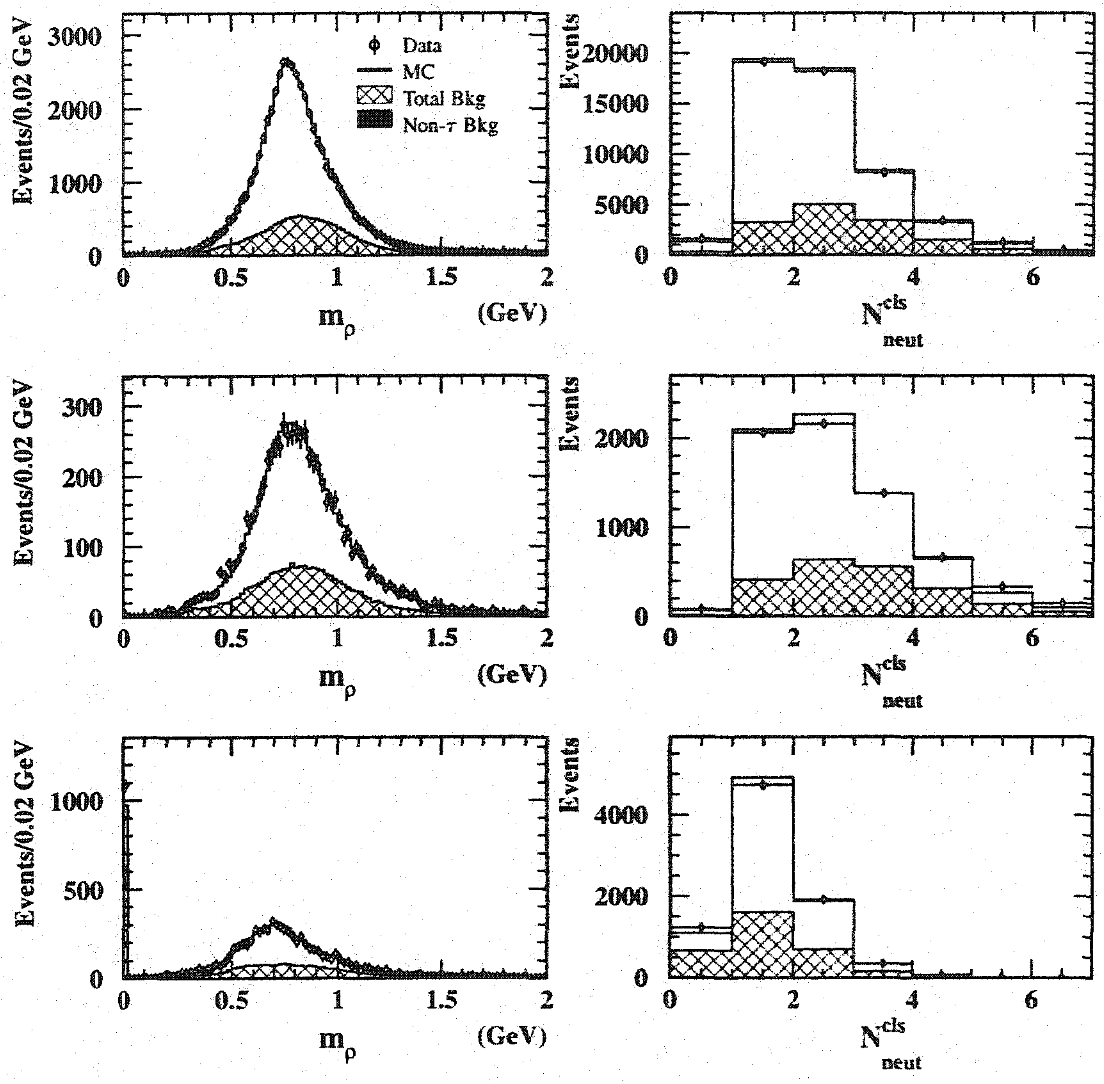

Figure 5.21: Depicted are distributions of m_ρ (left) and N^{cls}_{neut} (right), for $\tau \to \rho\nu_\tau$ selected events in the barrel (top), overlap (middle), and endcap (bottom) regions of the detector. The data are represented by the open circles with error bars, while the Monte Carlo signal is given by the open histogram, the tau background contributions shown hatched, and the non-tau contributions shaded.

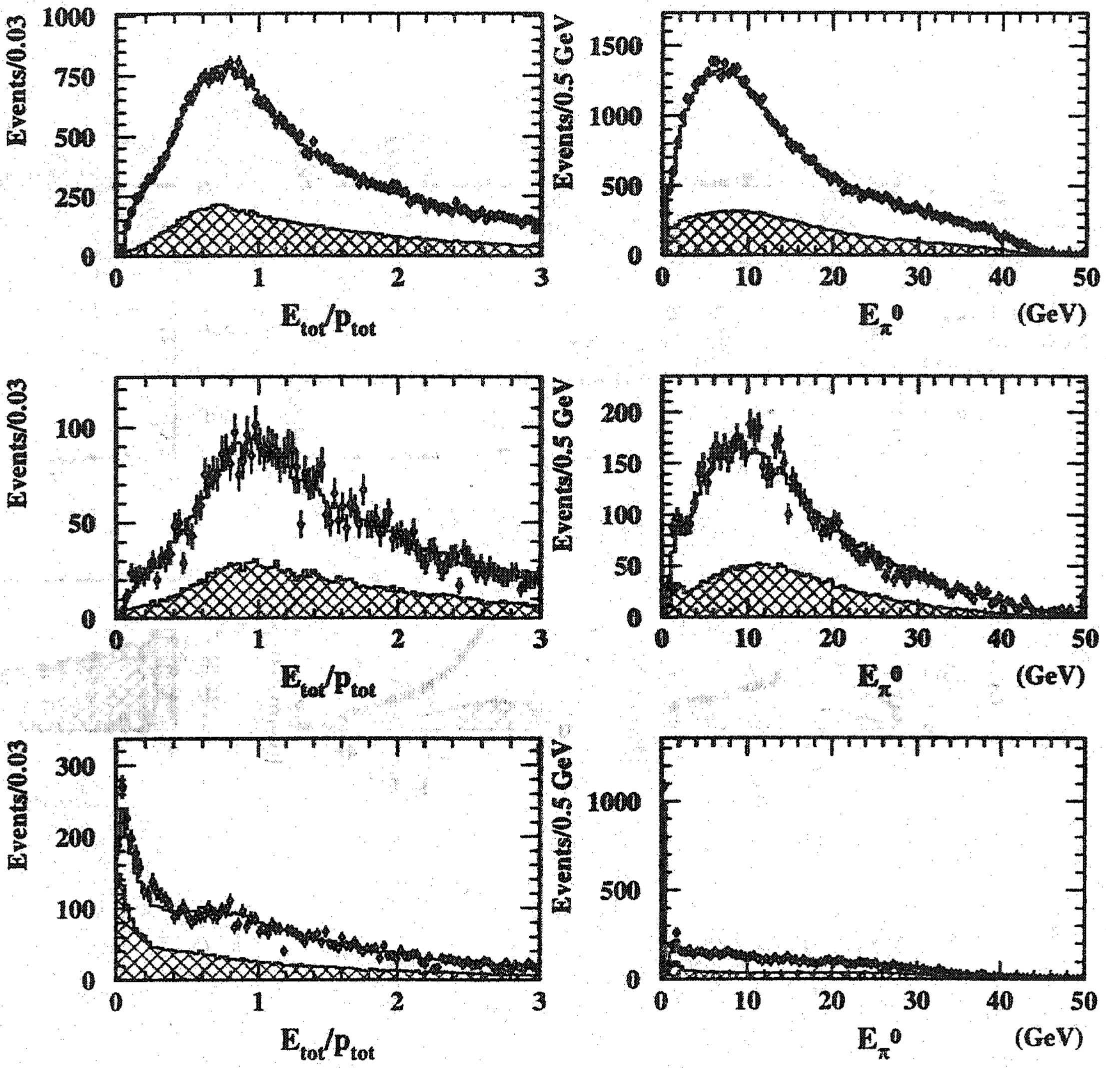

Figure 5.22: Depicted are distributions of E_{tot}/p (left) and E_{π^0} (right), for $\tau \rightarrow \rho\nu_\tau$ selected events in the barrel (top), overlap (middle), and endcap (bottom) regions of the detector. The data are represented by the open circles with error bars, while the Monte Carlo signal is given by the open histogram, the tau background contributions shown hatched, and the non-tau contributions shaded.

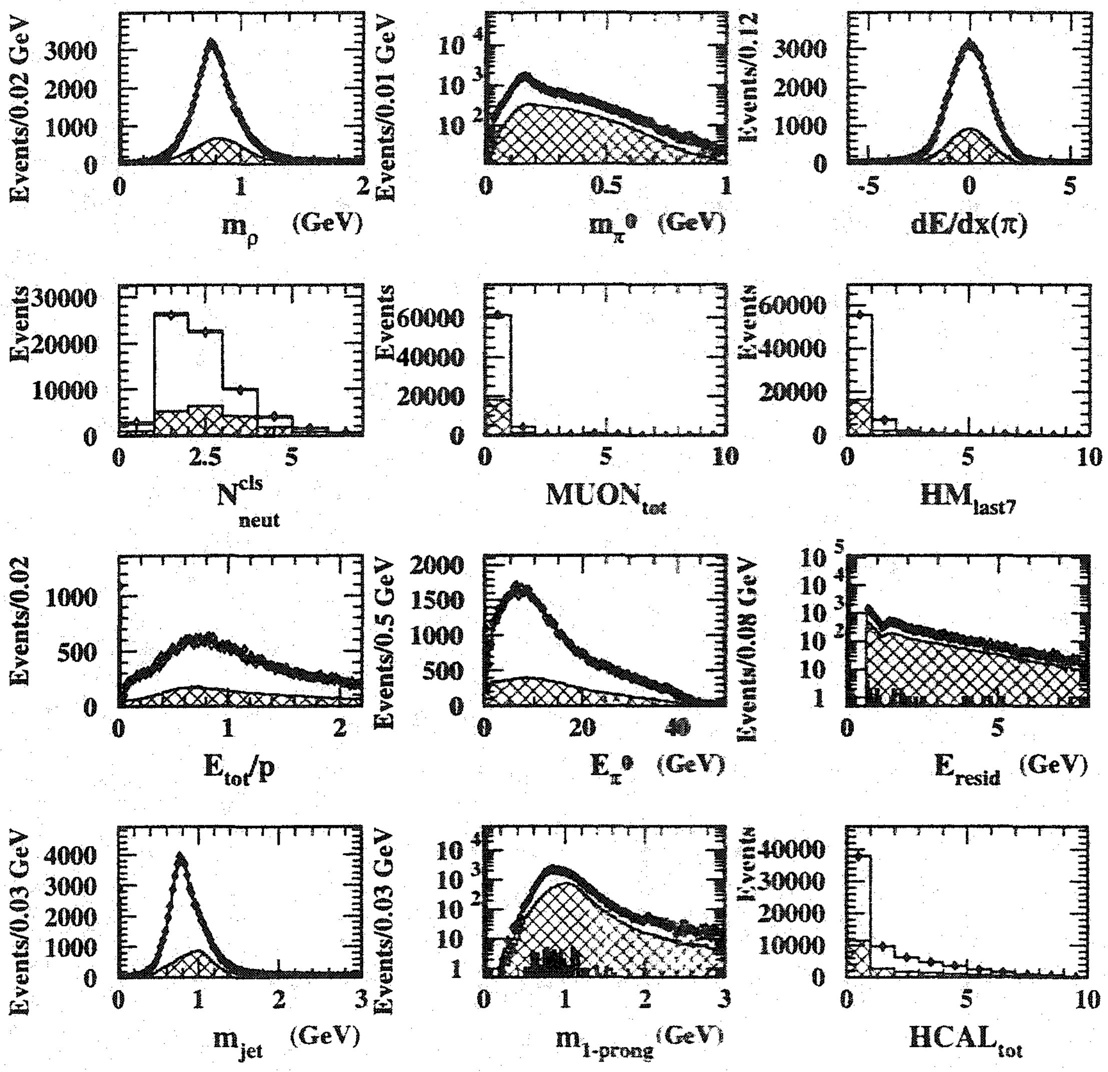

Figure 5.23: The distributions of all $\tau \to \rho\nu_\tau$ likelihood variables are given for selected $\tau \to \rho\nu_\tau$ events. The data are represented by the open circles with error bars, while the Monte Carlo signal is given by the open histogram, the tau background contributions shown hatched, and the non-tau contributions shaded.

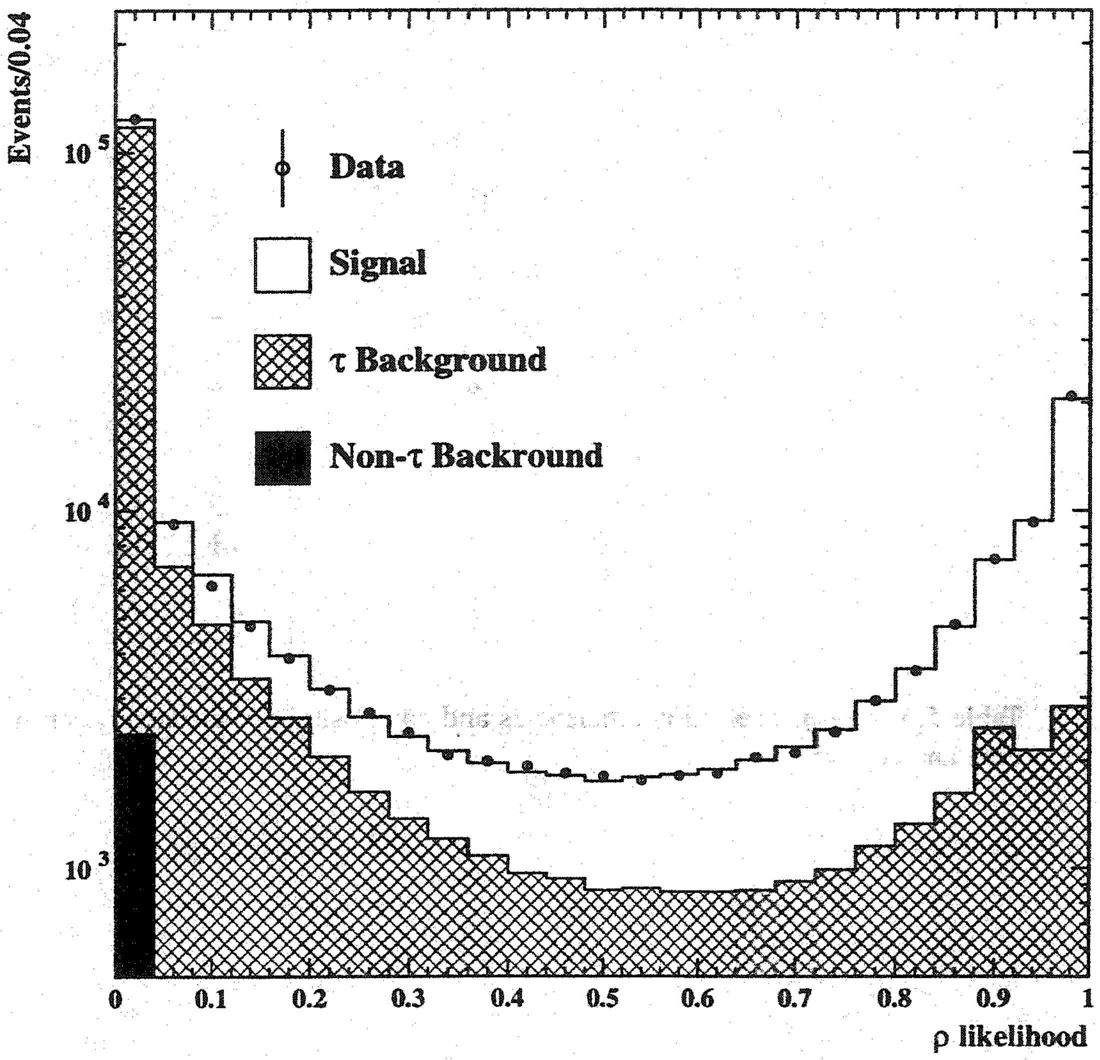

Figure 5.24: Presented is the combined likelihood distribution for the $\tau \rightarrow \rho\nu_\tau$ selection. The data are represented by the open circles with error bars, while the Monte Carlo signal is given by the open histogram, the tau background contributions shown hatched, and the non-tau contributions shaded.

	Barrel	Overlap	Endcap	All
Efficiency (%)	76.5	67.4	58.0	73.3
Composition (%)				
e$^-$	0.3	0.5	0.6	0.4
μ^-	0.3	0.7	0.6	0.4
π^- (K$^-$)	4.4	5.9	7.7	4.9
$\pi^-\pi^0$ or K$^-\pi^0(\rho)$	**72.7**	**68.3**	**65.3**	**71.4**
$\pi^-\pi^+\pi^-(a1)$	0.1	0.0	0.2	0.1
$\pi^-\pi^0\pi^0(a1)$	17.5	18.9	19.4	17.9
$\pi^-K^0(K^*)$	1.3	1.7	1.5	1.3
$\pi^-\pi^+\pi^-\pi^0$	0.1	0.0	0.2	0.1
$\pi^-\pi^0\pi^0\pi^0$	1.7	2.2	2.5	1.8
$K^0\pi^-\overline{K}^0$	0.1	0.2	0.2	0.1
$K^-\pi^0K^0$	0.2	0.2	0.2	0.2
$\pi^0\pi^0K^-$	0.1	0.1	0.1	0.1
$\pi^-\overline{K}^0\pi^0$	0.6	0.6	0.6	0.6
$\pi^-\pi^0 2\gamma$	0.1	0.1	0.1	0.1
$\pi^-\pi^0\gamma$	0.1	0.1	0.1	0.1
K^0K^-	0.3	0.3	0.3	0.3
e$^+$e$^-\rightarrow\mu^+\mu^-$	0.1	0.1	0.1	0.1
e$^+$e$^-\rightarrow$ e$^+$e$^-$	0.0	0.1	0.1	0.0
e$^+$e$^-\rightarrow$ q$\overline{\text{q}}$	0.2	0.0	0.1	0.1

Table 5.6: $\tau\rightarrow\rho\nu_\tau$ selection efficiencies and composition of events in each detector region and combined.

ure 5.25. The variables are plotted after tau pair selection but before the decay selection is applied. The good agreement between the data and Monte Carlo for these variables is apparent.

Four plots of selection variables, after the $\tau\rightarrow$ a$_1$ ν_τ selection has been made, are given in Figures 5.26 and 5.27. The variables are presented separately for each detector region and show good agreement between data and the Monte Carlo simulation. The small discrepancy that may be seen in the m$_{\text{a}_1}$ mass variable can be attributed to modelling effects and will be discussed in detail in Chapter 7. Plots of all of the variables used in this selection, with all detector regions combined, are given in Figure 5.28. The quality of the simulation of this combined set of variables is illustrated by the likelihood distribution

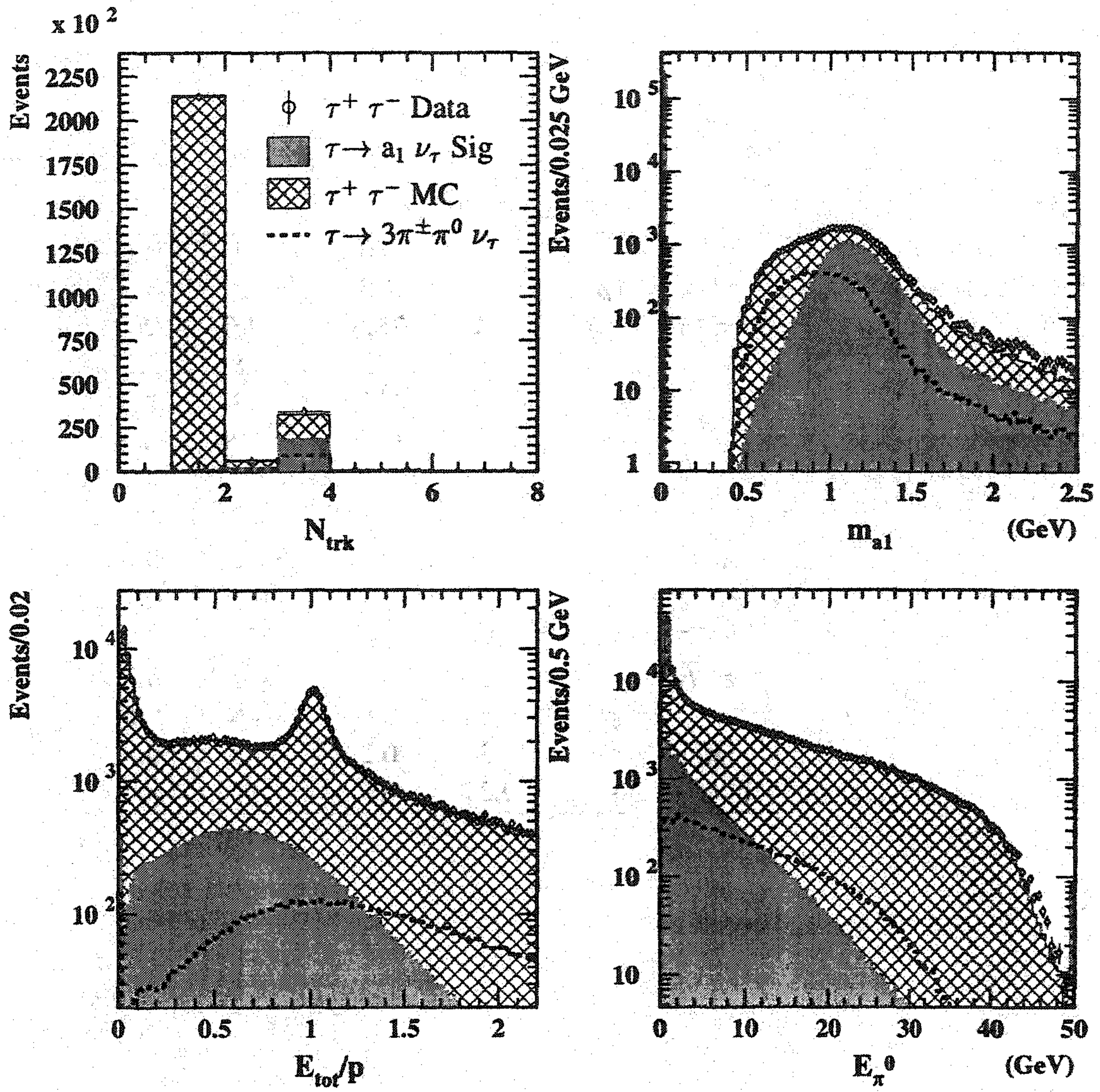

Figure 5.25: Distributions of number of non-conversion tracks, m_{a_1} , E_{tot}/p , and E_{π^0} are given for tau pair selected events over all detector regions. The circles with error bars represents the data, the hatched histogram the Monte Carlo for all tau decays, and the shaded area the Monte Carlo $\tau \rightarrow a_1\nu_\tau$ signal. To provide an indication of the separation between the signal and the predominant tau decay backgrounds, the distributions for the$\tau \rightarrow 3\pi^\pm\pi^0$ ν_τ channel are overlayed as the dashed distributions.

shown in Figure 5.29; the good agreement between data and Monte Carlo can be noted.

The $\tau \rightarrow \mathrm{a}_1\ \nu_\tau$ selection is 77% efficient with an estimated 25% background in the 22161 events selected. As indicated in Table 5.7, the largest backgrounds in this sample arise from $\tau \rightarrow 3\pi^\pm\pi^0\ \nu_\tau$ decays.

	Barrel	Overlap	Endcap	All
Efficiency (%)	78.2	75.2	71.2	77.2
Composition (%)				
π^- (K$^-$)	0.0	0.0	0.1	0.1
$\pi^-\pi^0$ or K$^-$ (ρ)	0.4	1.0	2.0	0.6
$\boldsymbol{\pi^-\pi^+\pi^-(\mathrm{a}_1)}$	**75.1**	**75.3**	**74.0**	**75.0**
$\pi^-\pi^0\pi^0(\mathrm{a}_1)$	0.1	0.3	0.8	0.2
$\pi^- K^0(K^*)$	1.2	1.2	1.3	1.2
$\pi^-\pi^+\pi^-\pi^0$	17.9	17.7	16.8	17.8
$\pi^-\pi^0\pi^0\pi^0$	0.0	0.1	0.1	0.0
$K^-\pi^+K^+$	1.0	0.7	0.7	1.0
$K^0\pi^-\overline{K}^0$	0.1	0.1	0.1	0.1
$K^-\pi^0K^0$	0.1	0.1	0.1	0.1
$K^-\pi^-\pi^+$	2.6	2.5	2.4	2.6
$\pi^-\overline{K}^0\pi^0$	0.2	0.2	0.2	0.2
$\pi^-\pi^+\pi^-\pi^0\pi^0$	0.6	0.6	0.6	0.6
K^0K^-	0.3	0.2	0.3	0.3
$\mathrm{e}^+\mathrm{e}^- \rightarrow \mathrm{q}\overline{\mathrm{q}}$	0.2	0.0	0.2	0.2

Table 5.7: $\tau \rightarrow \mathrm{a}_1\ \nu_\tau$ selection efficiencies and composition of selected events in each detector region and combined.

5.4 Additional Non-tau Background Rejection and Quality Cuts

Owing to the structural geometry of OPAL, certain detector regions must be treated with additional care. In particular, the overlap and endcap portions of the detector contain areas of imperfect sub-detector coverage. These areas can lead to an enhanced non-tau background which passes the nominal tau-pair selection, and thus additional selection constraints are required.

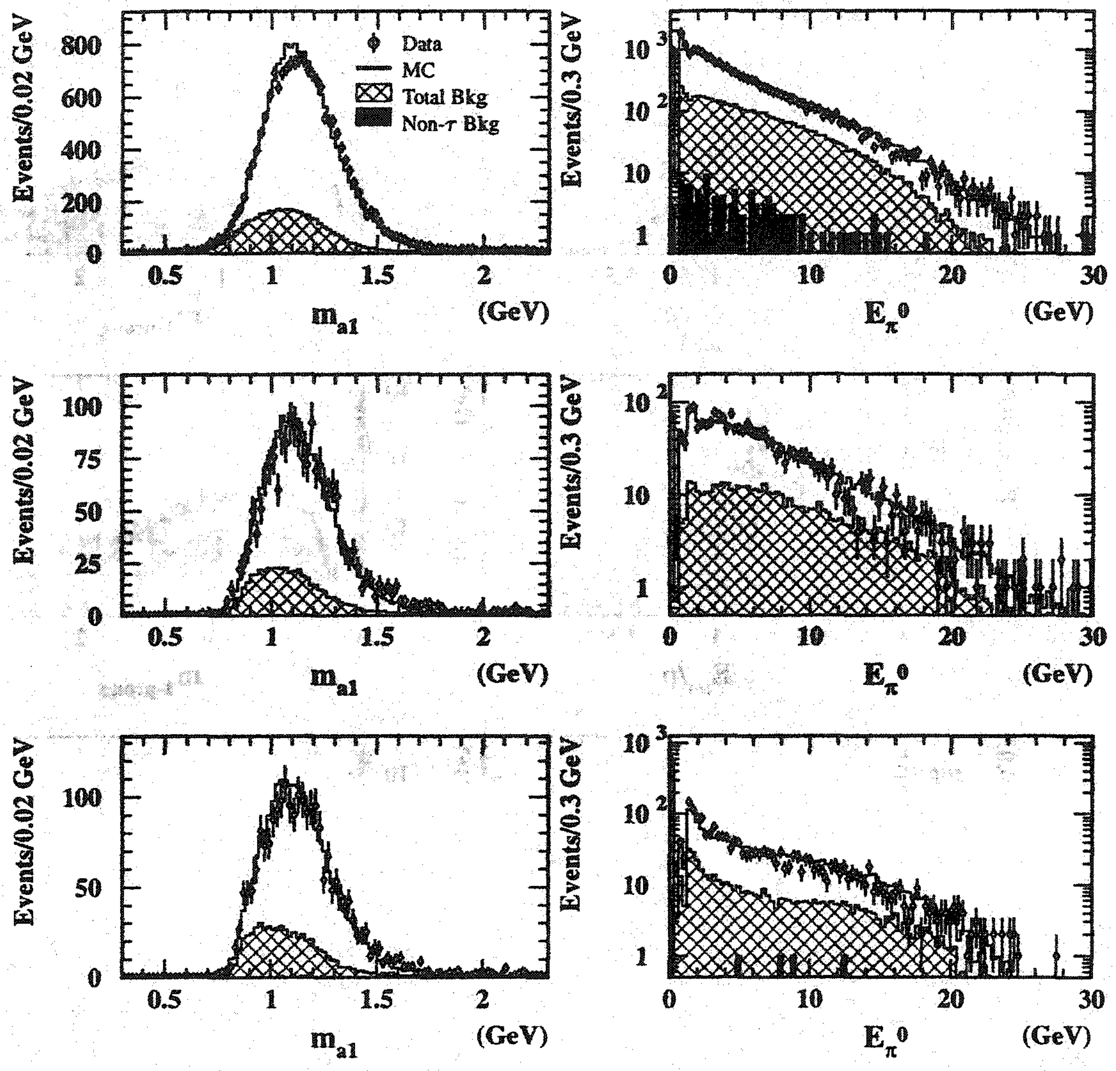

Figure 5.26: Depicted are distributions of m_{a_1} (left) and E_{π^0} (right), for $\tau \rightarrow a_1\nu_\tau$ selected events in the barrel (top), overlap (middle), and endcap (bottom) regions of the detector. The data are represented by the open circles with error bars, while the Monte Carlo signal is given by the open histogram, the tau background contributions shown hatched, and the non-tau contributions shaded.

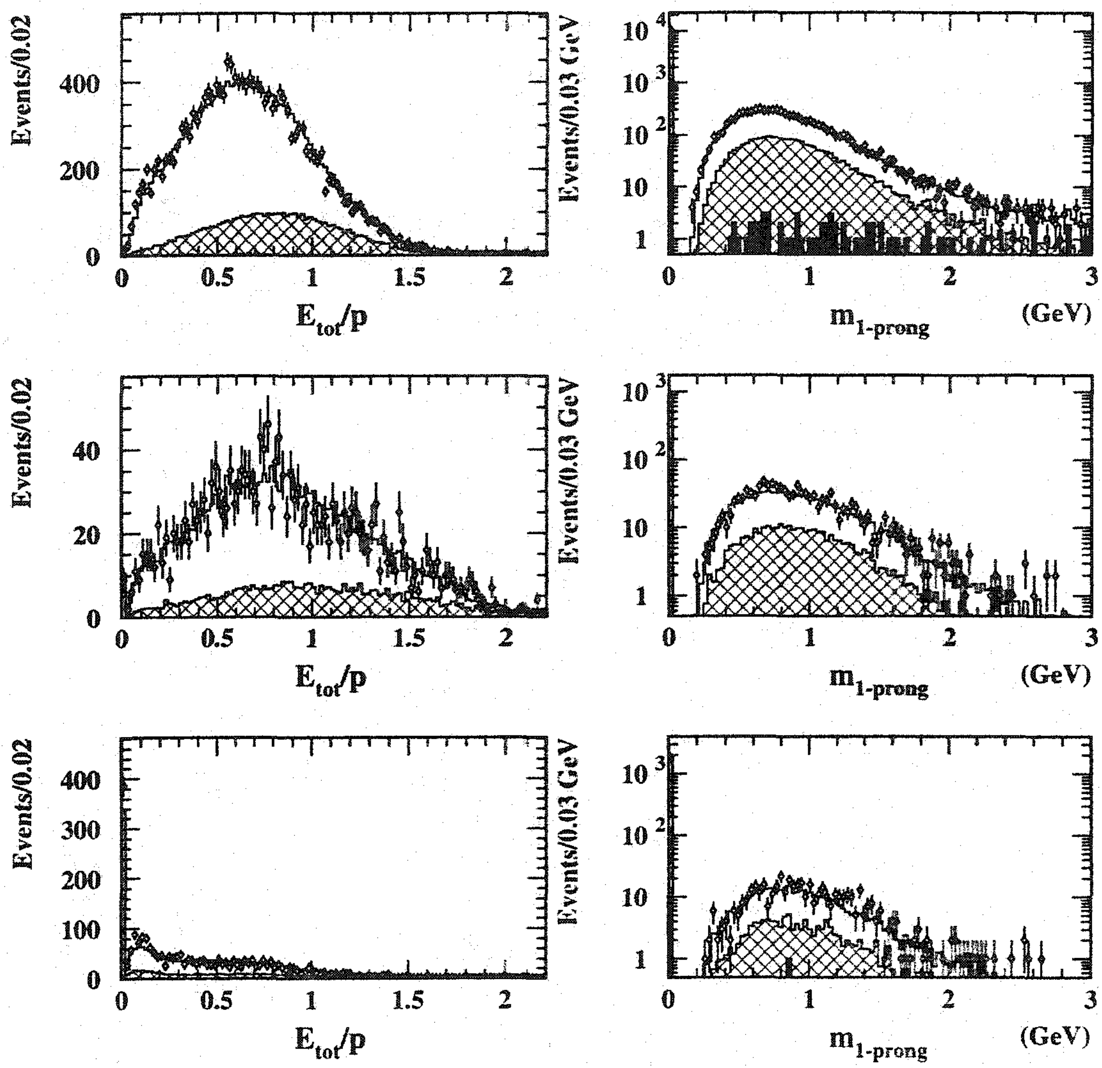

Figure 5.27: Depicted are distributions of E_{tot}/p (left) and m_{a_1} (right), for $\tau \rightarrow a_1\nu_\tau$ selected events in the barrel (top), overlap (middle), and endcap (bottom) regions of the detector. The data are represented by the open circles with error bars, while the Monte Carlo signal is given by the open histogram, the tau background contributions shown hatched, and the non-tau contributions shaded.

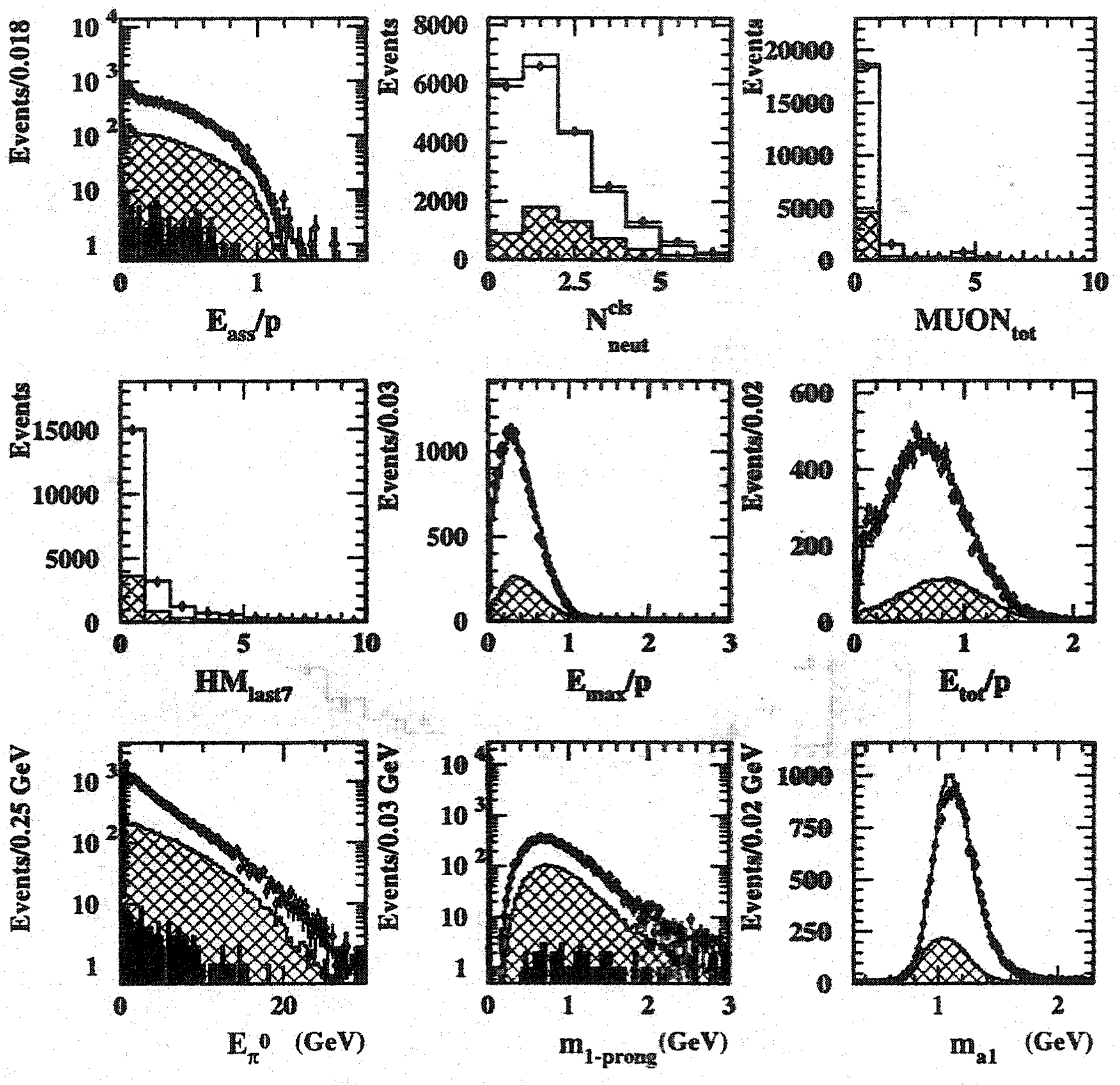

Figure 5.28: The distributions of all $\tau \to a_1\ \nu_\tau$ likelihood variables are given for selected $\tau \to a_1\nu_\tau$ events. The data are represented by the open circles with error bars, while the Monte Carlo signal is given by the open histogram, the tau background contributions shown hatched, and the non-tau contributions shaded.

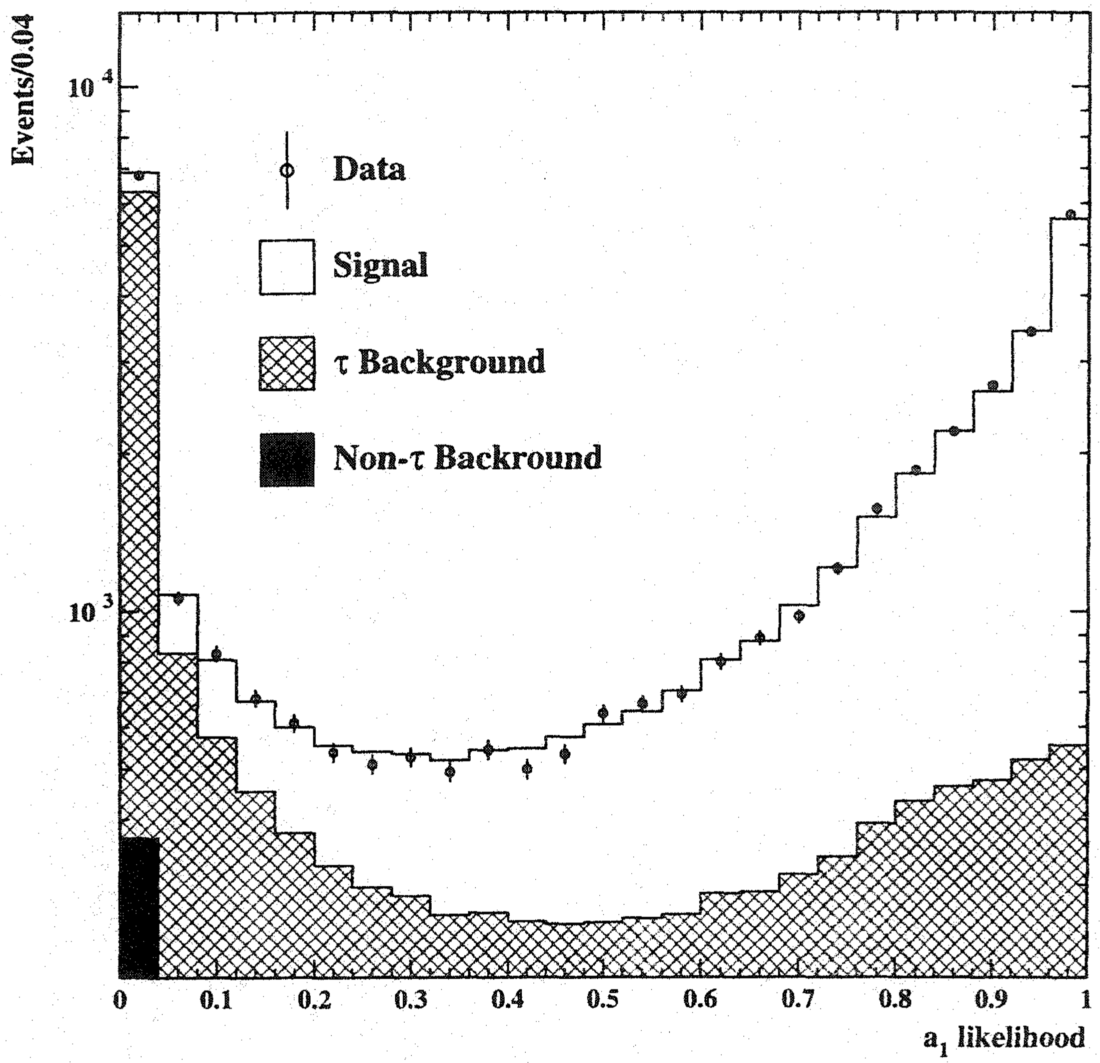

Figure 5.29: Presented is the combined likelihood distribution for the $\tau \rightarrow a_1\nu_\tau$ selection. The data are represented by the open circles with error bars, while the Monte Carlo signal is given by the open histogram, the tau background contributions shown hatched, and the non-tau contributions shaded.

Detailed in Appendix D are a series of additional non-tau background rejection and data quality cuts. The overall effects of these additional cuts are small, but the improved background rejection reduces the potential for systematic errors which might arise from an increased non-tau background contamination.

Monte Carlo studies indicate that the combined effect of these cuts reduces the tau pair selection efficiency by less than 1.5% while reducing $e^+e^- \rightarrow e^+e^-$ and $e^+e^- \rightarrow \mu^+\mu^-$ backgrounds by 35% and 50% respectively.

5.5 Selection Summary

The first part of this chapter outlines the method for selecting tau pair events from the general OPAL Z^0 data set. The selection, over the fiducial acceptance for this analysis, is 89% efficient with an estimated non-tau background of approximately 2%.

In the second part of the chapter, the selection of the five tau decay channels is described. The selection employs a likelihood technique using variables which exhibit discrimination power for identifying events in each of these decay modes. A summary of the selections is given in Table 5.8.

	$\tau \rightarrow e\bar{\nu}_e\nu_\tau$	$\tau \rightarrow \mu\bar{\nu}_\mu\nu_\tau$	$\tau \rightarrow \pi\ \nu_\tau$	$\tau \rightarrow \rho\nu_\tau$	$\tau \rightarrow a_1\ \nu_\tau$
Sample size	44,114	41,300	30,462	67,659	22,145
Efficiency	92%	87%	75%	73%	76%
Background	4.6%	3.3%	26%	29%	24%

Table 5.8: The number of decays in the sample, selection efficiency after tau pair selection within the fiducial acceptance and background for each decay mode selection are shown.

Once this sample of polarization sensitive tau decay events is selected, the next phase is to carry out fits of $\langle P_\tau \rangle$ and A^{FB}_{pol} . This is the focus of the following chapter.

Since the data not only include events generated at the Z^0 resonance peak, but also significant contributions from events collected at distinct off-peak energies, the fit uses separate Monte Carlo samples generated at these energies. The results of separate fits to each energy region are given below, and provide a test of the standard model expectations for the evolution of these parameters away from the Z^0 peak.

6.2 Fitting Procedure

It is not possible to determine the tau helicities on an event by event basis, thus fits to the distributions of polarization sensitive kinematic variables must be carried out to extract measurements of the polarization parameters. In Chapter 2 the appropriate set of kinematic variables for each decay mode is described. For $\tau \rightarrow e\bar{\nu}_e\nu_\tau$ decays, the scaled energy of the electron is used and is estimated in this analysis by the total measured ECAL cluster energy associated to the jet divided by the beam energy. The $\tau \rightarrow \mu\bar{\nu}_\mu\nu_\tau$ and $\tau \rightarrow \pi\, \nu_\tau$ channels use the scaled energy of the charged decay product, x_μ and x_π , which is estimated by the track momentum measured in the CT divided by the beam energy. The additional complexities of the $\tau \rightarrow \rho\nu_\tau$ and $\tau \rightarrow \mathrm{a}_1\, \nu_\tau$ channels are described in Chapter 2 and the optimal variables ω_ρ and ω_{a_1} introduced. The ω_ρ variable is constructed from the measured charged track momentum and the neutral cluster energy designated as arising from the π^0 , while ω_{a_1} is generated from the measured track momenta of the three charged decay products. The functional forms of the omega variables are found in Appendix A and B.

The joint distributions for τ-pair production and decay can be expressed as

$$\begin{aligned}\frac{d^3\sigma_{ij}}{d\cos\theta_{\tau^-}\, dx_i\, dx_j} = {} & \tfrac{3}{16}\sigma_{ij} \sum_{\lambda=\pm1} [(1+\cos^2\theta_{\tau^-} + \tfrac{8}{3}\mathrm{A}_{\mathrm{FB}}\cos\theta_{\tau^-}) + \\ & \lambda(\langle \mathrm{P}_\tau\rangle\,(1+\cos^2\theta_{\tau^-}) + \tfrac{8}{3}\mathrm{A}_{\mathrm{pol}}^{\mathrm{FB}}\cos\theta_{\tau^-})] \times \\ & [F_i(x_i, |\cos\theta_{\tau^-}|) + \lambda G_i(x_i, |\cos\theta_{\tau^-}|)] \\ & [F_j(x_j, |\cos\theta_{\tau^-}|) + \lambda G_j(x_j, |\cos\theta_{\tau^-}|)],\end{aligned} \tag{6.1}$$

where σ_{ij} is the cross-section to produce an $e^+e^- \rightarrow \tau^+\,\tau^-$ event in which one τ decays via channel i and the other via channel j. The first two lines of Equation 6.1 refer to the

Chapter 6

Fitting Procedure and Results

"The advantage of the emotions is that they lead us astray, the advantage of science is that it is not emotional" - Oscar Wilde

---

6.1 Introduction

In order to extract the estimates for $\langle P_\tau \rangle$ and $A_{\mathrm{pol}}^{\mathrm{FB}}$ from the data, Monte Carlo simulated reference distributions are used. A binned maximum likelihood fit is employed, fitting linear combinations of left-handed and right-handed Monte Carlo tau pair events, binned as a function of $\cos\theta$ and of the appropriate polarization sensitive variable. Minimization of the negative log of the likelihood distribution is carried out via the MINUIT software package [52].

A 'global combined' fit to all data collected at all energies, and including all five tau decay channels selected, is performed to extract the final measured values. Fits to separate detector $\cos\theta$ regions, to each of the five channels, and to each of the twenty tau pair identification classes, provide internal consistency checks on the measurements and are presented below along with the global fit values.

production of the τ-pairs while the third and fourth lines correspond to the τ decays. The summation over λ indicates that the summation is over positive and negative helicities. The symbol x_i represents the kinematic variable corresponding to channel i; x_e , x_μ , x_π , ω_ρ, or ω_{a_1} . The decay distributions for positive-helicity τ leptons are given by F_i+G_i and for negative-helicity taus by $F_i - G_i$. F_i and G_i represent the functions of x_i described in Chapter 2 as modelled by the Monte Carlo simulation and include the effects of the selection procedure, detector response, and radiation.

It is important to note that Equation 6.1, which is a function of $\cos\theta_{\tau^-}$ and the x_i and x_j variables, automatically includes the correlation between the decay distributions of the two τ leptons when analyzing events in which both τ's are identified as decaying via one of the five selected channels. If only one of τ's is so identified, the last line of Equation 6.1 is omitted and the distributions are a function of $\cos\theta_{\tau^-}$ and x_i only.

A binned maximum likelihood fit is performed to simultaneously extract $\langle \mathrm{P}_\tau \rangle$ and $\mathrm{A}_{\mathrm{pol}}^{\mathrm{FB}}$ by fitting the linear combination of the positive and negative helicity Monte Carlo distributions to the data. The values of x_i, x_j and $\cos\theta_{\tau^-}$ for each event are calculated and histograms filled with ten bins in $\cos\theta_{\tau^-}$ and ten bins in x_i for each $\sqrt{\mathrm{s}}$. A value for $\cos\theta_{\tau^-}$ is determined by averaging the measured $\cos\theta$ value for the τ^- cone with the negative of the $\cos\theta$ value for the τ^+ cone.

A separate set of histograms is filled for each combination of decay channel pairs. Since the kinematical distribution, for a given channel, of a completely right-handed set of τ^+ decays is assumed to be identical to the distribution of completely left-handed τ^- decays and vice versa, the τ^- and τ^+ decays for a given channel are binned together.

If only one τ decay is identified, then only bins in x_i and $\cos\theta_{\tau^-}$ are filled. The same procedure is performed for the Monte Carlo with a separate set of histograms filled for the positive and negative helicity τ events, binned in x_i, x_j and $|\cos\theta_{\tau^-}|$. This provides the product $[F_i + \lambda G_i][F_j + \lambda G_j]$ as a function of $|\cos\theta_{\tau^-}|$ in the Monte Carlo, which takes advantage of the fact that the detector is symmetric in $\cos\theta$. As a consequence, the forward and backward hemispheres use the same Monte Carlo sample and the correlations in the Monte Carlo samples result in a reduced Monte Carlo statistical error on $\mathrm{A}_{\mathrm{pol}}^{\mathrm{FB}}$.

The Monte Carlo statistics are taken into account in the likelihood fit in the manner described in Reference [53]. In order to identify the contribution to the total error arising from the data statistical error only, a second fit is performed which does not take into account the Monte Carlo statistical errors. The Monte Carlo statistical error is estimated from the quadratic difference between the error from the fit taking into account both data and Monte Carlo statistical errors and the error from the fit when only the data errors are taken into account. The Monte Carlo statistical error is quoted as part of the systematic error of the polarization results.

The effects on the measured polarization arising from misidentified τ decays are modelled by the Monte Carlo simulation. The helicity dependence of the misidentified decays is automatically taken into account in the product $[F_i + \lambda G_i][F_j + \lambda G_j]$. Contributions from the small non-τ background are estimated using Monte Carlo simulations of distributions in the relevant kinematic variables. As there is no helicity dependence in this background, these distributions are added to the linear combination of the right-handed and left-handed τ decay Monte Carlo distributions to form the complete reference distributions used in the fit.

The fit also depends on $\mathrm{A_{FB}}$ for which the measured value in the $\mathrm{Z^0} \to \tau^+\tau^-$ channel [15] at the appropriate $\sqrt{s}$ is used. Separate distributions for the different values of $\sqrt{s}$ are used in order to account for the $\mathrm{A_{FB}}$ dependence, but a single fit for $\langle \mathrm{P}_\tau \rangle$ and $\mathrm{A^{FB}_{pol}}$ is performed. Although there are potential dependences of the observables in the analysis on the exact value of $\sqrt{s}$ at which the data were collected, the use of beam-energy normalized observables renders the analysis relatively insensitive to such effects. However, in order to further reduce any such dependences, the data collected with $\sqrt{s}$ below 90.7 GeV and above 91.7 GeV are analyzed using Monte Carlo samples generated at fixed centre-of-mass energies where most of the off-peak data were collected. The off-peak data were collected with values of $\sqrt{s}$ within 0.2 GeV of the values used in the Monte Carlo generation.

6.3 Polarization Asymmetry Fit Results

The results of the global fit for $\langle P_\tau \rangle$ and A_{pol}^{FB}, including all five decay channels with data collected at all energies, are

$$\begin{aligned} \langle P_\tau \rangle &= (-14.10 \pm 0.73 \pm 0.55)\% \\ A_{pol}^{FB} &= (-10.55 \pm 0.76 \pm 0.25)\%, \end{aligned} \tag{6.2}$$

where the first error is statistical and the second systematic. The details regarding the estimation of the systematic errors are provided in the following chapter.

The statistical correlation between the two parameters is 0.7% and the total correlation, including both statistical and systematic correlations, is 2.5%. Although this result combines data collected at a number of different centre-of-mass energies, it can be treated to a very good approximation as though it were all collected at a single effective centre-of-mass energy of 91.30 GeV.

Figure 6.1 depicts the variation of P_τ as a function of $\cos\theta_{\tau^-}$ given by Equation 2.19 when the global fit values for $\langle P_\tau \rangle$ and A_{pol}^{FB} are used. Overlayed on the curve are fit values for the polarization in ten statistically independent $\cos\theta_{\tau^-}$ bins. The data are separated into the 10 $\cos\theta_{\tau^-}$ bins and a separate fit to P_τ, using all decay channels, is carried out for each $\cos\theta_{\tau^-}$ bin. As may be seen, the individual fits agree well with the global fit results. This may be viewed as a consistency check where it is seen that the results are consistent across the full fiducial acceptance. The fit values and errors for the separate $\cos\theta_{\tau^-}$ fits are also provided in Table 6.1.

$\cos\theta_{\tau^-}$	P_τ	$\cos\theta_{\tau^-}$	P_τ
-0.81	-0.019 ± 0.026	0.09	-0.162 ± 0.024
-0.63	0.003 ± 0.022	0.27	-0.199 ± 0.023
-0.45	-0.036 ± 0.022	0.45	-0.269 ± 0.022
-0.27	-0.099 ± 0.023	0.63	-0.243 ± 0.021
-0.09	-0.094 ± 0.024	0.81	-0.299 ± 0.025

Table 6.1: Listed are the P_τ fit values for each $\cos\theta_{\tau^-}$ bin.

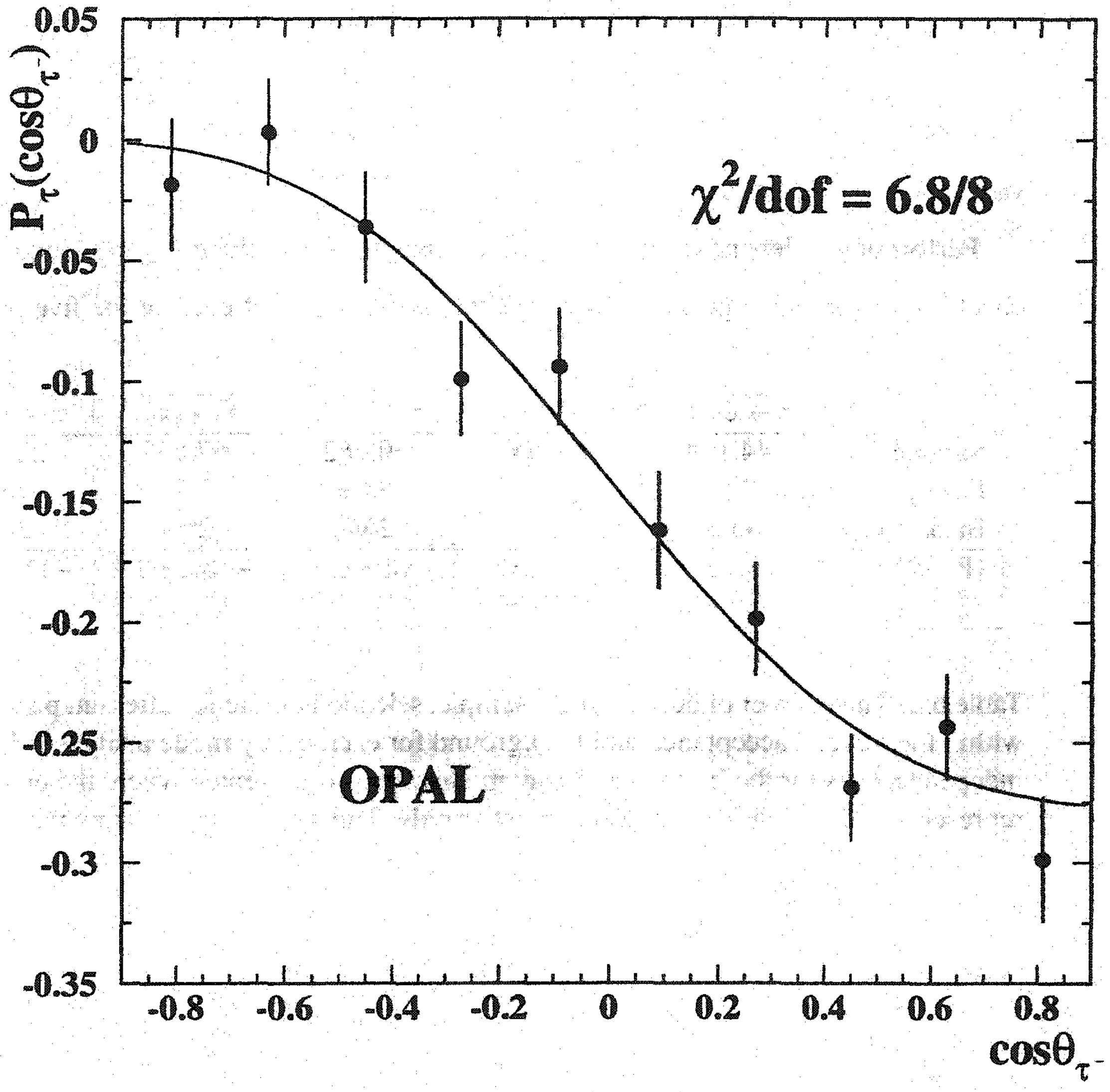

Figure 6.1: Shown is the variation of P_τ as a function of $\cos\theta_{\tau^-}$. The solid curve represents the theoretical variation given by Equation 2.19 when the global fit values for P_τ and A^{FB}_{pol} measured by this analysis are used. The points with error bars represent separate fits to the polarization in each of ten $\cos\theta_{\tau^-}$ bins. As may be seen, there is good agreement between the distribution predicted by the global fit values and the individual $\langle P_\tau \rangle$ fits indicating consistency of the analysis across the full geometric acceptance.

The implications of these global results will be discussed in Chapter 8 while the remainder of this chapter will further examine the internal consistency of the results.

6.4 Consistency Checks

The formulation of the polarization analysis lends itself well to many consistency checks; the most important of these are obtained from a comparison of fit results derived from various subsets of the data.

Performing independent fits to the five separate decay channels constitutes the first check. The results are given in Table 6.2 including details of each of the five selections.

	$\tau \to e\bar{\nu}_e\nu_\tau$	$\tau \to \mu\bar{\nu}_\mu\nu_\tau$	$\tau \to \pi\ \nu_\tau$	$\tau \to \rho\nu_\tau$	$\tau \to \mathrm{a}_1\ \nu_\tau$
Sample size	44,114	41,300	30,462	67,659	22,145
Efficiency	92%	87%	75%	73%	76%
Background	4.6%	3.3%	26%	29%	24%
$\langle P_\tau \rangle$ (%)	-18.7 ± 2.5	-16.4 ± 2.7	-13.8 ± 1.2	-13.2 ± 1.1	-11.7 ± 2.8
A^{FB}_{pol} (%)	-9.0 ± 2.6	-10.5 ± 2.8	-11.4 ± 1.3	-10.6 ± 1.1	-6.9 ± 2.8

Table 6.2: The number of decays in the sample, selection efficiency after tau pair selection within the fiducial acceptance and background for each decay mode analyzed. Results of independent fits for the individual decay modes are also presented where the error quoted represents that arising from the data statistics only. The measurements from the individual channels are correlated and therefore should not be combined in a simple average.

The fits are carried out in the single x_i variable for each channel, without accounting for the internal channel and cross-channel correlations arising from events in which both tau jets are selected. The values obtained for the five different channels are consistent with each other and with the global fit values. A χ^2 of 4.9 for four degrees of freedom is found when comparing the five values of $\langle P_\tau \rangle$ to the value from the global fit and 2.1 for four degrees of freedom when comparing the values of A^{FB}_{pol}.

The distributions of the polarization sensitive variables for each of the decay channels are shown in Figure 6.2. In all cases, the good agreement between the data and Monte Carlo global fit, across the full variable range, indicates the adequacy of the simulation of these variables and demonstrates the good overall consistency between the individual channel fits and the global fit.

The data may also be divided into the twenty statistically independent tau pair identification classes and fit values generated for each case. The results of these fits are shown in Figure 6.3 for $\langle P_\tau \rangle$ and Figure 6.4 for $A_{\rm pol}^{\rm FB}$. Using only statistical errors, the χ^2 probability describing the combined statistical significance comparing the different values to the global fit value is given and signifies good internal agreement for both fit parameters. This internal consistency indicates that the decay selections are not biased for any particular tau pair configuration and that no evidence for uncontrolled non-tau backgrounds exists. The ideograms depicted on these figures represent the sum of the Gaussians from each of the twenty fits and for each parameter. As is evident, the peaks of the ideograms agree well with the global fit values and the shapes are symmetric about the global values.

High statistics internal consistency is also examined for events which have both τ decays classified compared to those where only one τ decay is classified. These comparisons, also shown in Figures 6.3 and 6.4, indicate strong overall internal consistency of the results.

A non-negligible amount of data is collected off-peak; thus measurements of $\langle P_\tau \rangle$ and $A_{\rm pol}^{\rm FB}$ are also performed separately for data collected at centre-of-mass energies below, on, and above the Z^0 resonance peak. The three statistically independent measurements are quoted in Table 6.3. In order to compare the consistency between these measurements, they must be converted into measurements of A_τ or A_e using the technique described in Chapter 2. These asymmetry values, also quoted in Table 6.3, are consistent with each other. Because the conversions from $\langle P_\tau \rangle$ to A_τ and from $A_{\rm pol}^{\rm FB}$ to A_e assume the standard model centre-of-mass dependence of $\langle P_\tau \rangle$ and $A_{\rm pol}^{\rm FB}$, the agreement between the A_τ and A_e values in Table 6.3 indicates that the data are consistent with the standard model expectations for this centre-of-mass dependence.

Since data has been collected over a six year period, during which the detector configuration has changed, it is important to demonstrate that fits to data collected in each separate year produce polarization results consistent with the combined result. For data

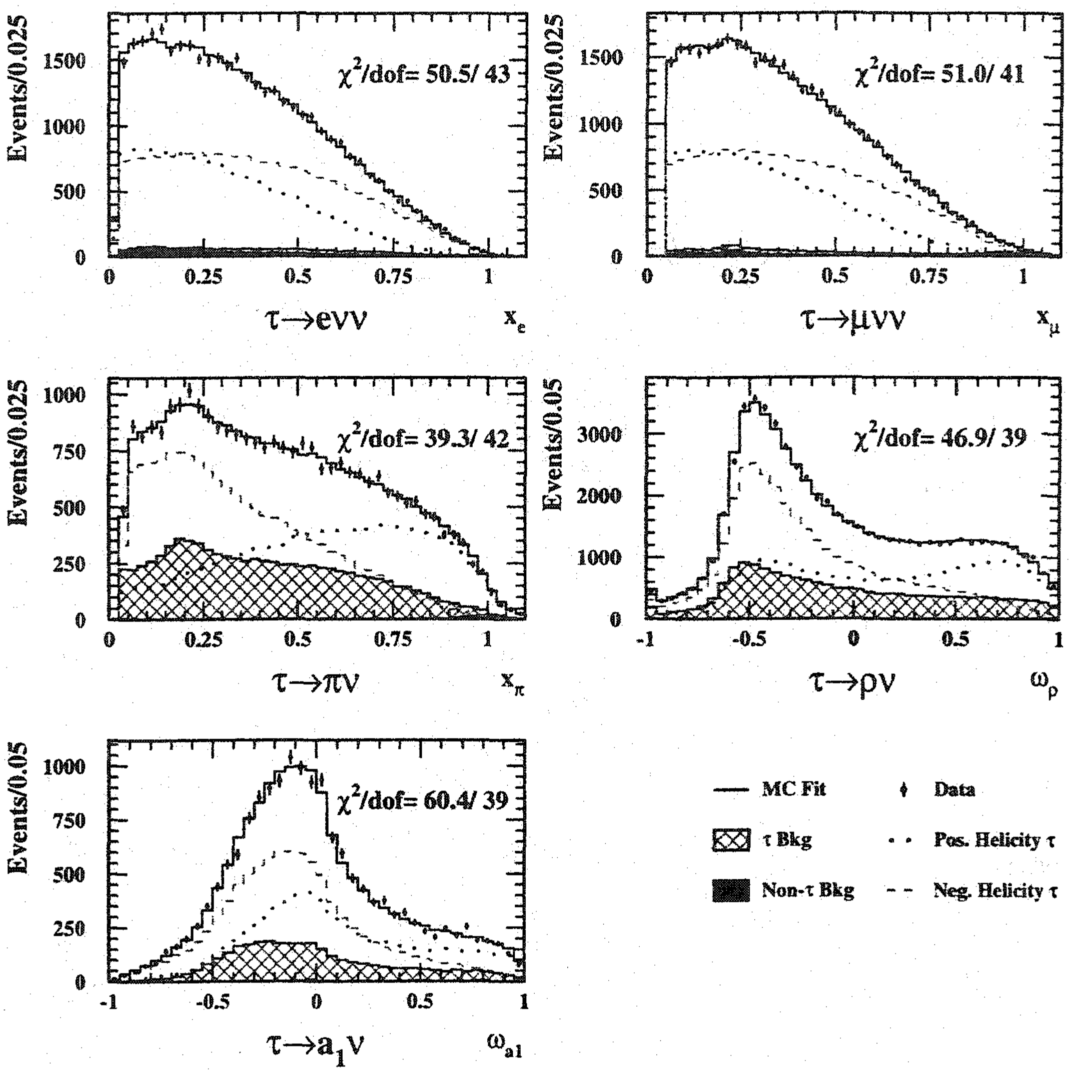

Figure 6.2: Distributions in the kinematic variables used in the fits as discussed in the text for the $\tau \rightarrow e\bar{\nu}_e\nu_\tau$, $\tau \rightarrow \mu\bar{\nu}_\mu\nu_\tau$, $\tau \rightarrow \pi\ \nu_\tau$, $\tau \rightarrow \rho\nu_\tau$, and $\tau \rightarrow a_1\ \nu_\tau$ channels where the data, shown by points with error bars, are integrated over the whole $\cos\theta_{\tau^-}$ range. Overlaying these distributions are Monte Carlo distributions for the positive (dotted line) and negative (dashed line) helicity τ leptons and for their sum including background, assuming a value of $\langle P_\tau \rangle = -14.10\%$ as reported in the text. The hatched histogram represent the Monte Carlo expectations of contributions from cross-contamination from other τ decays and the dark shaded histogram the background from non-τ sources. The level of agreement between the data and Monte Carlo distributions is quantified by quoting the χ^2 and the number of degrees of freedom.

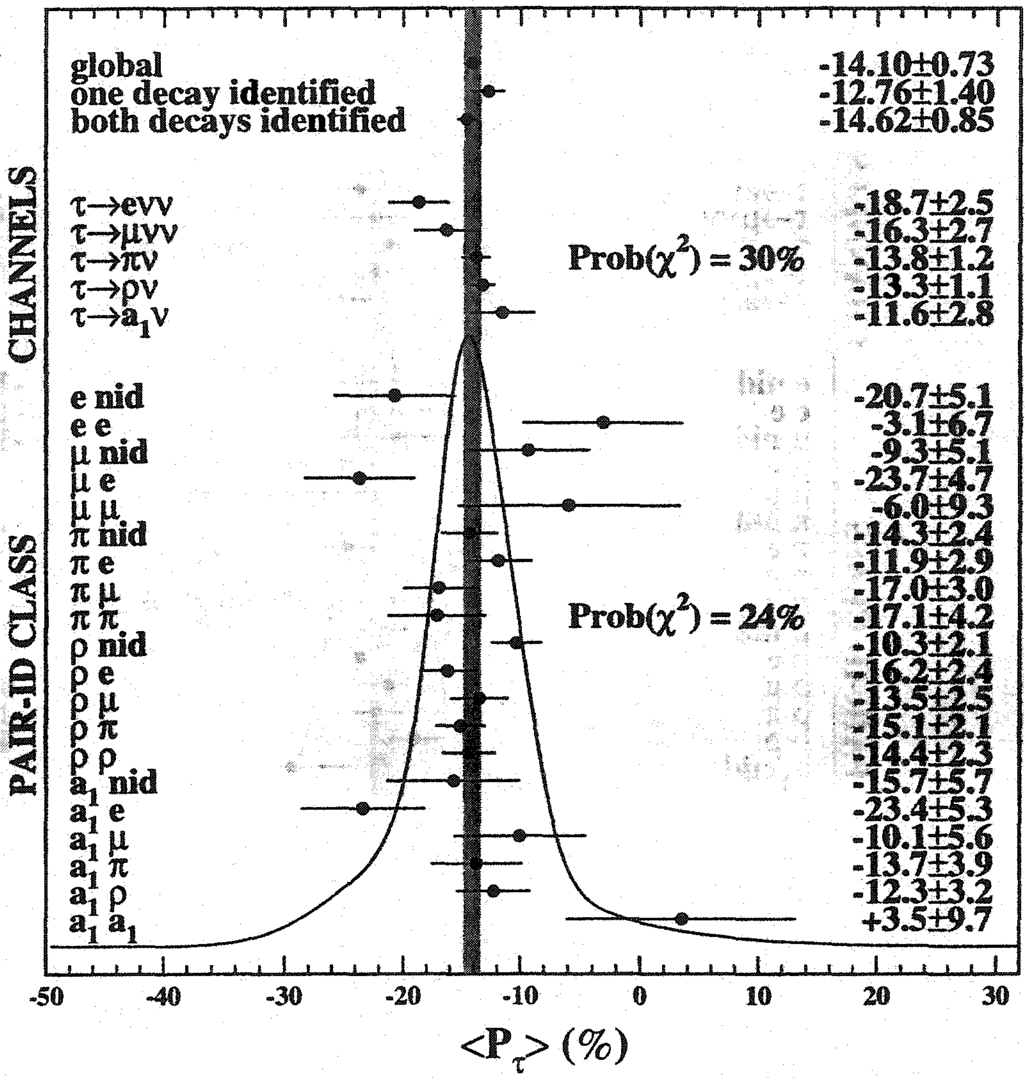

Figure 6.3: Internal consistency of the $\langle P_\tau \rangle$ results investigated as a function of the number of τ decays classified in the event and by pair-identification class. The ideogram formed from the sum of the individual Gaussians is superimposed on the pair-identification results. The χ^2 probabilities of the spreads about the global fit value are shown for each subsample and show good internal consistency in all cases. The label 'nid' refers to the case where the τ decay is not identified.

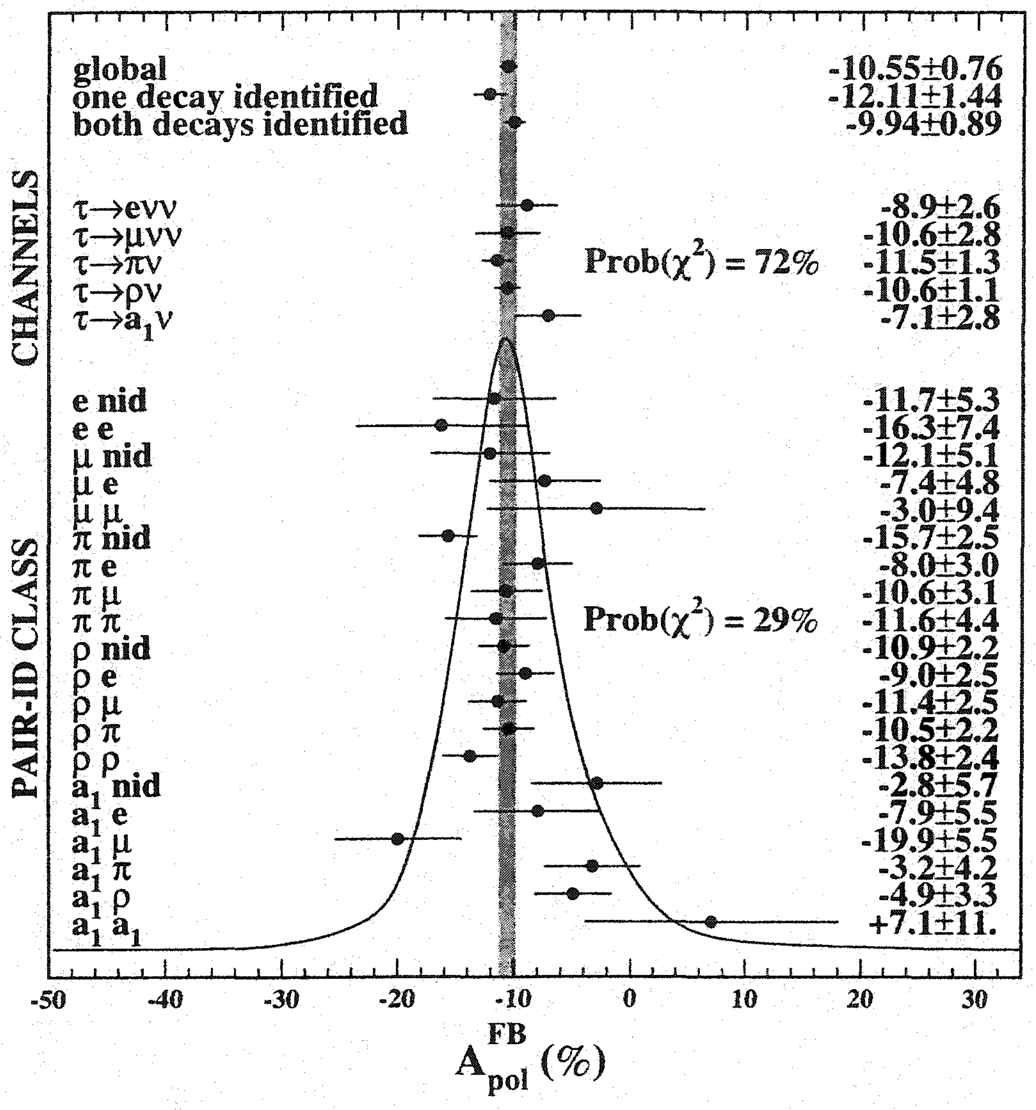

Figure 6.4: Internal consistency of the A_{pol}^{FB} results investigated as a function of the number of τ decays classified in the event and by pair-identification class. The ideogram formed from the sum of the individual Gaussians is superimposed on the pair-identification class results. The χ^2 probabilities of the spreads about the global fit value are shown for each subsample and show good internal consistency in all cases. The label 'nid' refers to the case where the τ decay is not identified.

$\sqrt{s}$ (GeV)	$\langle P_\tau \rangle$ (%)	A^{FB}_{pol} (%)	A_τ	A_e
89.5 ± 0.2	-15.9 ± 3.3	-8.0 ± 3.4	0.186 ± 0.039	0.125 ± 0.040
91.25 ± 0.05	-13.52 ± 0.78	-10.52 ± 0.81	0.1393 ± 0.0081	0.145 ± 0.011
93.0 ± 0.2	-18.1 ± 2.9	-11.3 ± 3.0	0.176 ± 0.028	0.146 ± 0.040

Table 6.3: Global fit values of $\langle P_\tau \rangle$ and A^{FB}_{pol} for data collected below, on and above the Z^0 resonance peak. The luminosity weighted values of $\sqrt{s}$ are quoted in the first column where the error reflects the spread in $\sqrt{s}$ values of the data combined in each fit. The neutral current asymmetry parameters with their statistical errors, based on the data collected at the different centre-of-mass energies, are also quoted.

collected at peak energies, Figure 6.5 shows the results of such fits for both $\langle P_\tau \rangle$ and A^{FB}_{pol} compared to the combined result; consistency across the data set is evident.

In analogy to the study of data collected during different operating years, in it also necessary to establish that Monte Carlo runs generated with different versions of the OPAL detector simulation software provide consistent polarization results. Figure 6.6 presents fits for $\langle P_\tau \rangle$ and A^{FB}_{pol} to the full data set using each of the four Monte Carlo runs. It is clear from these plots that the separate Monte Carlo runs produce consistent polarization results with no significant variations between runs apparent.

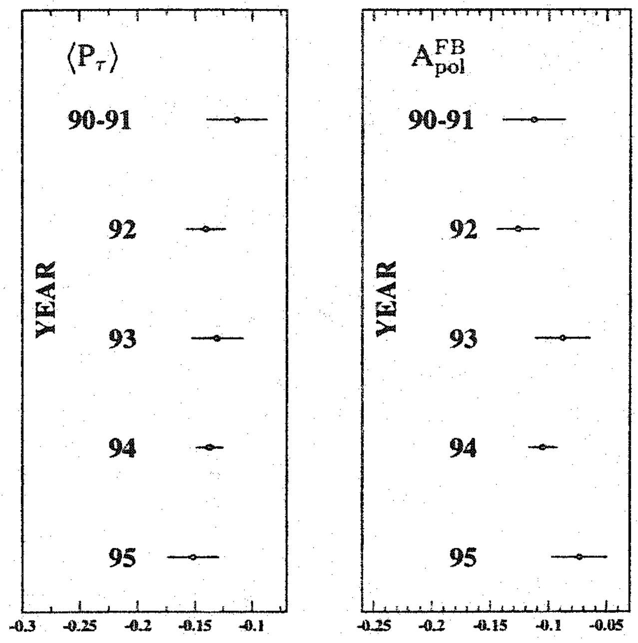

Figure 6.5: Separate fits to $\langle P_\tau \rangle$ and $A_{\rm pol}^{\rm FB}$ for each of the data years are presented for peak data only. The figures show consistency across all years of data taking.

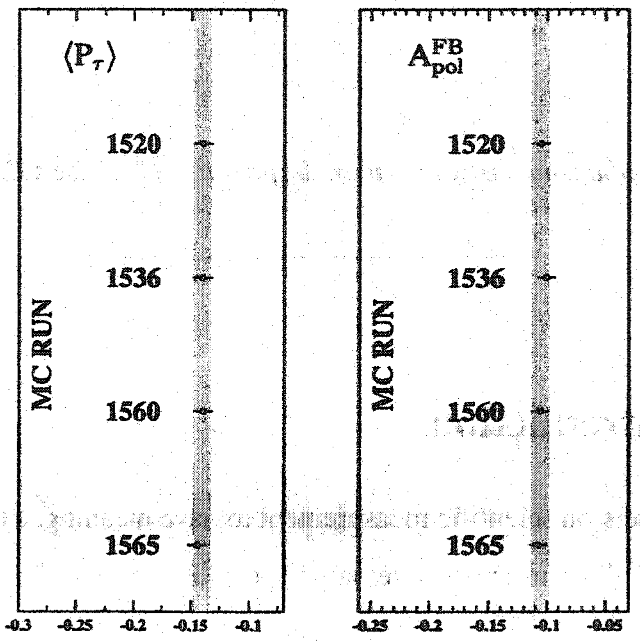

Figure 6.6: Separate fits to $\langle P_\tau \rangle$ and A^{FB}_{pol} using each of the Monte Carlo sets are presented. The figures show consistency for the separate fits indicating that the analysis is not sensitive to the specific Monte Carlo generation employed.

Chapter 7

Systematic Studies

"The habit of despair is worse than despair itself." Albert Camus

---

7.1 Introduction

For any precision scientific measurement to have meaning, a thorough quantitative understanding of all significant systematic effects is required. In this analysis, owing to both the complexity of the measurement and the intricacies of the OPAL detector, a multitude of potential systematic error sources must be examined. These studies may be roughly divided into three classes.

First to be considered are errors arising from an imperfect understanding of the operation of the OPAL sub-detectors. Since the analysis relies heavily on the use of Monte Carlo simulated events, both for the event selection and actual extraction of the parameter estimates, this class of systematic study requires a thorough examination of how well the Monte Carlo simulation, including detector effects, models the data. Examples of these studies include an examination of the momentum resolution and scale uncertainties of the CT measurements, investigation of the performance and modelling of the electromagnetic detector, and determination of the uncertainties associated with the response of the outer detectors.

The second type of systematic errors investigated are somewhat roughly termed here as physics modelling uncertainties. These include the effects of errors on measured quantities used as input to the analysis, such as the tau decay branching ratios and A_{FB} , and effects which arise from an imperfect understanding of the underlying physics, such as $\tau \rightarrow a_1 \nu_\tau$ decay modelling and decay radiation.

The remaining systematic studies do not, in general, give rise to systematic errors, and are composed of the large number of consistency checks, including those described in the previous chapter, that are carried out.

In order to estimate the systematic uncertainties arising from the first two classes, the methodology employed here consists of applying corrections to the Monte Carlo events representative of the uncertainty associated with a given quantity, propagating these effects from the selection through to the generation of the Monte Carlo fit distributions, and fitting to the unchanged data to generate new $\langle P_\tau \rangle$ and A_{pol}^{FB} parameter estimates. The difference between these new estimates and the nominal values is quoted as the systematic uncertainty associated with the quantity under investigation.

7.2 Detector Simulation

The simulation of OPAL detector effects is applied to Monte Carlo four vector events via a software package based on the GEANT simulation code [36]. This package contains the OPAL detector geometry and simulates the interaction of particles with detector material [35].

Data from OPAL technical specifications, test beam studies, and online performance have been used to generate and subsequently improve the simulation, but the modelling remains, of course, imperfect. For a given analysis, measurement uncertainties associated with this modelling can lead to systematic effects which must be evaluated and accounted for in an appropriate fashion.

The detector related uncertainties of greatest importance to this analysis are those associated with track measurements in the central tracking chambers and measurements of energy deposits in the ECAL. Small additional uncertainties from the modelling of the outer detectors must also be evaluated. For each case, various control samples are utilized in order to estimate the degree of modelling uncertainty.

7.2.1 Central Tracking

Accurate determination of track momenta in the central tracking chambers is crucial to the polarization measurement. Not only is track momentum used as the polarization sensitive variable for two of the decay channels, including the most sensitive $\tau \rightarrow \pi \nu_\tau$ channel, but track information is also incorporated into many of the likelihood selection variables.

Track momenta are measured at OPAL via the effects of the OPAL magnetic field on charged particle trajectories. The relationship between particle momentum p, track polar angle θ, radius of curvature R, and magnetic field strength B is given by

$$\mathrm{p} \sin\theta = \mathrm{kBR} \tag{7.1}$$

where k approximately depends only on the particle charge. From Equation 7.1 it can be seen that momentum measurement effects may be separated into those associated with the radius of curvature measurement, which is proportional to the transverse component of the momentum, and those arising from measurement of the polar angle.

Data and Monte Carlo muon pair events, with momenta near 45.6 GeV, are used to generate transverse momentum calibration corrections in order to improve the Monte Carlo simulation. A Gluckstern [54] formulation is employed to evolve the calibration to lower momenta with the assumption that the effects of multiple scattering, which dominate for low energy tracks, are well modelled. This assumption is tested with low momentum control samples such as two-photon events. Correction factors are applied both to the relative momentum scale and the resolution of the Monte Carlo as a function of track type, track charge, $\cos\theta$, and data taking year.

In order to evaluate the level of agreement between Monte Carlo and data for high energy tracks, subsequent to all corrections, muon pair events are re-examined. Figure

7.1 gives sample plots of the difference between the reciprocal of the transverse track momentum and the reciprocal of the beam energy scaled by $\sin\theta$ of the track for both Monte Carlo and data in each of the three detector regions. Overlayed on both plots are Gaussian fits to the distributions. A comparison of the mean and standard deviation parameters from these fits provides an indication of the accuracy with which the relative momentum scale and momentum resolution, respectively, are modelled.

For lower track energies, examination of $\gamma\gamma\mu^+\mu^-$events; the ρ resonance contribution to 3-prong $\tau\rightarrow$ a_1 ν_τ decays; and the K^0mass peak from both $e^+e^-\rightarrow$ $q\bar{q}$ and tau decay events, all provide confirmation of the estimated levels of uncertainty. Figures 7.2 and 7.3 show data and Monte Carlo $\gamma\gamma\mu^-\mu^-$distributions which indicate that the resolution estimates, summarized below, are consistent with those determined from the muon pair samples.

To extract the global shift values, each of the separate Monte Carlo runs is compared to the data using the described control samples. Figures 7.4 and 7.5 show, for muon pairs and $\gamma\gamma\mu^+\mu^-$events respectively, the differences between the data and each of the Monte Carlo runs with the level of systematic shift applied indicated by the dotted vertical lines. These plots justify the level of shifts applied and validate the corresponding systematic errors assigned.

Table 7.1 summarizes the estimated transverse momentum scale and resolution uncertainties. In order to determine the systematic effects on the measurement of $\langle P_\tau \rangle$ and A^{FB}_{pol}, shifts reflecting these uncertainties are applied to all Monte Carlo events and the analysis is re-run. The differences between the nominal $\langle P_\tau \rangle$ and A^{FB}_{pol} global fit values and those obtained by fitting with the reference distributions from the systematically shifted Monte Carlo events are also given in Table 7.1. The systematic shifts are applied both as an increase and decrease, but only the absolute values of the largest change in each of $\langle P_\tau \rangle$ and A^{FB}_{pol}, for the resolution and momentum scale separately, contribute to the total systematic error quoted. As may be seen, the uncertainty on the relative momentum scale dominates this contribution to the systematic error. Included in Table 7.1 are the shifts in the $\langle P_\tau \rangle$ and A^{FB}_{pol} fit values for each of the separate decay channels. Not surprisingly, the

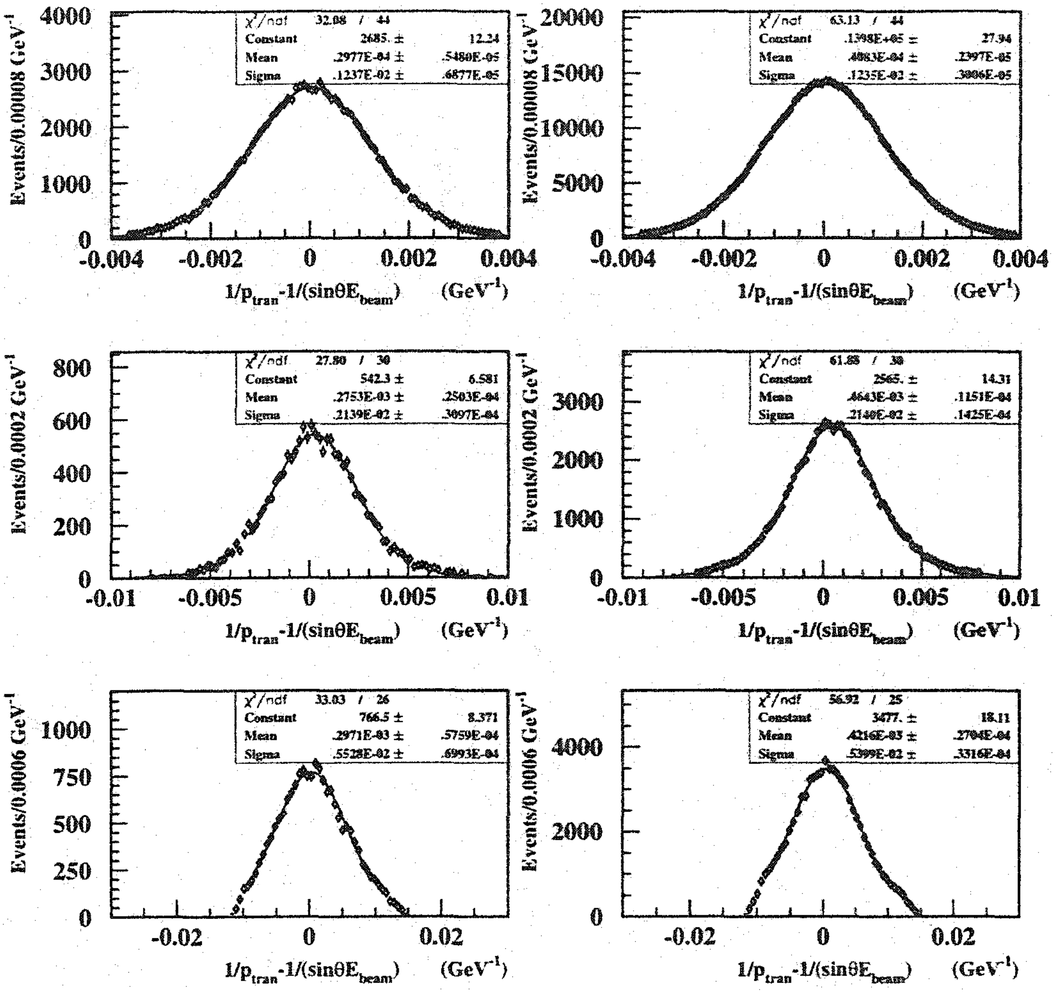

Figure 7.1: Shown are distributions of $1/p_{tran} - 1/\sin\theta E_{beam}$, where p_{tran} is the transverse track momentum, for muon pair events for data (left) and Monte Carlo (right). The top plots correspond to the barrel region of the detector, the middle plots to the overlap regions, and at the bottom to the endcap region. A Gaussian fit to each distribution is overlayed with the estimated fit parameters listed at the top right corner for each plot.

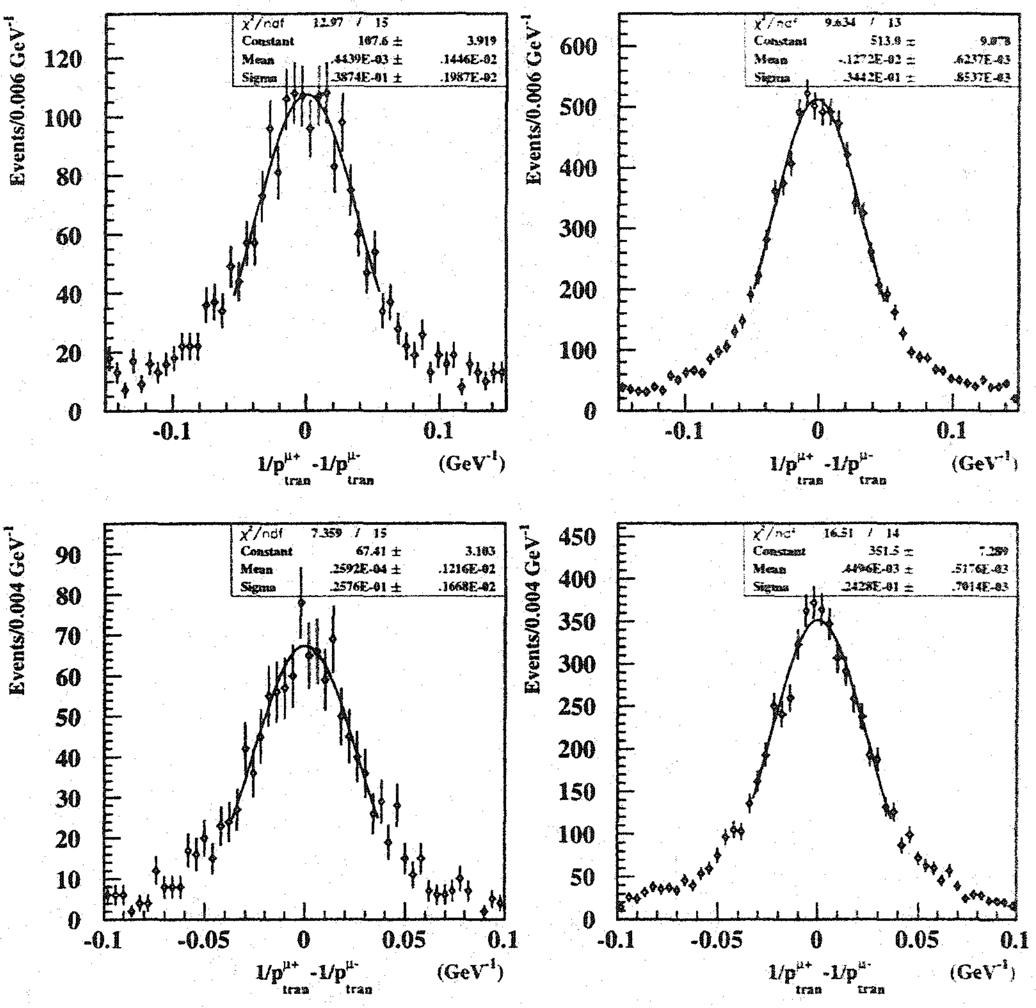

Figure 7.2: Plots of $1/\mathrm{p}_{\mathrm{tran}}^{\mu^+} - 1/\mathrm{p}_{\mathrm{tran}}^{\mu^-}$ for $\gamma\gamma\mu^+\mu^-$events are depicted for data (left) and Monte Carlo (right). All figures represent events in the barrel region of the detector. The figures at the top correspond to events in which the average muon momentum is between 0.25 and 0.5 GeV while the figures at the bottom correspond to an average muon momentum between 0.5 and 0.725 GeV.

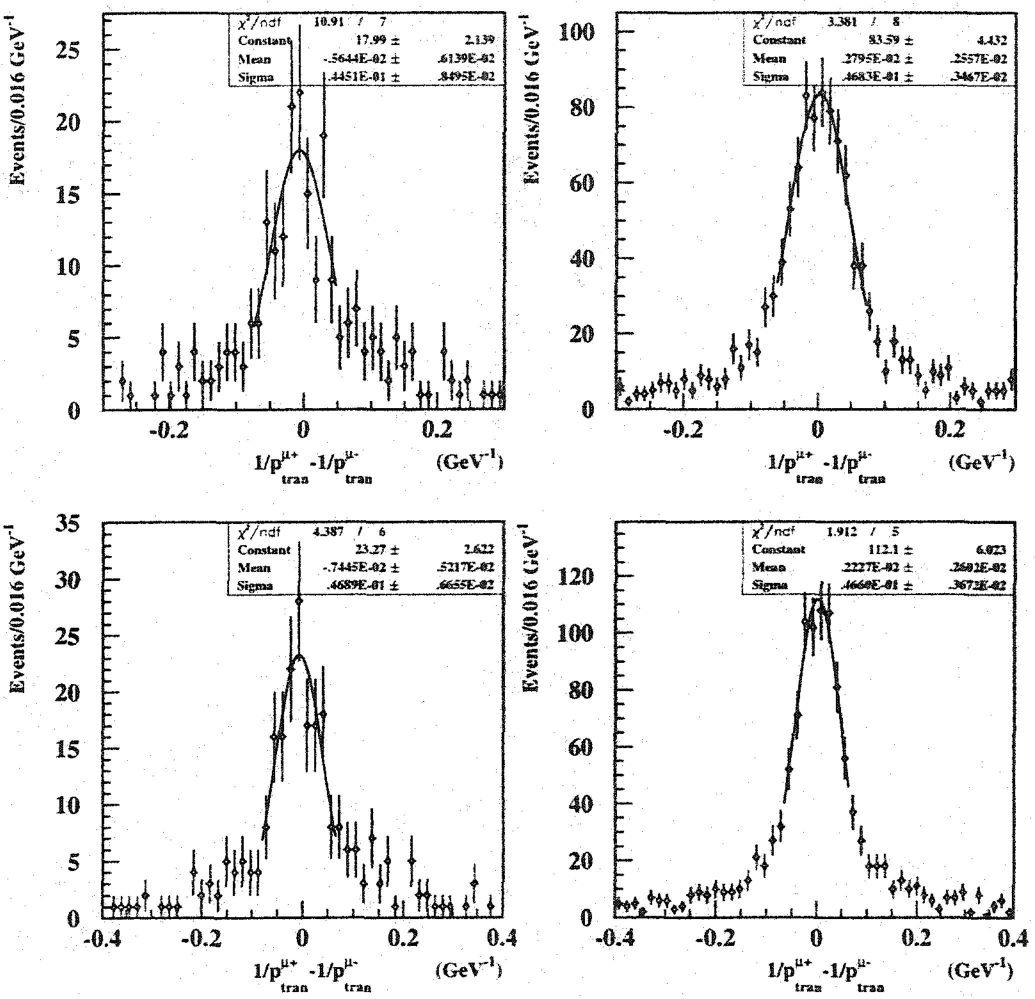

Figure 7.3: Data (left) and Monte Carlo (right) $\gamma\gamma\mu^+\mu^-$distributions of $1/\mathrm{p}_{\mathrm{tran}}^{\mu^+} - 1/\mathrm{p}_{\mathrm{tran}}^{\mu^-}$ are presented for the overlap (top) and endcap (bottom) regions of the detector. In all cases, the average muon momentum is required to be between 0.5 and 1. GeV.

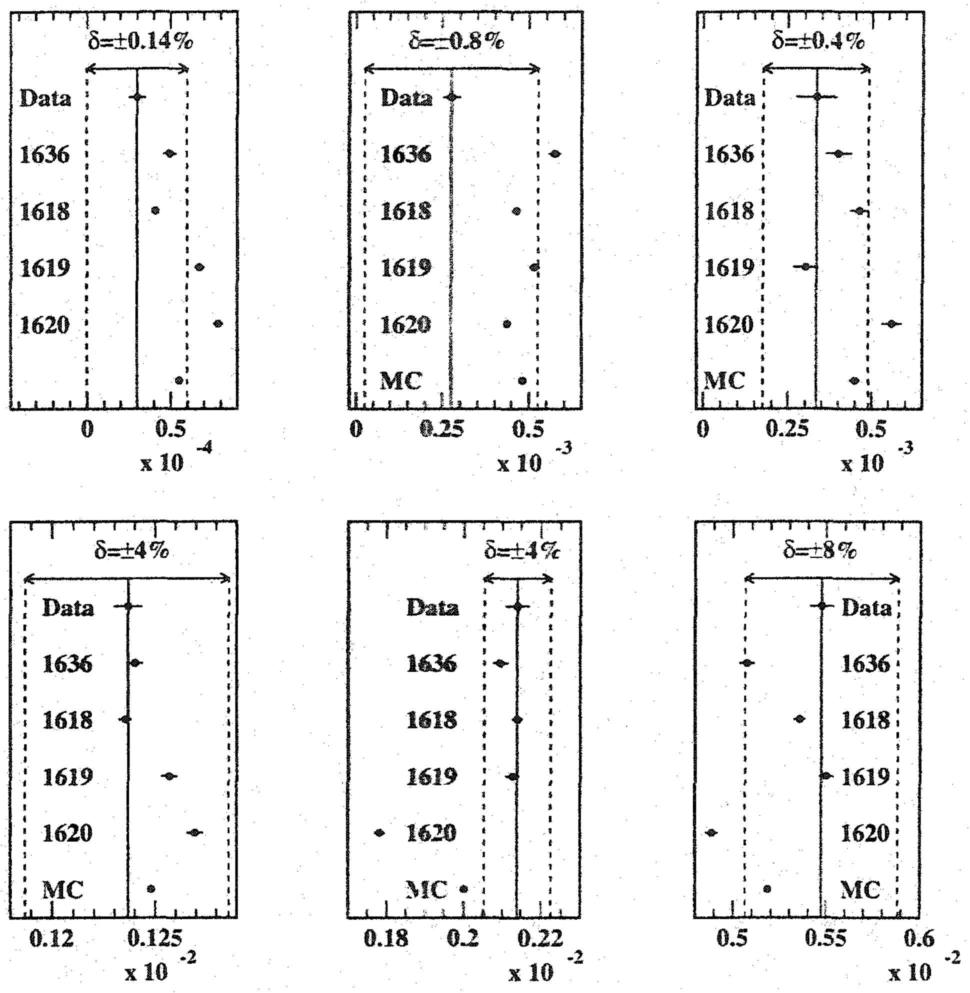

Figure 7.4: Shown are the means (top) and estimated standard deviations (bottom) for data and Monte Carlo $e^+e^- \rightarrow \mu^+\mu^-$ distributions of $1/p_{tran} - 1/\sin\theta E_{beam}$ in the barrel (left), overlap (middle), and endcap (right) detector regions. The vertical dotted lines indicate the level of systematic shift applied to the Monte Carlo for the determination of systematic errors associated with momentum modelling.

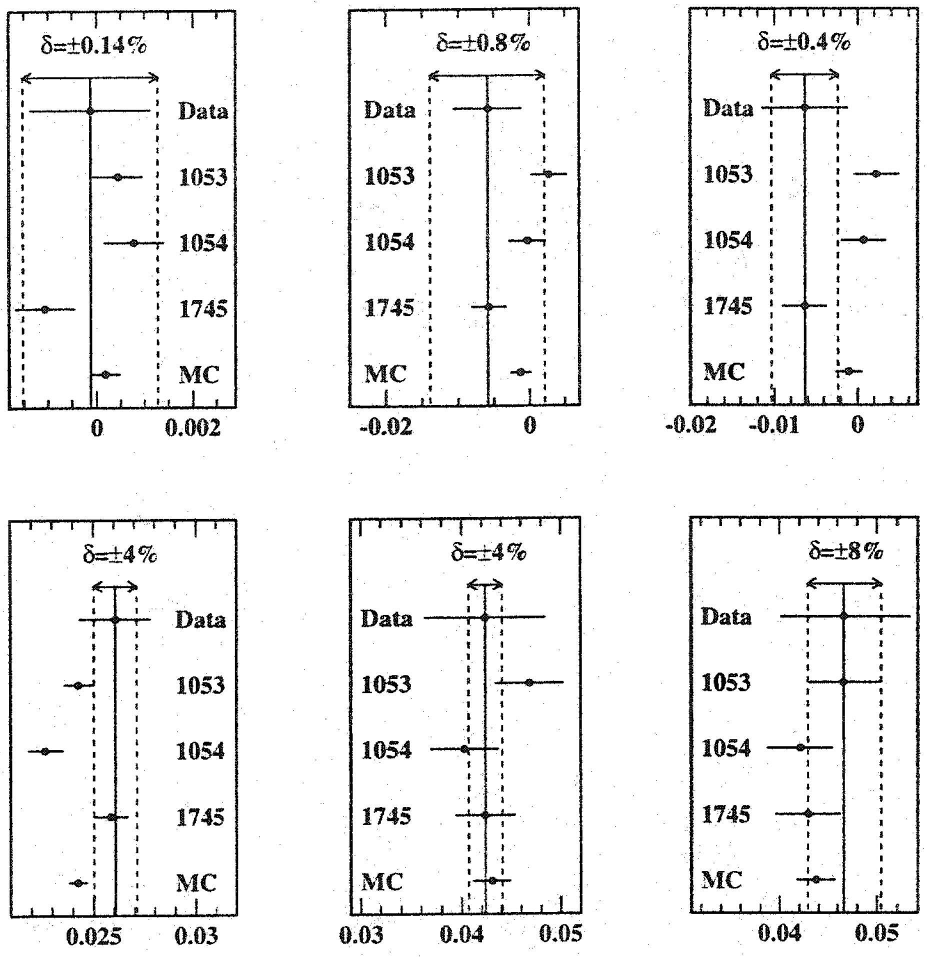

Figure 7.5: Shown are the means (top) and estimated standard deviations (bottom) for data and Monte Carlo $\gamma\gamma\mu^+\mu^-$ distributions of $1/\mathrm{p}_{\mathrm{tran}}^{\mu^+} - 1/\mathrm{p}_{\mathrm{tran}}^{\mu^-}$ in the barrel (left), overlap (middle), and endcap (right) detector regions. The vertical dotted lines indicate the level of systematic shift applied to the Monte Carlo for the determination of systematic errors associated with momentum modelling.

Systematic Effect	Barrel	Overlap	Endcap	$\Delta\langle \mathrm{P}_\tau\rangle$	$\Delta\ \mathrm{A}^{\mathrm{FB}}_{\mathrm{pol}}$
a) Scale Increase	0.14%	0.8%	0.4%	0.20	0.04
b) Scale Decrease	0.14%	0.8%	0.4%	-0.16	0.05
c) Resolution Increase	+4%	+4%	+8%	0.00	0.08
d) Resolution Decrease	-4%	-4%	-8%	0.08	0.01

	$\tau\to e\bar{\nu}_e\nu_\tau$		$\tau\to \mu\bar{\nu}_\mu\nu_\tau$		$\tau\to \pi\ \nu_\tau$		$\tau\to \rho\nu_\tau$		$\tau\to \mathrm{a}_1\ \nu_\tau$	
	ΔP_τ	ΔA^{FB}_{pol}	ΔP_τ	ΔA^{FB}_{pol}	ΔP_τ	ΔA^{FB}_{pol}	ΔP_τ	ΔA^{FB}_{pol}	ΔP_τ	ΔA^{FB}_{pol}
a)	0.07	0.09	-10.94	-0.07	0.70	0.08	0.21	0.02	0.00	0.02
b)	-0.15	0.06	20.09	0.12	-0.82	-0.04	-0.03	0.05	-0.03	-0.04
c)	-0.07	0.06	0.26	-0.02	-0.11	0.06	0.04	0.10	-0.17	0.01
d)	-0.24	-0.15	-0.16	-0.04	0.07	-0.02	0.16	0.08	0.04	0.00

Table 7.1: The transverse momentum systematic uncertainty shifts for both the relative momentum scale and resolution are given in the first table. The corresponding uncertainties on the $\langle \mathrm{P}_\tau\rangle$ and $\mathrm{A}^{\mathrm{FB}}_{\mathrm{pol}}$ global fit values, expressed in percent polarization, are also presented. Shown in the second table are the channel-by-channel uncertainties in $\langle \mathrm{P}_\tau\rangle$ and $\mathrm{A}^{\mathrm{FB}}_{\mathrm{pol}}$ for each of these transverse momentum studies.

greatest effects occur in the $\tau\to \mu\bar{\nu}_\mu\nu_\tau$ and $\tau\to \pi\ \nu_\tau$ channels for which the polarization is measured directly from the momentum distributions.

Equation 7.1 indicates that the momentum measurements also depend on the accuracy with which the polar angle of the track trajectory is measured; thus systematic studies of the measurement of this quantity must also be carried out.

Comparison of $|\cos\theta_{\mu^-}\ | - |\cos\theta_{\mu^+}\ |$ distributions for muon pairs, where $\cos\theta_{\mu^-}$ and $\cos\theta_{\mu^+}$ are the measured polar angles of the $\mu^-$and μ^+tracks respectively, are examined to determine the level of agreement between data and Monte Carlo. Figure 7.6 presents sample plots of these distributions, including Gaussian fits to both data and Monte Carlo. Although the discrepancy in resolution between data and Monte Carlo in the barrel region of the detector appears large, it will be seen that this effect does not significantly increase the overall systematic error. This is simply because the large modelling discrepancy only occurs for tracks with CZ hits, and such tracks have well measured polar angles. Hence a large relative difference in resolution is, in fact, only a small effect on a well measured quantity.

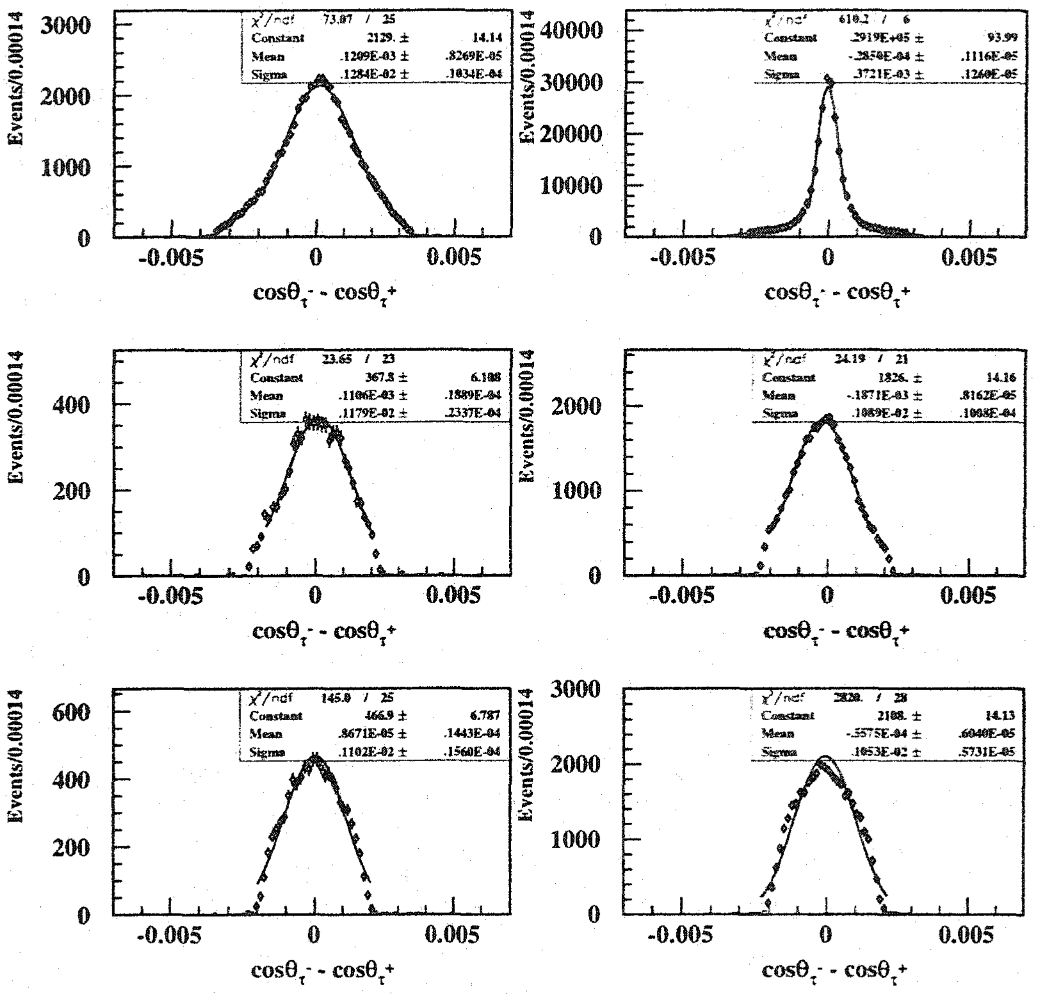

Figure 7.6: Distributions of $|\cos\theta_{\mu^-}| - |\cos\theta_{\mu^+}|$ are given for data (left) and Monte Carlo (right) $e^+e^- \rightarrow \mu^+\mu^-$ events. The barrel regions plots are shown at the top, the overlap region in the middle, and the endcap region at bottom.

The effects on $\langle P_\tau \rangle$ and A^{FB}_{pol} of absolute scale shifts, both in $\cos\theta$ and $|\cos\theta|$, and resolution uncertainties are assessed in a fashion analogous to that described for the transverse momentum. The results of these studies are provided in Table 7.2. As indicated,

Systematic Effect	Barrel	Overlap	Endcap	$\Delta\langle P_\tau \rangle$	ΔA^{FB}_{pol}
a) $\cos\theta$ Scale Increase	0.02%	0.04%	0.01%	0.01	0.01
b) $\cos\theta$ Scale Decrease	0.02%	0.04%	0.01%	0.00	-0.02
c) $\mid\cos\theta\mid$ Scale Increase	0.02%	0.04%	0.01%	-0.01	0.01
d) $\mid\cos\theta\mid$ Scale Decrease	0.02%	0.04%	0.01%	0.01	-0.02
e) Resolution Increase	+300%	+10%	+5%	0.11	-0.09
f) Resolution Decrease	off	-10%	-5%	0.00	0.03

	$\tau\to e\bar{\nu}_e\nu_\tau$		$\tau\to \mu\bar{\nu}_\mu\nu_\tau$		$\tau\to \pi\,\nu_\tau$		$\tau\to \rho\nu_\tau$		$\tau\to a_1\,\nu_\tau$	
	ΔP_τ	ΔA^{FB}_{pol}	ΔP_τ	ΔA^{FB}_{pol}	ΔP_τ	ΔA^{FB}_{pol}	ΔP_τ	ΔA^{FB}_{pol}	ΔP_τ	ΔA^{FB}_{pol}
a)	0.01	0.02	-0.10	-0.01	0.05	-0.02	-0.01	0.00	0.01	-0.02
b)	0.05	-0.02	0.14	0.01	-0.11	0.01	0.03	-0.02	-0.01	0.00
c)	0.03	0.00	0.04	0.01	-0.04	0.02	0.02	-0.01	0.02	-0.01
d)	0.03	0.00	0.00	-0.01	-0.02	-0.03	0.00	0.00	-0.01	-0.01
e)	0.28	0.03	0.15	0.02	-0.12	0.01	0.10	-0.06	0.09	0.16
f)	0.01	0.07	0.00	0.01	0.04	0.00	-0.06	-0.03	-0.37	0.05

Table 7.2: The first table shows the systematic shifts applied to the reconstructed Monte Carlo track $\cos\theta$ values in terms of both the scale and resolution. Included in the table are the corresponding effects on the $\langle P_\tau \rangle$ and A^{FB}_{pol} global fit values expressed in percent polarization. The second table provides the channel-by-channel effects for the same systematic studies.

the largest effect can be attributed to an imperfect modelling of the resolution of the polar angle measurement, with the uncertainty affecting all channels at a similar level.

The total systematic errors ascribed to track momentum measurement, including effects associated with determination of both transverse momentum and track polar angle, are estimated to be 0.0024 and 0.0013 for $\langle P_\tau \rangle$ and A^{FB}_{pol} respectively. These errors represent the influence of momentum measurement on the various polarization sensitive variables as well as effects relating to event selection. The combined systematic errors from these sources are also determined for each tau decay channel separately and given, along with the global results, in Table 7.13 at the end of this chapter. As noted above, the $\tau\to \mu\bar{\nu}_\mu\nu_\tau$ and $\tau\to \pi\,\nu_\tau$ channels are particularly sensitive to these systematic errors because the polarization sensitive variable for these channels is the measured track momentum.

7.2.2 dE/dx Modelling

Charged particles traversing the CJ experience ionization energy loss proportional to particle momentum. As indicated by Figure 3.6, this information is particularly useful for particle identification with the typical particle energies at OPAL. The emphasis for this analysis is primarily on the separation of electrons and hadrons, and hence two dE/dx pull variables, dE/dx(e) and dE/dx(π) , are employed by the selections.

In order to improve dE/dx modelling, $\tau \rightarrow e\bar{\nu}_e\nu_\tau$, $\tau \rightarrow \rho\nu_\tau$, and $\tau \rightarrow \mu\bar{\nu}_\mu\nu_\tau$ decays, selected without the use of dE/dx information, are utilized. Two independent correction algorithms have been developed with the algorithm that provides slightly better performance chosen for the nominal analysis.

Systematic errors associated with dE/dx uncertainty are evaluated through an examination of the $\tau \rightarrow e\bar{\nu}_e\nu_\tau$ dE/dx(e) and $\tau \rightarrow \pi\ \nu_\tau$ dE/dx(π) pull distributions for tau decays selected without the use of this information. Figures 7.7 and 7.8 provide an indication of the uncertainty between data and Monte Carlo for $\tau \rightarrow e\bar{\nu}_e\nu_\tau$ decays in dE/dx(e) and for $\tau \rightarrow \pi\ \nu_\tau$ decays in dE/dx(π) . The resolutions and means of these distributions are shifted in the Monte Carlo by amounts consistent with the level of disagreement shown and the analysis re-run.

Table 7.3 provides the details of these studies and the corresponding systematic shifts in the $\langle \mathrm{P}_\tau \rangle$ and $\mathrm{A}_{\mathrm{pol}}^{\mathrm{FB}}$ fit parameters. As may be seen, the largest effects can be attributed to uncertainty in the dE/dx resolution modelling and the total global errors are 0.0012 and 0.0008 for $\langle \mathrm{P}_\tau \rangle$ and $\mathrm{A}_{\mathrm{pol}}^{\mathrm{FB}}$ respectively. The channel-by-channel results, also given in Table 7.3, indicates that the $\tau \rightarrow e\bar{\nu}_e\nu_\tau$ is most sensitive to the dE/dx modelling.

7.2.3 Calorimetry

The separation of $\tau \rightarrow \pi\ \nu_\tau$, $\tau \rightarrow \rho\nu_\tau$, and multi-π^0 tau decays, primarily through an examination of ECAL cluster information, is essential to the success of this analysis. An

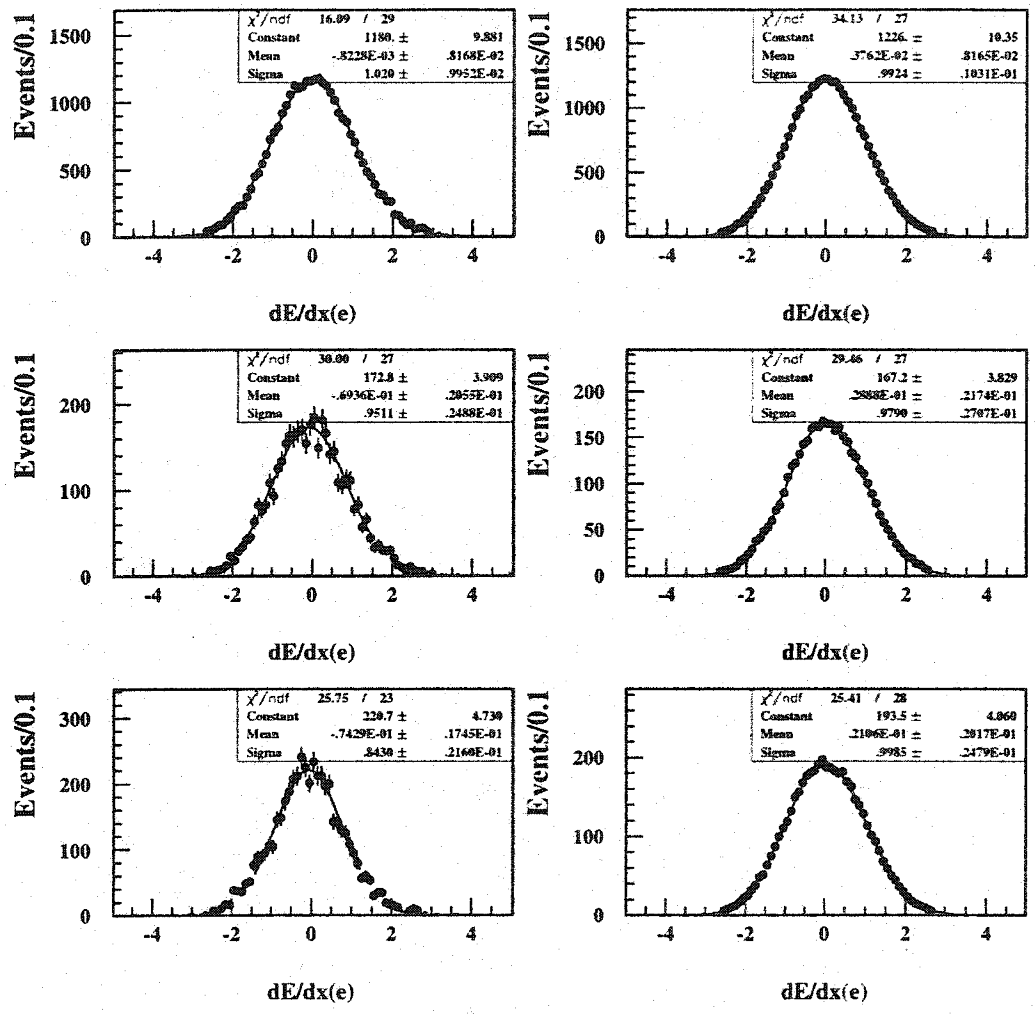

Figure 7.7: Data (left) and Monte Carlo (right) pull dE/dx(e) distributions for $\tau \rightarrow e\bar{\nu}_e\nu_\tau$ events selected with using this information are given for the barrel (top), overlap (middle), and endcap (bottom) regions of the detector.

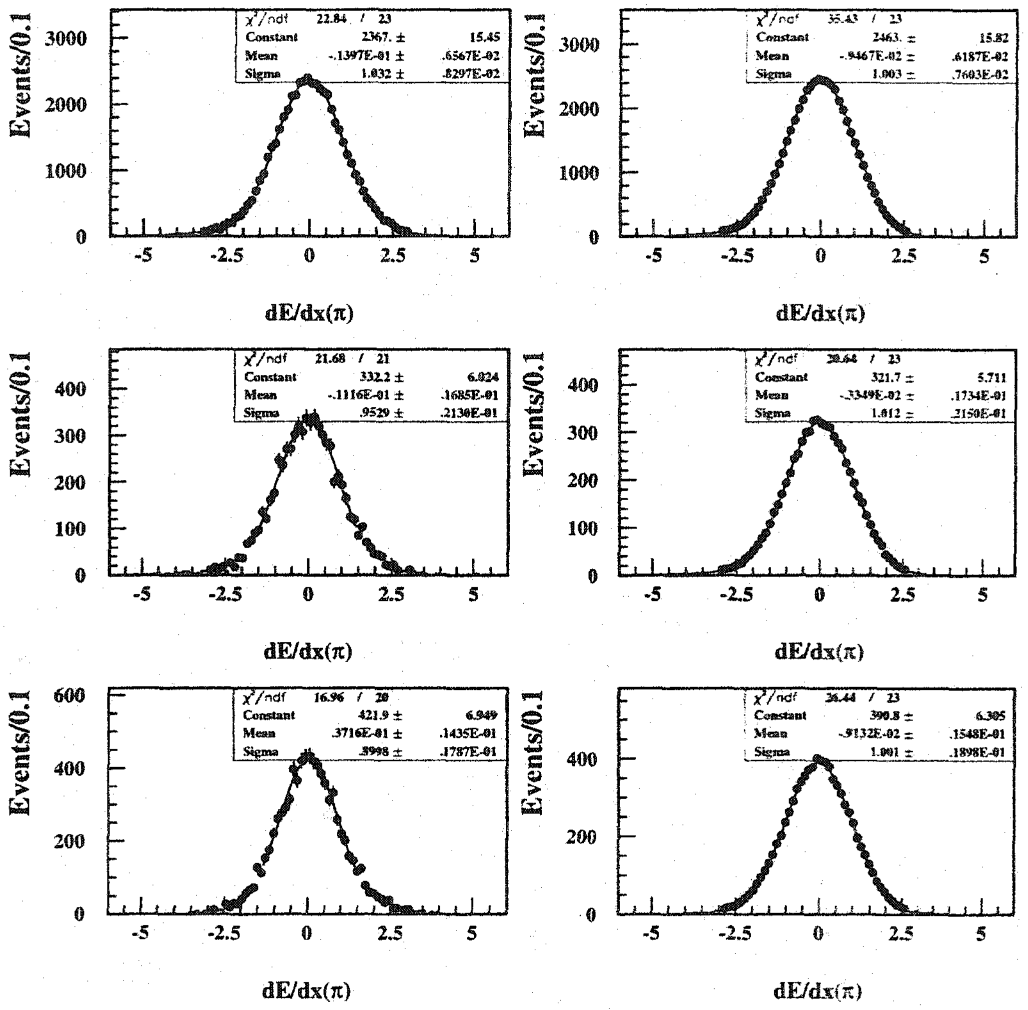

Figure 7.8: Data (left) and Monte Carlo (right) pull dE/dx(π) distributions for $\tau \rightarrow \pi \nu_\tau$ events selected without using this information are given for the barrel (top), overlap (middle), and endcap (bottom) detector regions.

Systematic Effect	Barrel	Overlap	Endcap	$\Delta\langle \mathrm{P}_\tau\rangle$	$\Delta\,\mathrm{A}^{\mathrm{FB}}_{\mathrm{pol}}$
a) dE/dx Scale Increase	1%	10%	10%	-0.01	-0.02
b) dE/dx Scale Decrease	1%	10%	10%	0.06	0.04
c) dE/dx Resolution Increase	3%	3%	16%	0.10	0.06
d) dE/dx Resolution Decrease	3%	3%	16%	0.08	0.05

	$\tau\to \mathrm{e}\bar{\nu}_{\mathrm{e}}\nu_\tau$		$\tau\to \mu\bar{\nu}_\mu\nu_\tau$		$\tau\to \pi\ \nu_\tau$		$\tau\to \rho\nu_\tau$		$\tau\to \mathrm{a}_1\ \nu_\tau$	
	ΔP_τ	ΔA^{FB}_{pol}	ΔP_τ	ΔA^{FB}_{pol}	ΔP_τ	ΔA^{FB}_{pol}	ΔP_τ	ΔA^{FB}_{pol}	ΔP_τ	ΔA^{FB}_{pol}
a)	-0.11	0.00	0.19	0.01	-0.05	-0.01	-0.01	-0.02	-0.04	-0.02
b)	0.08	-0.10	0.01	0.04	-0.05	0.01	0.10	0.04	0.02	-0.01
c)	0.39	0.03	0.11	0.07	0.26	0.07	0.07	0.06	0.11	0.03
d)	0.54	0.05	0.28	0.07	0.30	0.03	0.03	0.10	0.24	0.06

Table 7.3: At the top are given the systematic shifts applied to the Monte Carlo scale and resolution in the pull dE/dx distributions. Included are the estimated systematic uncertainties on $\langle \mathrm{P}_\tau\rangle$ and $\mathrm{A}^{\mathrm{FB}}_{\mathrm{pol}}$, expressed in percent polarization, associated with these shifts. At the bottom, the corresponding uncertainties for each individual decay channel are also given.

evaluation of the modelling of the ECAL detector, therefore, is of key importance. Such studies include the determination of systematic errors associated with cluster energy scale and resolution effects, cluster position measurement effects, and of ECAL shower modelling.

As indicated in Chapter 5, the ECAL clustering algorithm is based on a maximum entropy method as described in [51]. In order to improve the modelling of ECAL clusters in the Monte Carlo, control samples including $\mathrm{e}^+\mathrm{e}^-\to \mathrm{e}^-\mathrm{e}^-$ events, $\tau\to \mathrm{e}\bar{\nu}_{\mathrm{e}}\nu_\tau$ decays, and $\tau\to \pi\ \nu_\tau$ decays, all selected without the use of ECAL information, are utilized.

Two distinct types of energy corrections, determined separately for each of the three detector regions, are applied. First, Monte Carlo events only are corrected in order to improve the ECAL modelling in terms of cluster energy scale and resolution. Subsequently, additional corrections are applied, both to Monte Carlo and data, to account for the effects on the absolute ECAL energy scale by energy loss related to interactions of particles occurring before they enter the ECAL.

Once all corrections have been applied, the level of modelling agreement between data and Monte Carlo is assessed for each of the three detector regions. Based on the size of the corrections applied and further examinations of the control samples described above, systematic uncertainties associated with ECAL energy measurements are determined.

Figures 7.9 and 7.10 show sample E/E$_{\rm beam}$ and E$_{\rm ass}$/p plots for $e^-e^- \rightarrow e^+e^-$ events and $\tau \rightarrow e\bar{\nu}_e\nu_\tau$ tau decays selected without use of ECAL information. Figure 7.11 indicates the variation of the mean and resolution of E$_{\rm ass}$/p for $\tau \rightarrow e\bar{\nu}_e\nu_\tau$ selected tau decays in the barrel region as a function of track momentum.

The differences in the resolutions and means between the data and Monte Carlo distributions indicate the level of modelling uncertainty. As with the systematic studies already described, shifts reflecting these uncertainties are applied to the Monte Carlo, new polarization reference distributions generated, and new fits for $\langle P_\tau \rangle$ and A^{FB}_{pol} carried out. Since, it is not possible to improve the resolution of the Monte Carlo simulation for this case, the resolution error is estimated by decreasing the resolution only. The degree of the shifts applied and the associated determination of systematic uncertainties on $\langle P_\tau \rangle$ and A^{FB}_{pol} are provided in Table 7.4. Figures 7.12 and 7.13 summarize the differences between data and each of the Monte Carlo runs and justify the level of the applied systematic shifts.

Systematic Effect	Barrel	Overlap	Endcap	$\Delta\langle P_\tau \rangle$	$\Delta\ A^{FB}_{pol}$
a) Scale Increase	0.3%	0.6%	0.4%	0.14	0.08
b) Scale Decrease	0.3%	0.6%	0.4%	0.11	0.02
c) Resolution Increase	+0.3%	+1.0%	+1.0%	0.10	0.08

	$\tau \rightarrow e\bar{\nu}_e\nu_\tau$		$\tau \rightarrow \mu\bar{\nu}_\mu\nu_\tau$		$\tau \rightarrow \pi\ \nu_\tau$		$\tau \rightarrow \rho\nu_\tau$		$\tau \rightarrow a_1\ \nu_\tau$	
	ΔP_τ	ΔA^{FB}_{pol}	ΔP_τ	ΔA^{FB}_{pol}	ΔP_τ	ΔA^{FB}_{pol}	ΔP_τ	ΔA^{FB}_{pol}	ΔP_τ	ΔA^{FB}_{pol}
a)	-3.17	-0.03	-0.02	0.00	-0.18	-0.03	1.00	0.10	0.04	0.04
b)	2.80	0.03	0.11	0.00	0.06	-0.02	-0.24	0.11	-0.18	0.01
c)	-0.35	-0.12	0.18	0.07	-0.12	-0.02	0.41	0.15	-0.18	0.04

Table 7.4: Systematic shifts to the Monte Carlo ECAL energy scale and resolution are given in the first table, along with the corresponding uncertainties, expressed in percent polarization, on $\langle P_\tau \rangle$ and A^{FB}_{pol} global fits. The channel-by-channel effects of these studies are presented in the second table.

As may be seen, the resolution and relative scale uncertainties are of approximately

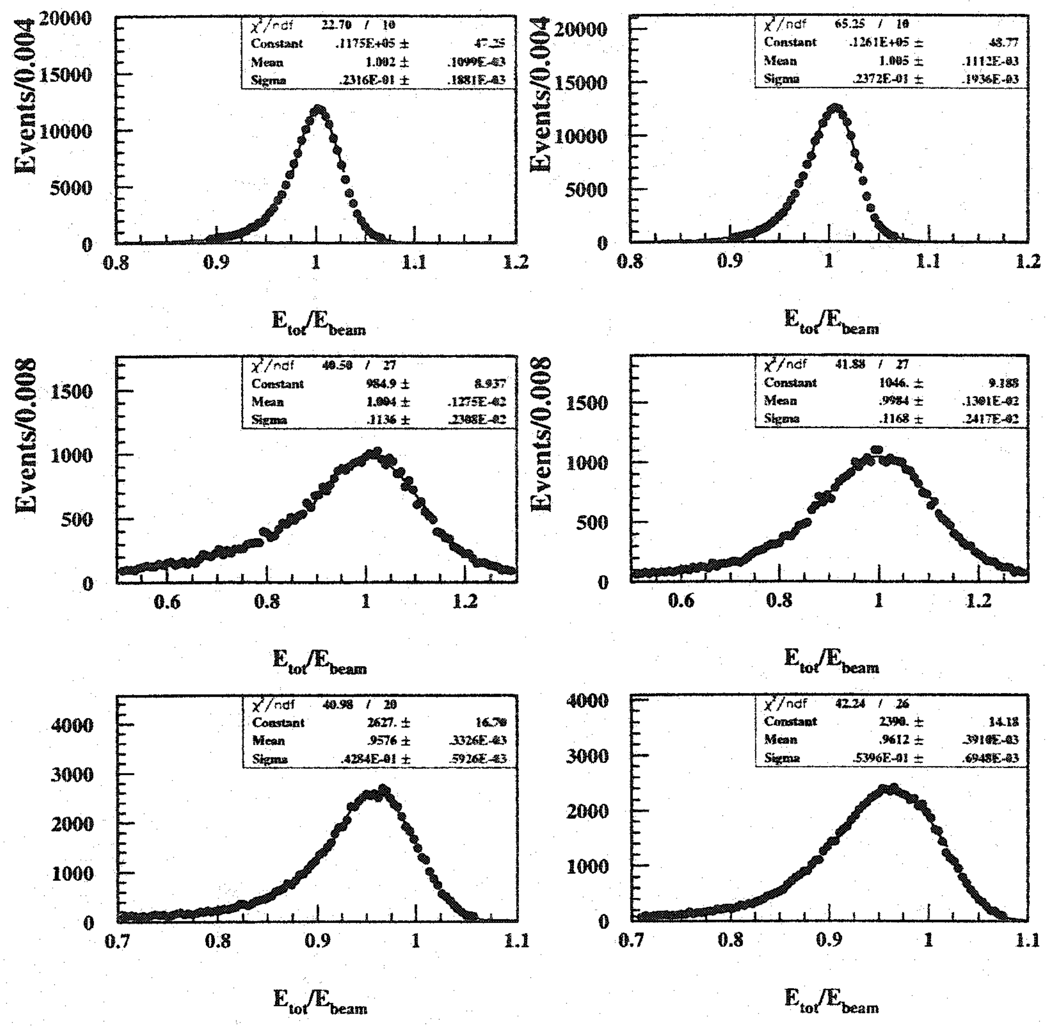

Figure 7.9: Distributions of total jet ECAL energy divided by beam energy are given for data (left) and Monte Carlo (right) $e^+e^- \rightarrow e^+e^-$ events. Each of the three detector regions are indicated separately and Gaussian fits to each plot, including the fit parameter values, are shown.

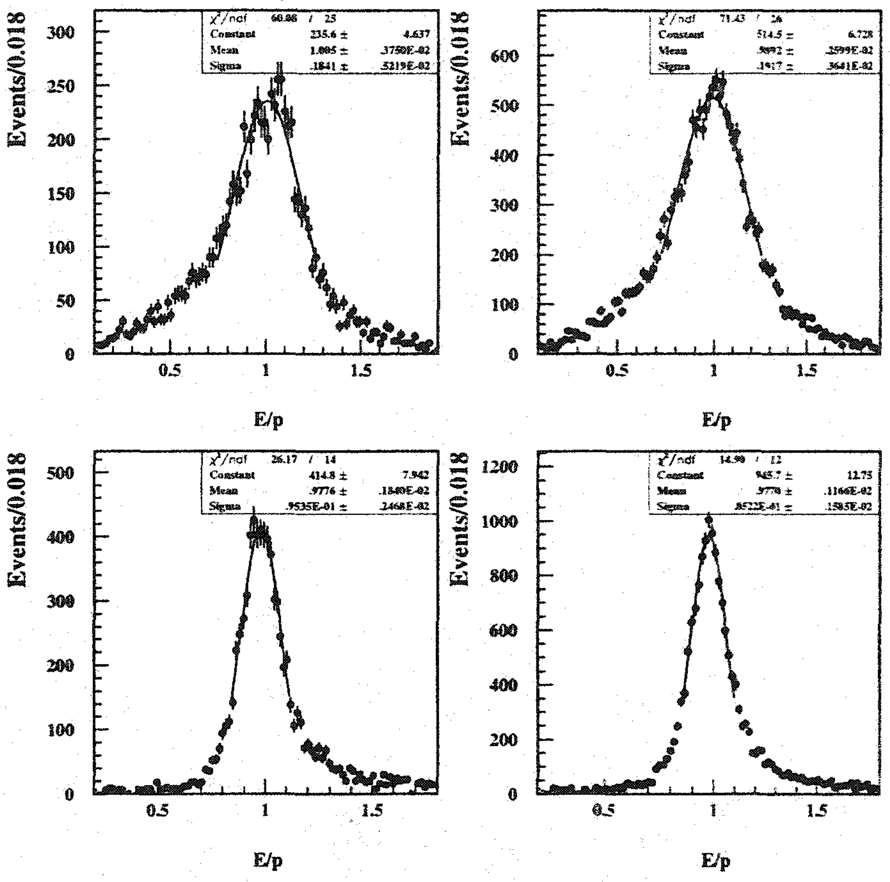

Figure 7.10: Distributions of total jet ECAL energy divided by track momentum are given for data (left) and Monte Carlo (right) $\tau\!\rightarrow e\bar{\nu}_e\nu_\tau$ selected jets. The overlap (top) and endcap (bottom) regions are indicated separately and Gaussian fits to each plot, including the fit parameter values, are shown.

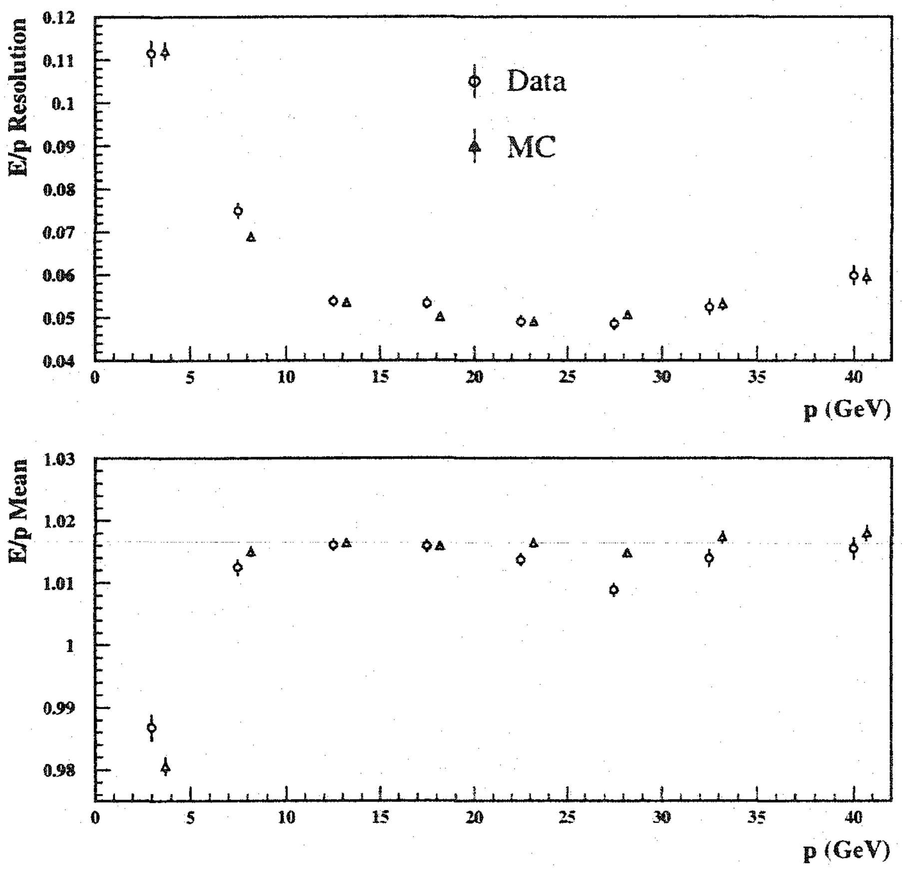

Figure 7.11: The first figure shows the estimated E_{ass}/p resolution as a function of track momentum for data and Monte Carlo $\tau \rightarrow e\bar{\nu}_e\nu_\tau$ events selected in the barrel region of the detector. The second figure compares the means of the same distributions for data and Monte Carlo.

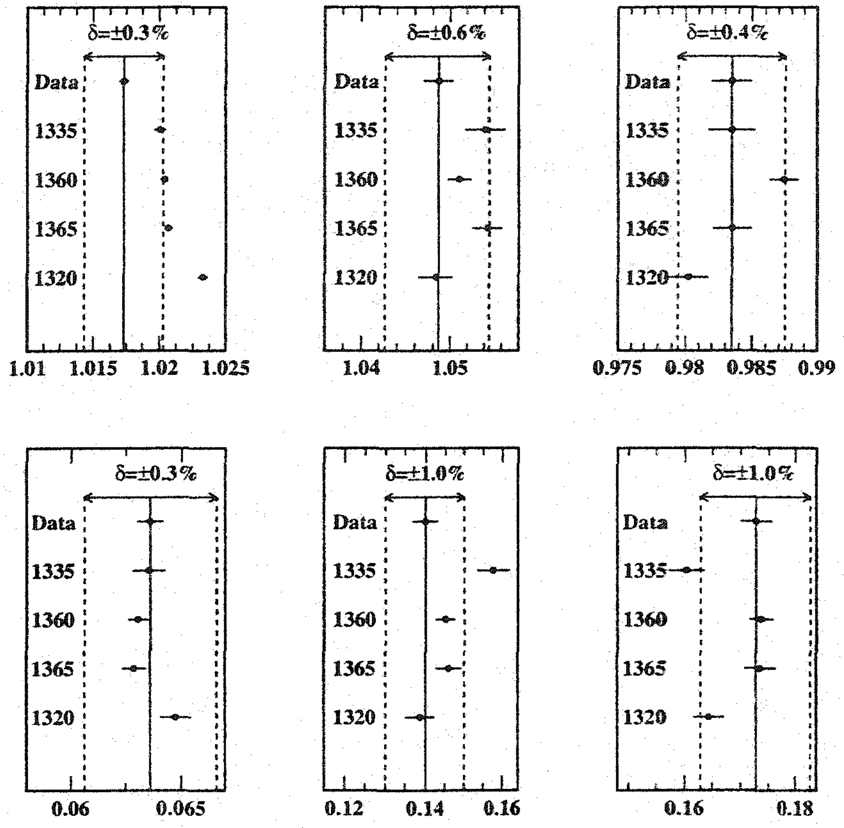

Figure 7.12: Shown are the means (top) and estimated standard deviations (bottom) for data and Monte Carlo $e^+e^- \rightarrow e^+e^-$ distributions of E/p in the barrel (left), overlap (middle), and endcap (right) detector regions. The vertical dotted lines indicate the level of systematic shift applied to the Monte Carlo for the determination of systematic errors associated with momentum modelling.

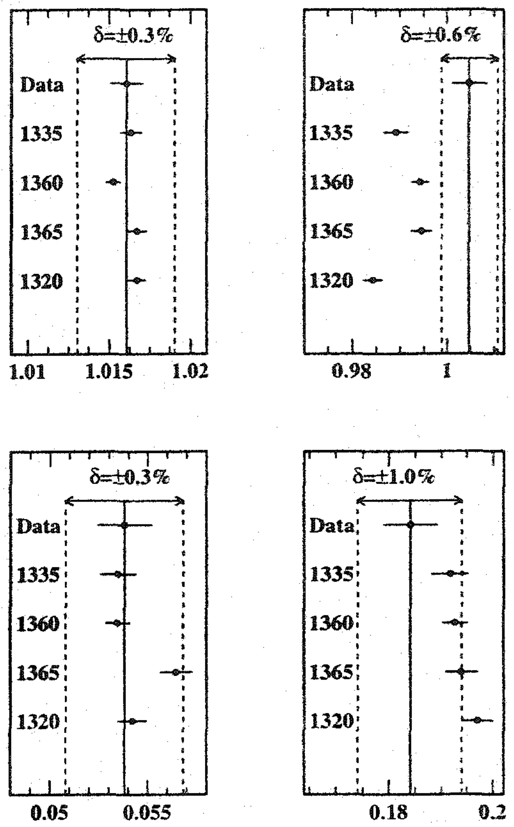

Figure 7.13: Shown are the means (top) and estimated standard deviations (bottom) for data and Monte Carlo $\tau \rightarrow e\bar{\nu}_e\nu_\tau$ distributions of E/p in the barrel (left), overlap (middle), and endcap (right) detector regions for events with (10 GeV < E < 15 GeV). The vertical dotted lines indicate the level of systematic shift applied to the Monte Carlo for the determination of systematic errors associated with momentum modelling.

equal importance with the principle sensitivity occurring in the $\tau \to e\bar{\nu}_e\nu_\tau$ and $\tau \to \rho\nu_\tau$ channels. The combined ECAL energy scale and resolution uncertainties for the global fit, given in Table 7.13 along with the channel-by-channel uncertainties, are estimated to be 0.0017 and 0.0011 for $\langle P_\tau \rangle$ and A^{FB}_{pol} respectively.

In addition to the actual measurement of energy deposited in the ECAL, it is necessary to determine the adequacy of the shower modelling and its effects when comparing data and Monte Carlo ECAL clusters. The approach taken here includes two complimentary studies.

First, since shower modelling affects the spatial distributions of ECAL clusters, an examination of such distributions provides an indication of the level of modelling uncertainty. Data and Monte Carlo ECAL-track and ECAL-presampler position measurements, separately in θ and ϕ, are compared and the uncertainties in these distributions quantified. Figures 7.14-7.17 provide sample plots which indicate, via Gaussian fits to these distributions, the level of agreement.

The estimated uncertainties, summarized in Table 7.5 are then used to extract the systematic uncertainties on the polarization fit parameters. As may be seen, these uncertainties represent a small contribution to the overall systematic uncertainty.

Shower modelling also affects the number of clusters identified by the clustering algorithm and the dispersement of energy among these clusters. In particular, since the analysis is sensitive to the number and energies of neutral clusters in each jet, the neutral cluster cutoff energies, defined in Chapter 5, are both increased and decreased by 50 MeV in order to study these effects. This degree of systematic shift alters the distribution of the number of neutral clusters for $\tau \to \pi\ \nu_\tau$ and $\tau \to \rho\nu_\tau$ selected events in a fashion that reflects the exhibited discrepancies between the Monte Carlo simulation and data. Figure 7.18 shows the distributions of the number of neutral clusters and the total neutral cluster energy for selected $\tau \to \pi\ \nu_\tau$ and $\tau \to \rho\nu_\tau$ events, including both shifted Monte Carlo cases. As may be seen, the degree of uncertainty assigned does adequately account for the differences between data and Monte Carlo. The effects of these cut variations on the $\langle P_\tau \rangle$ and A^{FB}_{pol} parameter fits are described in Table 7.5; the importance of this modelling

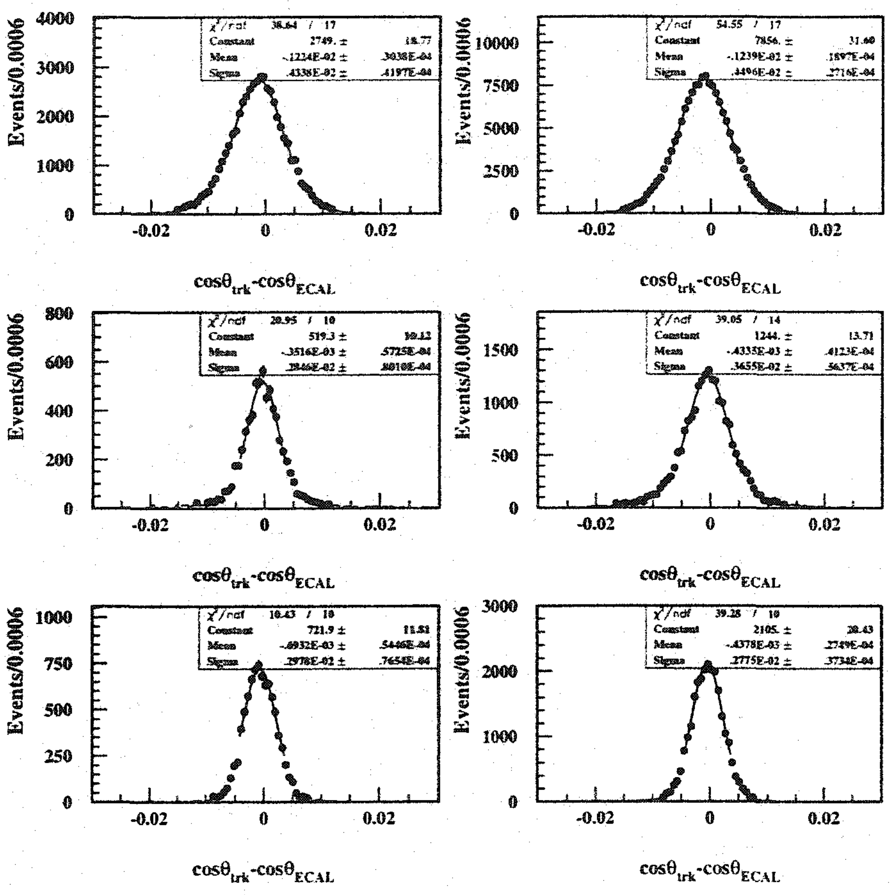

Figure 7.14: Depicted are plots of the difference between track theta position $\cos\theta_{\rm trk}$ and ECAL theta position $\cos\theta_{\rm ECAL}$ for selected $\tau \rightarrow e\bar{\nu}_e\nu_\tau$ events in the barrel (top), overlap (middle) and endcap (bottom) detector regions for data (left) and Monte Carlo (right) events. Gaussian fits to each distribution have been carried out in order to determine the level of agreement between Monte Carlo and data in terms of both the means and resolutions of these distributions.

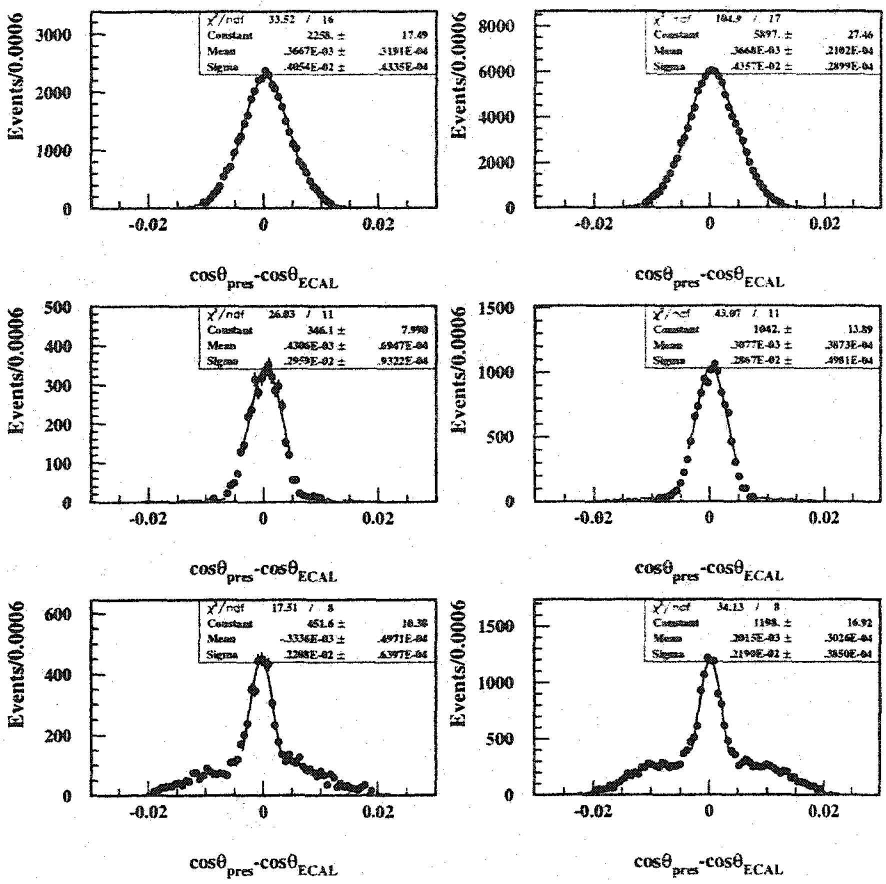

Figure 7.15: Depicted are plots of the difference between presampler theta position $\cos\theta_{\text{pres}}$ and ECAL theta position $\cos\theta_{\text{ECAL}}$ for selected $\tau \rightarrow e\bar{\nu}_e\nu_\tau$ events in the barrel (top), overlap (middle) and endcap (bottom) detector regions for data (left) and Monte Carlo (right) events. Gaussian fits to each distribution have been carried out in order to determine the level of agreement between Monte Carlo and data in terms of both the means and resolutions of these distributions.

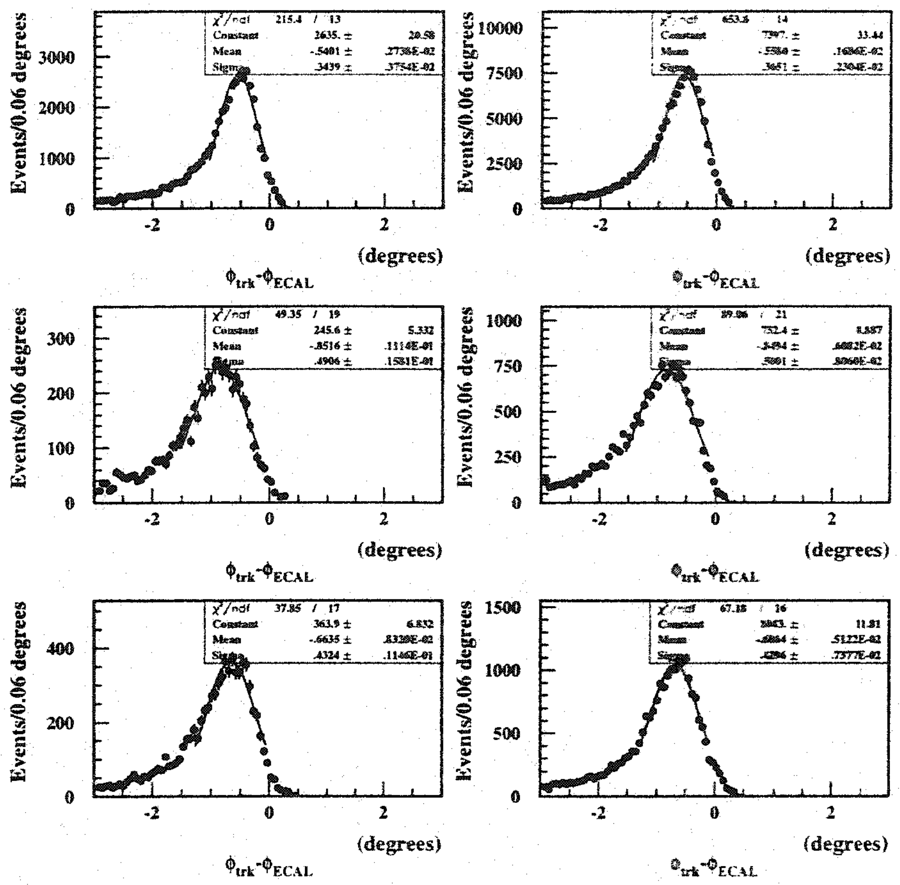

Figure 7.16: Depicted are plots of the difference between track phi position $\phi_{\rm trk}$ and ECAL phi position $\phi_{\rm ECAL}$ for selected $\tau \rightarrow e\bar{\nu}_e\nu_\tau$ events in the barrel (top), overlap (middle) and endcap (bottom) detector regions for data (left) and Monte Carlo (right) events. Gaussian fits to each distribution have been carried out in order to determine the level of agreement between Monte Carlo and data in terms of both the means and resolutions of these distributions.

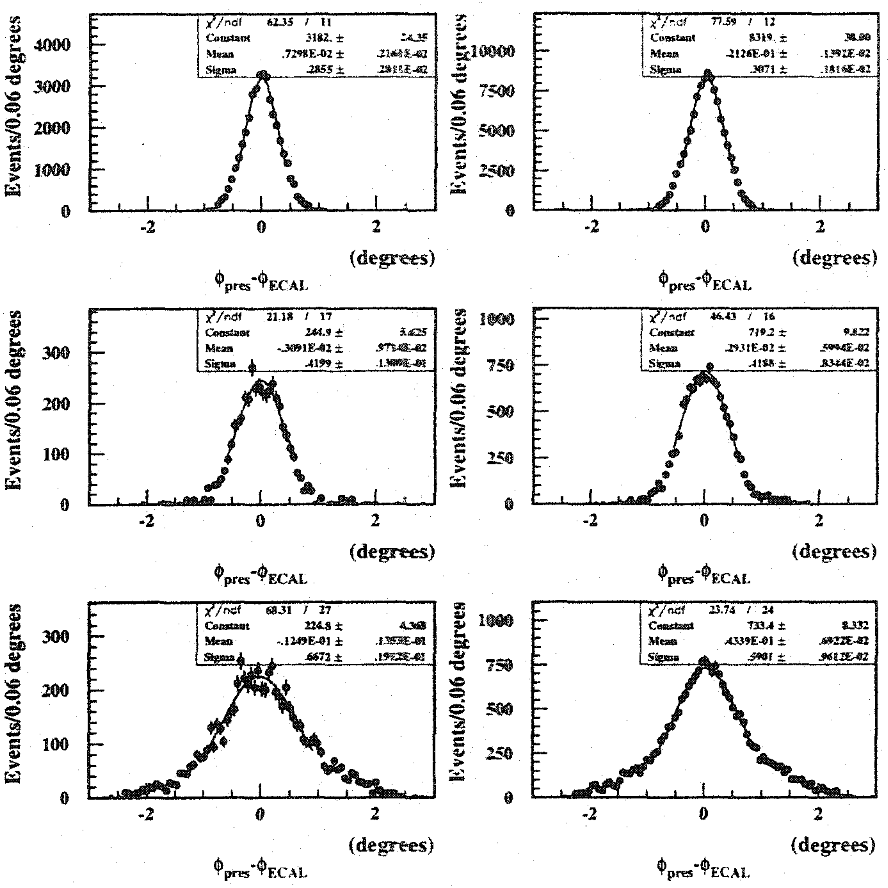

Figure 7.17: Depicted are plots of the difference between presampler phi position $\phi_{\rm pres}$ and ECAL phi position $\phi_{\rm ECAL}$ for selected $\tau \to e\bar{\nu}_e\nu_\tau$ events in the barrel (top), overlap (middle) and endcap (bottom) detector regions for data (left) and Monte Carlo (right) events. Gaussian fits to each distribution have been carried out in order to determine the level of agreement between Monte Carlo and data in terms of both the means and resolutions of these distributions.

Systematic Effect	Barrel	Overlap	Endcap	$\Delta\langle P_\tau \rangle$	ΔA^{FB}_{pol}
a) E_θ Scale Increase	0.045%	0.035%	0.07%	-0.01	0.00
b) E_θ Scale Decrease	0.045%	0.035%	0.07%	0.01	0.03
c) E_θ Resolution Increase	+0.028%	+0.055%	+0.078%	0.06	0.06
d) E_ϕ Scale Increase	2.5%	5%	5%	-0.06	-0.02
e) E_ϕ Scale Decrease	2.5%	5%	5%	0.06	0.01
f) E_ϕ Resolution Increase	+1.5%	+10%	+20%	0.06	0.06
g) E_{neut} Cut Increase	50 MeV	50 MeV	50 MeV	-0.12	0.03
h) E_{neut} Cut Decrease	50 MeV	50 MeV	50 MeV	0.23	0.02

	$\tau\rightarrow e\bar{\nu}_e\nu_\tau$		$\tau\rightarrow \mu\bar{\nu}_\mu\nu_\tau$		$\tau\rightarrow \pi\,\nu_\tau$		$\tau\rightarrow \rho\nu_\tau$		$\tau\rightarrow a_1\,\nu_\tau$	
	ΔP_τ	ΔA^{FB}_{pol}	ΔP_τ	ΔA^{FB}_{pol}	ΔP_τ	ΔA^{FB}_{pol}	ΔP_τ	ΔA^{FB}_{pol}	ΔP_τ	ΔA^{FB}_{pol}
a)	0.16	-0.02	0.03	0.00	-0.04	-0.05	0.01	0.04	-0.03	0.04
b)	-0.02	0.00	0.08	-0.01	-0.01	0.04	0.06	0.03	-0.03	-0.01
c)	-0.31	-0.01	0.13	0.07	-0.10	-0.04	0.35	0.14	-0.22	0.03
d)	0.08	0.01	0.00	0.02	-0.12	-0.01	-0.06	0.01	0.07	0.01
e)	0.08	-0.01	0.02	-0.02	0.05	0.00	0.05	0.00	0.01	0.01
f)	-0.07	0.03	0.10	0.04	-0.12	-0.04	0.34	0.14	-0.31	0.02
g)	-0.45	-0.04	0.03	-0.01	-0.21	-0.05	-0.03	0.04	-0.13	0.01
h)	0.51	0.02	0.07	-0.02	0.32	0.00	0.11	0.03	0.15	-0.03

Table 7.5: The first table presents systematic shifts applied to the Monte Carl ECAL cluster position measurements and to the neutral cluster energy thresholds. Included are the effects of these shifts on the global fit values of $\langle P_\tau \rangle$ and A^{FB}_{pol} expressed in percent polarization. The second table provides the effects of these shifts on the $\langle P_\tau \rangle$ and A^{FB}_{pol} parameter measurements for each of the separate tau decay channels.

uncertainty is evident.

The combined ECAL shower modelling uncertainties on the global fit values are 0.0025 and 0.0010 for $\langle P_\tau \rangle$ and A^{FB}_{pol} respectively. Table 7.13, included at the end of this chapter, indicates that the uncertainty from this source is of importance to all channels apart from the $\tau\rightarrow \mu\bar{\nu}_\mu\nu_\tau$ channel.

7.2.4 Outer Detectors

The HCAL and muon chambers are primarily used for the identification of muons and hadrons in an event. Thus, any potential systematic effects associated with the modelling of these detectors are expected to be revealed in the selection of $\tau\rightarrow \pi\,\nu_\tau$ and

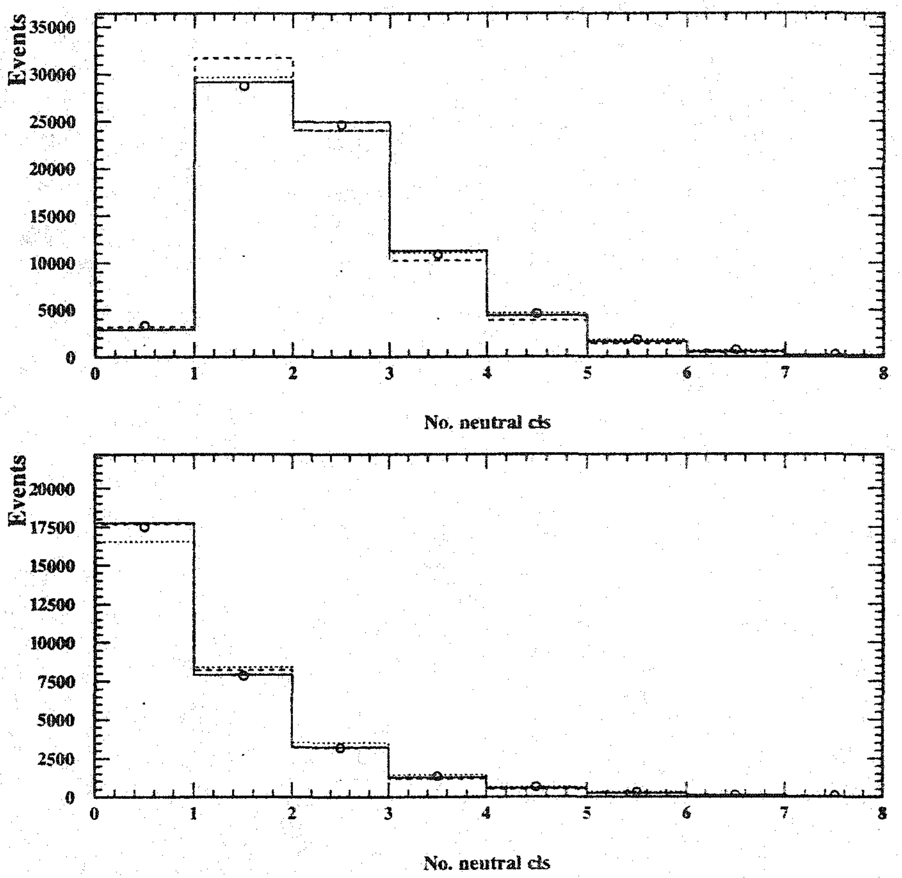

Figure 7.18: The distributions of the number of neutral clusters for selected $\tau \rightarrow \pi\nu_\tau$ (top) and $\tau \rightarrow \rho\nu_\tau$ (bottom) events are shown. The open circles with error bars represent the data while the solid histogram represents the Monte Carlo. The dashed and dotted histograms indicate the variation in the Monte Carlo distributions when the neutral cluster threshold energy cut is varied by 50 MeV.

$\tau \rightarrow \mu\bar{\nu}_\mu\nu_\tau$ decays.

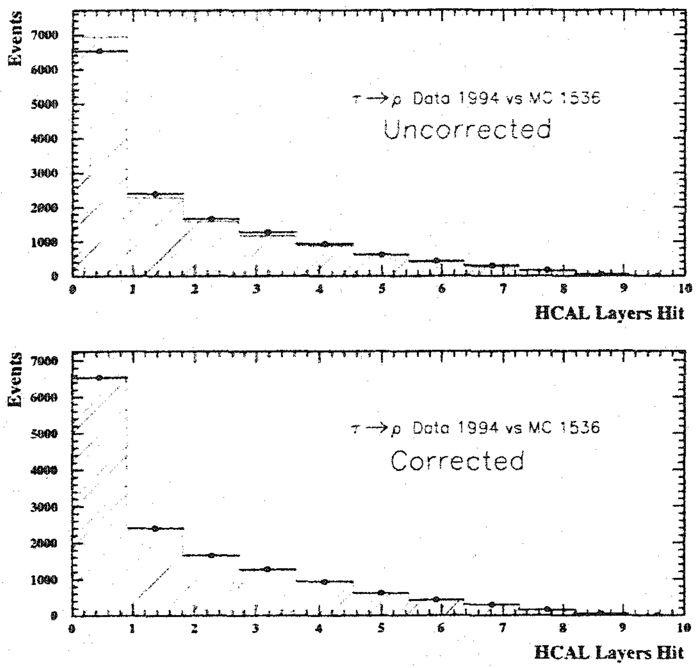

Figure 7.19: Shown are distributions of the number of HCAL layers with hits for $\tau \rightarrow \rho\nu_\tau$ events selected without the use of outer detector information. The figure at the top compares data and Monte Carlo before corrections have been applied while the figure at the bottom shows the agreement between data and Monte Carlo after correction.

In order to improve the modelling of these detectors, control samples of muon pair events, $\tau \rightarrow \rho\nu_\tau$ decays, and $\tau \rightarrow e\bar{\nu}_e\nu_\tau$ decays, all selected without using outer detector information, are employed. Figure 7.19 depicts distributions of the number HCAL layers with hits for $\tau \rightarrow \rho\nu_\tau$ decays and Figure 7.20 the number of muon chamber hits for muon pair events, both before and after corrections to the Monte Carlo are applied. As may be seen, the level of these corrections is small, but the agreement is improved.

In order to evaluate systematic effects associated with these detectors, fits to $\langle P_\tau \rangle$ and $A_{\text{pol}}^{\text{FB}}$ are carried out when the HCAL corrections and muon chamber corrections are separately turned off. For the muon chamber case, the full difference between the nominal fit values and those generated from the systematic test are quoted as the systematic errors.

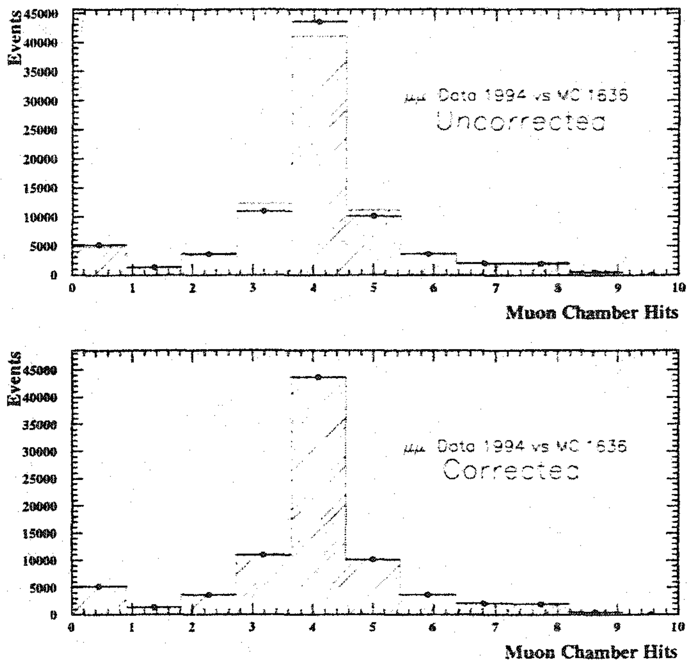

Figure 7.20: Shown are distributions of the number of muon chamber hits for muon pair events selected without the use of outer detector information. The figure at the top compares data and Monte Carlo before corrections have been applied while the figure at the bottom shows the agreement between data and Monte Carlo after correction.

An examination of the level of the HCAL corrections indicates that the uncertainty is 10% of the total correction, and thus the difference between the nominal and shifted values is scaled by this amount. This level of uncertainty is determined from the differences between data and Monte Carlo in the control samples after corrections have been applied.

The total global systematic errors associated with outer detector effects are estimated to be 0.0013 and 0.0005 for $\langle P_\tau \rangle$ and $A_{\rm pol}^{\rm FB}$ respectively. The systematic errors determined on a channel by channel basis are given in Table 7.13 and indicate, as expected, that the $\tau \rightarrow \mu \bar{\nu}_\mu \nu_\tau$ and $\tau \rightarrow \pi\ \nu_\tau$ channels are the most sensitive to outer detector modelling.

7.3 Physics Modelling

In addition to the systematic uncertainties arising from detector modelling considerations, there exist a number of important error sources associated with the underlying physics processes involved.

The Monte Carlo simulation relies on detailed knowledge of the theoretical models describing the production of the signal and background events; uncertainties in these models must be evaluated in the context of the $\langle P_\tau \rangle$ and $A_{\rm pol}^{\rm FB}$ measurements. Since these models require knowledge of various measured input parameters, such as the tau decay branching ratios, the effects of the uncertainties on these quantities must also be ascertained.

7.3.1 a_1 Modelling

The largest physics modelling systematic error can be attributed to the uncertainty in the modelling of the a_1 decay dynamics. The effect is large, not because of the contribution from the selected 3-prong a_1 channel itself, but primarily because of the significant 1-prong a_1 background in the $\tau \rightarrow \rho\nu_\tau$ channel.

The difficulty in modelling this channel lies with the relatively poor understanding of the energy dependent resonant structure of these decays and the potentially significant contribution of non-resonant terms.

The TAUOLA tau decay package, which is used to generate the Monte Carlo tau decay events for this analysis, utilizes the Kuhn-Santamaria (KS) [55] model and is employed as the default model for the nominal polarization fit. The width and mass of the a_1 are free parameters in this model and have been determined by OPAL measurements [56].

In order to test the sensitivity of the analysis to these KS parameters, the a_1 width and mass, for both the 1-prong and 3-prong Monte Carlo $\tau \rightarrow a_1\, \nu_\tau$ decays, is varied by the uncertainty on the OPAL measurement. The corresponding changes in the $\langle P_\tau \rangle$ and $A_{\rm pol}^{\rm FB}$ fit values, given in Table 7.6 for both the global and channel-by-channel studies, indicate that the sensitivity is small compared to other systematic error sources.

The variation of the a_1 mass and width parameters accounts for some of the KS model

Study	Global		$\tau \rightarrow \rho\nu_\tau$		$\tau \rightarrow$ a_1 ν_τ	
	ΔP_τ	ΔA_{pol}^{FB}	ΔP_τ	ΔA_{pol}^{FB}	ΔP_τ	ΔA_{pol}^{FB}
a_1 Width	0.07	0.01	0.10	0.01	0.33	0.04
a_1 Mass	0.03	0.01	0.05	0.00	0.13	0.02
IMR Model	0.21	0.01	0.37	0.01	0.34	0.12

Table 7.6: The estimated systematic uncertainties associated with the modelling of a_1 tau decays, both 1-prong and 3-prong, are presented in percent polarization. The first two rows represent variations in the a_1 decay parameters within the context of the Kuhn-Santamaria model while the last row corresponds to a reweighting of the Monte Carlo a_1 tau decays to reflect the Isgur-Morningstar-Reader model. Clearly the differences between these two models have are of more significance than the variation of parameters within a given model.

uncertainty, but does not significantly test the the overall weaknesses of the model itself. To accomplish this, a second model must be examined. For this analysis the Isgur-Morningstar-Reader model (IMR) [57], which employs a somewhat different approach than the KS model, is used.

The effect of the differences between the KS and IMR models is assessed by refitting the data with the Monte Carlo $\tau \rightarrow a_1 \nu_\tau$ decay events reweighted, as described in [58], to reflect the IMR model distributions in the Dalitz plot variables s_1 and s_2, and the invariant mass of the three pion system m_{a_1} . Here, $s_1 = (p_2 + p_3)^2$ and $s_2 = (p_1 + p_3)^2$ where, for the 3-prong case, p_3 is the four-momentum of the unlike-sign pion and p_2 is the more energetic of the two like-sign pions and, for the 1-prong case, p_3 is the four-momentum of the charged pion and p_2 is the more energetic of the two π^0 's.

The results of this study are given in Table 7.6 and indicate the importance of the a_1 modelling to this analysis.

In order to justify this evaluation of the modelling, Figure 7.21 shows the distributions of s_1, s_2, and m_{a_1} for the selected 3-prong a_1 data compared to the two Monte Carlo models. These plots indicate that the differences between data and Monte Carlo are well described by the differences in the two models, thus implying that the assigned modelling errors are accurate.

7.3.2 $\tau \to 3\pi^{\pm}\pi^{0}\ \nu_{\tau}$ Modelling

In analogy to the a_1 modelling systematic error described above, the modelling of $\tau \to 3\pi^{\pm}\pi^{0}\ \nu_{\tau}$ tau decays contains uncertainties which must be evaluated in the context of the polarization measurement. Such events dominate the background in the $\tau \to a_1\ \nu_{\tau}$ selection and, as seen in Table 7.13, dominate the systematic uncertainty in this channel.

As described by the CLEO experiment[59], the $\tau \to 3\pi^{\pm}\pi^{0}\ \nu_{\tau}$ decays are dominated by $\omega\pi$ and $\rho\pi$ final states. Figure 7.22 shows the invariant mass of the $\pi^{+}\ \pi^{-}\ \pi^{0}$ system for generated Monte Carlo $\tau \to 3\pi^{\pm}\pi^{0}\ \nu_{\tau}$ tau decay events. The ω resonance contribution is clearly seen as the peak near 0.8 MeV.

In order to determine the systematic error associated with the modelling of these events, the $\omega\pi$ contribution is reweighted in the Monte Carlo to reflect the relative contributions measured by CLEO and the analysis rerun. The total systematic error on the global fit values for $\langle P_{\tau} \rangle$ and $A_{\rm pol}^{\rm FB}$, as shown in Table 7.13, are assessed to be 0.0011 and 0.0004 respectively.

As a final note, uncertainties associated with the modelling of the remaining hadronic tau decays have been studied by refitting to the data with the helicity assignment of these events reversed. The differences between these fit values and the nominal values are insignificant and have no effect on the total systematic uncertainties assessed.

7.3.3 Tau Branching Ratios, $A_{\rm FB}$, and Miscellaneous Uncertainties

In order to generate Monte Carlo events that will accurately estimate the relative contributions of each background in a given tau decay selection, the relative branching ratios of the different decay channels must be input to the Monte Carlo generator.

For this analysis, the branching ratio values from the 2000 Particle Data Book [4] constrained fit have been used. The specific values and errors, along with the corresponding derived TAUOLA decay channel branching ratios are given in Appendix C.

The effects of the uncertainties on these branching ratios are evaluated by first increasing and then decreasing each branching ratio separately by its one standard deviation error. The results of this analysis on the $\langle P_{\tau} \rangle$ and $A_{\rm pol}^{\rm FB}$ fit values are presented in Table 7.7

and indicate that the K* and $\tau \rightarrow \pi\ \nu_\tau$ modes contribute the largest systematic errors. The combined global systematic errors from the branching ratio uncertainties, as shown at the end of the chapter in Table 7.13, are 0.0011 on $\langle P_\tau \rangle$ and 0.0002 on $A_{\rm pol}^{\rm FB}$.

Equation 2.19 characterizes the variation of P_τ with $\cos\theta_{\tau^-}$ and indicates the dependence on the three parameters $\langle P_\tau \rangle$, $A_{\rm pol}^{\rm FB}$, and $A_{\rm FB}$. While determining $\langle P_\tau \rangle$ and $A_{\rm pol}^{\rm FB}$ are manifestly the object of this analysis, the value of $A_{\rm FB}$ is measured as part of the OPAL lineshape analysis and used as input here. To evaluate the systematic effect of the uncertainty on the $A_{\rm FB}$ measurement, the input $A_{\rm FB}$ value is varied by its one standard deviation error and fits to $\langle P_\tau \rangle$ and $A_{\rm pol}^{\rm FB}$ subsequently carried out. As shown in Table 7.13, the effect is small with $\langle P_\tau \rangle$ changing by 0.0003 and $A_{\rm pol}^{\rm FB}$ by 0.0002.

As noted in Chapter 2, the Monte Carlo simulation includes initial and final state radiative corrections up to $O(\alpha^2)$ and electroweak corrections up to $O(\alpha)$. The effects of higher order corrections are negligible and do not contribute to the systematic error of this analysis.

The final systematic error source to be discussed arises from the uncertainty in the modelling of decay radiation. For the leptonic tau decays and the $\tau \rightarrow \pi\ \nu_\tau$ mode, decay radiation is well modelled.[1] For the decay of ρ and a_1 particles in the $\tau \rightarrow \rho\nu_\tau$ and $\tau \rightarrow a_1\ \nu_\tau$ channels, the Monte Carlo does include events with decay radiation, but the level of uncertainty in the modelling is unclear.

In order to study this uncertainty, $\tau \rightarrow \rho\nu_\tau$ and $\tau \rightarrow a_1\ \nu_\tau$ events generated with decay radiation are removed from the Monte Carlo and the analysis re-run. As shown in the summary section in Table 7.13, this study indicates that the effect is small and the estimated systematic uncertainties from this source are approximately 0.0001 for both $\langle P_\tau \rangle$ and $A_{\rm pol}^{\rm FB}$.

---

[1] KORALZ includes final state bremsstrahlung to $\mathcal{O}(\alpha^2)$ (including exclusive exponentiation); calculates the decay radiation in the leptonic decays to $\mathcal{O}(\alpha)$; and decay radiation in all semi-leptonic decay modes in the leading logarithmic approximation.

Decay Mode	Global	$\tau \rightarrow e\bar{\nu}_e\nu_\tau$	$\tau \rightarrow \mu\bar{\nu}_\mu\nu_\tau$	$\tau \rightarrow \pi\ \nu_\tau$	$\tau \rightarrow \rho\nu_\tau$	$\tau \rightarrow a_1\ \nu_\tau$
	$\Delta P_\tau \Delta A^{FB}_{pol}$	$\Delta P_\tau \Delta A^{FB}_{pol}$	$\Delta P_\tau \Delta A^{FB}_{pol}$	$\Delta P_\tau \Delta A^{FB}_{pol}$	$\Delta P_\tau \Delta A^{FB}_{pol}$	$\Delta P_\tau \Delta A^{FB}_{pol}$
K^0K^-	0.01 0.00	0.00 0.00	0.00 0.00	0.02 -0.01	0.02 0.00	-0.01 0.00
	-0.02 0.00	0.00 0.00	0.00 0.00	-0.02 -0.01	-0.01 0.00	0.00 0.00
$\pi^-\pi^0\gamma$	-0.02 0.00	-0.04 0.00	0.00 0.01	0.00 -0.01	-0.02 -0.01	-0.01 0.00
	0.01 0.00	0.04 0.00	0.01 0.01	-0.01 -0.01	0.02 -0.01	0.01 0.00
$\pi^-\pi^0 2\gamma$	-0.01 0.00	0.00 0.00	0.00 0.00	0.00 0.00	0.00 0.00	-0.01 0.00
	0.00 0.00	0.00 0.00	0.01 0.00	0.00 0.00	0.00 0.00	0.00 0.00
$\pi^-\pi^+\pi^-\pi^0\pi^0\pi^0$	-0.02 0.01	-0.03 0.00	-0.02 0.00	-0.01 0.00	-0.02 0.00	0.00 0.01
	0.01 0.01	0.03 0.00	0.02 0.00	0.00 0.00	0.02 0.00	-0.01 0.01
$\pi^-\pi^+\pi^-\pi^0\pi^0$	-0.01 0.00	-0.01 0.00	0.00 0.00	-0.01 0.00	0.00 0.00	-0.01 0.00
	0.00 0.00	0.01 0.00	0.01 0.00	0.00 0.00	0.01 0.00	0.01 0.00
$\pi^-\overline{K}^0\pi^0$	0.03 0.00	0.00 0.00	0.01 0.01	-0.01 0.00	0.08 -0.01	-0.02 0.01
	-0.03 0.00	0.00 0.00	-0.01 0.01	0.00 0.00	-0.08 -0.01	0.02 0.01
$K^-\pi^-\pi^+$	-0.01 0.00	-0.01 0.00	-0.03 0.00	0.00 -0.01	-0.01 0.01	-0.02 -0.02
	0.00 0.00	0.01 0.00	0.04 0.00	-0.01 -0.01	0.01 0.01	0.01 -0.02
$\pi^0\pi^0K^-$	0.00 0.00	-0.01 0.00	0.01 0.01	0.00 0.00	0.01 0.00	-0.01 0.01
	-0.01 0.00	0.01 0.00	-0.01 0.01	-0.01 0.00	-0.01 0.00	0.00 0.01
$K^-\pi^0K^0$	0.01 0.00	0.00 0.00	-0.01 0.00	0.01 -0.01	0.03 0.00	-0.01 0.00
	-0.02 0.00	0.00 0.00	0.01 0.00	-0.02 -0.01	-0.02 0.00	0.01 0.00
$K^0\pi^-\overline{K}^0$	0.01 0.00	0.00 0.00	0.00 0.00	0.01 -0.01	0.02 0.00	0.00 0.00
	-0.02 0.00	0.00 0.00	0.00 0.00	-0.02 -0.01	-0.02 0.00	-0.01 0.00
$K^-\pi^+K^+$	0.00 0.00	0.00 0.00	0.00 0.00	0.00 0.00	0.00 0.00	0.13 -0.01
	-0.01 0.00	0.00 0.00	0.00 0.00	0.00 0.00	0.00 0.00	-0.13 -0.01
$\pi^-\pi^+\pi^-\pi^+\pi^-\pi^0$	-0.01 0.00	0.00 0.00	0.00 0.00	0.00 0.00	0.00 0.00	0.00 0.00
	0.00 0.00	0.00 0.00	0.00 0.00	0.00 0.00	0.00 0.00	0.00 0.00
$\pi^-\pi^0\pi^0\pi^0$	-0.01 0.00	-0.02 0.00	0.03 0.00	0.00 -0.01	-0.01 0.00	-0.02 0.01
	0.00 0.00	0.02 0.00	-0.02 0.00	-0.01 -0.01	0.01 0.00	0.01 0.01
$\pi^-\pi^+\pi^-\pi^0$	-0.02 0.00	-0.02 0.00	0.00 0.00	-0.01 0.00	-0.02 0.01	-0.08 -0.01
	0.01 0.00	0.02 0.00	0.01 0.00	0.00 0.00	0.02 0.01	0.07 -0.01
$\pi^-K^0(K^*)$	0.06 0.00	0.01 0.00	0.00 0.00	0.10 -0.01	0.06 0.00	0.02 0.00
	-0.07 0.00	-0.01 0.00	0.00 0.00	-0.10 -0.01	-0.06 0.00	-0.02 0.00
$K^-\pi^0(K^*)$	0.01 0.00	0.00 0.00	-0.01 0.00	-0.01 -0.01	0.04 0.00	0.00 0.00
	-0.02 0.00	0.00 0.00	0.01 0.00	0.00 -0.01	-0.04 0.00	-0.01 0.00
K^-	-0.03 0.00	0.01 0.00	0.01 0.00	-0.05 0.00	-0.03 0.00	0.00 0.01
	0.02 0.00	-0.01 0.00	-0.01 0.00	0.04 0.00	0.03 0.00	0.00 0.01
$\pi^-\pi^0\pi^0(a1)$	0.00 0.00	0.01 0.01	0.01 0.00	0.00 0.00	0.01 0.00	-0.01 0.01
	-0.01 0.00	-0.01 0.01	-0.01 0.00	-0.01 0.00	-0.01 0.00	0.00 0.01
$\pi^-\pi^+\pi^-(a1)$	-0.01 0.01	-0.01 0.00	-0.01 0.00	-0.01 0.00	-0.02 0.01	0.01 0.03
	0.01 0.01	0.01 0.00	0.02 0.00	0.00 0.00	0.02 0.01	-0.02 0.03
$\pi^-\pi^0(\rho)$	-0.01 0.01	0.03 0.00	0.02 0.00	-0.03 0.00	-0.01 0.01	-0.01 0.01
	0.00 0.01	-0.03 0.00	-0.02 0.00	0.02 0.00	0.01 0.01	0.00 0.01
π^-	-0.06 0.00	0.05 0.00	0.05 -0.01	-0.08 0.01	-0.10 0.01	0.00 0.01
	0.06 0.00	-0.05 0.00	-0.05 -0.01	0.07 0.01	0.10 0.01	-0.01 0.01
μ^-	-0.01 0.00	0.03 0.00	-0.04 0.01	0.00 -0.01	-0.01 0.00	-0.01 0.01
	0.00 0.00	-0.03 0.00	0.05 0.01	-0.01 -0.01	0.01 0.00	0.00 0.01
e^-	-0.01 0.00	0.00 0.00	0.02 0.00	-0.01 0.00	-0.01 0.00	-0.01 0.01
	0.00 0.00	0.00 0.00	-0.01 0.00	0.01 0.00	0.01 0.00	0.00 0.01

Table 7.7: Shown are the systematic shifts in the $\langle P_\tau \rangle$ and A^{FB}_{pol} fit values, expressed in percent polarization, when the branching ratio for each of the listed tau decay channels is varied by +1 σ (first line) and -1 σ (second line). Note that only the 'visible' decay products are given to denote each decay mode.

7.4 Additional Consistency Checks

Complex precision measurements typically require numerous consistency and cross-checks before being ultimately finalized, and this analysis is no exception. While it is not possible to describe all of the many consistency checks here, the most important and instructive of these will be discussed in what follows.

7.4.1 Tau and Non-Tau Background Checks

Although the non-tau backgrounds carry no polarization information themselves, the kinematics of these events are such that the distributions in the polarization sensitive variables of these backgrounds are substantially different from the signal distributions. Incorrect Monte Carlo modelling can lead to uncontrolled non-tau backgrounds which could potentially bias the polarization fit results.

To ensure that these backgrounds are adequately described by the Monte Carlo, distributions of acolinearity, acoplanarity, and total transverse momentum for each non-tau pair identification class are examined. As evinced by Figures 5.1-5.2, these distributions are substantially different for tau pairs and non-tau events.

Data and Monte Carlo distributions of these three variables are compared, with the Monte Carlo luminosity weighted to the data. Thus, not only are differences in the shapes of the distributions important, but also the overall normalizations. Figures 7.23-7.24 provide examples of the distributions for e-e and μ-μ tau pair identification classes most susceptible to non-tau background contamination. The distributions are well described by the Monte Carlo and give no indications of uncontrolled non-tau backgrounds.

Since the two-photon cross-sections do not fall as quickly away from the Z^0 resonance as the tau pair cross-section, there is an effective enhancement of two-photon background in the data collected at off-peak energies. Depicted in Figures 7.25-7.28 are sample acolinearly, acoplanarity, and total transverse plots for data collected above and below the Z^0 peak compared to the off-peak Monte Carlo distributions. Again, the tau pair identification classes in which majority of the non-tau backgrounds reside are shown and, as can be seen, no evidence for uncontrolled backgrounds is found.

Not only is it important to check the non-tau background sources, the tau backgrounds must also be demonstrated to be accounted for properly. While the detector and physics modelling systematic error studies described above are expected to account for any discrepancies, additional checks provide confidence in these assigned errors.

A powerful method for doing this is to compare the number of selected events in each tau pair identification class predicted by the luminosity weighted Monte Carlo with the number of events actually selected in the data. Table 7.8 gives the number of such events for each of the twenty pair identification classes. The good agreement between the data and the expected numbers of events in the different decay topologies evident from this table helps validate the overall efficiencies and purities estimated for each decay topology.

	nid	e	μ	π	ρ	a_1
e	12053 11793	3599 3584				
μ	11406 11211	6737 6601	2746 2707			
π	8382 8200	4786 4847	4302 4325	1669 1645		
ρ	18006 18186	10649 10782	10178 10230	7504 7460	8225 8482	
a_1	5503 5630	3736 3753	3537 3581	2428 2548	5631 5669	867 915

Table 7.8: Number of τ-pair events in each pair-identification class is presented as the first number in each cell. The expected number of events from Monte Carlo estimates using absolute luminosity scaling are shown on the second line. The label 'nid' refers to the case where the τ decay is not identified.

7.4.2 Non-tau Cross-section Check

As additional checks on the effects of the non-tau background contamination, the cross-sections for each non-tau source are separately increased and decreased by 10% and new fits for $\langle P_\tau \rangle$ and $A_{\rm pol}^{\rm FB}$ carried out. While the cross-sections for these processes are known to better than 0.5% [5], this level of shift is applied in order to examine the sensitivity of the results to relatively large changes in these background sources.

The results of this study, given in Table 7.9, indicate that the analysis is reasonably insensitive to the relative weighting of these background sources. In particular, the $e^+e^- \rightarrow e^+e^-$ and $e^+e^- \rightarrow \mu^+\mu^-$ backgrounds, which can potentially affect the polarization kinematic distributions in sensitive regions, exhibit minimal affect on the polarization results.

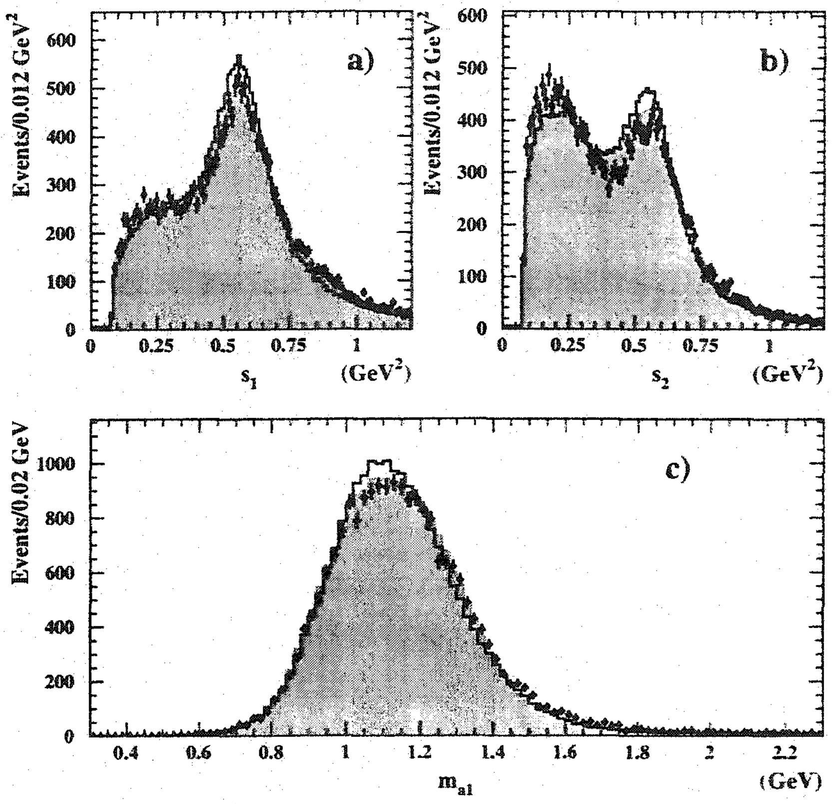

Figure 7.21: Distributions of (a) $s_1 = (p_2 + p_3)^2$, (b) $s_2 = (p_1 + p_3)^2$, and (c) m_{a_1} are presented for selected $\tau \rightarrow a_1 \nu_\tau$ tau decays. The points with error bars represent the data, the open histogram represents the Monte Carlo under the Kuhn-Santamaria model, and the shaded histogram represents the Monte Carlo when the Isgur-Morningstar-Reader model is employed. The discrepancies between data and Monte Carlo are adequately described by the variation in the Monte Carlo distributions when comparing these two models.

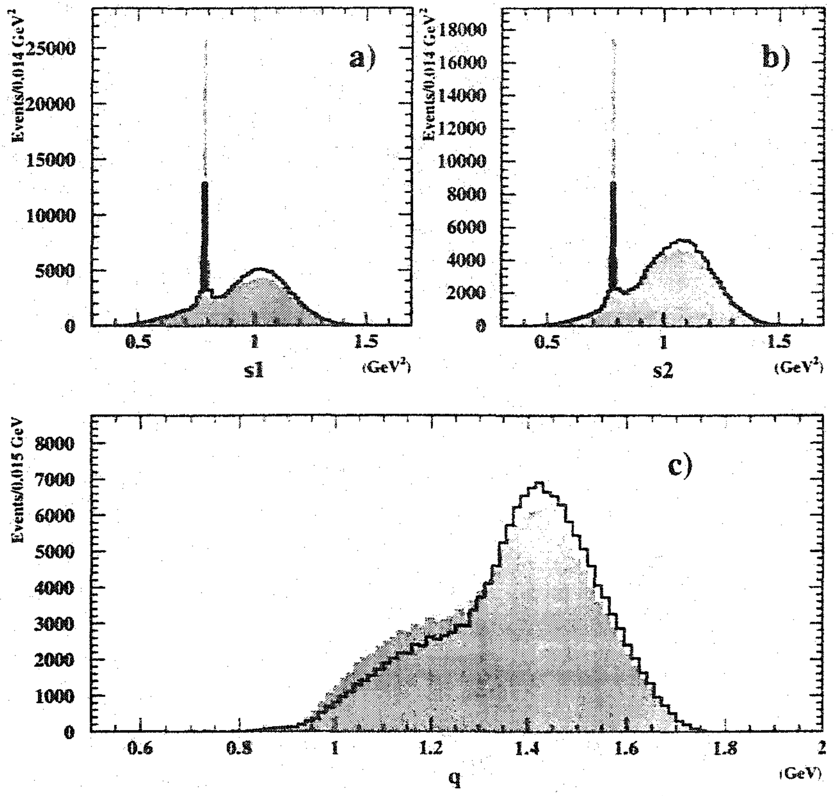

Figure 7.22: Distributions of (a) $s_1 = (p_1 + p_3 + p_4)^2$, (b) $s_2 = (p_2 + p_3 + p_4)^2$, and (c) q are presented for Monte Carlo four-vector $\tau \to 3\pi^{\mp}\pi^0\ \nu_\tau$ tau decays. Here, p_3 is the four-momentum of the unlike-sign charged pion, p_4 is the four-momentum of the neutral pion, p_1 is the four-momentum of the higher energy like-sign pion, p_1 is the four-momentum of the lower energy like-sign pion, and q is the invariant mass of the four pion system. The open histogram indicates the KORALZ default while the shaded histogram represents the variation generated by reweighting the $\omega\pi$ contribution to the decay. The level of reweighting is determined by an examination of CLEO data.

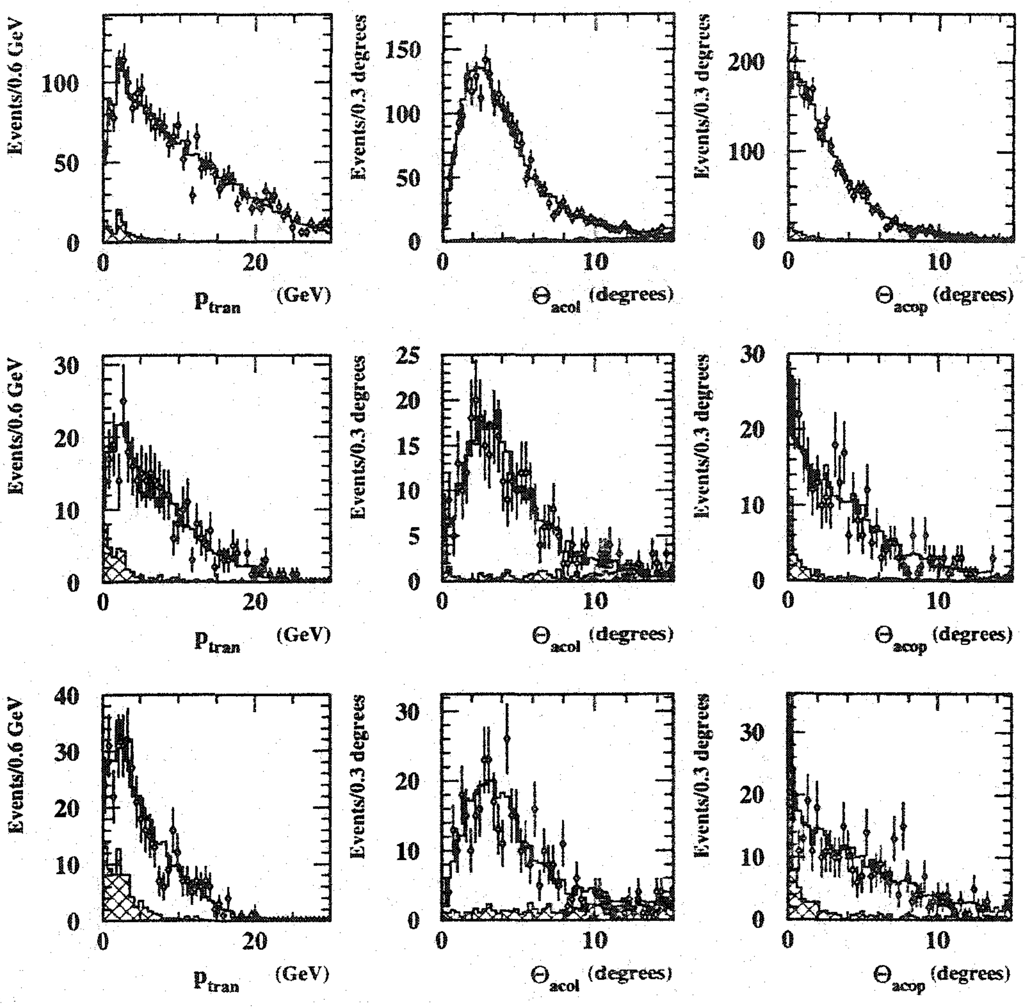

Figure 7.23: Shown are distributions of net transverse momentum (left column), acolinearity (middle column), and acoplanarity (right column) in the barrel (top row), overlap (middle row), and endcap (bottom row) regions of the detector for peak tau pair events when both taus have been selected as decaying through the electron channel. Discrepancies between the data represented by points with error bars and Monte Carlo represented by the open histograms could indicate uncontrolled non-tau background contamination. As may be seen, no evidence for such contamination appears in these figures.

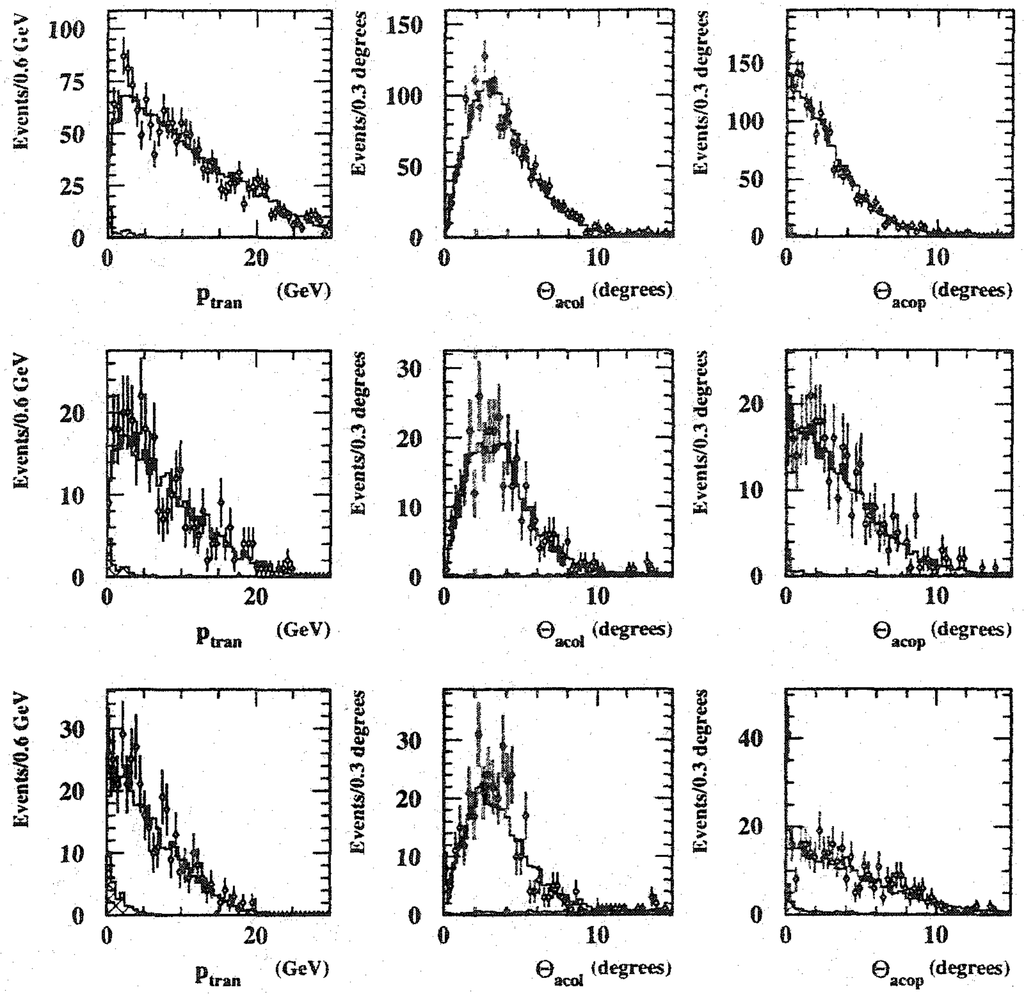

Figure 7.24: Shown are distributions of net transverse momentum (left column), acolinearity (middle column), and acoplanarity (right column) in the barrel (top row), overlap (middle row), and endcap (bottom row) regions of the detector for peak tau pair events when both taus have been selected as decaying through the muon channel. Discrepancies between the data represented by points with error bars and Monte Carlo represented by the open histograms could indicate uncontrolled non-tau background contamination. As may be seen, no evidence for such contamination appears in these figures.

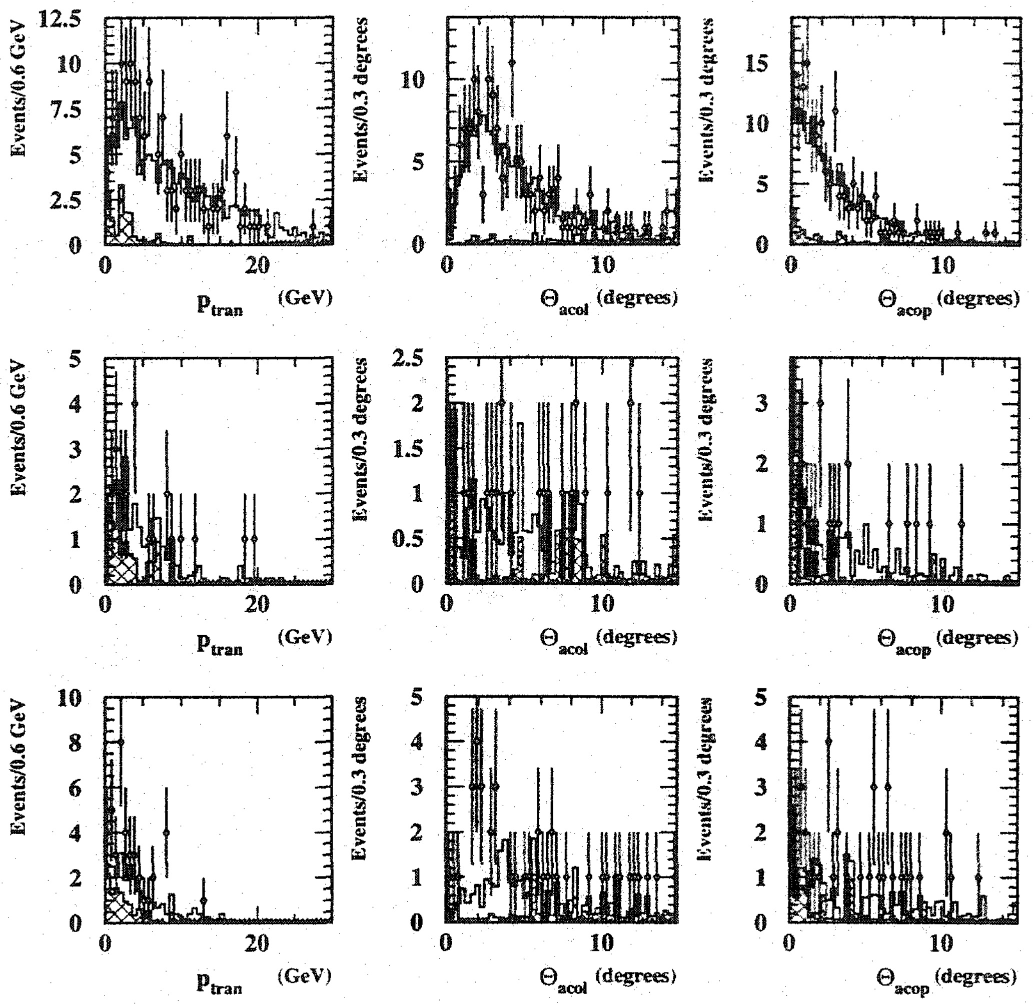

Figure 7.25: Shown are distributions of net transverse momentum (left column), acolinearity (middle column), and acoplanarity (right column) in the barrel (top row), overlap (middle row), and endcap (bottom row) regions of the detector for peak-2 tau pair events when both taus have been selected as decaying through the electron channel. Discrepancies between the data represented by points with error bars and Monte Carlo represented by the open histograms could indicate uncontrolled non-tau background contamination. As may be seen, no evidence for such contamination appears in these figures.

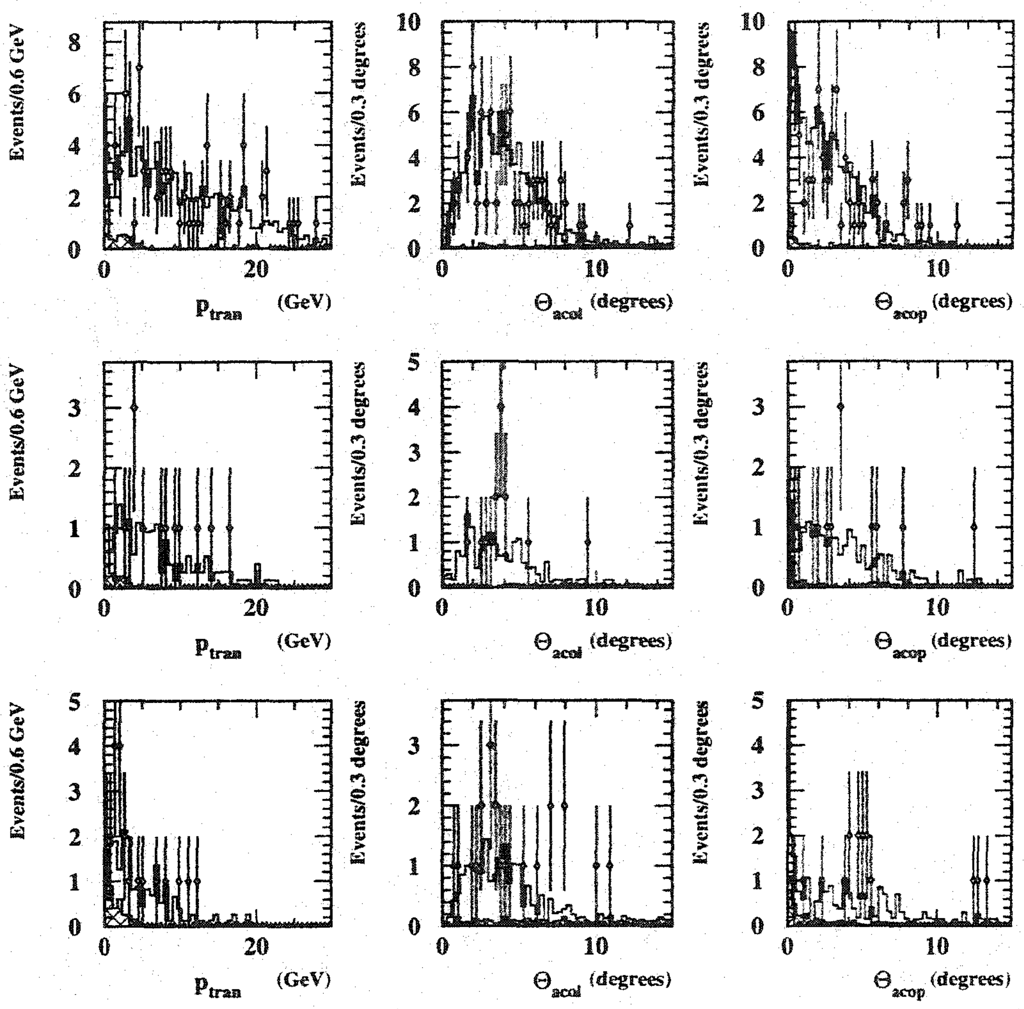

Figure 7.26: Shown are distributions of net transverse momentum (left column), acolinearity (middle column), and acoplanarity (right column) in the barrel (top row), overlap (middle row), and endcap (bottom row) regions of the detector for peak-2 tau pair events when both taus have been selected as decaying through the muon channel. Discrepancies between the data represented by points with error bars and Monte Carlo represented by the open histograms could indicate uncontrolled non-tau background contamination. As may be seen, no evidence for such contamination appears in these figures.

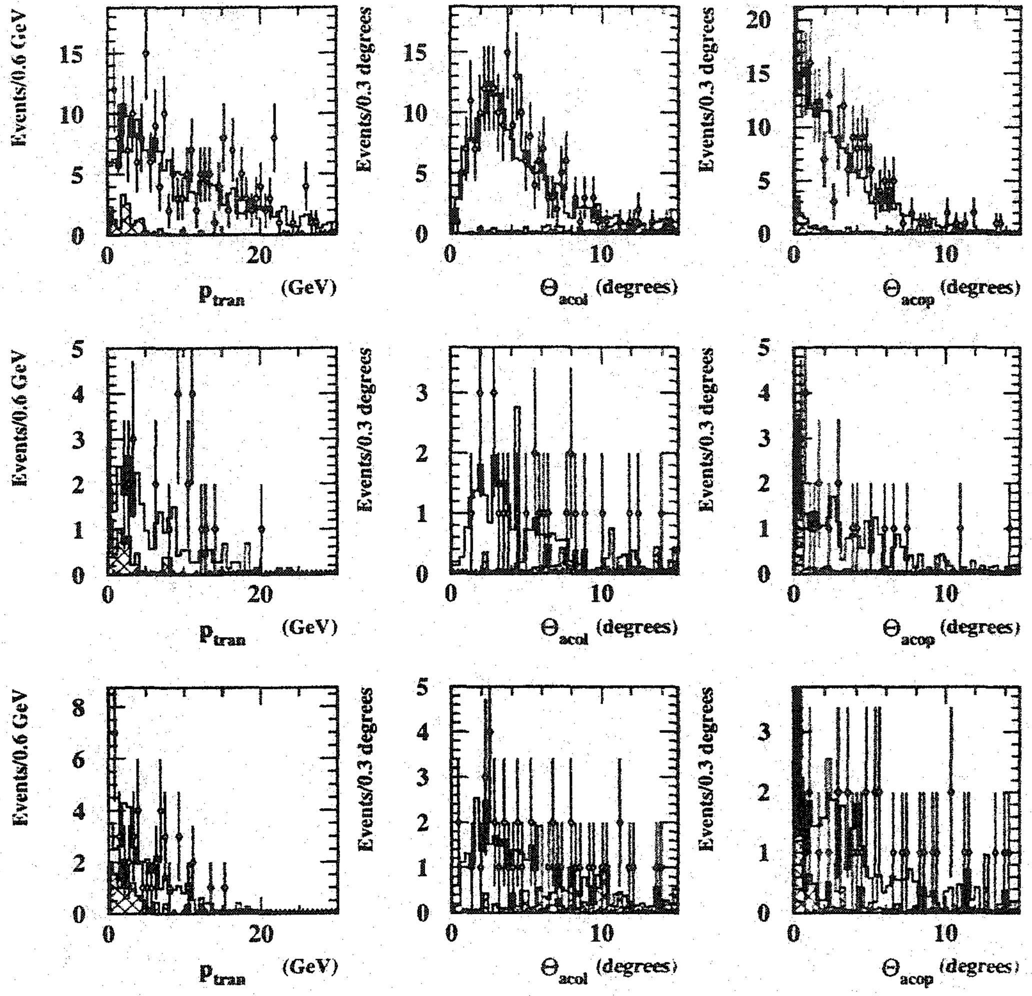

Figure 7.27: Shown are distributions of net transverse momentum (left column), acolinearity (middle column), and acoplanarity (right column) in the barrel (top row), overlap (middle row), and endcap (bottom row) regions of the detector for peak+2 tau pair events when both taus have been selected as decaying through the electron channel. Discrepancies between the data represented by points with error bars and Monte Carlo represented by the open histograms could indicate uncontrolled non-tau background contamination. As may be seen, no evidence for such contamination appears in these figures.

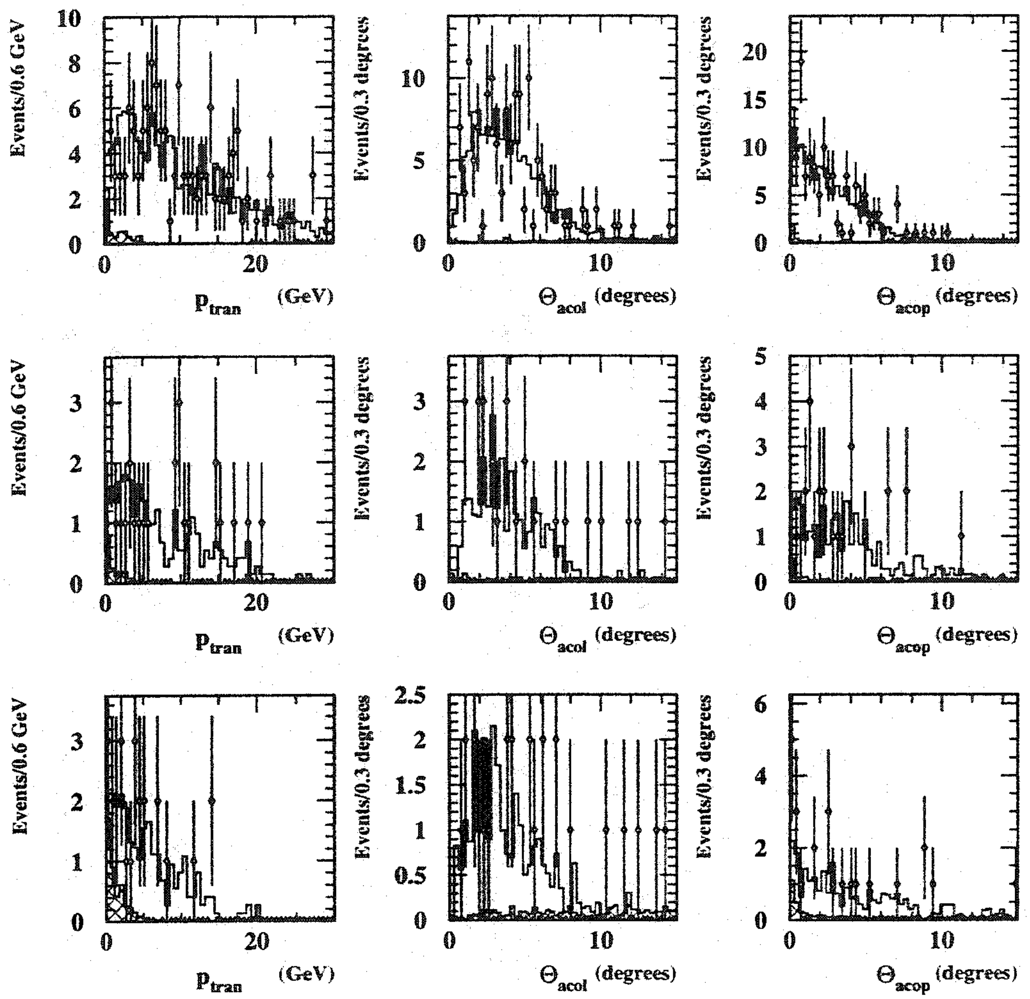

Figure 7.28: Shown are distributions of net transverse momentum (left column), acolinearity (middle column), and acoplanarity (right column) in the barrel (top row), overlap (middle row), and endcap (bottom row) regions of the detector for peak+2 tau pair events when both taus have been selected as decaying through the muon channel. Discrepancies between the data represented by points with error bars and Monte Carlo represented by the open histograms could indicate uncontrolled non-tau background contamination. As may be seen, no evidence for such contamination appears in these figures.

Systematic change	Global	$\tau\rightarrow e\bar{\nu}_e\nu_\tau$	$\tau\rightarrow \mu\bar{\nu}_\mu\nu_\tau$	$\tau\rightarrow \pi\ \nu_\tau$	$\tau\rightarrow \rho\nu_\tau$	$\tau\rightarrow a_1\ \nu_\tau$
	$\Delta\langle P_\tau\rangle$ ΔA^{FB}_{pol}	$\Delta\langle P_\tau\rangle$ ΔA^{FB}_{pol}	$\Delta\langle P_\tau\rangle$ ΔA^{FB}_{pol}	$\Delta\langle P_\tau\rangle$ ΔA^{FB}_{pol}	$\Delta\langle P_\tau\rangle$ ΔA^{FB}_{pol}	$\Delta\langle P_\tau\rangle$ ΔA^{FB}_{pol}
$e^+e^-\rightarrow \mu^+\mu^-$ 1.1σ	0.00 0.00	0.00 0.00	-0.36 0.05	0.05 0.01	0.02 0.0	0.01 0.00
$e^+e^-\rightarrow \mu^+\mu^-$ 0.9σ	0.00 -0.01	0.00 0.00	0.37 -0.05	-0.06 -0.02	-0.01 0.00	0.00 0.00
$e^+e^-\rightarrow q\bar{q}$ 1.1σ	0.01 0.00	0.00 0.00	0.00 0.00	0.00 0.00	0.01 0.00	0.02 -0.01
$e^+e^-\rightarrow q\bar{q}$ 0.9σ	0.00 0.00	0.00 0.00	0.00 0.00	-0.01 0.00	-0.01 0.00	-0.01 0.01
$e^+e^-\rightarrow e^+e^-$ 1.1σ	0.00 0.00	-0.30 -0.23	0.00 0.00	0.00 0.00	0.01 0.01	0.00 0.00
$e^+e^-\rightarrow e^+e^-$ 0.9σ	0.01 0.00	0.30 0.23	0.00 0.00	-0.01 -0.01	-0.01 -0.01	0.00 0.00
$\gamma\gamma\mu^+\mu^-1.1\sigma$	0.01 0.00	0.00 0.00	0.05 0.00	0.00 0.00	0.00 0.00	0.00 0.00
$\gamma\gamma\mu^+\mu^-0.9\sigma$	0.00 0.00	0.00 0.00	-0.06 0.00	0.00 0.00	0.00 0.00	0.00 0.00
$\gamma\gamma e^+e^-1.1\sigma$	0.02 0.00	0.36 0.02	0.00 0.00	0.00 0.00	0.00 0.00	0.00 0.00
$\gamma\gamma e^+e^-0.9\sigma$	-0.02 0.00	-0.36 -0.02	0.00 0.00	0.00 0.00	0.00 0.00	0.00 0.00

Table 7.9: Presented are the variations in the fit parameter values when each of the non-tau background cross-sections are increased and decreased by 10%. The variations are expressed in percent polarization.

7.4.3 Multihadron Background Check

As indicated in the tau pair selection section of Chapter 5, the primary difference between tau pair and $e^+e^- \rightarrow q\bar{q}$ events is the low event track multiplicity of the former compared to the latter. This means that the majority of $e^+e^- \rightarrow q\bar{q}$ background contaminating the tau pair sample will be in the form of fake multi-track tau jets; hence it is in the a_1 channel where $e^+e^- \rightarrow q\bar{q}$ background is expected to be prevalent.

An excellent method for ensuring that this background is well controlled is to examine the distribution of total tracks associated to tau jets when the opposite tau jet has been selected as a $\tau \rightarrow a_1\ \nu_\tau$ decay. Figure 7.29 shows plots of this distribution for each of the three detector regions. The data and Monte Carlo distributions show good agreement indicating that the $e^+e^- \rightarrow q\bar{q}$ background is well modelled.

7.4.4 Variable Dropping Cross Check

To ensure that the analysis is not unduly sensitive to the inclusion of any particular variable, the likelihood selections are regenerated with variables from the nominal selection removed. In each instance, a given variable is removed and a new set of likelihood distributions generated. The analysis is then completely re-rerun with the new selection applied to both Monte Carlo and data and new estimates for $\langle P_\tau \rangle$ and A^{FB}_{pol} generated. Table 7.10 gives the differences between these new values and the nominal fit values for when various variables important to the analysis are dropped.

As may be seen in the table, several of the variables listed have an effect on the fit values. However, it must be remembered that appreciable statistical effects can occur when such alterations are made. The fact that the variations are, in all cases, less than the total systematic error gives confidence that the selections are not overly sensitive to any given variable and provides a general indication that the evaluated systematic uncertainties are reasonable.

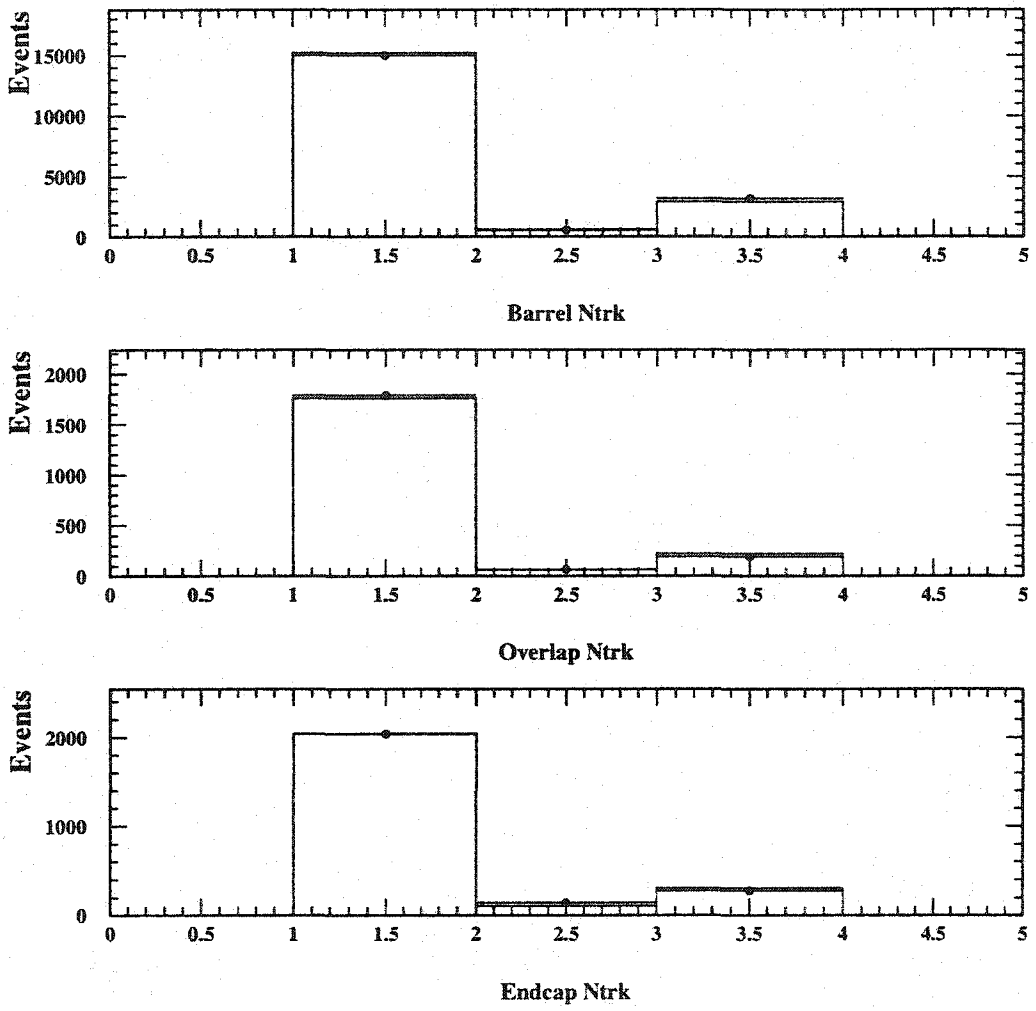

Figure 7.29: Shown are the number of tracks in tau jets opposite those selected as $\tau \rightarrow a_1 \nu_\tau$ decays. The good agreement between the data, represented by the points with error bars, and the Monte Carlo, represented by the open histogram, provides confidence that no uncontrolled $e^+e^- \rightarrow q\bar{q}$ background is contaminating this sample.

Variable Dropped	Global	$\tau\rightarrow e\bar{\nu}_e\nu_\tau$	$\tau\rightarrow \mu\bar{\nu}_\mu\nu_\tau$	$\tau\rightarrow \pi\ \nu_\tau$	$\tau\rightarrow \rho\nu_\tau$	$\tau\rightarrow a_1\ \nu_\tau$
	$\Delta\langle P_\tau\rangle$ ΔA^{FB}_{pol}	$\Delta\langle P_\tau\rangle$ ΔA^{FB}_{pol}	$\Delta\langle P_\tau\rangle$ ΔA^{FB}_{pol}	$\Delta\langle P_\tau\rangle$ ΔA^{FB}_{pol}	$\Delta\langle P_\tau\rangle$ ΔA^{FB}_{pol}	$\Delta\langle P_\tau\rangle$ ΔA^{FB}_{pol}
$HCAL_{tot}$	-0.12 -0.01	0.01 -0.01	-1.04 0.10	0.07 0.07	-0.18 -0.03	-0.03 0.02
$MUON_{tot}$	-0.02 0.01	0.04 -0.01	0.44 -0.21	0.28 0.08	-0.06 0.13	-0.48 0.00
ϕ_{pres}	0.03 0.00	-0.05 -0.06	0.37 -0.11	0.01 0.17	0.25 0.03	0.00 0.01
dE/dx(e)	-0.23 -0.09	-0.06 0.27	-0.27 -0.02	-0.19 -0.21	-0.20 0.28	-0.06 -0.51
dE/dx(π)	0.30 0.31	0.78 0.61	0.46 0.24	1.00 0.25	-0.29 0.50	-0.12 -0.26
$MU\text{-}CT_{wght}$	0.00 -0.12	-0.12 -0.22	0.20 -0.32	-0.06 -0.05	0.25 0.06	-0.26 0.30
m_ρ	0.40 0.17	0.60 0.37	0.05 0.00	-0.02 -0.02	0.58 0.40	0.03 -0.06
E_{ass}/p	0.06 -0.27	0.36 -0.72	-0.51 0.28	-0.35 -0.71	-0.03 0.05	0.88 0.19
E_{tot}/p	-0.17 0.01	-0.37 -0.08	0.16 0.05	-0.52 -0.11	0.00 0.06	-1.10 1.27
E_{ass}	-0.17 -0.01	0.00 0.03	-0.77 0.06	-0.23 -0.14	-0.02 0.00	0.03 -0.01
E_{neut}/p	-0.06 -0.04	-0.15 0.02	0.02 0.11	-0.10 -0.16	0.11 0.12	0.03 0.04
m_{jet}	0.28 0.15	0.06 -0.05	0.13 -0.15	0.00 0.25	0.56 0.16	0.05 0.04

Table 7.10: The variations in the fit parameter estimates, expressed in percent polarization, are given for cases when the indicated variable is dropped out of the likelihood selection.

7.4.5 Fit Bias Check

One of the most important checks for this analysis is to ensure that no systematic biases have been introduced in the fit estimates for $\langle P_\tau \rangle$ and A^{FB}_{pol} .

The many consistency checks discussed in Chapter 6 provide strong indications that no biases exist. As is shown, the channel-by-channel fits are in good agreement signifying consistency and lack of bias across the selected decay channels. The tau pair identification consistency check provides an even stronger check; again, it is shown that no evidence for biases in a given class exists.

In addition to these tests, a number of additional studies are carried out to ensure that no unaccounted for biases have been introduced into the analysis.

First, Monte Carlo studies are undertaken to determine whether the tau pair selection is sensitive to the generated polarization of the event sample. Table 7.11 indicates the polarization before and after tau pair selection for Monte Carlo as a function of $\cos\theta_{\tau^-}$. As may be seen, no bias from the selection is introduced in the barrel region of the detector, but the overlap and endcap regions do exhibit small biases. This is not a difficulty, in principal, as long as the data are well modelled and the generated polarization values, in contrast to the selected values, are used to renormalize the Monte Carlo reference distributions.

To the extent that the Monte Carlo does not describe the data well, the systematic error studies discussed in the detector and physics modelling sections of this chapter have already been taken into account. An important question remains. Are there any remaining unaccounted for sources of systematic effects or biases? One particular case that must be considered is whether the generation of the selections, in particular the tau decay likelihood selections, using Monte Carlo created with a pre-set polarization value has any effect on the final results. In order to examine this question, two studies are undertaken.

First, a Monte Carlo study is undertaken in which subsamples of the Monte Carlo, generated average polarizations ranging from $\langle P_\tau \rangle$ =-1.0 to $\langle P_\tau \rangle$ =+1.0 and with forward-backward polarization asymmetries ranging from A^{FB}_{pol} =-3/4 to A^{FB}_{pol} =+3/4, are fit with the nominal Monte Carlo reference distributions. The results of this study are shown

Region	Generated $\langle P_\tau \rangle$	Selected $\langle P_\tau \rangle$
$0.00 < \lvert\cos\theta_{\tau^-}\rvert < 0.09$	-0.1378 ± 0.0026	-0.1372 ± 0.0027
$0.09 < \lvert\cos\theta_{\tau^-}\rvert < 0.18$	-0.1331 ± 0.0025	-0.1330 ± 0.0027
$0.18 < \lvert\cos\theta_{\tau^-}\rvert < 0.27$	-0.1352 ± 0.0025	-0.1382 ± 0.0027
$0.27 < \lvert\cos\theta_{\tau^-}\rvert < 0.36$	-0.1368 ± 0.0024	-0.1358 ± 0.0026
$0.36 < \lvert\cos\theta_{\tau^-}\rvert < 0.45$	-0.1366 ± 0.0024	-0.1380 ± 0.0025
$0.45 < \lvert\cos\theta_{\tau^-}\rvert < 0.54$	-0.1370 ± 0.0023	-0.1365 ± 0.0025
$0.54 < \lvert\cos\theta_{\tau^-}\rvert < 0.63$	-0.1350 ± 0.0022	-0.1359 ± 0.0024
$0.63 < \lvert\cos\theta_{\tau^-}\rvert < 0.72$	-0.1349 ± 0.0021	-0.1383 ± 0.0023
$0.72 < \lvert\cos\theta_{\tau^-}\rvert < 0.81$	-0.1377 ± 0.0020	-0.1680 ± 0.0024
$0.81 < \lvert\cos\theta_{\tau^-}\rvert < 0.90$	-0.1381 ± 0.0019	-0.1536 ± 0.0023
$0.00 < \lvert\cos\theta_{\tau^-}\rvert < 0.90$	-0.1363 ± 0.0007	-0.1420 ± 0.0008

Table 7.11: Presented are the Monte Carlo polarizations in 10 $\cos\theta_{\tau^-}$ bins both before and after the tau pair selection is applied. No indications of polarization bias are evident in the barrel region of the detector while small biases do exist in the overlap and endcap regions. These small biases are appropriately accounted for in the fitting algorithm.

in Figures 7.30 and 7.31 and indicate that, within statistical fluctuations, the reference distributions extract the correct polarization values from the test samples.

For the second study, two separate sets of new tau selection likelihood distributions are generated; the first one using only right-handed taus and the second using only left-handed taus. The analysis is then rerun with each of these new selections and parameter estimates for $\langle P_\tau \rangle$ and A^{FB}_{pol} determined. As can be seen in Table 7.12, the differences between these new values and the nominal fit are small, thus indicating that no significant unaccounted for bias is introduced by the tau decay selection procedure.

7.5 Summary

In the first section of this chapter, the detector modelling systematic errors are evaluated. It is shown that uncertainties associated with momentum measurements in the central tracking system and cluster measurements in the ECAL dominated and are of similar importance. The modelling of the outer detectors and of the dE/dx distributions is also important, but of less impact to the overall systematic errors.

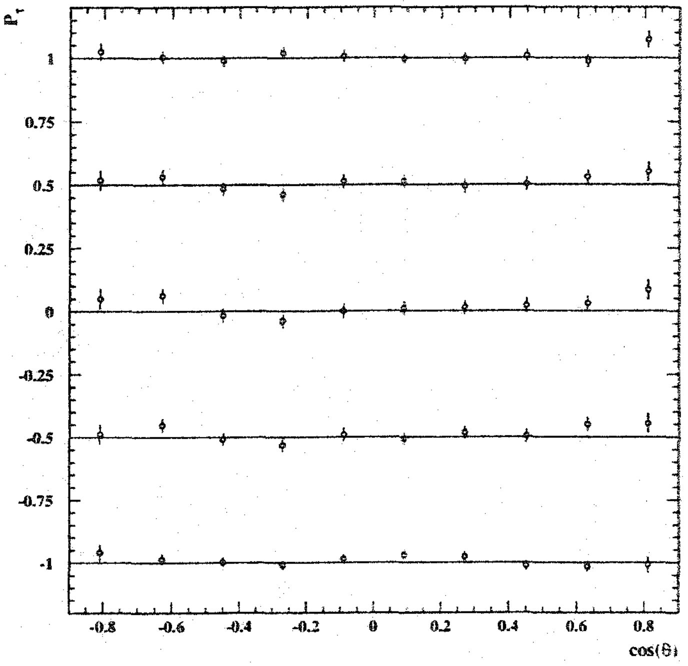

Figure 7.30: Shown are a series five fits to Monte Carlo samples generated with $A_{\mathrm{pol}}^{\mathrm{FB}} = 0$ and $\langle P_\tau \rangle$ ranging from 1 to -1. The solid lines represent the input polarization value and the open circles with error bars represent the polarization fit values in each of 10 $\cos\theta_{\tau^-}$ bins. The good agreement between the input and fit values indicates that the fitting procedure, after detector simulation and selection effects are applied, reproduces the input values in an unbiased fashion.

Systematic uncertainties associated with the modelling of the underlying physics and measured input parameters are described in the second section of the chapter. The errors here are dominated by uncertainty in the a_1 decay modelling and by the finite Monte Carlo statistics. Other modelling considerations, such as decay radiation, and the effects of uncertainties on measured input parameters, such as the tau branching ratios, prove to make only small contributions to the overall systematic uncertainties.

Section 7.4 explores a wide range of consistency checks which, in concert with those provided in Chapter 6, confirm the validity of the systematic error studies and provide confidence in the overall stability of the analysis.

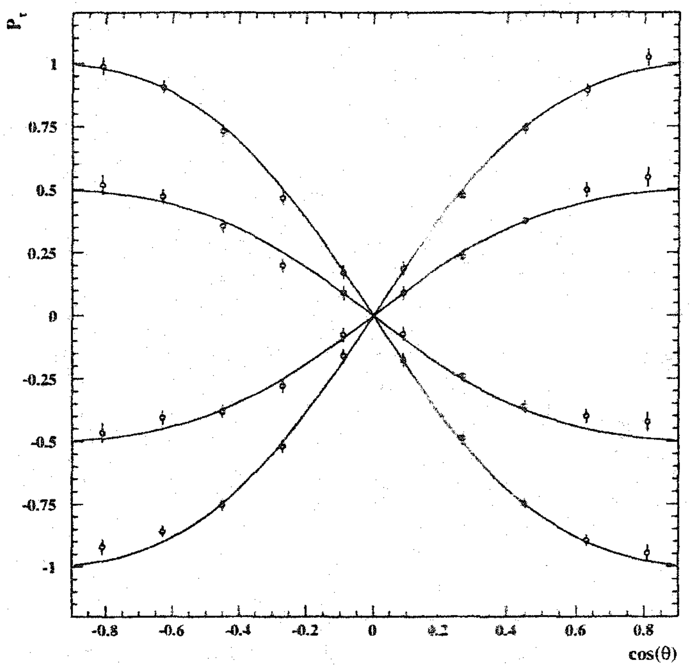

Figure 7.31: Shown are a series five fits to Monte Carlo samples generated with $\langle P_\tau \rangle = 0$ and A^{FB}_{pol} ranging from $3/4$ to $-3/4$. The solid lines represent the input polarization value and the open circles with error bars represent the polarization fit values in each of 10 $\cos\theta_{\tau^-}$ bins. The good agreement between the input and fit values indicates that the fitting procedure, after detector simulation and selection effects are applied, reproduces the input values in an unbiased fashion.

The final total systematic errors have been ascertained to be 0.0055 and 0.0025 on $\langle P_\tau \rangle$ and A^{FB}_{pol} respectively. Table 7.13 provides the channel-by-channel systematic error results for each of the systematic error sources along with the results from the global fit.

Fit	$\langle P_\tau \rangle$	A^{FB}_{pol}
Nominal	-0.1410±0.0073	-0.1055±0.0076
Right-Handed Likelihood	-0.1426±0.0073	-0.1010±0.0076
Left-Handed Likelihood	-0.1403±0.0074	-0.1007±0.0077

Table 7.12: The nominal global fit values are compared to the analogous fit values when the likelihood selection distributions are generated from a completely right-handed set of Monte Carlo tau events and when they are generated with a completely left-handed set of tau events. The variation from the nominal values are small indicating that no large biases are introduced by generating the likelihood distributions with Monte Carlo events generated with the polarizaton given in Table 7.11.

	$\Delta\langle P_\tau\rangle$ and ΔA_{pol}^{FB}											
	e		μ		π		ρ		a_1		Global fit	
Momentum scale/resolution	0.4	0.2	2.1	0.1	0.8	0.1	0.3	0.1	0.4	0.2	0.24	0.13
ECAL scale/resolution	3.2	0.1	0.2	0.1	0.2	–	1.1	0.2	0.3	0.1	0.17	0.11
HCAL/MUON modelling	0.1	–	1.1	0.1	0.5	0.1	–	–	–	–	0.13	0.05
dE/dx errors	0.6	0.1	0.3	0.1	0.3	0.1	0.1	0.1	0.3	0.1	0.12	0.08
Shower modelling in ECAL	0.6	0.1	0.2	0.1	0.4	0.1	0.5	0.2	0.4	0.1	0.25	0.10
Branching ratios	0.1	–	0.1	–	0.2	–	0.2	–	0.2	0.1	0.11	0.02
$\tau \rightarrow a_1\ \nu_\tau$ modelling	–	–	–	–	–	–	0.4	–	0.5	0.1	0.22	0.02
$\tau \rightarrow 3\pi \geq 1\pi^0\ \nu_\tau$ modelling	–	–	–	–	–	–	–	–	1.2	0.1	0.11	0.04
A_{FB}	–	0.2	–	–	–	–	–	–	–	–	0.03	0.02
Decay radiation	–	–	–	–	–	–	–	–	0.1	–	0.01	0.01
Monte Carlo statistics	0.7	0.2	0.8	0.3	0.3	0.1	0.3	0.1	0.8	0.2	0.22	0.10
total	3.4	0.4	2.6	0.4	1.2	0.2	1.3	0.3	1.7	0.3	0.55	0.25

Table 7.13: Tabulation of systematic errors contributing to $\langle P_\tau\rangle$ and A_{pol}^{FB} when these asymmetries are expressed as a percentage, for each of the five decay modes analyzed and the global fit. In each column the error on $\langle P_\tau\rangle$ is given first followed by that on A_{pol}^{FB}. Systematic error correlations between the five channels are fully incorporated into the systematic error on the global result. In the second to sixth columns a dash indicates that the listed effect contributes less than 0.05%.

The value of carrying out the systematic error analysis on the global fit, which automatically includes the correlations between channels, is evident when comparing the channel-by-channel errors to the global error from a given source. For example, the global momentum scale/resolution error on $\langle P_\tau \rangle$ calculated by combining the channel-by-channel errors, weighted by the statistical power of each channel to measure $\langle P_\tau \rangle$, would give 0.0035 compared to 0.0023 for the global fit analysis.

It is also apparent that, for the global fit, the most important of the error sources contribute at a similar level. Consequently, a significant reduction in any one of these systematic uncertainties will not reduce the overall systematic uncertainty by an appreciable amount, thus implying that the current systematic error analysis can not be greatly improved upon.

The final fit results, including both statistical and systematic errors, are

$$\begin{aligned} \langle P_\tau \rangle &= (-14.10 \pm 0.73 \pm 0.55)\% \\ A_{\rm pol}^{\rm FB} &= (-10.55 \pm 0.76 \pm 0.25)\%. \end{aligned} \tag{7.2}$$

where the combined statistical and systematic correlations are estimated to be 2.5%. The systematic correlations are determined by carrying out the full systematic studies analyses on both the two parameter fit when universality is not assumed and a one parameter fit when universality is assumed.

Chapter 8

Discussion and Summary

"Do I understand you correctly? You spent all of this time just to get that number???"
Anonymous

8.1 Asymmetry Parameters, Universality, and $\sin^2\theta_{\mathrm{eff}}^{\mathrm{lept}}$

The definition of the neutral coupling asymmetry parameters is given in Chapter 2 and the relationship between these parameters and $\langle P_\tau \rangle$ and $A_{\mathrm{pol}}^{\mathrm{FB}}$ discussed. In order to carry out the universality test and to interpret these measurements, it is useful to transform the global fit parameter values of equation 6.2 into these quantities.

Using the program ZFITTER to effect this transformation gives

$$\begin{aligned} A_\tau &= 0.1456 \pm 0.0076 \pm 0.0057, \\ A_e &= 0.1454 \pm 0.0108 \pm 0.0036, \end{aligned} \tag{8.1}$$

where the combined statistical and systematic correlation between these values is 2.5%. The ratio of A_τ and A_e gives

$$A_\tau / A_e = 1.00 \pm 0.091 \pm 0.042 \tag{8.2}$$

where the statistical and systematic errors have been combined, and the universality of the couplings is manifest. The two values may then be combined to produce the result

$$A_\ell = 0.1455 \pm 0.0062 \pm 0.0038 \tag{8.3}$$

with universality assumed.

Also described in Chapter 2 is the relationship between the neutral coupling asymmetry parameters and the ratio of the vector and axial-vector couplings. Using Equation 2.17, A_τ and A_e may be written as

$$\begin{aligned} g_V^\tau / g_A^\tau &= 0.0732 \pm 0.0048, \\ g_V^e / g_A^e &= 0.0731 \pm 0.0057, \end{aligned}$$

and the combined result gives

$$g_V^\ell / g_A^\ell = 0.0732 \pm 0.0037. \tag{8.4}$$

Finally, using Equation 2.18, the combined results can be expressed as

$$\sin^2 \theta_{\mathrm{eff}}^{\mathrm{lept}} = 0.23172 \pm 0.00092. \tag{8.5}$$

8.2 Combined Lineshape and Asymmetry Results from OPAL

The tau polarization results can be combined with the measurements from the leptonic partial widths and forward-backward asymmetries published by OPAL[15] to provide measurements of g_V^ℓ and g_A^ℓ for electrons, muons and τ leptons separately. While A_τ and A_e provide measurements of g_V^ℓ / g_A^ℓ for the τ and electron, the leptonic partial widths of the Z^0 provide measurements of ${g_V^\ell}^2 + {g_A^\ell}^2$ for all three lepton flavours. The forward-backward asymmetries determine $(g_V^e g_V^\ell)/(g_A^e g_A^\ell)$ for electrons, muons and τ leptons yielding additional information about g_V^τ / g_A^τ and g_V^e / g_A^e, and provide the only means of measuring g_V^μ / g_A^μ at LEP.

m_ZGeV	91.1858 ± 0.0030
Γ_ZGeV	2.4948 ± 0.0041
σ_h^0 (nb)	41.501 ± 0.055
R_e	20.902 ± 0.084
R_μ	20.811 ± 0.058
R_τ	20.832 ± 0.091
$A_{FB}^{0,e}$	0.0089 ± 0.0044
$A_{FB}^{0,\mu}$	0.0159 ± 0.0023
$A_{FB}^{0,\tau}$	0.0145 ± 0.0030
A_e	0.1454 ± 0.0114
A_τ	0.1456 ± 0.0095

Table 8.1: The first nine parameters are the result of fitting the model-independent Z^0 parameters to the measured cross-sections and asymmetries measured by OPAL [15]. The parameters A_e and A_τ are the result of this τ polarization measurement.

	m_Z	Γ_Z	σ_h^0	R_e	R_μ	R_τ	$A_{FB}^{0,e}$	$A_{FB}^{0,\mu}$	$A_{FB}^{0,\tau}$	A_e	A_τ
m_Z	1.00	0.05	0.03	0.11	0.00	0.00	−0.05	0.08	0.06	0.00	0.00
Γ_Z	0.05	1.00	−0.35	0.01	0.02	0.01	0.00	0.00	0.00	0.00	0.00
σ_h^0	0.03	−0.35	1.00	0.15	0.22	0.14	0.01	0.01	0.01	0.00	0.00
R_e	0.11	0.01	0.15	1.00	0.09	0.04	−0.20	0.03	0.02	0.00	0.00
R_μ	0.00	0.02	0.22	0.09	1.00	0.06	0.00	0.01	0.00	0.00	0.00
R_τ	0.00	0.01	0.14	0.04	0.06	1.00	0.00	0.00	0.01	0.00	0.00
$A_{FB}^{0,e}$	−0.05	0.00	0.01	−0.20	0.00	0.00	1.00	−0.02	−0.01	0.00	0.00
$A_{FB}^{0,\mu}$	0.08	0.00	0.01	0.03	0.01	0.00	−0.02	1.00	0.02	0.00	0.00
$A_{FB}^{0,\tau}$	0.06	0.00	0.01	0.02	0.00	0.01	−0.01	0.02	1.00	0.00	0.01
A_e	0.00	0.00	0.00	0.00	0.00	0.00	0.00	0.00	0.00	1.00	0.03
A_τ	0.00	0.00	0.00	0.00	0.00	0.00	0.00	0.00	0.01	0.03	1.00

Table 8.2: Error correlation matrix for the 11 parameters entering the fit for the leptonic couplings presented in Table 8.1.

The OPAL measurements of the hadronic and leptonic cross-sections and leptonic forward-backward asymmetries at the Z^0 pole are summarized in terms of nine model-independent Z^0 parameters as defined in Reference [15]: the mass (m_Z), width (Γ_Z) and the hadronic pole cross-section (σ_h^0) of the Z^0 resonance; the ratios of the hadronic to leptonic partial widths (R_e,R_μ and R_τ); and the leptonic pole forward-backward asymmetries ($A_{FB}^{0,\mu}$,$A_{FB}^{0,\mu}$ and $A_{FB}^{0,\tau}$). The values of these nine parameters, together with the polarization asymmetries reported here, are displayed in Table 8.1 and the error correlation matrix in Table 8.2.

	Without lepton universality	With lepton universality	standard model prediction
A_e	0.1375 ± 0.0093		
A_μ	0.154 ± 0.024		
A_τ	0.1449 ± 0.0091		
A_ℓ		0.1424 ± 0.0054	$0.1450^{+0.0030}_{-0.0084}$

Table 8.3: The leptonic neutral current asymmetry parameters obtained from a fit to the Z^0 parameters given in Table 8.1. In the last column is given the value of the parameter calculated in the context of the standard model assuming the parameter variations given in the text.

	A_e	A_μ	A_τ
A_e	1.00	−0.43	−0.09
A_μ	−0.43	1.00	0.04
A_τ	−0.09	0.04	1.00

Table 8.4: Error correlation matrix for the measurements of the leptonic neutral current asymmetry parameters, which are presented in Table 8.3.

Information from the tau polarization and forward-backward asymmetry measurements can be combined to provide measurements of the three leptonic neutral current asymmetry parameters, A_e , A_μ and A_τ . These and their error correlation maxtrix are shown in Tables 8.3 and 8.4. The results for the three lepton species are consistent with each other and agree well with the prediction of the standard model[1] which is also shown in Table 8.3. Assuming lepton universality,

$$\mathrm{A}_\ell = 0.1424 \pm 0.054. \tag{8.6}$$

This can also be expressed in terms of the effective weak mixing angle:

$$\sin^2\theta_{\mathrm{eff}}^{\mathrm{lept}} = 0.23211 \pm 0.00068. \tag{8.7}$$

The eleven model-independent Z^0 parameters listed in Table 8.1 can also be used to determine the neutral current vector and axial-vector couplings for each lepton species. The results and the error correlation matrix are given in Tables 8.5 and 8.6 and are illustrated in Figure 8.1. Evident from these results is the universality of the coupling constants which can be quantified in terms of the ratios of the couplings [2]:

$$\frac{\mathrm{g}_\mathrm{A}^\mu}{\mathrm{g}_\mathrm{A}^e} = 1.0011 \pm 0.0025, \quad \frac{\mathrm{g}_\mathrm{A}^\tau}{\mathrm{g}_\mathrm{A}^e} = 1.0021 \pm 0.0029, \quad \frac{\mathrm{g}_\mathrm{A}^\tau}{\mathrm{g}_\mathrm{A}^\mu} = 1.0009 \pm 0.0027,$$

$$\frac{\mathrm{g}_\mathrm{V}^\mu}{\mathrm{g}_\mathrm{V}^e} = 1.12\pm^{0.24}_{0.21}, \qquad \frac{\mathrm{g}_\mathrm{V}^\tau}{\mathrm{g}_\mathrm{V}^e} = 1.06\pm^{0.11}_{0.10}, \qquad \frac{\mathrm{g}_\mathrm{V}^\tau}{\mathrm{g}_\mathrm{V}^\mu} = 0.94\pm^{0.18}_{0.14}.$$

The axial-vector couplings are found to be the same at the 0.3% level. The vector couplings are also the same but, because of the small size of the vector couplings, the relative uncertainties on the ratio of vector couplings are much larger. These errors have been significantly reduced by adding information from the tau polarization to the lineshape and forward-backward asymmetry measurements[15].

Combining the values of the coupling constants from the different lepton species under the assumption of lepton universality yields the values

$$\begin{aligned} \mathrm{g}_\mathrm{A}^\ell &= -0.50089 \pm 0.00045, \\ \mathrm{g}_\mathrm{V}^\ell &= -0.0358 \pm 0.0014. \end{aligned}$$

---

[1] The standard model calculations require the full specification of the fundamental standard model parameters. The main parameters are the masses of the Z^0 boson (m_Z), the top quark (m_t) and the Higgs boson (m_H), and the strong and electromagnetic coupling constants, α_s and α. As in Reference [15] the calculation of standard model predictions use the following values and ranges: $m_Z = 91.1856 \pm 0.0030$ GeV, $m_t = 175 \pm 5$ GeV, $m_H = 150^{+850}_{-60}$ GeV, $\alpha_s = 0.119 \pm 0.002$, and $\alpha(m_Z{}^2)^{-1} = 128.886 \pm 0.090$. The choice of these parameter values and ranges is discussed in Reference [15].

[2] These ratios can have correlations as high as approximately 50% between them.

where the correlation between g_A^ℓ and g_V^ℓ is -19%, which is approximately the same as the -21% correlation between g_A^ℓ and $\sin^2\theta_{\text{eff}}^{\text{lept}}$. These are in good agreement with the predictions of the standard model, which are included in Table 8.5.

	Without lepton universality	With lepton universality	Standard Model prediction
g_A^e	-0.50062 ± 0.00062		
g_A^μ	-0.50117 ± 0.00099		
g_A^τ	-0.50165 ± 0.00124		
g_A^ℓ		-0.50089 ± 0.00045	$-0.50130^{+0.00047}_{-0.00013}$
g_V^e	-0.0346 ± 0.0023		
g_V^μ	$-0.0388^{+0.0060}_{-0.0064}$		
g_V^τ	-0.0365 ± 0.0023		
g_V^ℓ		-0.0358 ± 0.0014	$-0.0365^{+0.0022}_{-0.0008}$

Table 8.5: Axial-vector and vector couplings obtained from a fit to the parameter set given in Table 8.1. In the last column we give the values of the couplings calculated in the context of the standard model assuming the parameter variations given in the text.

8.3 Comparison With Other Experiments

An important aspect of the description of any experimental measurement is the comparison of results, where possible, with similar measurements from other experiments. For the tau polarization measurement, it is not only the comparison of results that is of importance, but ultimately the combining of independent measurements in order to produce parameter estimates which are as accurate as possible. The polarization measurement presented here is dominated by statistical errors; hence the reduction of the statistical error through combining the results provides a significant improvement. As will be seen, such an improvement in precision allows important constraints on the mass of a standard model Higgs particle to be made.

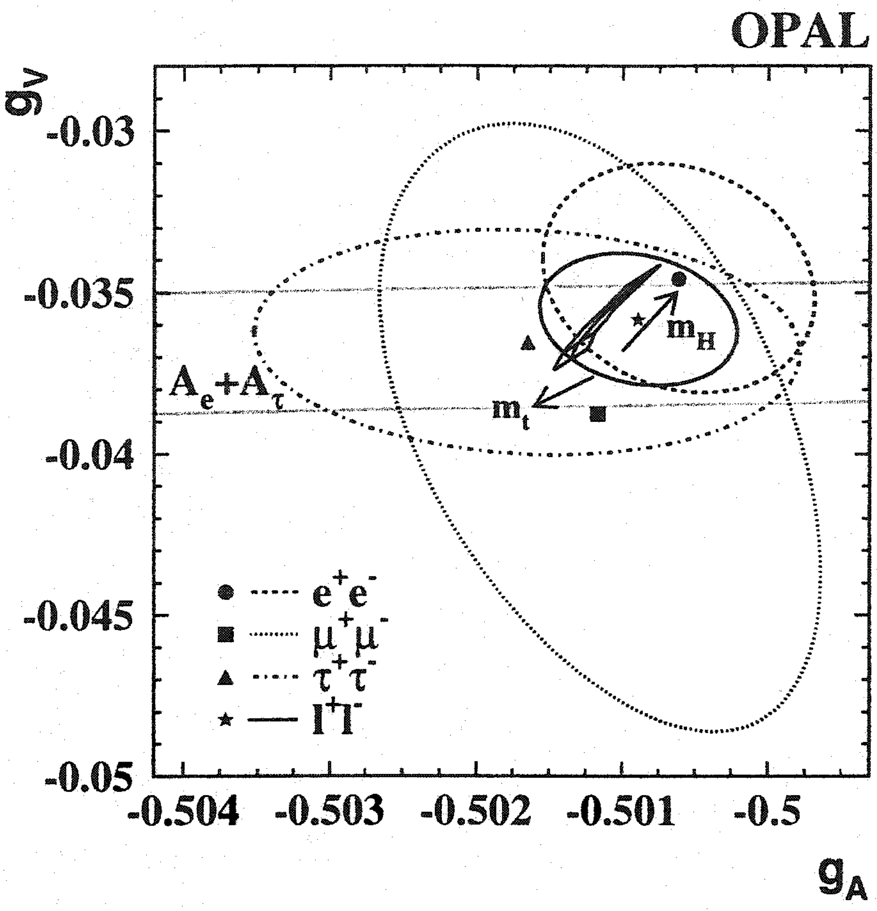

Figure 8.1: g_V^ℓ *vs* g_A^ℓ as determined from the OPAL measurements of the leptonic partial widths of the Z^0, forward-backward asymmetries and tau polarization measurements. The ellipses represent the 68% confidence level contours in the g_V^ℓ -g_A^ℓ plane for each lepton species separately (dotted and dashed) and for all leptons assuming universality (solid). The central values are displayed at the centre of the ellipses as a circle, square, triangle and star for electrons, muons, tau leptons and all leptons under universality, respectively. The standard model prediction is shown with variations from the top quark mass (170 to 180 GeV) and Higgs mass (90 to 1000 GeV) indicated. The OPAL tau polarization measurements of A_τ and A_e constrain g_V^ℓ and g_A^ℓ to lie between the pair of horizontal lines at the 68% confidence level.

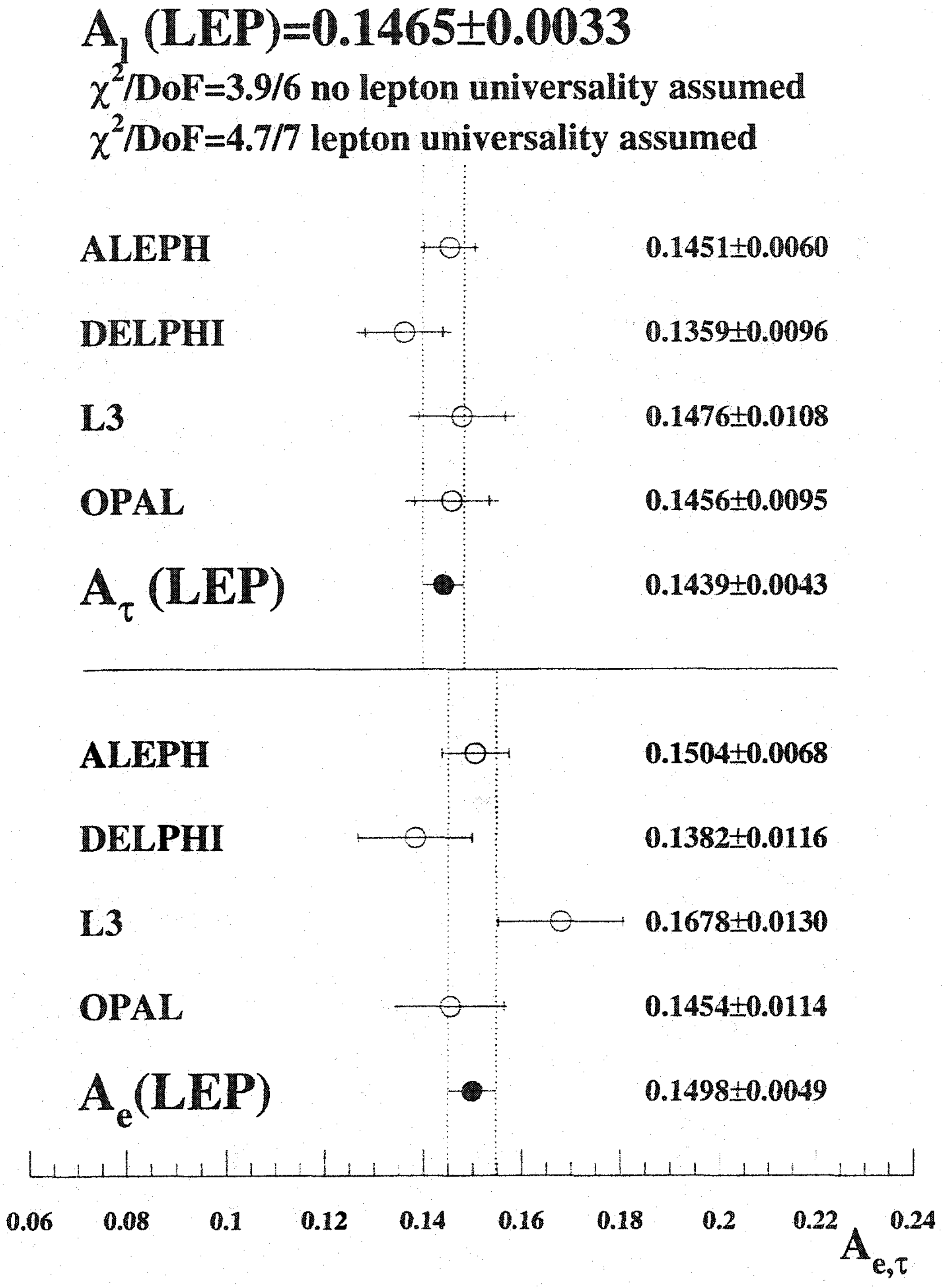

Figure 8.2: LEP combined polarization asymmetry results.

	g_A^e	g_A^μ	g_A^τ	g_V^e	g_V^μ	g_V^τ
g_A^e	1.00	−0.17	−0.13	−0.19	0.07	0.01
g_A^μ	−0.17	1.00	0.29	0.19	−0.46	−0.03
g_A^τ	−0.13	0.29	1.00	−0.04	0.03	−0.08
g_V^e	−0.19	0.19	−0.04	1.00	−0.45	−0.04
g_V^μ	0.07	−0.46	0.03	−0.45	1.00	0.03
g_V^τ	0.01	−0.03	−0.08	−0.04	0.03	1.00

Table 8.6: Error correlation matrix for the measurements of the axial vector and vector couplings, without assuming lepton universality, which are presented in Table 8.5.

Since there are four complementary LEP experiments, each making separate tau polarization measurements, a comparison of these results is discussed first. Figure 8.2 gives the neutral current asymmetry results for each experiment where both A_τ and A_e show good agreement [60]-[62]. The ratio of the combined A_τ and A_e results is also given and indicates that universality holds. Without assuming universality the combined A_τ and A_e results correspond to $\sin^2\theta_{\text{eff}}^{\text{lept}}$ values of

$$\begin{aligned} A_\tau &: \sin^2\theta_{\text{eff}}^{\text{lept}} = 0.23210 \pm 0.00056 \\ A_e &: \sin^2\theta_{\text{eff}}^{\text{lept}} = 0.23136 \pm 0.00065 \end{aligned} \tag{8.8}$$

while the LEP combined A_ℓ measurement from the tau polarization gives [5]

$$A_\ell : \sin^2\theta_{\text{eff}}^{\text{lept}} = 0.23159 \pm 0.00041. \tag{8.9}$$

In addition to the polarization measurements, the LEP experiments also extract estimates of the neutral current asymmetry parameters through measurement of the forward-backward asymmetry A_{FB} [5]. Figure 8.3 gives the corresponding $\sin^2\theta_{\text{eff}}^{\text{lept}}$ results for lepton, b quark, and c quark measurements. These results are consistent with the tau polarization results and of similar precision.

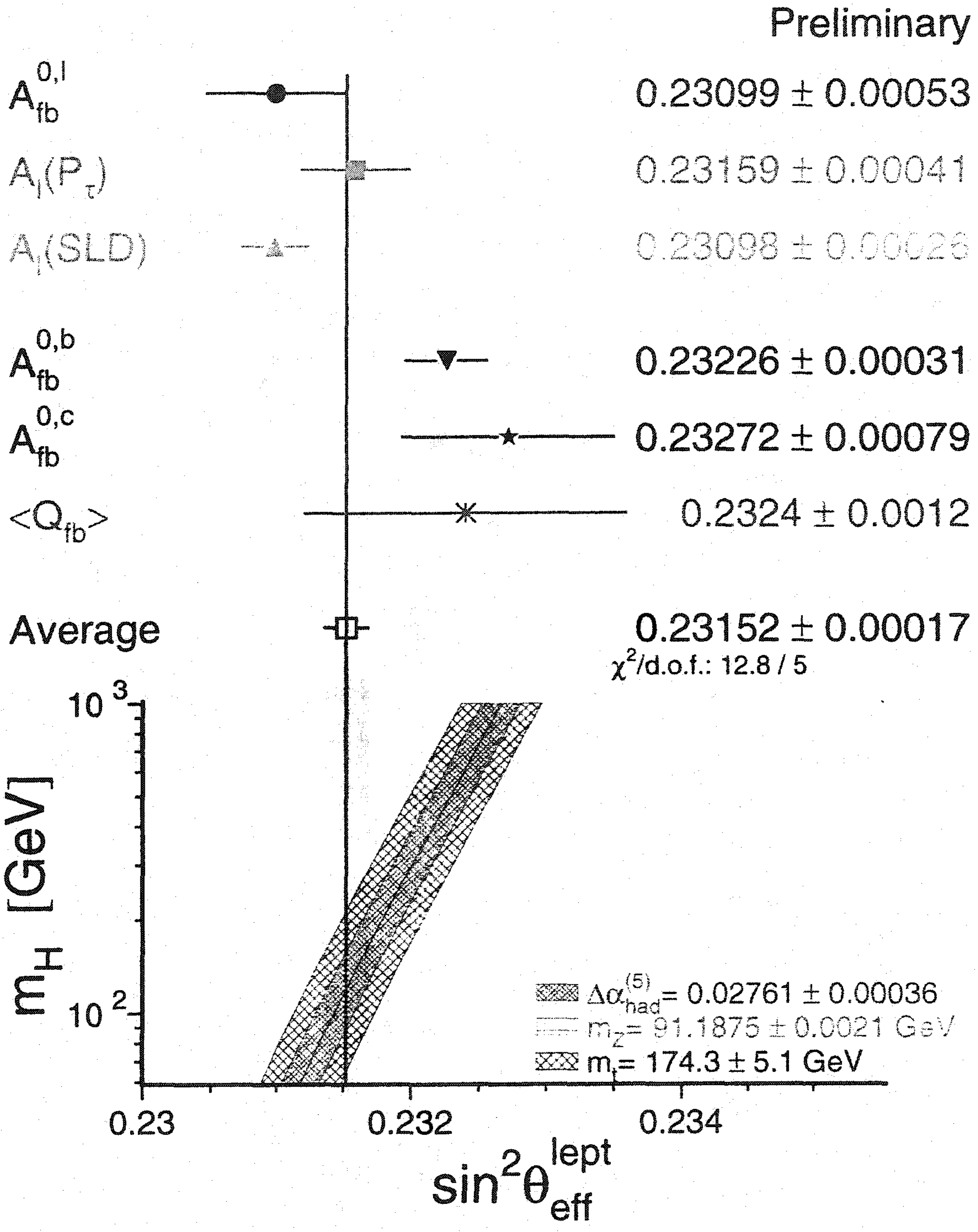

Figure 8.3: Electroweak asymmetry $\sin^2 \theta_{\text{eff}}^{\text{lept}}$ results.

The SLD experiment at the Stanford Linear Collider is able to produce another independent and complimentary measurement of $\sin^2\theta_{\text{eff}}^{\text{lept}}$ [63]. By utilizing polarized electron beams, SLD can measure the left-right asymmetry, A_{LR}, in the production of Z^0 particles. Owing to the parity violating nature of the Z^0 coupling, more Z^0 's are produced with a predominantly left-handed beam than than a right-handed beam.

Combining the A_{LR} measurement with the additional forward-backward asymmetry measurements produces

$$A_\ell \ : \sin^2\theta_{\text{eff}}^{\text{lept}} \ = 0.23152 \pm 0.00017. \tag{8.10}$$

An examination of Figure 8.3 reveals that much of the precision on the combined result can be attributed to two contributions: the SLD measurement and the LEP b-quark forward-backward asymmetry results. But these measurements of $\sin^2\theta_{\text{eff}}^{\text{lept}}$ are not in good agreement with each other; their difference is more than 3 standard deviations away from zero (0.00128 ± 0.00040). However, the combined LEP polarization measurement has essentially the same precision as the b-quark measurement and, interestingly enough, has a central value between the SLD and b-quark measurements. It is still not clear that the disagreement can be attributed to statistical fluctuations, but the inclusion of the tau polarization measurements indicates that such an assumption may be reasonable.

This is a clear illustration of the necessity of making numerous complimentary measurements of the fundamental standard model parameters and underlines the significance of the tau polarization measurement.

As noted in Chapter 2, in addition to the importance of measuring $\sin^2\theta_{\text{eff}}^{\text{lept}}$ as a fundamental parameter in itself, it turns out that the measured value of $\sin^2\theta_{\text{eff}}^{\text{lept}}$, in the context of the standard model, is sensitive to the mass of the Higgs particle. $\sin^2\theta_{\text{eff}}^{\text{lept}}$ is also sensitive to the mass of the top quark, but using as input the measured top mass from the Tevatron experiments [9][10], an indirect measurement of the Higgs mass can be made. Figure 8.3 indicates that the combined measurements of $\sin^2\theta_{\text{eff}}^{\text{lept}}$ favour a light Higgs on the order of 100 GeV [5]. When all electroweak data is combined, the indirect measurement of the mass of a standard model Higgs particle is 60^{+52}_{-29} GeV.

8.4 Summary

Precision measurements of the tau polarization asymmetries, extracted from data collected by the OPAL detector at LEP, have been presented.

The analysis requires the initial selection of high purity tau pair events, followed by the selection of tau decays corresponding to five polarization sensitive tau decay modes. Events have been selected in as large a fiducial acceptance as possible in order to improve statistics and maximize sensitivity. In particular, events are selected within a polar acceptance of $|\cos\theta| < 0.9$.

Detailed systematic studies have been carried out to determine the sensitivity of the analysis to both physics and detector related uncertainties. The cross-channel correlations among the selected tau decay channels have properly been accounted for during these studies. Numerous additional cross-checks on the stability of the results have been carried out, all of which indicate that the accuracy of the results may be viewed with confidence.

The polarization asymmetries provide precise determinations of the neutral current asymmetry parameters

$$\begin{aligned} \mathrm{A}_\tau &= 0.1456 \pm 0.0076 \pm 0.0057, \\ \mathrm{A}_e &= 0.1454 \pm 0.0108 \pm 0.0036. \end{aligned} \tag{8.11}$$

A comparison of these parameters provides a test of lepton universality in the neutral weak sector. The results indicate that the lepton universality hypothesis holds, and hence the results may be combined to produce an accurate measurement of the lepton neutral current asymmetry

$$\mathrm{A}_\ell = 0.1455 \pm 0.0073. \tag{8.12}$$

As described in Chapter 2, the neutral coupling asymmetry parameters are related to the ratio of neutral current vector and axial vector coupling constants and thereby to the weak mixing angle. Thus the primary goal of the analysis is to make a precise determination of the weak mixing angle

$$\sin^2\theta_{\mathrm{eff}}^{\mathrm{lept}} = 0.23172 \pm 0.00092. \tag{8.13}$$

This result can be combined with the analogous results from the other LEP experiments and finally compared and combined with the complementary measurements of $\sin^2\theta_{\rm eff}^{\rm lept}$ indicated in Figure 8.3. The noted potential discrepancy among the results emphasizes the importance of the tau polarization contribution to these measurements of the fundamental standard model parameter. $\sin^2\theta_{\rm eff}^{\rm lept}$.

Appendix A

$\tau \rightarrow \rho\nu_\tau$ ω Variable

The ω variable constructed from $\tau \rightarrow \rho\nu_\tau$ decay information is given by [16][18]

$$\omega_\rho = \frac{\mathrm{W_R}(\cos\theta^*, \cos\psi) - \mathrm{W_L}(\cos\theta^*, \cos\psi)}{\mathrm{W_R}(\cos\theta^*, \cos\psi) + \mathrm{W_L}(\cos\theta^*, \cos\psi)}, \tag{A.1}$$

where

$$\begin{aligned}
\mathrm{W_{R(L)}}(\theta, \psi) &= \frac{3}{8(\mathrm{m}_\tau^2 + 2\mathrm{m}_\rho^2)} \\
& [\quad (1 + \mathrm{P}_\tau)\sin^2\psi[(\mathrm{m}_\tau \sin\eta\cos\frac{\theta^*}{2} - \mathrm{m}_\rho\cos\eta\sin\frac{\theta^*}{2})^2 + \mathrm{m}_\rho^2\sin^2\frac{\theta^*}{2}] \\
& + \quad (1 - \mathrm{P}_\tau)\sin^2\psi[(\mathrm{m}_\tau \sin\eta\sin\frac{\theta^*}{2} + \mathrm{m}_\rho\cos\eta\cos\frac{\theta^*}{2})^2 + \mathrm{m}_\rho^2\cos^2\frac{\theta^*}{2}] \\
& + \quad 2(1 + \mathrm{P}_\tau)\cos^2\psi(\mathrm{m}_\tau\cos\eta\cos\frac{\theta^*}{2} + \mathrm{m}_\rho\sin\eta\sin\frac{\theta^*}{2})^2 \\
& + \quad 2(1 - \mathrm{P}_\tau)\cos^2\psi(\mathrm{m}_\tau\cos\eta\sin\frac{\theta^*}{2} - \mathrm{m}_\rho\sin\eta\cos\frac{\theta^*}{2})^2 \,].
\end{aligned} \tag{A.2}$$

Here, m_ρ is the ρ mass, m_τ is the tau mass, and η represents the Wigner rotation angle given by

$$\cos^2\eta = \frac{\mathrm{m}_\tau^2 - \mathrm{m}_\rho^2 + (\mathrm{m}_\tau^2 + \mathrm{m}_\rho^2)\cos\theta^*}{\mathrm{m}_\tau^2 + \mathrm{m}_\rho^2 + (\mathrm{m}_\tau^2 - \mathrm{m}_\rho^2)\cos\theta^*}, \tag{A.3}$$

and recalling that

$$\begin{aligned}
\cos\theta^* &= \frac{2\mathrm{m}_\tau^2\mathrm{x}_\rho - \mathrm{m}_\tau^2 - \mathrm{m}_\rho^2}{\mathrm{m}_\tau^2 - \mathrm{m}_\rho^2}, \\
\cos\psi &= \frac{\mathrm{m}_\rho}{\sqrt{\mathrm{m}_\rho^2 - 4\mathrm{m}_\pi^2}}(2x_\rho - 1),
\end{aligned} \tag{A.4}$$

with $\mathrm{x}_\rho = \mathrm{E}_\rho/\mathrm{E}_\tau$.

Setting $P_\tau = +1$ gives the distribution for completely right-handed $\tau \rightarrow \rho\nu_\tau$ decays, $W_R(\cos\theta^*, \cos\psi)$, while setting $P_\tau = -1$ gives the distribution for completely left-handed $\tau \rightarrow \rho\nu_\tau$ decays, $W_L(\cos\theta^*, \cos\psi)$

Appendix B

$\tau \rightarrow \mathrm{a}_1\ \nu_\tau\ \omega$ Variable

The ω variable constructed from $\tau \rightarrow \mathrm{a}_1\ \nu_\tau$ decay information is given by [64][65][16]

$$\omega_{\mathrm{a}_1} = \frac{\mathrm{R_R} - \mathrm{R_L}}{\mathrm{R_R} + \mathrm{R_L}}, \tag{B.1}$$

where $\mathrm{R_{R(L)}}$ is the $\tau \rightarrow \mathrm{a}_1\ \nu_\tau$ decay distribution for right(left)-handed decays given by

$$\mathrm{R_{R(L)}}(\cos\theta^*, \cos\psi, \gamma, \mathrm{s}, \mathrm{s}_1, \mathrm{s}_2) \propto \sum_{\mathrm{X=A,C,D,E}} \mathrm{L_X W_X}, \tag{B.2}$$

where $\mathrm{L_X}$ and $\mathrm{W_X}$ are the leptonic and hardonic tensor functions respectively, given below, and the distribution depends on the six variables defined Table B.1. The polarization dependence if found in the leptonic tensor functions $\mathrm{L_X}$; the right-handed distribution,

$\cos\theta^*$	the angle θ^* between the a_1 and τ momenta in the τ rest frame
$\cos\psi$	the angle ψ between the perpendicular to the a_1 decay plane and the a_1 flight direction in the rest frame of the a_1
γ	the angle γ in the a_1 rest frame between the unlike-sign pion momentum in the a_1 rest frame and the a_1 flight direction projected into the a_1 decay plane
s	the 3π-invariant mass-squared
s_1	the invariant mass-squared of the $\pi^+\pi^-$ combination with the higher value
s_2	the invariant mass-squared of the $\pi^+\pi^-$ combination with the lower value

Table B.1: The six observables used in the construction of the $\tau \rightarrow \mathrm{a}_1\ \nu_\tau\ \omega$ variable are presented.

R_R, is obtained by setting $P_\tau = +1$ and the left-handed distribution, R_L, is obtained by setting $P_\tau = -1$. Note that the factor γ_{VA} is the negative of the tau neutrino helicity which is assumed to be left-handed ($\gamma_{VA} = 1$) in this analysis. Additional hadronic structure functions for the more general case of decays to 3 mesons vanish for the 3 pion case of interest here; hence the sum in Equation B.2 is over (A,C,D,E).

B.1 Leptonic Tensor Functions L_X

The leptonic tensor functions for $\tau \rightarrow a_1\ \nu_\tau$ decays relevant to this analysis are

$$\begin{aligned}
L_A &= \frac{2}{3}K_1 + K_2 + \frac{1}{3}\bar{K}_1(3\cos^2\psi - 1)/2 \\
L_C &= -\frac{1}{2}\bar{K}_1 \sin^2\psi \cos 2\gamma \\
L_D &= \frac{1}{2}\bar{K}_1 \sin^2\psi \sin 2\gamma \\
L_E &= \bar{K}_3 \cos\psi
\end{aligned}$$

where

$$\begin{aligned}
K_1 &= 1 - \gamma_{VA}P_\tau\ \cos\theta^* - (\frac{m_\tau^2}{s})(1 + \gamma_{VA}P_\tau\ \cos\theta^*) \\
K_2 &= \frac{m_\tau^2}{s}(1 + \gamma_{VA}P_\tau\ \cos\theta^*) \\
K_3 &= \gamma_{VA} - P_\tau\ \cos\theta^* \\
\bar{K}_1 &= K_1(3\cos^2\eta - 1)/2 - \frac{3}{2}K_4 \sin 2\eta \\
\bar{K}_3 &= K_3\cos\eta - K_5\sin\eta \\
K_4 &= \sqrt{\frac{m_\tau^2}{s}}\gamma_{VA}P_\tau\ \sin\theta^* \\
K_5 &= \sqrt{\frac{m_\tau^2}{s}}P_\tau\ \sin\theta^* \\
\cos\eta &= \frac{m_\tau^2 - s + (m_\tau^2 + s)\cos\theta^*}{m_\tau^2 + s + (m_\tau^2 - s)\cos\theta^*}.
\end{aligned}$$

B.2 Hadronic Structure Functions W_X

The hadronic structure functions for $\tau \rightarrow a_1 \nu_\tau$ decays relevant to this analysis are

$$\begin{aligned}
W_A &= -V_1^2|F_1|^2 - V_2^2|F_2|^2 - 2V_1V_2\mathrm{Re}(F_1F_2^*) \\
W_C &= -(V_1^2+2h)|F_1|^2 - (V_2^2+2h)|F_2|^2 - (2V_1V_2-4h)\mathrm{Re}(F_1F_2^*) \\
W_D &= -\sqrt{h}\{2\sqrt{-V_1^2-h}|F_1|^2 - 2\sqrt{-V_2^2-h}|F_2|^2\} \\
&\quad + \frac{1}{s\sqrt{h_0}}(s - m_\pi^2 + s_3)(s_1 - s_2)\mathrm{Re}(F_1F_2^*) \\
W_E &= 3\sqrt{hh_0}\mathrm{Im}(F_1F_2^*)
\end{aligned}$$

where

$$\begin{aligned}
V_1^2 &= -(s_2 - 4m_\pi^2) - (s_3 - s_1)^2/(4s) \\
V_2^2 &= -(s_1 - 4m_\pi^2) - (s_3 - s_2)^2/(4s) \\
V_1V_2 &= -(s/2 - s_3 - m_\pi^2/2) - (s_3 - s_1)(s_3 - s_2)/(4s) \\
h_0 &= -4m_\pi^2 + (2m_\pi^2 - s_1 - s_2)^2/s \\
h &= (s_1s_2s_3 - m_\pi^2(s - m_\pi^2)^2)/(h_0 s) \\
s_3 &= \text{invariant mass-squared of the two like-sign pions}
\end{aligned}$$

and F_1 and F_2 are model dependent form factors [64][65]. In the Kuhn-Santamaria model used by this analysis, the form factors are given by

$$\begin{aligned}
F_1(s_1, s_2, s) &= -\frac{2\sqrt{2}i}{3f_{a\rho\pi}}B_{W_{a_1}}(s)B_\rho(s_2) \\
F_2(s_1, s_2, s) &= F_1(s_2, s_1, s),
\end{aligned}$$

where $B_{W_{a_1}}(s)$ and $B_\rho(s_2)$ denote a_1 and ρ Breit-Wigner resonances respectively and $f_{a\rho\pi}$ is the coupling strength.

Appendix C

Tau Decay Branching Ratios

Decay Mode	Branching Ratio
$\tau \rightarrow \mathrm{e}^- \bar{\nu}_e \nu_\tau$	0.178199 ± 0.000600
$\tau \rightarrow \mu^- \bar{\nu}_\mu \nu_\tau$	0.173582 ± 0.000700
$\tau \rightarrow \pi^- \nu_\tau$	0.110703 ± 0.001230
$\tau \rightarrow \pi^- \pi^0 \nu_\tau (\rho)$	0.253817 ± 0.001438
$\tau \rightarrow \pi^- \pi^+ \pi^- \nu_\tau (\mathrm{a}_1)$	0.096005 ± 0.001320
$\tau \rightarrow \pi^- \pi^0 \pi^0 \nu_\tau (\mathrm{a}_1)$	0.091060 ± 0.001420
$\tau \rightarrow \mathrm{K}^- \nu_\tau$	0.006944 ± 0.000270
$\tau \rightarrow \mathrm{K}^- \pi^0 \nu_\tau (\mathrm{K}^*)$	0.004484 ± 0.000330
$\tau \rightarrow \pi^- \mathrm{K}^0 \nu_\tau (\mathrm{K}^*)$	0.008933 ± 0.000400
$\tau \rightarrow \pi^- \pi^+ \pi^- \pi^0 \nu_\tau$	0.044103 ± 0.001170
$\tau \rightarrow \pi^- \pi^0 \pi^0 \pi^0 \nu_\tau$	0.013515 ± 0.001100
$\tau \rightarrow \pi^- \pi^+ \pi^- \pi^+ \pi^- \nu_\tau$	0.000770 ± 0.000060
$\tau \rightarrow \pi^- \pi^+ \pi^- \pi^+ \pi^- \pi^0 \nu_\tau$	0.000212 ± 0.000050
$\tau \rightarrow \mathrm{K}^- \pi^+ \mathrm{K}^+ \nu_\tau$	0.001548 ± 0.000145
$\tau \rightarrow \mathrm{K}^0 \pi^- \overline{\mathrm{K}}^0 \nu_\tau$	0.001156 ± 0.000200
$\tau \rightarrow \mathrm{K}^- \pi^0 \mathrm{K}^0 \nu_\tau$	0.001535 ± 0.000210
$\tau \rightarrow \pi^0 \pi^0 \mathrm{K}^- \nu_\tau$	0.000560 ± 0.000240
$\tau \rightarrow \mathrm{K}^- \pi^- \pi^+ \nu_\tau$	0.001757 ± 0.000850
$\tau \rightarrow \pi^- \overline{\mathrm{K}}^0 \pi^0 \nu_\tau$	0.001757 ± 0.000850
$\tau \rightarrow \pi^- \pi^+ \pi^- \pi^0 \pi^0 \nu_\tau$	0.004921 ± 0.000404
$\tau \rightarrow \pi^- \pi^+ \pi^- \pi^0 \pi^0 \pi^0 \nu_\tau$	0.001165 ± 0.000800
$\tau \rightarrow \pi^- \pi^0 2\gamma \nu_\tau$	0.000659 ± 0.000094
$\tau \rightarrow \pi^- \pi^0 3\pi^0 \nu_\tau$	0.000542 ± 0.000077
$\tau \rightarrow \pi^- \pi^0 \pi^+ \pi^- \gamma \nu_\tau$	0.000083 ± 0.000012
$\tau \rightarrow \pi^- \pi^0 \gamma \nu_\tau$	0.000470 ± 0.000565
$\tau \rightarrow \mathrm{K}^0 \mathrm{K}^- \nu_\tau$	0.001521 ± 0.000170

Table C.1: Branching ratios and errors corresponding to each of the 26 TAUOLA tau decay modes calculated from the PDG fit values [4] and used as input to this analysis.

Appendix D

Additional Non-tau Background Rejection and Quality Cuts

D.1 Pre-Decay Selection Cuts

The non-tau background cuts described in this section are specifically designed to improve muon pair and $e^+e^- \to e^+e^-$ non-tau background rejection. The first three sets of cuts discussed target the $e^+e^- \to \mu^+\mu^-$ background while the last removes additional $e^+e^- \to e^+e^-$ background.

Events in which the most energetic track from both tau jets is pointing towards a detector region without active muon chambers are rejected if

$$\begin{array}{rcl} \theta_{\mathrm{acol}} & < & 1.2^\circ, \\ \mathrm{E}^{\tau^-}_{\mathrm{max}} < 2\ \mathrm{GeV} & \mathrm{OR} & \mathrm{E}^{\tau^+}_{\mathrm{max}} < 2\ \mathrm{GeV}, \\ \mathrm{E}^{\tau^-}_{\mathrm{tot}}/\mathrm{E}_{\mathrm{beam}} < 0.5 & \mathrm{AND} & \mathrm{E}^{\tau^+}_{\mathrm{tot}}/\mathrm{E}_{\mathrm{beam}} < 0.5, \text{ and} \\ \mathrm{P}^{\mathrm{tot}}_{\mathrm{trk}}/\mathrm{E}_{\mathrm{beam}} & > & 1.5, \end{array}$$

where θ_{acol} is the acolinearity between the two tau jets, $\mathrm{E}^{\tau^\pm}_{\mathrm{max}}$ is the most energetic cluster associated to the $\tau^\pm$ jet, $\mathrm{E}^{\tau^-}_{\mathrm{tot}}/\mathrm{E}_{\mathrm{beam}}$ is the total jet cluster energy divided by beam energy, and $\mathrm{P}^{\mathrm{tot}}_{\mathrm{trk}}/\mathrm{E}_{\mathrm{beam}}$ is the total track momentum divided by the beam energy.

When at least one of the tau jets has its most energetic track pointing towards a detector region without active muon chambers, an event is rejected if

$$\theta_{\mathrm{acop}} \ < \ 0.4^\circ,$$

$$\begin{aligned} \mathrm{E}^{\mathrm{cls}}_{\mathrm{tot}}/\mathrm{E}_{\mathrm{beam}} &< 0.8. \\ \mathrm{P}^{\tau^-}_{\mathrm{max}}/\mathrm{E}_{\mathrm{beam}} > 0.8 \quad \mathrm{OR} \quad & \mathrm{P}^{\tau^+}_{\mathrm{max}}/\mathrm{E}_{\mathrm{beam}} > 0.8, \text{ and} \\ \mathrm{P}^{\mathrm{tot}}_{\mathrm{trk}}/\mathrm{E}_{\mathrm{beam}} &> 1.5. \end{aligned}$$

where θ_{acop}, the acoplanarity, is the angle in the transverse plane between the direction of the momentum of the most energetic jet and the negative of the direction of the second most energetic jet, $\mathrm{E}^{\mathrm{cls}}_{\mathrm{tot}}$ is the total event cluster energy, $\mathrm{P}^{\tau^\pm}_{\mathrm{max}}$ is the most energetic track associated to the $\tau^\pm$ jet.

The final muon pair cuts remove potential background in cases where the most energetic track is close to an anode or cathode plane in the CJ. Such events in the overlap and endcap regions are rejected if

$$\begin{aligned} |\cos\theta_{\tau^-}| &> 0.76, \\ \theta_{\mathrm{acop}} &< 1.0^\circ, \text{ and} \\ \mathrm{E}^{\mathrm{cls}}_{\mathrm{tot}} &< 5.0\ \mathrm{GeV}. \end{aligned}$$

and either

$$6.5^\circ < mod(\phi_{trk(P_{max})}, 15^\circ) < 8.5^\circ,$$

or

$$14.5^\circ < \mathrm{mod}(\phi_{trk(P_{max})}, 15^\circ) < 0.5^\circ,$$

where $\phi_{trk(P_{max})}$ is the ϕ position of the most energetic track in the event. Note that, in the OPAL CJ, anode planes correspond to $\phi = 7^\circ$ and cathode planes to $\phi = 15^\circ$.

Analogous to the first two sets of cuts designed to reduce muon pair background, an additional cut designed to reduce $\mathrm{e}^+\mathrm{e}^- \rightarrow \mathrm{e}^+\mathrm{e}^-$ background in the endcap region is applied. Events with

$$\begin{aligned} |\cos\theta_{\tau^-}| &> 0.85, \text{ and} \\ \mathrm{E}^{\mathrm{cls}}_{\mathrm{tot}}/\mathrm{E}_{\mathrm{beam}} &> 1.6, \end{aligned}$$

are rejected since such events are, to a high degree of probability, $\mathrm{e}^+\mathrm{e}^- \rightarrow \mathrm{e}^+\mathrm{e}^-$ background events.

D.2 Post-Decay Selection Cuts

Since the predominant non-tau backgrounds arise from production of various fermion anti-fermion pairs, it is important to recognize that the non-tau events will tend to populate specific tau pair event classes. In particular, $e^+e^- \to \mu^+\mu^-$ and $\gamma\gamma\mu^+\mu^-$backgrounds will tend to be selected as μ-μ, μ-nid, and μ-π tau pair events; $e^+e^- \to e^+e^-$ and $\gamma\gamma e^-e^-$ backgrounds will contaminate e-e, and e-nid events; while the $e^+e^- \to q\bar{q}$ backgrounds will predominantly occur in the a_1 -a_1 and a_1 -nid classes.

In order to further reduce the non-tau backgrounds contaminating these tau pair identification classes, additional event cuts are applied after the tau decay selections are applied.

In cases where both taus in an event are identified as decaying to muons, the event is rejected when

$$\begin{aligned} \mathrm{P}_{\mathrm{trk}}^{\mathrm{tot}}/\mathrm{E}_{\mathrm{beam}} &> 0.9, \text{and} \\ \theta_{\mathrm{acop}} &< 2.0^\circ, \end{aligned}$$

and either

$$7.25^\circ < \mathrm{mod}(\phi_{trk(P_{max})}, 15) < 7.75^\circ,$$

$$\text{OR}$$

$$\mathrm{P}_{\mathrm{max}}^{\tau^\pm}/\mathrm{E}_{\mathrm{beam}} > 0.88 \quad ,$$

are true. Tau pair events classed as μ-μ are also rejected if

$$\begin{aligned} \mathrm{P}_{\mathrm{trk}}^{\mathrm{tot}}/\mathrm{E}_{\mathrm{beam}} &> 1.4, \\ \mathrm{P}_{\mathrm{trk}}^{\mathrm{max}}/\mathrm{E}_{\mathrm{beam}} &> 0.75, \text{and} \\ \theta_{\mathrm{acop}} &< 0.25^\circ, \end{aligned}$$

where $\mathrm{P}_{\mathrm{trk}}^{\mathrm{max}}/\mathrm{E}_{\mathrm{beam}}$ is the momentum of the most energetic track in the event.

A tight acoplanarity cut placed on tau pair events classified with one tau decaying through the muon channel and the other decaying through any channel but the electron, given by

$$\begin{aligned} \mathrm{P}_{\mathrm{trk}}^{\mathrm{max}}/\mathrm{E}_{\mathrm{beam}} &> 0.8, \text{ and} \\ \theta_{\mathrm{acop}} &< 0.2^\circ, \end{aligned}$$

further reduces the non-tau background in these classes. For the specific cases in which the second tau is identified as decaying through the $\tau \rightarrow \pi\ \nu_\tau$ channel, events are rejected when

$$\begin{aligned} \mathrm{P}_{\mathrm{trk}}^{\tau\rightarrow\ \mu\bar{\nu}_\mu\nu_\tau}/\mathrm{E}_{\mathrm{beam}} &> 0.85, \text{ and} \\ \theta_{\mathrm{acop}} &< 1.0^\circ. \end{aligned}$$

Electron pair events are the dominate background in the e-e tau pair class. A reduction of this background is effected by rejecting events in this classification when

$$\begin{aligned} \mathrm{E}_{\mathrm{tot}}^{\mathrm{cls}}/\mathrm{E}_{\mathrm{beam}} &> 1.0, \\ \mathrm{P}_{\mathrm{trk}}^{\mathrm{tot}}/\mathrm{E}_{\mathrm{beam}} &> 1.0, \text{ and} \\ \theta_{\mathrm{acop}} &< 0.2^\circ, \end{aligned}$$

or when

$$\mathrm{E}_{\mathrm{tot}}^{\mathrm{cls}}/\mathrm{E}_{\mathrm{beam}} > 1.8.$$

Additional $e^+e^- \rightarrow e^+e^-$ background, contaminating tau pair events in which at least one tau is identified as decaying through the electron channel, is removed by rejecting events when

$$\begin{aligned} \mathrm{E}_{\mathrm{tot}}^{\mathrm{cls}}/\mathrm{E}_{\mathrm{beam}} &> 1.2, \\ \mathrm{P}_{\mathrm{trk}}^{\mathrm{tot}}/\mathrm{E}_{\mathrm{beam}} &> 1.6, \text{ and} \\ \theta_{\mathrm{acop}} &< 0.2^\circ. \end{aligned}$$

or when

$$\begin{aligned} \mathrm{E}_{\mathrm{tot}}^{\mathrm{cls}}/\mathrm{E}_{\mathrm{beam}} &> 1.5, \\ \mathrm{P}_{\mathrm{trk}}^{\mathrm{tot}}/\mathrm{E}_{\mathrm{beam}} &> 1.6, \text{ and} \\ \theta_{\mathrm{acop}} &< 0.5^\circ. \end{aligned}$$

Tau pair events categorized as e-π are also rejected as $e^+e^- \to e^+e^-$ background if

$$\begin{aligned} P_{\mathrm{trk}}^{\tau\to\,\pi\,\nu_\tau}/E_{\mathrm{beam}} &> 0.85, \text{ and} \\ E_{\mathrm{tot}}^{\tau\to\,e\bar{\nu}_e\nu_\tau}/E_{\mathrm{beam}} &> 0.85, \end{aligned}$$

and events categorized as e-nid are rejected if the most energetic track associated to the nid tau jet has

$$E_{\mathrm{ass}}/p > 0.8.$$

Finally, in addition to the preceding post-decay selection cuts, a final set of cuts is applied in order to reduce background arising from muon chamber acceptance holes.

Tau pair events in which at least one tau is selected as $\tau\to\pi\,\nu_\tau$ are rejected if

$$\begin{aligned} 75^\circ < \mathrm{mod}(\phi_{\mathrm{trk}}^{\tau\to\,\pi\,\nu_\tau}.\,180) &< 105^\circ, \\ \cos\theta_{\mathrm{trk}}^{\tau\to\,\pi\,\nu_\tau} &> 0.7, \\ P_{\mathrm{trk}}^{\tau\to\,\pi\,\nu_\tau} &> 30\ \mathrm{GeV}, \\ E_{\mathrm{max}}^{\tau\to\,\pi\,\nu_\tau} &< 10\ \mathrm{GeV}, \text{ and} \\ P_{\mathrm{trk}}^{\mathrm{opp}} &> 20\ \mathrm{GeV}, \end{aligned}$$

where $P_{\mathrm{trk}}^{\mathrm{opp}}$ is the momentum of the highest energy track in the tau jet opposite the $\tau\to\pi\nu_\tau$ candidate.

Similary, tau pair events in which at least one tau is selected as $\tau\to\mu\bar{\nu}_\mu\nu_\tau$ are rejected if

$$\begin{aligned} 75^\circ < \mathrm{mod}(\phi_{\mathrm{trk}}^{\tau\to\,\mu\bar{\nu}_\mu\nu_\tau}.\,180) &< 105^\circ, \\ \cos\theta_{\mathrm{trk}}^{\tau\to\,\mu\bar{\nu}_\mu\nu_\tau} &> 0.6, \\ P_{\mathrm{trk}}^{\tau\to\,\mu\bar{\nu}_\mu\nu_\tau} &> 30\ \mathrm{GeV}, \text{ and} \\ P_{\mathrm{trk}}^{\mathrm{opp}} &> 15\ \mathrm{GeV}, \end{aligned}$$

where $P_{\mathrm{trk}}^{\mathrm{opp}}$ is the momentum of the highest energy track in the tau jet opposite the $\tau\to\mu\bar{\nu}_\mu\nu_\tau$ candidate.

D.3 Miscellaneous Quality Cuts

Various additional quality cuts are applied to remove tau jets with particles entering problematic detector regions or exhibiting features that indicate potential measurement errors. Such cuts include the rejection of tau jets with a primary track near to an anode plane, of jets emerging towards gaps in the ECAL, and of events with apparent charge misidentification.

Potential CJ track mismeasurements can occur for tracks emerging near anode planes. In order to reduce effects associated with such tracks, a series of cuts is applied to remove tau jets in which the primary track is close to an anode plane.

First, the simple geometric cut

$$7.0^\circ < \mathrm{mod}(\phi_{\mathrm{trk}}, 15) < 8.0^\circ$$

is applied to remove jets in which the most energetic track is within 0.5° of an anode plane. For jets containing only a single charged track, the upper limit for rejection is increased to 8.25°.

Next, single track jets are further removed if the associated track has one or fewer CV axial wire hits associated with it and

$$7.0^\circ < \mathrm{mod}(\phi_{\mathrm{trk}}, 15) < (7.75 + 7.75/P_{\mathrm{trk}}^{\mathrm{trans}})^\circ$$

where $P_{\mathrm{trk}}^{\mathrm{trans}}$ is the transverse momentum of the track.

Finally, single track jets are also rejected if $\mathrm{mod}(\phi_{\mathrm{trk}}, 15) < 8.5^\circ$ and

$$7.0^\circ < \mathrm{mod}(\phi_{\mathrm{trk}}, 15) < (8.0 + 2.4/P_{\mathrm{trk}}^{\mathrm{trans}})^\circ.$$

Since the ECAL detector does contain small regions of poor coverage, single track tau jets with the track pointing towards these regions are removed. Such jets are rejected when

$$0.213 < \ |\cos\theta_{\mathrm{trk}}|\ < 0.216$$

$$\mathrm{OR}$$

$$0.596 < \ |\cos\theta_{\mathrm{trk}}|\ < 0.598$$

or when

$$89.75^\circ < \mathrm{mod}(\phi_{\mathrm{trk}}, 180) < 90.25^\circ.$$

Finally, a last quality cut is applied to remove the small fraction tau pair events which exhibit charge misassignment. Since track charge is determined from the track curvature measured by the CJ, charge misassignment implies a potentially large error in track momentum measurement.

Thus, all tau pair events in which both taus have been classified as decaying through one of the five channels of interest, and in which the total event charge is non-zero, are rejected. Here, the total event charge is calculated as the sum of the charge of all tracks in the event which are not identified as conversions.

Bibliography

[1] F. Halzen and A.D. Martin, *Quarks & Leptons*, (John Wiley & Sons, Toronto, 1984).

[2] P. Renton, *Electroweak Interactions*, (Cambridge University Press, Cambridge, 1990).

[3] D.H. Perkins, *Introduction to High Energy Physics*, (Addison-Wesley Publishing Company, Inc., Don Mills, 1987).

[4] *Review of Particle Properties* Eur. Phys. J. **C 15** (2000).

[5] The LEP Collaborations ALEPH, DELPHI, L3 and OPAL, the LEP Electroweak Working Group, and the SLD Heavy Flavour and Electroweak Groups, *A Combination of Preliminary LEP Electroweak Measurements and Constraints on the standard model*, CERN-EP-2001-021, February 2001.

[6] ALEPH, DELPHI, L3 and OPAL Collaborations and the LEP working group for Higgs boson searches, *Search for the Standard Model Higgs Boson at LEP*, CERN-EP-2001-055, July 2001.

[7] P. W. Higgs, Phys. Lett. **12** (1964), 132.

[8] G. Abbiendi *et al.* [OPAL Collaboration], hep-ex/0103045.

[9] T. Affolder *et al.* [CDF Collaboration], Phys. Rev. **D63** (2001), 032003.

[10] B. Abbott *et al.* [D0 Collaboration], Phys. Rev. **D58** (1998), 052001.

[11] S. Glashow, Nucl. Phys. **22**(1961), 579;

S. Weinberg, Phys. Rev. Lett. **19**(1967), 1264;

A. Salam, *Elementary Particle Theory*, ed. N. Svartholm (Almquist and Wiksells, Stockholm, 1968), 367.

[12] Y. Tsai, in *C71-08-24.03* Phys. Rev. **D4** (1971), 2821 [Erratum-ibid. **D13** (1971), 771].

[13] E. D. Commins, S. B. Ross, D. DeMille and B. C. Regan, Phys. Rev. **A50** (1994), 2960.

[14] C. S. Wu, E. Ambler, R. W. Hayward, D. D. Hoppes and R. P. Hudson, Phys. Rev. **105** (1957) 1413.

[15] G. Abbiendi *et al.* [OPAL Collaboration], Eur. Phys. J. C **19** (2001), 587.

[16] A. Rouge, *In Orsay 1990, Proceedings, Tau lepton physics (QCD161:W671:1990) 213-222, and Preprint - Rouge, A. (rec.Mar.91) 10 p.*

[17] K. Hagiwara, A. D. Martin and D. Zeppenfeld, Phys. Lett. B **235** (1990), 198.

[18] M. Davier, L. Duflot, F. Le Diberder and A. Rouge, Phys. Lett. B **306** (1993), 411.

[19] G. . Altarelli, R. . Kleiss and C. . Verzegnassi, *Geneva, Switzerland: CERN (1989) 453 p. CERN Geneva - CERN 89-08 (89,rec.Dec.), 453 p.*

[20] D. Bardin, P. Christova, M. Jack, L. Kalinovskaya, A. Olchevski, S. Riemann and T. Riemann, "ZFITTER v.6.21: A semi-analytical program for fermion pair production in e+ e- annihilation," Comput. Phys. Commun. **133** (2001), 229.

[21] K. Ahmet *et al.* [OPAL Collaboration], Nucl. Instrum. Meth. **A305** (1991), 275.

[22] S. Myers, CERN-91-08 *Presented at CERN Accelerator School: The LEP Collider from Design to Approval and Commissioning, Geneva, Switzerland, Nov 26, 1990, CAS: CERN accelerator school, 6th John Adams Memorial lecture.*

[23] Lep Injector Study Group Collaboration, "Lep Design Report. Vol. 1. The Lep Injector Chain," CERN-LEP/TH/83-29.

[24] P. P. Allport *et al.* [OPAL Collaboration], Nucl. Instrum. Meth. **A346** (1994), 476.

[25] J. R. Carter *et al.*, Nucl. Instrum. Meth. **A286** (1990), 99.

[26] H. M. Fischer *et al.*, Nucl. Instrum. Meth. **A283** (1989), 492.

[27] H. Mes *et al.*, Nucl. Instrum. Meth. **A265** (1988), 445.

[28] P. Mattig, Private Communication (OPAL Technical Note TN324).

[29] G. Artusi *et al.*, Nucl. Instrum. Meth. **A279** (1989), 523.

[30] G. Abbiendi *et al.* [OPAL Collaboration], Eur. Phys. J. **C13** (2000), 213.

[31] R. J. Akers *et al.*, Nucl. Instrum. Meth. **A357** (1995), 253.

[32] M. Arignon *et al.*, Nucl. Instrum. Meth. **A313** (1992), 103.

[33] B. Vokurka, Private Communication (OPAL Technical Note TN433 (1996)).

[34] L. Arnaudon *et al.*, Z. Phys. **C66** (1995), 45.

[35] J. Allison *et al.*, Nucl. Inst. and Meth. **A317** (1992) 47.

[36] R. Brun, F. Bruyant, M. Maire, A.C. McPherson, and P. Zanarini, *GEANT3*, CERN DD/EE/84-1 (1987).

[37] S. Jadach, B.F.L Ward and Z. Wąs, (KORALZ 3.8) Comp. Phys. Comm. **66** (1991) 276;

S. Jadach, B.F.L Ward and Z. Wąs, (KORALZ 4.0) Comp. Phys. Comm. **79** (1994) 503;

S. Jadach, B. F. Ward and Z. Was, (KORALZ 4.02) Comp. Phys. Comm. **124** (2000) 233.

Events were generated with KORALZ 4.02 setting $s'/s > 0.00156$ and TAUOLA

2.6 with four pion decays modelled according to:
R. Decker, M. Finkemeier, P. Heiliger and H. H. Jonsson, Z. Phys. **C70** (1996) 247.

[38] S. Jadach, W. Placzek and B.F.L. Ward, (BHWIDE) Phys.Lett. **B390** (1997) 298.

[39] S. Jadach, J.H. Kühn and Z. Wąs, (TAUOLA) Comp. Phys. Comm. **64** (1990) 275;
S. Jadach, *et al.*, (TAUOLA 2.4) Comp. Phys. Comm. **76** (1993) 361.

[40] R. Battacharya, J. Smith and G. Grammer, Phys. Rev. **D15** (1977) 3267;
J. Smith, J.A.M. Vermaseren and G. Grammer, Phys. Rev. **D15** (1977) 3280.

[41] T. Sjöstrand, Comp. Phys. Comm. **39** (1986) 347;
M. Bengtsson and T. Sjöstrand, Comp. Phys. Comm. **43** (1987) 367;
M. Bengtsson and T. Sjöstrand, Nucl. Phys. **B289** (1987) 810.

[42] OPAL Collab., P. Acton *et al.*, Z. Phys. **C58** (1993) 387.

[43] (PHOJET 1.05c used with JETSET 7.408):
R. Engel and J. Ranft, Phys. Rev. **D54** (1996) 4244;
R. Engel, Z. Phys. **C66** (1995) 203;
A. Buijs, W. G. Langeveld, M. H. Lehto and D. J. Miller, (TWOGEN) Comp. Phys. Comm. **79** (1994) 523.

[44] G. Marchesini, B. R. Webber, G. Abbiendi, I. G. Knowles, M. H. Seymour and L. Stanco, hep-ph/9607393.

[45] J. Hilgart, R. Kleiss, F. Le Diberder, Comp. Phys. Comm. **75** (1993) 191.

[46] J. Fujimoto *et al.*, Comput. Phys. Commun. **100** (1997) 128 [hep-ph/9605312].

[47] OPAL Collab., G. Alexander *et al.*, Z. Phys. **C72** (1996) 365.

[48] OPAL Collaboration, Z. Phys. **C53**(1992), 539.

[49] M. A. Thomson, Private Communication (OPAL Technical Note TN490).

[50] D. Karlen, Computers in Physics, 12:4 (1998) 380.

[51] M. A. Thomson, Nucl. Instrum. Meth. **A382** (1996), 553.

[52] F. James and M. Roos, Comp. Phys. **10**(1975), 343.

[53] R. Barlow and C. Beeston, Comp. Phys. Comm. **77** (1993) 219.

[54] R. L. Gluckstern, Nucl. Instrum. Meth. **24** (1963), 381.

[55] J.H. Kühn and A. Santamaria Z. Phys. **C48** (1990) 445;
J.H. Kühn and E. Mirkes, Z. Phys. **C56** (1992) 661.

[56] OPAL Collab., R. Akers *et al.*, Z. Phys. **C67** (1995) 45.

[57] N. Isgur, C. Morningstar and C. Reader, Phys. Rev. **D39** (1989) 1357.

[58] P. R. Poffenberger, Z. Phys. **C71** (1996) 579.

[59] K. W. Edwards *et al.* [CLEO Collaboration], Phys. Rev. **D61** (2000), 072003.

[60] A. Heister *et al.* [ALEPH Collaboration], hep-ex/0104038.

[61] P. Abreu *et al.* [DELPHI Collaboration], Eur. Phys. J. **C14** (2000) 585.

[62] M. Acciarri *et al.* [L3 Collaboration], Phys. Lett. **B429** (1998) 387.

[63] K. Abe *et al.* [SLD Collaboration], Phys. Rev. Lett. **86** (2001), 1162.

[64] J. H. Kuhn and E. Mirkes, Z. Phys. **C56** (1992), 661 [Erratum-ibid. **C67** (1992), 364].

[65] T. Geralis and W.G. Scott, Private Communication (OPAL Technical Note TN271).